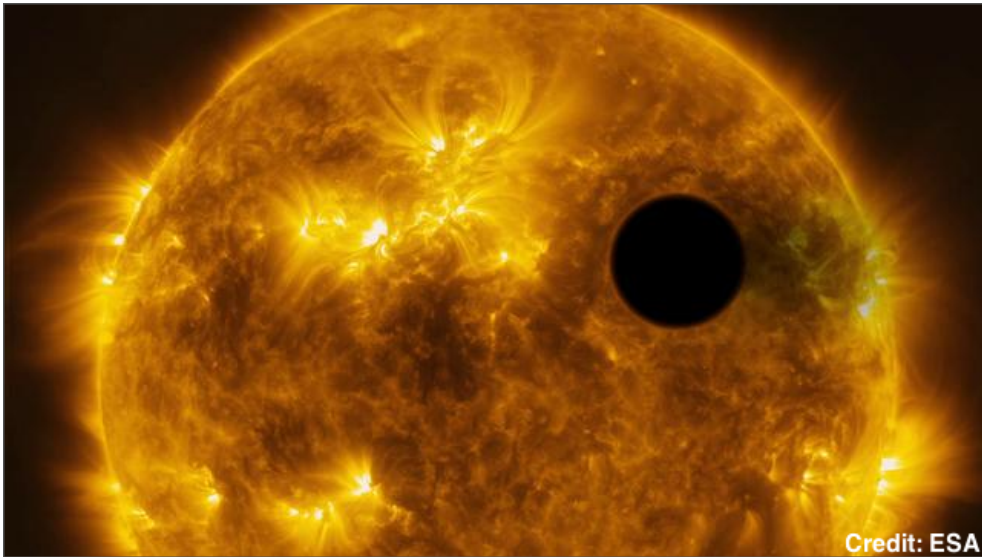


Transmission Spectroscopy: First Glimpses of Far-Off Worlds



Catherine Mary Huitson

Submitted by Catherine Mary Huitson to the University of Exeter as a thesis for the degree of Doctor of Philosophy in Physics, September, 2013.

This thesis is available for Library use on the understanding that it is copyright material and that no quotation from the thesis may be published without proper acknowledgement.

I certify that all material in this thesis which is not my own work has been identified and that no material has previously been submitted and approved for the award of a degree by this or any other University.

Signed:

Catherine Huitson

Date:

Abstract

Since the first discovery of a transiting planet in 2000, transmission spectroscopy has proved essential for characterising the rapidly increasing number of known exoplanets. When a planet is in a favourable alignment, it periodically passes (transits) in front of its host star, during which time it blocks a fraction of the stellar light. During a transit, the starlight passes through the planetary atmosphere, causing the signatures of atoms or molecules present in that atmosphere to imprint themselves on the stellar spectrum, allowing direct observation of a planet's atmospheric composition. At the start of this thesis, only two planets (HD 189733b and HD 209458b) had been studied in any detail, mainly from space. The two planets showed surprisingly different qualities for two objects with only a small temperature difference between them, and motivated both wider and more detailed studies of the exoplanet population. Since the start of my PhD, the amount of exoplanet knowledge has grown rapidly, with observations from the ground becoming important, and with studies branching out towards new planets. There are several contributions made by this thesis to the field.

Chapter 3 details the detection of the resolved sodium D doublet in the atmosphere of HD 189733b, a planet with a featureless broad-band transmission spectrum dominated by Rayleigh scattering. The results confirmed the presence of sodium absorption as well as resolving the feature for the first time, and placing constraints on relative abundances. Furthermore, in Chapter 4, I outline a method based on earlier work which allows observers to retrieve atmospheric temperature information from resolved spectral features. This method is applied to the observations of HD 189733b, showing that the planet has a hot thermosphere similar to HD 209458b. The models are then also used in later chapters.

I then present the first results from a ground-based optical long-slit spectroscopic survey in Chapter 5, and the first results from a space-based optical-near-IR spectroscopic survey in Chapter 6. From the ground, I detect absorption from sodium in the atmosphere of XO-2b, making this the first planet with sodium and potassium detected in its atmosphere. I also find that the Na I D feature lacks broad line wings, suggesting haze or cloud cover. From space, I observed the transmission spectrum of WASP-19b, finding solar abundance water features and a likely lack of predicted TiO features. WASP-19b is the first planet to have confirmed water features at solar-abundance level. In Chapter 7, I conclude and discuss future work, including a project aimed at understanding why WASP-19b lacks TiO features, and projects which move beyond the hot Jupiter class.

Contents

1	Introduction	16
1.1	Context and Focus	16
1.1.1	Context and History	16
1.1.2	The Focus of this Thesis	17
1.2	Known Exoplanets	18
1.2.1	Detection Methods	18
1.2.2	Properties of Known Exoplanets	19
1.2.3	Population Statistics	19
1.3	The Transit Method	21
1.3.1	Analytic Transit Models	23
1.3.2	Transit Transmission Spectroscopy	24
1.3.3	Limb Darkening	26
1.3.4	Stellar Spots	29
1.4	Introduction to Secondary Eclipses	32
1.4.1	Secondary Eclipse Spectroscopy and Day Side Temperature Profiles	33
1.4.2	Bond Albedo and Thermal Recirculation Efficiency	34
1.4.3	Phase Curves	37
1.5	Literature Review on Exoplanet Atmospheres	38
1.5.1	Model Predictions for Hot Jupiters	38
1.5.2	Observations of Well-Studied Targets	46
1.5.3	Further Observations of More Planets	56
1.6	Challenges for the Future and My Contribution	66
2	Research Methodology	68
2.1	Instrumental and Observational Techniques	68
2.1.1	Spectroscopy	68
2.1.2	Detector Types Used in this Thesis	71
2.1.3	Sources of Noise	73
2.1.4	Observational Techniques	75

2.2	Instruments Used for this Thesis	77
2.2.1	The Hubble Space Telescope (HST)	77
2.2.2	The Grand Telescopio Canarias (GTC)	80
2.2.3	Cerro Tololo Inter-American Observatory (CTIO)	81
2.2.4	Summary	83
2.3	Analysis Techniques	84
2.3.1	Least Squares Fitting	84
2.3.2	Markov Chain Monte Carlo (MCMC)	88
2.3.3	Nelder-Mead Simplex Algorithm	89
2.3.4	Quantifying Uncertainties and the Goodness of Fit	90
3	Transmission Spectroscopy of Sodium in HD 189733b with HST STIS	96
3.1	Aims and Introduction	96
3.2	Observations and Data Reduction	97
3.2.1	Observations	97
3.2.2	Extracting Spectra	98
3.3	HST STIS Light Curve Fitting	99
3.3.1	Limb Darkening	101
3.4	Analysis	103
3.4.1	Spectral Absorption Depth Profile of the Na I Doublet	103
3.4.2	Integrated Absorption Depth Profile of the Na I Doublet	107
3.4.3	The Effect of Occulted Starspots	109
3.4.4	Broadband 5808-6380 Å Spectrum	111
3.5	Discussion	115
3.5.1	The Optical Transmission Spectrum of HD 189733b	115
3.5.2	Interpretation of the Narrow Absorption Lines	116
3.6	Summary and Conclusions	119
4	Measuring Atmospheric Temperature Profiles from Transmission Spec-	
	troscopy	121
4.1	Aims and Introduction	121
4.2	The Model Spectral Absorption Depth Profile	123
4.3	Determining Upper Atmospheric Temperatures from an Absorption Profile	126
4.3.1	Reference Pressure and Pressure Scales	128
4.4	Applications to Specific Planets	129
4.4.1	Applying the Models to Sodium Observations of HD 189733b	130
4.4.2	Applying the Models to Sodium Observations of HD 209458b	141
4.5	Summary and Conclusions	145

5	GTC Long-Slit Transmission Spectroscopy of XO-2b	147
5.1	Aims and Introduction	147
5.2	Observations	149
5.2.1	Reduction	150
5.3	Analysis	152
5.3.1	Parameterised Slit Losses	154
5.3.2	Common-Mode Slit Losses and Differential Transmission Spectra	156
5.3.3	Extracting the Planetary Transmission Spectrum	158
5.4	Discussion	161
5.4.1	Atmospheric Model Fits	161
5.4.2	Comparison with Previous Observations of Potassium	165
5.4.3	Future Observations	165
5.5	Conclusions	166
6	The First Results from the Optical HST Transmission Spectral Survey of Hot Jupiters	168
6.1	Aims and Introduction	168
6.2	Observations and Data Reduction	170
6.3	STIS Analysis	177
6.3.1	Un-occulted Spot Correction	177
6.3.2	De-Trending the STIS White Light Curves	183
6.3.3	Optical Transmission Spectra	187
6.3.4	Searching for Specific Optical Features	195
6.4	WFC3 Analysis	203
6.4.1	De-Trending the WFC3 Light Curves	203
6.4.2	System Parameters	207
6.4.3	Near-IR Transmission Spectrum	208
6.5	Discussion	210
6.5.1	Optical to Near-IR Transmission Spectrum of WASP-19b	211
6.5.2	Optical Transmission Spectrum	213
6.5.3	Significance of the Near-IR Water Features	215
6.5.4	Interpretation	219
6.6	Conclusions	221
7	Conclusions	224
7.1	Summary of Achievements	225
7.1.1	The Medium-Resolution Transmission Spectrum of HD 189733b	225

7.1.2	The Upper Atmospheric Terminator T - P Profiles of HD 189733b and HD 209458b	225
7.1.3	Transmission Spectrum of XO-2b Using Ground-Based Long-Slit Spectroscopy	226
7.1.4	The Optical to Near-IR Transmission Spectrum of WASP-19b	226
7.2	Further Work	227
7.2.1	Current Projects	228
7.2.2	Future Projects	229
7.3	Final Thoughts	230
	Appendices	232
A	Constants	232
B	Acronyms	233
C	Definitions	235
D	Derivations	245
D.1	Transit Geometry	245
D.2	Derivation of Atmospheric Scale Height	250
D.3	Derivation of the Barometric Law	251
D.4	Determining Day-Side Temperature from Secondary Eclipse Depth	251
D.5	Day-Side Temperature as a Function of Different Recirculation Factors	252
D.6	Equations for Grating Spectrometers	254

List of Figures

1.1	Masses and Orbital Periods of Known Exoplanets	19
1.2	Figure Showing Population Statistics of Known Exoplanets	20
1.3	Illustration of a Primary Transit and Resulting Light Curve	21
1.4	Optical Depth at the Transit Radius vs. Ratio of Planetary Radius to Scale Height	25
1.5	Predicted Signals in Transit of Known Exoplanets	26
1.6	Plot Showing the Effects of Limb Darkening at Different Wavelengths .	27
1.7	Plots Showing the Effect of Occulted Starspots on a Transit Light Curve	30
1.8	Illustration of a Primary and Secondary Transit and the Resulting Light Curve	32
1.9	Model Cloudless and Cloudy Transmission Spectra	40
1.10	Model Cloudless Transmission Spectrum Using GCM	40
1.11	Model Transmission Spectra including TiO	41
1.12	Atmospheric Models of Sulphur Chemistry	43
1.13	Model Transmission Spectra for Different C/O Ratios	44
1.14	Different Model Clear Atmosphere Transmission Spectra	45
1.15	Optical-Near-IR Transmission Spectrum of HD 209458b	48
1.16	Literature Temperature-Pressure Profile of HD 209458b	49
1.17	Current Observed Properties of HD 189733b	52
1.18	Infra-Red Transmission Spectra of GJ 1214b	55
1.19	Optical Transmission Spectra of GJ 1214b	56
1.20	Transmission Spectra of WASP-12b	59
1.21	Emission Spectra of WASP-19b	61
1.22	Figure Showing Possible Correlation Between Stellar Activity and Strato- spheres	62
1.23	Figure Showing Recirculation Efficiencies as a Function of Irradiation .	63
1.24	Figure Showing Thermal Phase Variations as a Function of Irradiation	65
2.1	Diagram of a Diffraction Grating	70
2.2	Response of WFC3 Detector with Increasing Count Levels	73

2.3	Photograph of the Hubble Space Telescope in Space	77
2.4	Photograph of the Grand Telescopio Canarias at La Palma	80
2.5	Photograph of the SMARTS Telescopes at the CTIO	81
2.6	Light Path for CTIO 1.3 m Instrument ANDICAM	82
3.1	Example HST STIS CCD Output Spectrum	98
3.2	Raw STIS G750M White Light Curves	99
3.3	STIS G750M White Light Curves With Systematics Removed	100
3.4	Differential Limb Darkening in the Line Core of Visit 55	105
3.5	Spectral Absorption Depth Profile of Na I In HD 189733b	106
3.6	Averaged Integrated Absorption Depth Profile of Sodium in HD 189733b	107
3.7	Integrated Absorption Depth Profile of Sodium in HD 189733b in Spot- ted and Non-Spotted Exposures	110
3.8	Spotted Exposures in Transit with Best Fitting Spot Models for HD 189733b	111
3.9	Light Curve Residuals After Removing Occulted Spots	112
3.10	Occulted Spot Amplitudes as a Function of Wavelength for G750M Band	113
3.11	STIS Transmission Spectrum of HD 189733b in 100 Å Bins From 5808- 6380 Å	114
3.12	Comparison of the G750M Results with Broad-Band Data	116
4.1	Schematic of a Planetary Transit	124
4.2	Model Na I Absorption Profiles Calculated Using Voigt Functions	128
4.3	Transmission Spectrum of Sodium in HD 189733b as a Function of Planetary Altitude	131
4.4	Doppler (Red) Shift as a Function of Planetary Phase due to the Planet's Motion	132
4.5	Doppler (Red) Shift as a Function of Planetary Phase for an HST Visit	133
4.6	Isothermal Model Fits to Na I Data in HD 189733b	134
4.7	Temperature-Altitude Profile for HD 189733b	136
4.8	Altitude-Pressure Profile for HD 189733b at Derived Temperatures	138
4.9	Altitude-Pressure Profile for HD 189733b at $T = 2800$ K	138
4.10	Terminator T - P Profile for HD 189733b	140
4.11	Integrated AD Profile for HD 209458b along with a Model Profile	142
4.12	Terminator T - P Profiles for HD 189733b and HD 209458b	144
5.1	Image of GTC Long-Slit Spectra on the CCD	149
5.2	Lamp Image used for Wavelength Calibrating GTC Spectra	151
5.3	Example GTC R500R and R500B Grism Spectra of XO-2b	152
5.4	White Light Curves for GTC Spectra of XO-2b	153

5.5	GTC R500R White Light Curve With Slit-Loss Parameterization Model	155
5.6	GTC Light Curves for Different Bands after De-trending using White Light Residuals	156
5.7	Wavelength and Time Dependence of GTC Slit-Loss Systematics . . .	157
5.8	Correlation Coefficients for Each Wavelength When De-trending using Common Mode Method	158
5.9	Differential Spectrum of XO-2b Around the Na I Feature	159
5.10	The Effects of Using Different Spectral and Reference Bins on the XO-2b Transmission Spectrum	160
5.11	Differential Transit Light Curve around the Sodium Feature Compared to the Continuum	161
5.12	Standard Model Fit to the XO-2b Transmission Spectrum	162
5.13	Analytic Model Fits to the Transmission Spectrum of XO-2b at Different Temperatures	163
5.14	Model Fit to the XO-2b Transmission Spectrum Assuming a Narrow Na I Feature	163
5.15	Theoretical Temperature-Pressure Profiles for XO-2b	164
5.16	Preliminary Light Curve of XO-2b Using 10 Arcsecond Slit	167
6.1	Residual Plot of Difference in Counts Between Different WFC3 Reads for WASP-19b	173
6.2	Difference in Counts Between Different WFC3 Reads for WASP-19b Compared to Photon Noise Level	175
6.3	Extracted Spectrum of WASP-19 from Each Read for the Brightest Exposure	176
6.4	Raw STIS White Light Curves of WASP-19b Transits	177
6.5	Long-Duration Variability Monitoring Photometry of WASP-19	181
6.6	De-Trended STIS White Light Curves for WASP-19b Transits	184
6.7	Model Wavelength-Dependent Un-occulted Spot Dimming for the G750L Range	188
6.8	Raw Light Curves for G750L Spectral Bins	190
6.9	G750L Transmission Spectrum of WASP-19b	191
6.10	STIS G430L Transit Light Curves of WASP-19b in Spectral Bins	193
6.11	Stellar Spot Spectrum Measured from Occulted Spots Compared to Models	194
6.12	Differential Optical Transit Light Curves for TiO and K I Features	198
6.13	Differential ADs in the K I Feature Compared to the Continuum for Various Band Sizes	200
6.14	Na I Bandwidths Compared with STIS G750L Sensitivity Curve	201

6.15 Planetary Radius Ratios in the Na I Feature for Various Band Sizes . . .	202
6.16 WFC3 Raw White Light Curve of WASP-19b Transit	204
6.17 WFC3 Corrected White Light Curve of WASP-19b Transit Using Divide- oot	205
6.18 WFC3 Corrected White Light Curve of WASP-19b Transit Using a Pa- rameterised Model	206
6.19 Transit Light Curves of WASP-19b for WFC3 Spectral Bins	208
6.20 WFC3 Transmission Spectrum of WASP-19b	209
6.21 Model Wavelength-Dependent Un-occulted Spot Dimming for the G141 Band	211
6.22 Model T - P Profiles Used for the Model Transmission Spectra of WASP- 19b	212
6.23 STIS WASP-19b Transmission Spectrum Compared to Models	213
6.24 Optical Transmission Spectra of WASP-19b in 400 and 200 Angstrom Bins	215
6.25 WFC3 Transmission Spectrum Compared to Atmospheric Models	216
6.26 Differential Stellar Spectra at Different Temperatures Using High Reso- lution Models	218
1 Illustration Showing the Relationship Between Inclination and Impact Parameter	245
2 Illustration of the Planet at First Contact with its Host Star	246
3 Illustration of Transit Duration as a Function of Inclination	246
4 Figures Illustrating Transit Geometry	248
5 Illustration of the Path of Light through a Transmission Grating	254
6 Illustration of the Path of Light through a Reflection Grating	255

List of Tables

2.1	STIS gratings used in this project	78
2.2	GTC OSIRIS grisms used in this project	81
2.3	Summary of Observations Used in this Project	83
3.1	Dates and Notes for all HST STIS G750M Visits for HD 189733b	97
3.2	Goodness of Fit for Different Parameters in STIS G750M Light Curves	102
3.3	Spectrum Absorption Depth of Na I In HD 189733b at Each Wavelength	106
3.4	Na I Absorption Depths for Each Bandwidth in HD 189733b	108
3.5	Radius Ratios for HD 189733b in 100 Å Bins from 5808-6380 Å	114
4.1	Fitting Statistics for Various Sodium Models and Temperatures in HD 189733b	135
4.2	Temperature-Pressure Profile Derived from IAD Profile for HD 209458b	143
5.1	List of Targets for the GTC Transmission Spectral Survey	147
6.1	List of Targets for the HST Transmission Spectral Survey	169
6.2	Dates of HST Observations of WASP-19b	170
6.3	Stellar Dimming Values During the STIS Visits Due to Activity	180
6.4	Literature Optical R_P/R_* Values for WASP-19b	186
6.5	Spot Correction Factors Used for Each G750L Band	187
6.6	Limb Darkening Coefficients for Each G750L Band	188
6.7	Fitted R_P/R_* Values for G750L Spectral Bins	191
6.8	Fitted Spot Amplitude Parameters for Each G430L Band	193
6.9	Wavelength Ranges and Model Predictions for Differential Spectral In- dices	197
6.10	Measured Differential Absorption Depth Values for TiO, Na I and K I Features	198
6.11	Fitting Statistics for Different Systematic Removal Methods for WFC3 White Light Curve	206

6.12 System Parameters for the WASP-19 System Determined from WFC3 Data	207
6.13 Limb Darkening Coefficients for WFC3 Spectral Bands	209
6.14 R_p/R_* Values for WASP-19b in WFC3 Spectral Bins	210
1 Constants Used in this Work	232

Declaration

The work described in Chapters 3 to 6 of this thesis have been published in scientific journals in the form of papers written either almost entirely by me, or in the form of papers collaborated on by me.

The work detailed in Chapter 3 is essentially all my own work, although it benefited from discussions with David Sing, Alfred Vidal-Madjar, Frédéric Pont, Gilda Ballester, Alain Lecavelier des Etangs and Jean-Michel Désert. The results are published in Huitson et al. (2012).

The work in Chapter 4 benefitted from being able to compare my models with those calculated previously by Alfred Vidal-Madjar and Alain Lecavelier des Etangs, whose method I followed to construct the models. The part of the chapter focussed on HD 189733b is published in Huitson et al. (2012). The part of the chapter dealing with results for HD 209458b was published in Vidal-Madjar et al. (2011a), where my contribution was to discover an error in the original paper and to use my models to check the revised results. The transmission spectrum was calculated by collaborators.

The work detailed in Chapter 5 was a combined effort between myself and David Sing, although the steps outlined in this thesis describe the contributions that I made specifically. Where I have mentioned results from his part of the work, it is credited. The results appear in Sing et al. (2012), where my contribution was to reduce and analyse one out of two observed transits and to interpret the resulting spectrum from both transits. I therefore wrote large parts of the discussion. David Sing was responsible for both leading and detailing the observations in the paper. Atmospheric models not described in Chapter 4 were provided by Jonathan Fortney.

The work detailed in Chapter 6 is essentially all my own work, although the variability monitoring photometry was reduced by Paul Wilson, and the cosmic ray removal routine was written by Nikolay Nikolov. The model transmission spectra used were provided by Jonathan Fortney and Adam Burrows. The work also benefited from discussions with these and many other collaborators, most notably David Sing, Frédéric Pont, Gilda Ballester, Suzanne Aigrain, Neale Gibson and Drake Deming among others. The work is published in Huitson et al. (2013). Throughout the thesis, I made use of a fitting code adapted from D. Sing.

Publications

- *Temperature-Pressure Profile of the Hot Jupiter HD 189733b from HST Sodium Observations: Detection of Upper Atmospheric Heating*,
Huitson, C. M., Sing, D. K., Vidal-Madjar, A., Ballester, G. E., Lecavelier des Etangs, A., Désert, J.-M., Pont, F., 2012, MNRAS, 422, 2477
- *The Upper Atmosphere of the Exoplanet HD209458b Revealed by the Sodium D Lines: Temperature-Pressure Profile, Ionization Layer and Thermosphere (Corrigendum)*,
Vidal-Madjar, A., **Huitson, C. M.**, Lecavelier Des Etangs, A., Sing, D. K., Ferlet, R., Désert, J.-M., Hébrard, G., Boisse, I., Ehrenreich, D., Moutou, C., 2011, A&A, 533, C4 (Corrigendum to original paper by A. Vidal-Madjar: 2011, A&A, 527, A110)
- *GTC OSIRIS Transiting Exoplanet Atmospheric Survey: Detection of Sodium in XO-2b from Differential Long-Slit Spectroscopy*,
Sing, D. K., **Huitson, C. M.**, Lopez-Morales, M., Pont, F., Désert, J.-M., Ehrenreich, D., Wilson, P. A., Ballester, G. E., Fortney, J. J., Lecavelier des Etangs, A., Vidal-Madjar, A., 2012, MNRAS, 426, 1663
- *An HST Optical to Near-IR Transmission Spectrum of the Hot Jupiter WASP-19b: Detection of Atmospheric Water and Likely Absence of TiO*,
Huitson, C. M., Sing, D. K., Pont, F., Fortney, J. J., Burrows, A. S., Wilson, P. A., Ballester, G. E., Nikolov, N., Gibson, N. P., Deming, D., Aigrain, S., Henry, G. W., Lecavelier des Etangs, A., Showman, A. P., Vidal-Madjar, A., Zahnle, K., MNRAS, accepted, ArXiv:1307.2083.

Acknowledgements

There have been a great many people who have helped me reach this point, and to whom I owe a great deal. Firstly, I am immensely grateful to my PhD supervisor, David Sing, who is both an exceptional supervisor as well as being a huge source of knowledge in the exoplanet field. He has always had time for my questions and has always had the vision to push me further than I thought I was able to go. I am also grateful to others in the department for taking the time to share their wealth of knowledge with me, as well as to collaborators outside the department, especially Frédéric Pont, Nikolay Nikolov, Alfred Vidal-Madjar and Gilda Ballester. I am lucky to have been in such a strong research community during my PhD, allowing for many discussions at the cutting edge of the field.

There are also several people from my undergraduate days at Cardiff to whom I owe special thanks. Firstly, Peter Ade, who first taught me to think like a scientist, and who took the time to shape my thinking during a summer project. I also owe thanks to Haley Gomez for her support during my final year projects, Carole Tucker for her support and advice throughout, and Bernard Richardson who allowed me onto the physics course, despite my having swapped courses several times.

From my personal life, I am eternally grateful to my parents, who have always supported me in my passions. They never pressed me into a particular direction, but allowed me to be free and to make my own choices knowing that they were always behind me. I am also grateful to my husband, Scott Huitson, for putting up with the stress involved in completing a PhD over the recent years, for looking after me when I needed it, and for coming with me on my journey even though it meant making sacrifices. It is wonderful to have someone by my side who truly understands me.

Finally, this work has made extensive use of the NASA/ESA Hubble Space Telescope, the GTC and the CTIO 1.3 m telescope. I am very grateful to the staff of these three instruments for their prompt and thorough replies to so many questions. Throughout my PhD, I have been funded through STFC.

Catherine Huitson
Exeter, U.K.
September 2013

Chapter 1

Introduction

1.1 Context and Focus

1.1.1 Context and History

Although the possibility of life on other worlds has been contemplated for generations, the first discovery of an extrasolar planet came only as recently as 1992, when Wolzszczan & Frail (1992) measured timing variations of pulses from the 6.2 ms pulsar PSR 1257+12. The timing variations suggest that the pulsar is orbited by a planetary system composed of at least two terrestrial type planets of $\sim 3 - 4 M_{\oplus}$.

The first exoplanet¹ discovery was rapidly followed by the first detection of an extrasolar giant planet around a sun-like star, 51 Pegasi b, in 1995 (Mayor & Queloz 1995). Mayor & Queloz (1995) measured orbital motions of the star, which had to be induced by an orbital companion, and found the presence of a Jupiter-mass planet. A further breakthrough occurred when Charbonneau et al. (2000); Henry et al. (2000) found a planet that was inclined in such a way that the planet passed between the star and the observer during its orbit. They confirmed the presence of the planet, HD 209458b, by measuring the resulting flux dimming as the planet crossed in front of the star (transit).

The discovery of transiting exoplanets proved to be very important when, in 2002, Charbonneau et al. (2002) showed that it was possible to detect and characterise their atmospheres as the light from the host star is filtered through the planet's atmosphere during transit. The technique of studying an exoplanet's atmosphere during transit (called transmission spectroscopy) is a very powerful tool for understanding exoplanets, and is the primary focus of this thesis.

¹Short term for "extrasolar planet" i.e. a planet outside of the Solar system.

1.1.2 The Focus of this Thesis

I have used a variety of spectroscopic techniques to study the atmospheres of close-in² gas giant exoplanets. While I feel that the overarching impetus of the exoplanet research field is to one day search for life on other planets, that goal is some time away. In studying the more accessible planetary types, there are two main benefits. Firstly, the observational techniques developed now can be constantly refined to a point where habitable planets can be characterised as new instruments become available. Secondly, close-in giant planets give us access to atmospheric observations of a new planetary type, allowing us to learn a great deal about fundamental atmospheric physics. As such, this thesis focuses on characterisation of “hot Jupiters”, with the use of both existing and new techniques.

The Importance of Studying Hot Jupiters

Hot Jupiters are gas giants which orbit ≤ 0.1 AU from their stellar hosts, and were some of the first exoplanets to be detected. The extreme conditions experienced in hot Jupiter atmospheres provide an important laboratory for the studies of dynamics in a new regime. Hot Jupiters are unlike any planet type in our Solar system, and so their chemistry and formation history is likely to be vastly different from anything that we encounter in the Solar system. Hot Jupiters are also the most favourable targets for atmospheric characterisation due to their low densities and large atmospheric signals.

Although hot Jupiters have dominated characterisation studies, their atmospheric physical processes are still poorly understood. Observations of exoplanet atmospheres are extremely challenging, requiring high precision. The challenges are such that, in many cases, broad atmospheric properties are the only constraints that observations can provide, and very few planets are well understood. In the rest of this chapter, I will provide a brief summary of transit observational techniques as well as a literature review, showing the current scarcity of observations and understanding. The main focus in the methodology section is on transiting planets. I will then outline the goals of this thesis, which aim to improve on the existing literature.

²Planets orbiting close to their host stars.

1.2 Known Exoplanets

1.2.1 Detection Methods

There are several different detection methods for exoplanets, which are sensitive to different populations of planets. The main methods are pulsar timing, radial velocity, transits, direct imaging and gravitational microlensing. Pulsar timing makes use of the fact that millisecond pulsars have very stable rotation periods, and any timing variations can indicate planetary companions. The pulsar timing method can be sensitive to small planets of a few Earth masses. Also sensitive to small planets is the gravitational microlensing method, where planets are detected during events when a foreground star magnifies the light of a background star through gravitational lensing. If the foreground star has a planetary companion, it makes a small contribution to the lensing effect.

At the other end of the scale, radial velocity (RV) and the transit method are most sensitive to large, close-in planets. RV searches infer the possible presence of a planet by the planet's gravitational effect on the host star and the resulting Doppler shift of the stellar spectrum. For planets with favourable inclinations, the planet passes in front of the host star during its orbit, referred to as the transit. During transit, the flux dimming due to the planet's passage can be measured, even though the star and planet are not resolved. Often, transits are used to confirm RV detections. Both transit and RV methods are now starting to be sensitive to small planets if they are close-in to their host stars. The direct imaging method is sensitive to another planetary regime again, since large planets at large orbital distances from their host stars can be directly imaged.

1.2.2 Properties of Known Exoplanets

There are just under 750 known extrasolar planets, for which we know the orbital periods, semi-major axes and lower limits on the masses³. Figure 1.1 shows the masses and orbital periods of the known planets discovered with each of the detection methods.

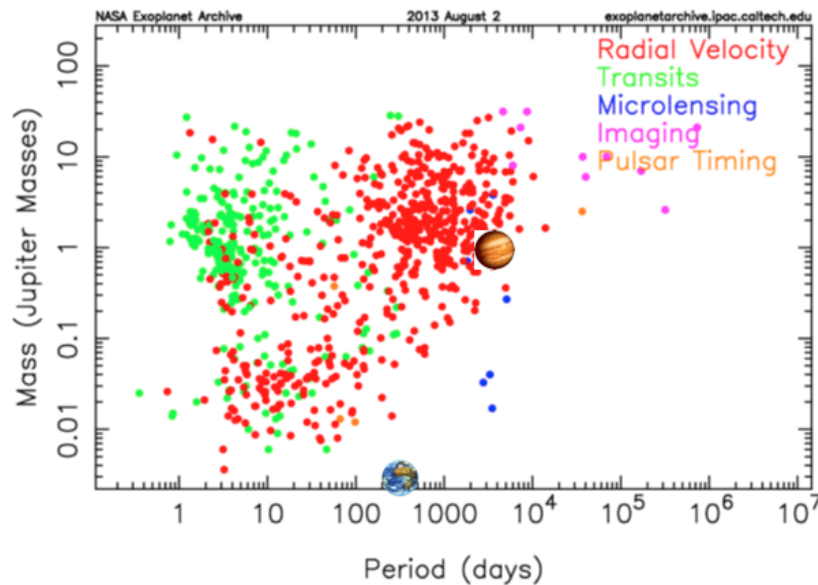


Figure 1.1: Masses and orbital periods of known exoplanets discovered using different detection methods. Plot from the NASA Exoplanet Archive (<http://exoplanetarchive.ipac.caltech.edu/index.html> [accessed 01-Sep-2013]). I have also placed icons on the plot to indicate the properties of Earth and Jupiter.

1.2.3 Population Statistics

In the search towards Earth-like planets, it is important to assess whether the Solar system as a whole represents a typical planetary system and how common the different types of planets are. While no Earth-like planets have been found yet, there are significant numbers of discovered hot Jupiters and super-Earths, and these discoveries give some insights into the types of stellar system that are prevalent. With a large number of exoplanets discovered, some constraints can be placed on the frequency of different types of planet.

The first interesting result from recent surveys is that, although hot Jupiters dominated initial exoplanet detections and still dominate exoplanet characterisation studies, they are comparatively rare, with only $\sim 0.5 - 1.5$ % of stars hosting a hot Jupiter (see Wright et al. 2012 and references therein). Furthermore, most hot Jupiters are not part of multiple-planet systems (Steffen et al. 2012). The occurrence

³Number of known exoplanets from <http://exoplanets.org/> [accessed 01-Sep-2013].

of Jupiter-sized planets in general, however, is higher, with $\sim 10\%$ of stars hosting a gas giant planet (e.g. Cumming et al. 2008).

RV surveys have observed that the frequency of planet occurrence decreases rapidly with increasing planet mass for close-in (< 0.25 AU) planets over all mass ranges studied (Howard et al. 2010; Mayor et al. 2011; Howard 2013). Results from the Kepler space mission⁴ have confirmed the trend found by the RV surveys more confidently for smaller planets, although it uses the transit method of detection and so measures radii rather than masses. Another interesting result is the occurrence frequency of super-Earths and sub-Neptune mass objects, of which there are none in our Solar system. The current surveys suggest that there is no specific scarcity of these kinds of planets. Howard (2013) provide an overview of the statistics in Figure 1.2.

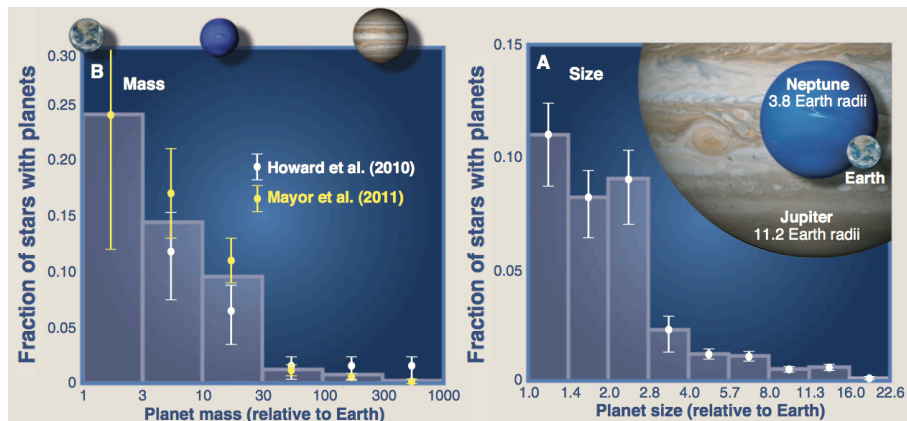


Figure 1.2: Figure adapted from Howard (2013) showing population statistics from RV and Kepler surveys. The left plot shows data from RV surveys with references in the figure. The right plot shows data from Kepler taken from Petigura et al. (2013); Howard et al. (2012).

⁴See http://www.nasa.gov/mission_pages/kepler/ for more information [accessed 01-Sep-2013].

1.3 The Transit Method

During a transit, observers see the planet pass in front of its host star and block some of the stellar light (around 1-2 % for a hot Jupiter). The measurement of the system's flux as a function of time is called a "transit light curve" (see Figure 1.3). There is a lot of information which can be obtained from transiting planets which cannot be obtained for other planets. Around 250 of the known exoplanets are transiting⁵.

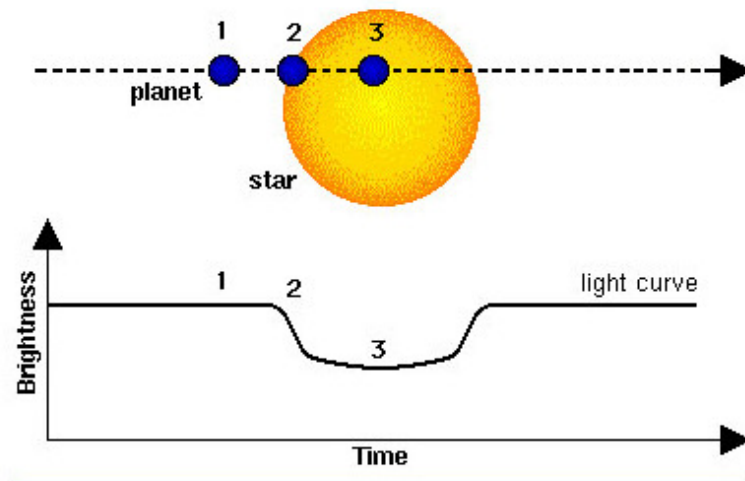


Figure 1.3: Image from Centre National d'Études Spatiales (CNES) showing the flux dimming that is observed as a planet passes in front of a star.

Three important properties can be directly measured from an exoplanet transit: the transit depth, δ , the transit shape, and the transit duration, T_{dur} . Under certain assumptions, the directly measured quantities can be used to obtain important parameters about the planet, such as its radius, R_p , orbital inclination, i , and orbital separation, a . The following equations assume that the planet is dark, that the planetary orbit is circular, that the star is slowly rotating and the stellar disc is circular, and that the stellar disc is of uniform intensity. For a hot Jupiter, the orbital separation between planet and star is small and so the orbits are tidally circularised on short timescales. The assumption that the planet is dark is valid for a tidally locked planet, where the planet always has the same side facing the star and the night side is viewed during transit. The assumption of a slow rotating star, and hence a circular stellar disc, is valid for the Sun (e.g. Gough 2012). I discuss departures from uniform stellar intensity later on in this chapter in Sections 1.3.3 and 1.3.4.

Firstly, the transit depth can be used to measure the area of the planet compared to that of the star (Seager & Mallén-Ornelas 2003). The amount of flux dimming during the transit is equal to the ratio of the stellar and planetary disc areas:

⁵Number of transiting exoplanets from <http://exoplanets.org/> [accessed 01-Sep-2013].

$$\delta = \frac{L_{\star} - L_{\text{transit}}}{L_{\star}} = \frac{4\pi R_{\star}^2 \sigma_{SB} T_{\star}^4 - (4\pi R_{\star}^2 - 4\pi R_{\text{p}}^2) \sigma_{SB} T_{\star}^4}{4\pi R_{\star}^2 \sigma_{SB} T_{\star}^4} = \frac{4\pi R_{\text{p}}^2 \sigma_{SB} T_{\star}^4}{4\pi R_{\star}^2 \sigma_{SB} T_{\star}^4}, \quad (1.1)$$

where L_{\star} is the luminosity of the star, L_{transit} is the luminosity of the system when the planet passes in front of the star and blocks a fraction of light, R_{\star} is the radius of the star, R_{p} is the radius of the planet, σ_{SB} is the Stefan-Boltzmann constant, and T_{\star} is the temperature of the star. Further simplifying gives a very simple relation that enables the planetary radius ratio to be determined from the transit depth:

$$\delta = \frac{R_{\text{p}}^2}{R_{\star}^2}. \quad (1.2)$$

This allows observers to determine the radius of a planet from its transit. The radius of the star is either known or estimated from its spectral type.

The RV method only constrains the minimum mass, $M \sin i$. If the orbit is inclined, observers only see a component of the stellar wobble and hence cannot estimate the planet's true mass. For transiting planets, the orbital inclination can be worked out from the light curve by measuring how long the transit takes, knowing its orbital period, P , from the RV observations, and its orbital separation. Knowing the period means that Kepler's third law can be used to find the orbital separation:

$$\frac{a^3}{P^2} = \frac{G(M_{\star} + M_{\text{p}})}{4\pi^2}. \quad (1.3)$$

Here, a is the orbital separation, P is the orbital period, G is the gravitational constant, M_{\star} is the mass of the star (again estimated from its spectral type) and M_{p} is the mass of the planet (Haswell 2010). Assuming $M_{\text{p}} \ll M_{\star}$ and re-arranging gives

$$a \approx \left(GM_{\star} \left(\frac{P}{2\pi} \right)^2 \right)^{\frac{1}{3}}, \quad (1.4)$$

allowing determination of the of the planet's orbital separation. In this case, it is assumed that M_{\star} and R_{\star} are well known, which is the case for most exoplanet transmission spectroscopy candidates. Assuming $a \gg R_{\star} \gg R_{\text{p}}$, the orbital inclination can be derived from the transit duration:

$$T_{\text{dur}} \approx \frac{P}{\pi} \left[\left(\frac{R_{\star}}{a} \right)^2 - \cos^2 i \right]^{\frac{1}{2}}, \quad (1.5)$$

(derivation in Appendix D.1; see also Seager & Mallén-Ornelas 2003, Haswell 2010). Usually, a planet is confirmed and basic orbital parameters determined before transmission spectroscopy is conducted.

1.3.1 Analytic Transit Models

In order to measure the depth of a planetary transit and hence determine R_p/R_* , the transit shape has to be accurately modelled. In this project, I make use of the analytical models of Mandel & Agol (2002), which compute model transit light curves using the radius ratio, R_p/R_* , and the projected distance between the planet and star centres from the point of view of the observer as input parameters. The algorithm can incorporate non-uniform stellar intensities as defined in Section 1.3.3. The full details of the algorithm including prescriptions for non-uniform intensity are given in Mandel & Agol (2002), but I will provide a brief overview here of the uniform-disc models, since they illustrate the process of fitting a transit light curve.

Below, I use the notation that Mandel & Agol (2002) use, which is that d is the centre-to-centre distance between the planet and the star as seen by the observer, r_p is the radius of the planet, r_* is the radius of the star, $z = d/r_*$ is the normalised separation of the centres and $p = r_p/r_*$ is the radius ratio. The ratio of obscured to unobscured flux is $1 - \lambda(p, z)$, where

$$\lambda(p, z) = \begin{cases} 0 & \text{for } 1 + p < z \\ \frac{1}{\pi} \left[p^2 \kappa_0 + \kappa_1 \right] - \sqrt{\frac{4z^2 - (1+z^2-p^2)^2}{4}} & \text{for } |1 - p| < z \leq 1 + p \\ p^2 & \text{for } z \leq 1 - p \\ 1 & \text{for } z \leq p - 1 \end{cases} \quad (1.6)$$

and, $\kappa_1 = \cos^{-1}[(1 - p^2 + z^2)/2z]$, $\kappa_0 = \cos^{-1}[(p^2 + z^2 - 1)/2pz]$. The top case is where the star is unobscured, the second case is during ingress or egress or for a planet in a grazing orbit, the third is between 2nd and 3rd contact during a transit (where the whole of the planetary disc is in front of the stellar disc) and the fourth is when a planet totally occults a star. Mandel & Agol (2002) provide an IDL implementation of their algorithms, which I make use of, and which is available at <http://www.astro.washington.edu/agol> [accessed 01-Sep-2013]. In order to determine transit parameters from data, I use the algorithm and fit the transit light curve for a value of R_p/R_* and the z parameter which is derived in Appendix D.1 as

$$z = \frac{a}{R_*} \left[\sin^2(2\pi\phi) + \cos^2 i \cos^2(2\pi\phi) \right]^{\frac{1}{2}}, \quad (1.7)$$

where ϕ is the planetary orbital phase, which varies from 0 to 1 throughout the orbit, with the primary transit occurring at $\phi = 0$. In my routines, i and a/R_* are fitted parameters, while I calculate ϕ based on known literature values of the central transit time, T_o , and planetary orbital period. It is, however, possible to fit for these two param-

ters as well, with data of sufficient quality. Usually for transmission spectroscopy, all parameters except for the radius contrast⁶, baseline stellar flux and de-trending parameters are held fixed between different wavelength fits, and so do not affect many of the conclusions.

1.3.2 Transit Transmission Spectroscopy

Aside from the opaque disc of the bulk of the planet causing an observable dimming, atmospheric properties can also be measured from the translucent atmosphere. As the light of the host star passes through the planet's atmosphere, certain wavelengths will be absorbed, depending on the species present in the planet's atmosphere. If a particular wavelength is strongly absorbed by the planetary atmosphere, then more of the stellar light will be blocked during transit, leading to a greater transit depth, and a larger inferred planetary radius. The planetary transit depth (or radius ratio) as a function of wavelength is called the transmission spectrum and is equal to the depth due to the opaque planetary disc plus the wavelength-dependent depth due to the translucent atmosphere, $\Delta z(\lambda)$, (Brown 2001):

$$\delta(\lambda) = \left(\frac{R_P + \Delta z(\lambda)}{R_\star} \right)^2. \quad (1.8)$$

Features in the transmission spectrum allow determination of the elements or molecules present in the atmosphere. The “atmosphere” that is probed for a gas giant is the region above the point where the planet's atmosphere becomes so optically thick that it absorbs all light at all wavelengths. Planets with clouds can prevent radiation from being transmitted deep into the planet, meaning that the observable atmosphere may not be as large in terms of height as for a cloud-free atmosphere.

Under certain assumptions, which are discussed in Chapter 4, it can be shown that the planetary radius measured in transmission spectroscopy minus the radius of the opaque disc is given by

$$\Delta z(\lambda) = \frac{k_B T}{\mu g} \ln \left(\frac{(\sum_i \sigma_i(\lambda) \xi_i) P_o}{\tau_{\text{eq}}} \sqrt{\frac{2\pi R_P}{k_B T \mu g}} \right), \quad (1.9)$$

where k_B is Boltzmann's constant, T is the planet's atmospheric temperature, μ is the mean molecular weight of the atmosphere, g is the surface gravity of the planet's atmosphere, $\sigma_i(\lambda)$ is the absorption cross-section as a function of wavelength for each opacity source, i , in the atmosphere, P_o is the reference pressure for $\Delta z = 0$, ξ_i is the abundance of each opacity source in the atmosphere, τ_{eq} is the optical depth at the

⁶Throughout this thesis, I often use “radius contrast” to refer to the R_P/R_\star ratio.

transit radius, and R_p is the radius of the opaque planetary disc. The optical depth at the transit radius, τ_{eq} , is the optical depth at $\Delta z(\lambda)$, such that a sharp occulting disc of radius $R_p + \Delta z(\lambda)$ produces the same absorption depth as the planet with its translucent atmosphere. Lecavelier Des Etangs et al. (2008a) calculated τ_{eq} by numerical integration and found that the value is constant at 0.56 for $R_p/H \sim 30 - 3000$ (see Figure 1.4). Here H denotes atmospheric pressure scale height⁷, which is the altitude over which pressure changes by a factor e . It is defined as $k_B T / \mu g$ for an atmosphere in hydrostatic equilibrium and which behaves as an ideal gas. The scale height is derived in Appendix D.2 and discussed more in Chapter 4. The assumption of $\tau_{\text{eq}} = 0.56$ is valid in most regions studied in transmission spectroscopy. For example, R_p/H varies from ~ 280 -560 for $T = 1000$ to 2000 K for a typical hot Jupiter.

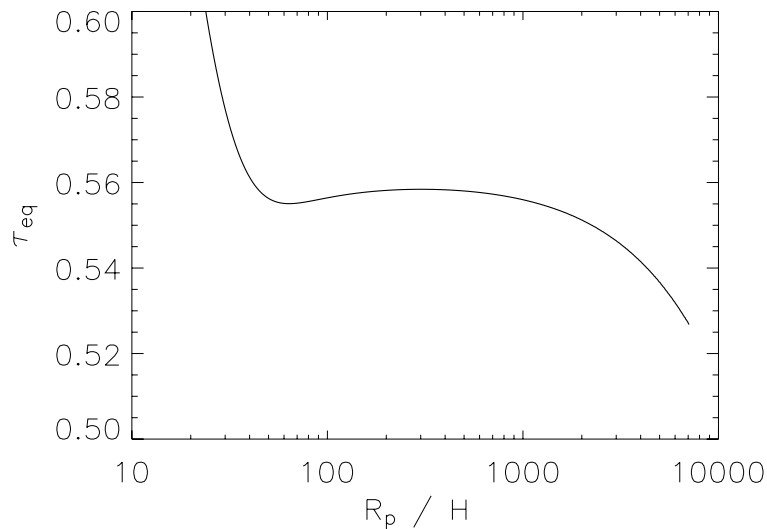


Figure 1.4: Plot from Lecavelier Des Etangs et al. (2008a) showing their calculations of τ_{eq} as a function of the ratio of planetary radius to atmospheric scale height.

Equation (1.9) was first derived by Lecavelier Des Etangs et al. (2008a), and derived in a slightly different form by Guillot (2010). It is used in Chapter 4 to calculate model transmission spectra. Equation (1.9) is useful because it allows an observer to determine whether they are likely to see any spectral features based on the planet’s radius, temperature and surface gravity. Figure 1.5 shows the expected signal strengths for one scale height for known transiting planets.

⁷Note that I often refer to this quantity simply as the “scale height”.

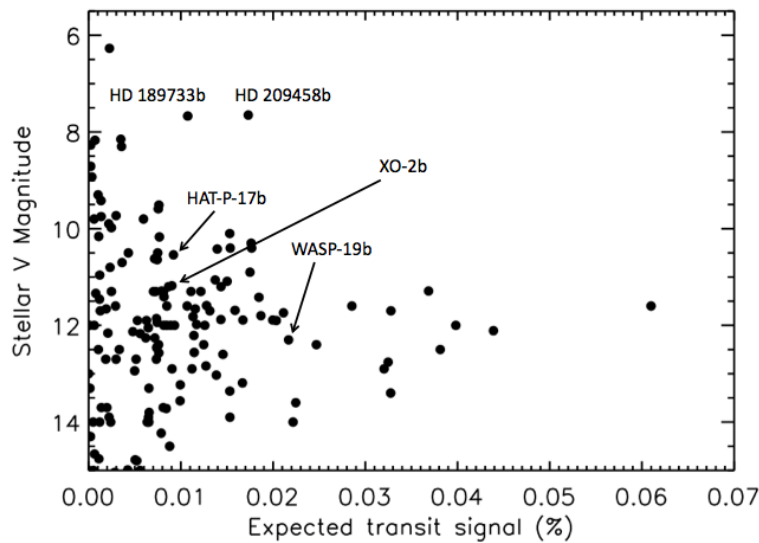


Figure 1.5: Predicted signals in transit for 1 isothermal scale height based on stellar temperature and orbital distance between each planet and its host star. Planets marked are focussed on specifically by me, either in this work or in upcoming work. Planet parameters are from <http://exoplanet.eu/> [accessed 01-Sep-2013].

Transmission spectroscopy is powerful not only in constraining atmospheric composition, but also in constraining other properties. For example, the presence or absence of certain species can place constraints on the atmospheric temperature, and knowing the dominant opacity sources has implications for the planet's energy budget. Also, constraints can be placed on whether or not cloud cover is important, by determining whether expected spectral features are washed out and a featureless spectrum is seen (which would be the case if the atmosphere contains a high-altitude opaque absorber which hides other spectral features).

1.3.3 Limb Darkening

Transmission spectroscopy is a very useful technique, but it requires precise knowledge of the transit depth variation as a function of wavelength, since spectral signatures are small. Therefore, before proceeding to discuss other techniques and literature, I need to firstly outline two important considerations for transmission spectroscopy: limb darkening and starspots.

In Section 1.3.1, I outlined transit models assuming a uniform stellar disc. In reality, the stellar disc is not uniform due to “limb darkening”. Hayek et al. (2012) explain the phenomenon of stellar limb darkening as variations in brightness across the surface of the star due to the fact that the path length, s , along the line of sight through the stellar atmosphere depends on the viewing angle onto the stellar atmosphere. For photons emitted at depth h at a point with an angle θ to the viewing angle, the path

length through the stellar atmosphere to the surface is (Haswell 2010)

$$s \approx \frac{h}{\cos(\theta)}. \quad (1.10)$$

The shorter path length at the observed disc centre means that photons from the deeper atmosphere escape at the centre of the disc, while photons observed from the limb⁸ emerge from higher, cooler regions in the stellar atmosphere. Since the deeper regions are hotter, photons will be emitted at higher energies (shorter wavelengths) in the disc centre compared to the limb, meaning that the disc appears progressively dimmer towards the limb (Hayek et al. 2012). The result is that a transiting planet will block more light when it passes in front of the centre of the star than when it passes in front of the limb of the star. This leads to a curving of the light curve towards the edges of the transit, rather than a square shaped dip. Furthermore, because the effect is temperature-dependent, the limb darkening effects on a transit light curve are more noticeable for shorter wavelengths, as shown in Figure 1.6. The blue lines are much more curved, because limb darkening has a greater effect, compared to the square shaped red lines.

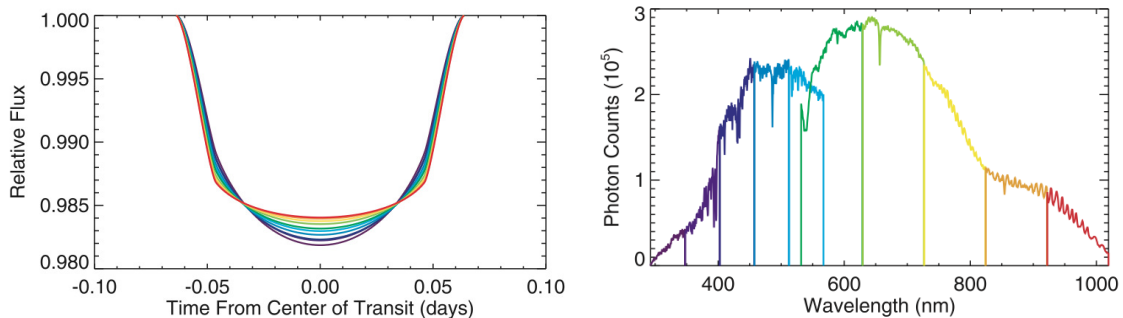


Figure 1.6: Image from Knutson et al. (2007b) showing model limb darkened light curves using a four-parameter non-linear limb darkening law (left) for the bandpasses of their observations (right). The model light curves all have the same transit radius.

The form of the limb darkening depends on opacity and emissivity at each depth in the stellar atmosphere, which changes with composition and the thermodynamic properties of the atmosphere. Since limb darkening is usually not measured directly or in detail for a given exoplanet host star, observers have to rely on the results from stellar atmosphere models when fitting transit light curves, which are constrained by observations mainly of the Sun but also of other stars (Bigot et al. 2006; Hajian et al. 1998; Mérand et al. 2010). Stellar atmosphere model spectra can be computed for a variety of angles in radial direction from the disc centre. Observers can then fit the function of intensity, I , vs $\mu = \cos(\theta)$ using a variety of laws. The most commonly used

⁸The edge of the stellar disc as seen by the observer.

are listed here:

Linear Law:

$$\frac{I(\mu)}{I(\mu = 1)} = 1 - u(1 - \mu), \quad (1.11)$$

Quadratic Law:

$$\frac{I(\mu)}{I(\mu = 1)} = 1 - a(1 - \mu) - b(1 - \mu)^2, \quad (1.12)$$

Non-Linear Law:

$$\frac{I(\mu)}{I(\mu = 1)} = 1 - c_1(1 - \mu^{1/2}) - c_2(1 - \mu) - c_3(1 - \mu^{3/2}) - c_4(1 - \mu^2), \quad (1.13)$$

where u , a , b , c_1 , c_2 , c_3 and c_4 are constants. The parameter μ governs the gradient of the intensity drop between the centre and limb of the disc. Higher order relationships are more flexible and fit the data more closely, but involve more parameters to be fitted (Claret 2000).

When using the ATLAS 1D stellar atmosphere models of Kurucz (1993)⁹, Sing et al. (2008a) found that the models overpredicted the strength of the limb darkening when using a 4th order law. By comparing with data from the Sun, Sing et al. (2008a) found that the over-prediction was worse by > 20 % for μ values below 0.05 (see Sing et al. 2008a and references therein). Sing et al. (2009) found that omitting the first μ -containing term on the right in Equation (1.13) gave a superior fit to transit data, and is consistent with solar observations and 3D stellar models, where the intensity distribution near the limb varies smoothly (see Sing et al. 2009 and references therein).

The stellar atmosphere models of Kurucz (1993) are only one dimensional, and therefore not perfect descriptions of the mechanics in the stellar atmosphere. Hayek et al. (2012) produced 3D model atmospheres for the host stars of the two most studied exoplanets, which do provide better fits to the data, and allow a 4th order correction to be used.

⁹Available at <http://kurucz.harvard.edu/> [accessed 01-Sep-2013].

1.3.4 Stellar Spots

Like the Sun, many host stars have stellar spots (“starspots”), and some are considerably more active than the Sun, showing optical flux variations of the order of a few per cent over one stellar rotation period, as different parts of the stellar surface rotate in and out of view of the observer. Starspots introduce two, opposite, effects on the measurement of transiting exoplanets depending on whether or not the planet passes in front of them during its transit.

Occulted Starspots

During a planetary transit, it is possible that the planet will cross a region of the stellar surface which contains a stellar spot or cluster of spots. Starspots are dimmer than the surrounding stellar surface, so when a transiting planet crosses a starspot, it blocks a lower amount of flux than when it passes in front of a non-spotted region of the star. The crossing of a stellar spot (or cluster of spots) results in a ‘bump’ in the transit light curve, where the measured flux from the system is temporarily higher than the prediction from the non-spotted transit model (see Figure 1.7). Not accounting for occulted starspots will cause the observer to underestimate the planetary radius.

Furthermore, the effect of occulted starspots on a planetary transit is wavelength-dependent (as also seen in Figure 1.7). Starspots are cooler than the surrounding stellar surface, which means that their flux contrast with the non-spotted surface is greater for shorter wavelengths. Additionally, some stellar spectral features have a dependence on temperature, meaning that the contrast between the starspot spectrum and the non-spotted stellar spectrum may be more complicated, and contain spectral features. Differential spectral features in stellar spots compared to the non-spotted surface are a problem for exoplanet transmission spectroscopy because they could introduce spurious spectral features. Some previous studies of transmission spectroscopy with active exoplanet host stars have simply omitted the data points clearly crossing occulted spots. Alternatively, some studies fitted for the stellar spot amplitude as a function of wavelength using the occulted spot shape from the white light curve and assuming that the spot shape does not change as a function of wavelength (e.g. Sing et al. 2011b; Huitson et al. 2012). In this way, the impact of occulted spots on the transmission spectrum can be directly measured.

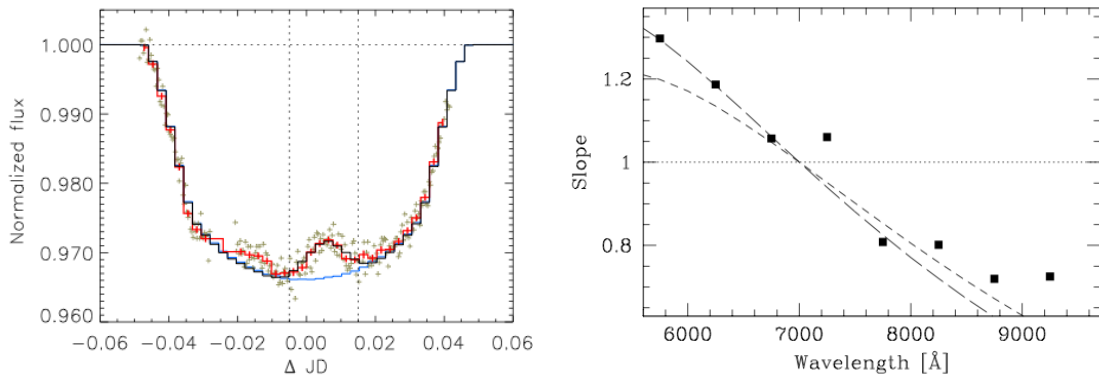


Figure 1.7: *Left:* Image from Wolter et al. (2009) showing a light curve of the transit of CoRoT-2b, where a bump can be seen as the planet crosses a starspot. Wolter et al. (2009) used planetary transits to try to understand the starspots on the surface of the star. The blue line shows a model of what the transit should look like if it didn't cross a starspot. The black line shows the model of a planet crossing a single starspot. The red line is the data (grey) averaged into 224 sec bins. There is a second bump to the left in the red line, which could indicate a second starspot not included in the model. *Right:* Image from Pont et al. (2008) showing the slope of the feature in their optical spectral light curve compared to wavelength (squares show the data points and dashed lines show occulted spot models). It can be seen that the feature is more dramatic at shorter wavelengths, as the data points show an increase in slope with decreasing wavelength.

Un-occulted Starspots

More difficult to quantify is the effect of un-occulted starspots, which are starspots on the surface of the star that are not crossed by the planet during its transit. Un-occulted starspots reduce the brightness of the star compared to the non-spotted ideal and hence cause the planetary radius to be overestimated. Un-occulted starspots cannot be directly detected on exoplanet-hosting stars, but must be inferred. For active stars, long duration monitoring of the stellar flux is required, covering a period of months before, during, and after the desired transit observation. The stellar variations give an indication of the activity level and the flux level of the star during the transit observations compared to the non-spotted level, thus allowing the out-of-transit baseline flux to be corrected.

One problem is that there are most likely always some spots on the stellar surface, meaning that the maximum flux observed during variability monitoring of this type is not the non-spotted stellar flux. In order to calibrate transmission spectra, the stellar flux level during a transit observation needs to be calibrated with respect to the non-spotted surface. Aigrain et al. (2012) found that the scatter in a variability monitoring light curve gives a reasonable estimate of the difference between the true non-spotted stellar flux level and the maximum flux observed during variability

monitoring (see Chapter 6).

In practice, depending on the stellar spot temperature, spectral features in the transmission spectrum ($\Delta z(\lambda)$) are not drastically affected at wavelengths longer than 6000 Å. What is most significantly affected is the absolute R_p/R_* value, which does not affect the determination of whether specific atmospheric features are present, but does affect the ability to compare one dataset with another for the same planet taken at different times. Also, the effects on the transmission spectra of planets are more severe at blue wavelengths. Two of the targets studied in this thesis are very active, and so the issues surrounding occulted and un-occulted starspots are discussed in much more detail in those chapters (Chapters 3 and 6).

1.4 Introduction to Secondary Eclipses

Often referred to as “occultations” in the exoplanet field, a secondary eclipse occurs when the planet passes behind the host star from the observer’s point of view, as shown in Figure 1.8. While I did not use any secondary eclipse data in this thesis, such observations provide an important complement to transit observations. As such, I outline the basic methods here, to provide context to my work.

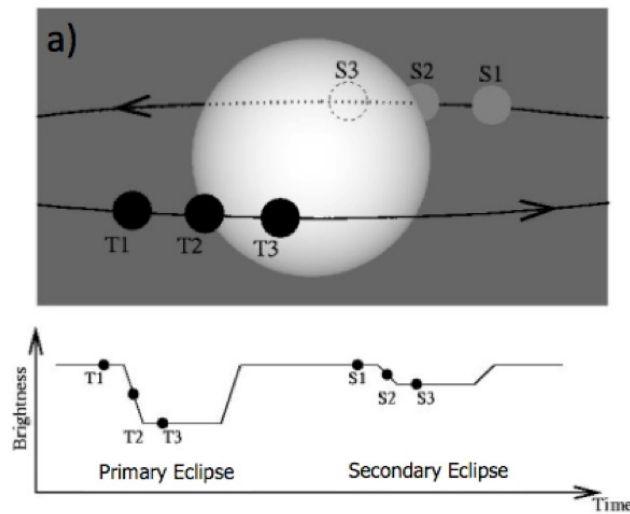


Figure 1.8: Image from López-Morales (2011) showing an example light curve that results as a planet orbits its star. It includes the flux decrement seen due to the planet’s primary transit and due to its secondary eclipse. The decrement resulting from secondary eclipse is significantly shallower than that of the primary transit.

The resulting drop in light (eclipse depth) during the secondary eclipse compared to just before and just after the secondary eclipse tells observers the brightness of the planet. The measurement of the eclipse depth has the advantage of being free from the effects of starspots and assumptions of limb darkening structure. The flux observed from the planet is a combination of reflected light from the host star and emitted light from the lower regions of the planet. Since the planet will be considerably cooler than the star, measuring the eclipse depth in the IR is assumed to measure only the thermally emitted component of the planet’s light, with a negligible reflected component. The eclipse depth measured in the IR therefore gives the temperature of the side of the planet facing the observer, at the particular altitude probed by that wavelength. For a tidally locked planet, the IR secondary eclipse depth measures the temperature of the day side. Measuring the optical eclipse depth is more sensitive to reflected light, and can be used to infer the presence of reflective clouds. Intrinsic thermal emission from the planet due to Kelvin-Helmholtz contraction is negligible compared to other emission sources for the day side of a planet (Haswell 2010).

1.4.1 Secondary Eclipse Spectroscopy and Day Side Temperature Profiles

The flux from the planet compared to the star at a given wavelength is given by (Haswell 2010)

$$\frac{f_{\text{day},\lambda}(\alpha)}{f_{\star,\lambda}} = \left(\frac{R_P}{a}\right)^2 p_\lambda \Phi_\lambda(\alpha) + \frac{B_\lambda(T_{\text{day}})}{B_\lambda(T_\star)} \left(\frac{R_P}{R_\star}\right)^2. \quad (1.14)$$

The first term is the reflected light contribution. The fraction of starlight reflected is a function of wavelength, which is expressed in the wavelength-dependent geometric albedo, p_λ . The amount of light reflected to an observer varies with phase angle, α , where $\alpha = 0$ when the planet passes behind the star. $\Phi_\lambda(\alpha)$ is the phase function that gives the flux at phase angle α . The second term is the thermal emission contribution, where $B_\lambda(T_{\text{day}})$ is the emitted blackbody spectrum of the planet, and $B_\lambda(T_\star)$ is the brightness temperature of the star, estimated as a function of wavelength by knowing the star's spectral type (Haswell 2010; Cowan et al. 2007). In this equation, a is the distance of the planet from the star, R_P is the radius of the planet and R_\star is the radius of the star.

For IR observations, the reflection component can be neglected and the planet can be treated as a blackbody emitter, which allows the day-side temperature to be derived from the secondary eclipse depth, ΔF_{SE} (full derivation in Haswell 2010 and Appendix D.4):

$$T_{\text{day}} = \frac{hc}{\lambda k_B} \left[\ln \left[\left(\exp \left(\frac{hc}{\lambda k_B T_\star} \right) - 1 \right) \frac{F}{\Delta F_{SE}} \left(\frac{R_P}{R_\star} \right)^2 + 1 \right] \right]^{-1}, \quad (1.15)$$

where h is Planck's constant, k_B is Boltzmann's constant and c is the speed of light in a vacuum. Different wavelengths probe to different altitudes in the atmosphere. Thus measuring the day side temperature as a function of wavelength can give a temperature profile of the planet's atmosphere as a function of altitude. How far a given wavelength penetrates into the atmosphere depends on the dominant opacity sources at that wavelength. Therefore, it is useful to observe both the transmission and emission spectra of a planet, since the transmission spectrum can constrain atmospheric abundances and hence dominant opacity sources.

It is possible to detect atmospheric spectral features when constructing the emission spectrum (eclipse depth as a function of wavelength). If a particular atmospheric layer is observed, then it is possible to see absorption features in that layer if the one beneath it is hotter. Conversely, if the atmospheric layer that is observed is hotter than the one beneath, then atmospheric features are seen in emission. Thus, the "emission spectrum" can contain both absorption and emission features depend-

ing on the atmospheric temperature structure. Such observations can be used to detect the presence of molecules such as water and CO, and also to infer the presence of “inversion layers”, regions where temperature increases as a function of altitude.

Transmission and emission spectroscopy are complementary techniques. Transmission spectroscopy has little dependence on temperature and pressure structure, and thus is very useful for constraining atmospheric abundances and dominant opacities. Emission spectroscopy gives physical information about temperature structure as well as showing atmospheric features, but there is a degeneracy between temperature structure and atmospheric composition, since it is unclear what altitude is being sampled unless the dominant opacity sources at the observational wavelength are known. Transmission spectroscopy can reduce this degeneracy. Additionally, transmission spectroscopy is sensitive to atmospheric features in the optical range, whereas emission spectroscopy is sensitive to longer-wavelength features. Furthermore, the transmission and emission spectra are measured from different parts of a tidally locked planet; the transmission spectrum from the day-night terminator and the emission spectrum from the day side.

1.4.2 Bond Albedo and Thermal Recirculation Efficiency

Integrating the wavelength-dependent geometric albedo, p_λ , over wavelength and phase, to get the total light reflected from the planet’s surface, gives the Bond albedo, A_B . Knowing the Bond albedo allows an observer to deduce the energy balance in a planet. Furthermore, knowing the Bond albedo and knowing the thermal brightness of a planet at a given wavelength can give an indication of how much stellar heat and radiation is recirculated from the day side of the planet to the night side (thermal recirculation efficiency). Thermal recirculation efficiency can be quantified in a number of ways (see Spiegel & Burrows 2010 and references therein). Firstly, the most commonly used factor is the geometrical f factor, where

$$T_{\text{day}} = T_\star \left(\frac{R_\star}{a} \right)^{1/2} [f(1 - A_B)]^{1/4} \quad (1.16)$$

and T_{day} is the planet’s day-side temperature (measured from an IR eclipse depth), T_\star is the stellar temperature, R_\star is the radius of the star, and a is the orbital separation of the star and planet (Spiegel & Burrows 2010; López-Morales & Seager 2007). Perfect redistribution corresponds to $f = 1/4$ and zero redistribution corresponds to $f = 2/3$. There is a ‘beaming factor’ that increases f by a factor of 4/3 due to the day-side temperature being peaked toward the centre of the disc (Spiegel & Burrows 2010). Were that not the case, the value of f for zero redistribution would be 1/2. In the case for perfect redistribution, f is still equal to 1/4 and no beaming factor is included,

because perfect redistribution implies that the day side is uniform in temperature. A derivation excluding the beaming effect is given in Appendix D.5.

Alternatively, thermal recirculation efficiency can be quantified in terms of the fraction, P_n , of incident stellar flux which is removed from the day side to the night side, for a given pressure level. The value of P_n ranges from 0 for no redistribution, to 0.5 for the day side and night side having the same temperatures (totally efficient redistribution). In this formalism, the day-side temperature would be given by

$$T_{\text{day}} = T_{\star} \left(\frac{R_{\star}}{a} \right)^{1/2} \left[\frac{1}{2} (1 - P_n) (1 - A_B) \right]^{1/4}. \quad (1.17)$$

The factor of $\frac{1}{2}$ comes from the fact that each hemisphere of the planet is treated as a blackbody with surface area $2\pi R_p^2$ (further derivation in Appendix D.5). This equation suggests that $f = \frac{1}{2}(1 - P_n)$, and it can be seen that $f = 1/4$ for $P_n = 0.5$. This is correct for totally efficient redistribution where the day side will have a uniform temperature. However, this formalism does not account for the beaming effect which occurs if redistribution is not perfect (Spiegel & Burrows 2010). In this case,

$$f = \frac{2}{3}(1 - P_n). \quad (1.18)$$

The temperature of the planet can be calculated from the secondary eclipse depth in the IR using Equation (1.15). At long enough wavelengths, the albedo can be assumed to be zero, although it is more useful to measure the albedo if possible. To determine the Bond albedo, optical observations of the secondary eclipse depth can be used to measure the flux reflected from the planet, $F_{P_{\text{ref}}}$, which can be compared to that of the star. At optical wavelengths, the thermal emitted component in Equation (1.14) is assumed to be negligible, meaning that

$$F_{P_{\text{ref}}} = F_{\star} A_g \frac{R_p^2}{a^2}, \quad (1.19)$$

where F_{\star} is the stellar surface flux, A_g is the geometric albedo and R_p is the radius of the planet (López-Morales & Seager 2007). The geometric albedo, A_g , is the wavelength-dependent geometric albedo, p_{λ} , integrated over all wavelengths, at a phase angle of 0 (Seager 2010). Observers cannot technically measure the albedo at a phase angle of 0 because the planet will be behind the star. The assumption is therefore made that the albedo at secondary eclipse is close to the albedo at phase angle 0. While observations only typically cover a small number of wavelengths, the value of A_g is inferred from these measurements. Also, it is not possible to directly measure A_B because observers do not have access to the reflected spectrum at all phase angles, so it must be inferred from the observational measurements. Seager

(2010) show that $A_g = \frac{2}{3}A_B$ for a Lambert sphere, which has a phase function of $\Phi_\lambda(\alpha) = \cos \alpha$. Again this is an assumption. Re-arranging Equation (1.19) shows that A_B can be derived from the fraction of the stellar flux, F_\star , reflected back from the planet:

$$A_B = \frac{3}{2} \frac{F_{P_{\text{ref}}}}{F_\star} \left(\frac{a^2}{R_p^2} \right). \quad (1.20)$$

Knowing both the Bond albedo and planetary temperature from secondary eclipse depths at different wavelengths allows the recirculation factor at the relevant altitude to be calculated using Equation (1.16) or (1.17). There are complications with such measurements, because the reflected light overlaps in wavelength with the thermally emitted light from the planet. This means that often there are multiple values of T_{day} , A_B and f or P_n that match a given dataset. Furthermore, different wavelengths will probe different pressure regimes, and so the measured day-side temperature and albedo may not directly correspond to one another. Often, the albedo is assumed to be 0, based on model predictions (e.g. Seager & Sasselov 2000). Both cases of efficient and inefficient redistribution have been observed.

Note that, while “equilibrium temperature” is generally used to mean the case where the energy emitted is exactly balanced by the energy absorbed, there are many different recirculation efficiencies for which this applies. The “equilibrium temperature” therefore has a different meaning, and also implies not only a balance of absorbed vs emitted energy, but also that the energy is emitted from the whole sphere of the planet uniformly i.e. that $f = 1/4$. I therefore use “equilibrium temperature” to mean the case where the energy emitted is exactly balanced by the energy absorbed and where thermal recirculation is perfectly efficient, unless stated otherwise.

1.4.3 Phase Curves

Albedo measurements are challenging because the reflected light from a planet is often not very bright. Therefore, very few albedos have been conclusively measured and recirculation efficiencies are often calculated from secondary eclipse depths in the IR based on an assumption of albedo.

A more direct way to constrain the efficiency of atmospheric thermal recirculation is to observe the planet's phase curve. For a phase curve observation, the system is observed during a whole or half orbit of the planet around the host star. For a tidally locked transiting planet, a phase curve shows a gradually increasing brightness after inferior conjunction, when the night side is observed, with the maximum flux near superior conjunction when the day side is visible. The amplitude of a thermal (IR) phase curve measures the day-night temperature contrast, and hence constrains the efficiency of heat redistribution from day side to night side.

Furthermore, the thermal phase curve can also constrain horizontal wind speeds by observing the timing of the peak in planetary flux relative to the secondary eclipse, which corresponds to the hottest planetary longitude ("hotspot"). For a tidally locked planet, the strong temperature contrast between the permanent day and night sides along with the orbital rotation creates an eastward equatorial jet, which offsets the hotspot downstream horizontally in the planet's atmosphere from the sub-stellar point. The peak in flux is then observed before the secondary eclipse (Showman et al. 2009; Showman & Polvani 2011). Measurement of the offset of the hotspot from the secondary eclipse time gives an indication of the ratio $\tau_{\text{rad}}/\tau_{\text{adv}}$, where τ_{rad} is the radiative timescale and τ_{adv} is the advective timescale (Showman & Guillot 2002). Measuring a phase curve does not require that the planet is transiting. However, an assumption of orbital inclination has to be made in the case of non-transiting planets to properly interpret the phase curve amplitude.

1.5 Literature Review on Exoplanet Atmospheres

This literature review includes work from transmission, emission and phase curves since they are complementary techniques, and this is the only way to provide a full overview of the current knowledge regarding hot Jupiters. The literature review also contains references to my published work detailed in Chapters 3 to 6.

1.5.1 Model Predictions for Hot Jupiters

The first quantitative model exoplanet atmospheres were produced by Seager & Sasselov (2000) based on the assumption that hot Jupiter atmospheres are similar to those of brown dwarfs and on the observed parameters for HD 209458b, a very favourable target orbiting a bright, Sun-like star (Section 1.5.2). Brown dwarfs have similar T_{eff} values to hot Jupiters (ranging from ~ 1100 to ~ 1600 K), although are less irradiated. The dominant opacity sources expected in brown dwarfs and cool L dwarfs by Seager & Sasselov (2000) are H_2O , TiO , CO , CH_4 , $\text{H}_2\text{-H}_2$, and $\text{H}_2\text{-He}$ collision induced opacities, the alkali-metal lines, particularly the Na I D and K I D doublets¹⁰, and Rayleigh scattering from H, He and H_2 . In planets within the temperature range ~ 1100 to ~ 1600 K, alkali metals should have strong signatures, since many other absorbers will have condensed out. Brown (2001) and Hubbard et al. (2001) also predict strong resonance lines of Na I and K I and an atmosphere otherwise dominated by H_2 , H_2O , CO and CH_4 . Such atmospheric features are predicted to be at the 10^{-4} level above the continuum, requiring high precisions to detect.

There have been several improvements since the first models, including the addition of extra opacity sources and effects such as thermal ionisation. For the most studied and favourable targets, Fortney et al. (2010) produced transmission spectra by solving for radiative transfer combined with the general circulation model (GCM) of Showman et al. (2009). Such a process means that the effects of opacities in the atmosphere on radiative transfer are able to feed back into the temperature profile of the GCM. A similar process was performed by Burrows et al. (2010) using the University of Reading's Intermediate GCM (see Burrows et al. 2010 and references therein). Such a task is lengthy and computationally intensive, however, so most model transmission and emission spectra are based on 1D model temperature-pressure (T - P) profiles. Hereafter, references to the formalisms of Fortney et al. (2010) and Burrows et al. (2010) refer only to the transmission spectral models based on 1D T - P profiles, unless stated otherwise.

¹⁰Hereafter referred to as Na I and K I doublets or features. When I mention Na I or K I, I always refer to the D lines unless specified otherwise.

Both the model sets of Fortney et al. (2010) and Burrows et al. (2010) include chemical equilibrium of neutral and ionic species. Chemical mixing ratios and opacities assume solar metallicity and local chemical equilibrium accounting for condensation and thermal ionisation but no photoionisation. As with the earlier models, the alkali lines dominate both optical spectra, but there are some differences between current models due to different opacity databases.

Models which depart from solar abundance ratios have been generated by Madhusudhan et al. (2011b) and Madhusudhan (2012). These models allow for a range of C/O ratios. Madhusudhan et al. (2011b) generated model emission spectra for a range of C/O ratios, which can be used to interpret data, while Madhusudhan (2012) generated model transmission spectra. The predictions from the original as well as newer models are discussed in detail below for different parts of the spectra.

Alkali Features and Rayleigh Scattering

Two example model spectra from Seager & Sasselov (2000) are given in Figure 1.9. It can be seen that the expected transmission spectrum changes depending on whether or not there is high-altitude cloud cover. If opaque clouds are present at low pressures in the atmosphere, then they can obscure the atmospheric regions below, making them inaccessible to transmission spectroscopy. Thus, observers see only the narrow cores of the predicted atmospheric lines. For a deeper cloud base, the transmission spectrum is able to measure deeper regions which have higher densities, pressures and temperatures, and hence where the spectral lines are broader.

Similarly, high-altitude opaque clouds can hide the parts of the predicted Rayleigh signature where the Rayleigh scattering cross-section is lowest. However, there is a potential for high-altitude clouds to be formed of very small grains (hazes) which will themselves produce a scattering signature. In this case, the entire optical spectrum may be dominated by a Rayleigh signature, and this is seen in observations (e.g. Section 1.5.2).

Although models have advanced to include a number of different molecules and effects, such as thermal ionisation, the alkali features and Rayleigh scattering are still predicted to dominate hot Jupiter atmospheres if high-altitude clouds are absent. Figure 1.10 shows results from the full 3D simulation based on the formalism of Fortney et al. (2010), and the dominant absorbers are similar to the original spectra computed by Seager & Sasselov (2000). Hot Jupiters are predicted to have low albedos due to the strong absorption from Na I and K I in the atmosphere (Seager et al. 2000; Sudarsky et al. 2000).

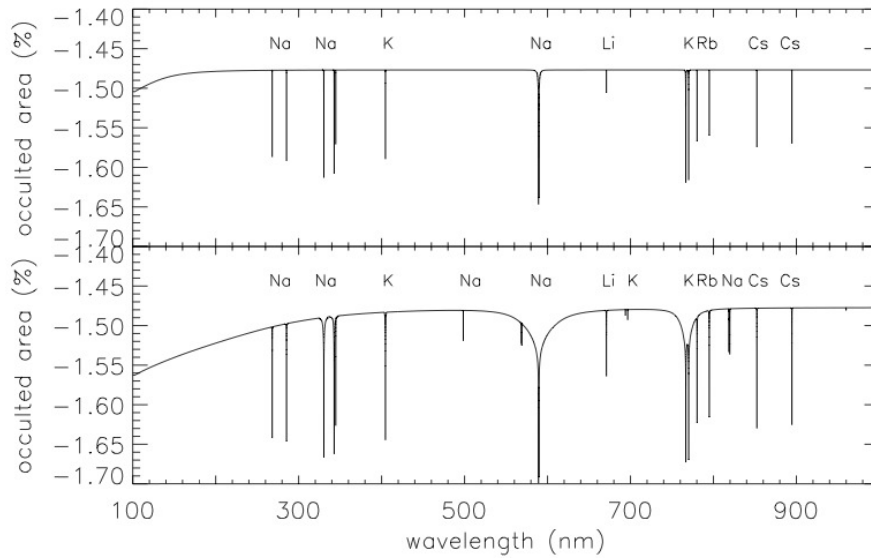


Figure 1.9: Model transmission spectrum from Seager & Sasselov (2000), showing expected absorption lines for a hot Jupiter similar to HD 209458b. *Upper plot:* High clouds at 2.4×10^{-3} bar, where only the narrow cores of spectral features are observable due to obscuring material. *Lower plot:* Low clouds at 0.2 bar, where the lines are deeper and the pressure-broadened regions can be observed. Rayleigh scattering can also be seen to be more important in this case, at the blue end of the spectrum. Note that 1 bar = 100kPa.

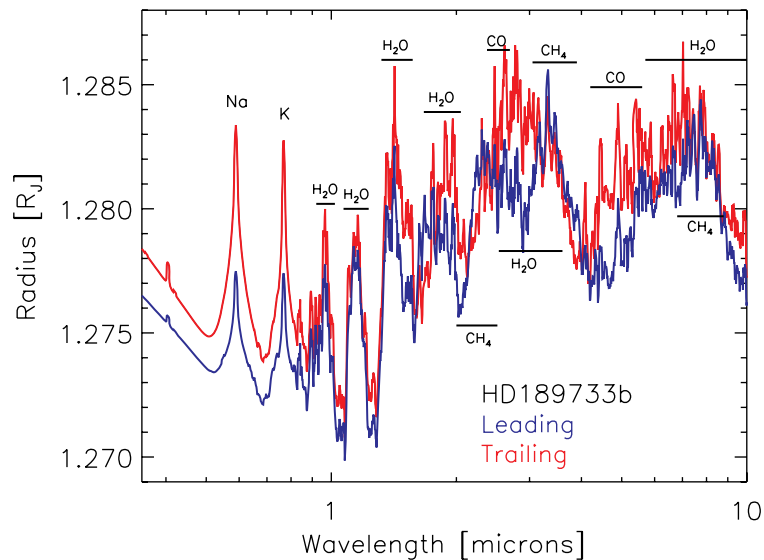


Figure 1.10: Model transmission spectra using GCMs to model the exoplanet's atmospheres from Fortney et al. (2010), showing the transmission spectrum from the leading and trailing edge of the planet HD 189733b, which has $T_{\text{eq}} \sim 1200$ K.

The Potential Importance of TiO

The new and old models only agree for a certain temperature range, however. Seager & Sasselov (2000) predicted no molecular features such as TiO in planets, because these are expected to have condensed out of the gas phase. However, TiO can be present and important in hotter planets at around $T \sim 2000$ K, and large TiO bands could obscure the alkali lines in transmission, depending on atmospheric dynamics (see Figure 1.11).

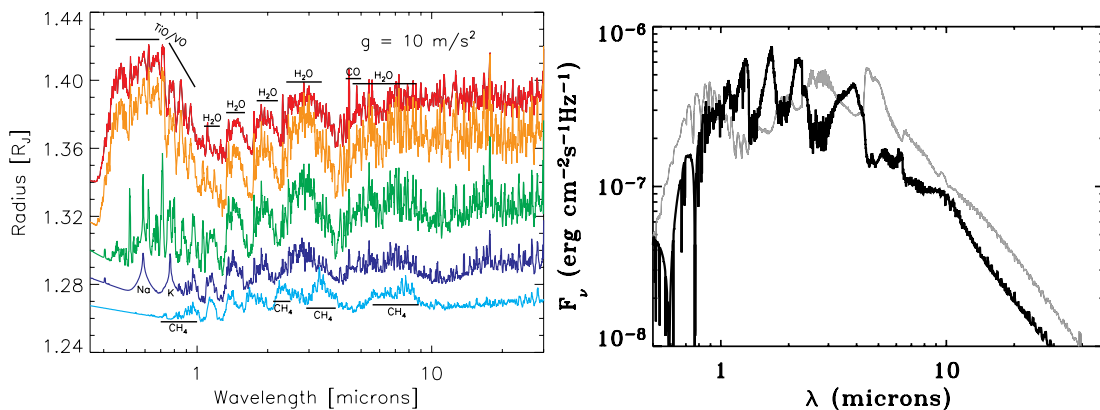


Figure 1.11: *Left*: Model isothermal transmission spectra from Fortney et al. (2010) from temperatures of 500 K (bottom) to 2500 K (top), in increments of 500 K. *Right*: Model emission spectra including TiO (grey line) and without TiO (black line) from Hubeny et al. (2003); Burrows et al. (2006) for a planet of $T_{\text{eq}} \sim 2230$ K.

Fortney et al. (2008) highlighted the potential importance of TiO and included it in their atmospheric models above a certain temperature. TiO is potentially important because it could contribute towards strong thermal inversions (stratospheres) seen in secondary eclipses. It has been predicted that TiO could trap incoming stellar irradiation high in the atmosphere, causing upper atmospheric heating and lower atmospheric cooling, thus causing thermal inversions (Hubeny et al. 2003; Burrows et al. 2006, 2007, 2008; Fortney et al. 2008). Figure 1.11 also shows model emission spectra for the cases with and without TiO in the atmosphere from Hubeny et al. (2003); Burrows et al. (2006).

It is still unclear whether observers should expect to see TiO in the upper atmospheres of hot Jupiters, however. The fraction of TiO in the upper atmosphere is very dependent on macroscopic mixing, and could be depleted from the upper atmosphere by “cold-trapping”. A cold trap is a region of atmosphere cooler than the atmosphere above and below it and cold-trapping occurs when a gas condenses into a solid in such a region and is unable to be lifted up into hotter regions where it could exist in the gaseous state again. Showman et al. (2009); Spiegel et al. (2009) found that TiO is potentially cold-trapped out of the upper atmosphere vertically even for planets

with T_{eq} above 2000 K. Furthermore, Spiegel et al. (2009) found that even for WASP-12b, a planet with $T_{\text{eq}} = 2600$ K, with no cold trap on the day side, an effective eddy diffusion coefficient¹¹ of $K_{zz} = 1.6 \times 10^7 \text{ cm}^2 \text{ s}^{-1}$ or higher is required to lift enough TiO into the upper atmosphere to cause a strong inversion, meaning that TiO can be trapped in very low-altitude atmospheric regions where mixing is inefficient. Additionally, condensation may occur on the night side even at higher altitudes. Parmentier et al. (2013) used a 3D GCM to model the night side cold trap and found effective K_{zz} values that best matched their 3D model results. Comparing their effective K_{zz} values to those required to maintain enough TiO in the upper atmosphere to cause a strong thermal inversion, they found that the night side cold trap will be able to deplete TiO efficiently if the particles can condense into sizes above a few microns. Additionally, an atmosphere with a high C/O ratio will reduce the amount of TiO in the atmosphere (Madhusudhan et al. 2011a; Madhusudhan 2012).

Sulphur Containing Species

At temperatures between 1200 and 2000 K, Zahnle et al. (2009b) predicted that thermal inversions could be caused by sulphur-containing species and considered the importance of H_2S , S, S_2 and HS in hot Jupiter atmospheres. They found that H_2S is the important S-containing species at lower altitudes, whereas S is the most important at high altitudes, below 0.001 bar (See Figure 1.12). Surprisingly, they find that the results are not sensitive to temperature and insolation, which suggests that thermochemical equilibrium is more important than photochemistry or kinetics. S_2 absorbs in the UV between 240 and 340 nm at temperatures above 1200 K, while HS should absorb strongly between 300 and 460 nm. Such features should be detectable using transmission spectroscopy, as shown in Figure 1.12. Additionally, Zahnle et al. (2009a) showed that sulphur-containing soots could form on planets with temperatures between 800 and 1200 K.

¹¹A coefficient which governs the efficiency of vertical transport and wind speeds in one-dimensional models.

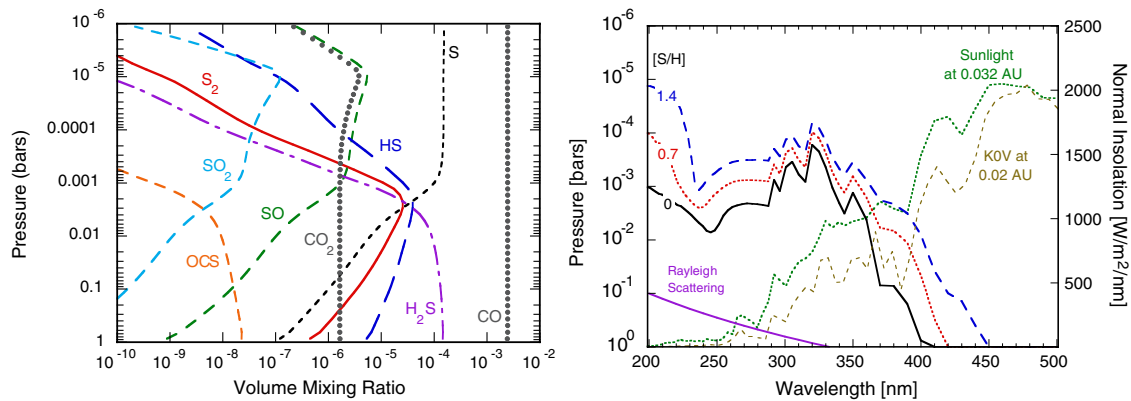


Figure 1.12: *Left*: Mixing ratios of various important sulphur-containing species as a function of pressure for an isothermal 1400 K atmosphere from Zahnle et al. (2009b). *Right*: Pressure levels of the $\tau = 1$ surface as a function of wavelength for three different metallicities from Zahnle et al. (2009b). Two incident stellar spectra, one for the Sun and another for a K0V dwarf are shown for comparison.

IR Molecules

Models developed over recent years predict many molecules in the near-IR, including H_2O , CO and CH_4 , depending on planetary temperatures and chemical composition (Brown 2001; Sharp & Burrows 2007; Fortney et al. 2010; Burrows et al. 2010). The presence of many predicted molecules depends on temperature and atmospheric abundance ratios. The CO/CH_4 ratio depends critically on temperature. For hotter atmospheres, above ~ 700 K for a pressure of 10^{-3} bar, CO will dominate over CH_4 , and CO features will be seen in the IR transmission spectrum rather than CH_4 features (see Figure 1.11). Thus, observations of the CO/CH_4 ratio can constrain the atmospheric temperature. Additionally, the C/O ratio is important in determining dominant atmospheric opacity sources, with H_2O and CO_2 becoming more abundant when $\text{C}/\text{O} < 1$ and CH_4 , HCN and C_2H_2 enhanced if $\text{C}/\text{O} > 1$ (Madhusudhan 2012; Moses et al. 2013). Model transmission spectra for different C/O ratios are shown in Figure 1.13.

Transmission spectroscopy in the near-IR of relatively hot planets is very useful because opacities in the 1-1.6 μm range are dominated by water, with methane opacities at these wavelengths having disappeared. Therefore, observation at these wavelengths can directly constrain the C/O ratio and can be useful in constraining longer-wavelength observations, where bandheads are composed of both CO and H_2O .

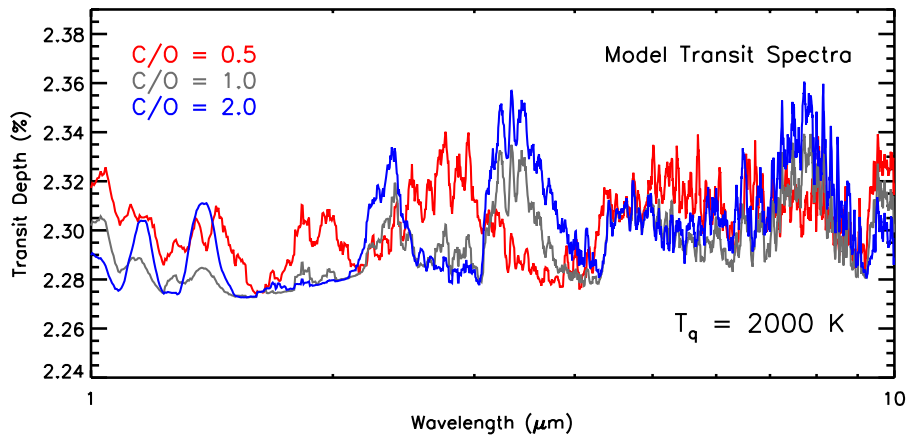


Figure 1.13: Model transmission spectra from Madhusudhan (2012) assuming different C/O ratios (the solar C/O ratio is 0.5, Lodders 2003).

Atmospheric Escape

Since many hot Jupiters orbit so close to their host stars, they receive extreme amounts of stellar irradiation and it is possible that the planets may experience atmospheric escape. For example, Ehrenreich & Désert (2011) predicted escape rates for many exoplanets by comparing each planet's gravitational potential energy to the stellar X/EUV energy deposited in the atmosphere, and found rates between 10^6 and 10^{13} g s^{-1} depending on the planetary system. Atmospheric escape can be measured directly in the UV transmission spectrum for the brightest targets by looking for signatures of neutral or ionised species and measuring the blueshift of the spectral lines.

Model Differences and Future Work

There are some differences between existing models. For example, the opacity database included in the models of Burrows et al. (2010); Howe & Burrows (2012) includes CrH, FeH, CaH and TiH among others, which are not included in the models of Fortney et al. (2008, 2010) (see references within these papers for details of opacity lists and abundances used). Figure 1.14 shows transmission spectra based on both formalisms for the same planet. Clearly there are differences, however since the precisions required to detect features in transmission are so high, many observations are not able to distinguish between the two models. Currently, many observations are limited to simply confirming whether or not TiO is present in the atmosphere, or whether there is high altitude cloud cover. For the purposes of observations, therefore, these two models represent a similar case of exoplanet atmosphere.

However, not all models agree to such an extent. For example, Shabram et al. (2011) compared models based on the formalism of Fortney et al. (2010) to models developed by Beaulieu et al. (2010), and found differences which are larger than

can be explained by differences in opacity databases alone. By comparison with simple analytic relations, they showed that the amplitude of features in the models of Beaulieu et al. (2010) are larger than expected for exoplanet atmospheres (also shown in Figure 1.14).

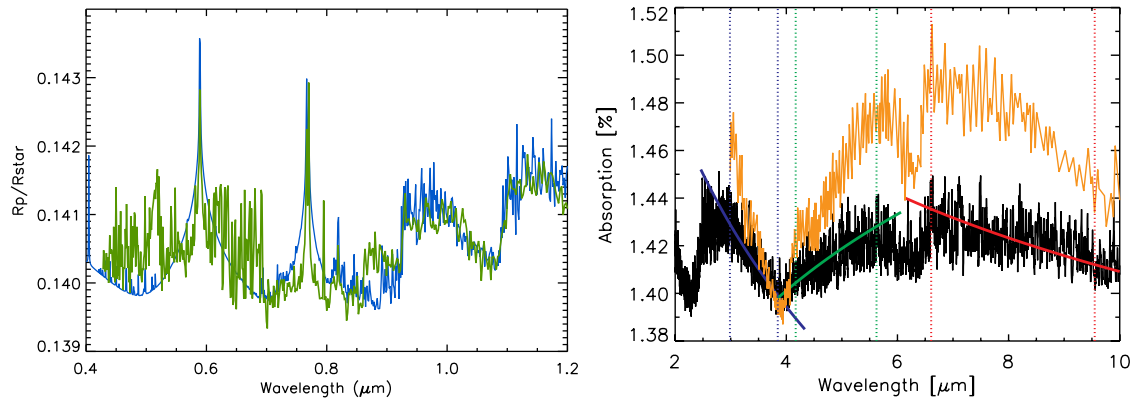


Figure 1.14: *Left*: Model transmission spectra from Fortney et al. (2010) (blue) and Burrows et al. (2010) (green). Both formalisms use solar abundances but the models of Burrows et al. (2010) include some opacities which are not included in the models of Fortney et al. (2010). Both models are for the planet WASP-19b, which has an equilibrium temperature of ~ 2000 K. *Right*: Figure from Shabram et al. (2011) comparing their models (black) with those of Beaulieu et al. (2010) (orange) and simple analytic models (green and red lines). Both models are for a 1500 K isothermal atmosphere with the same surface gravity.

There are also some important neglected effects in all the current models for hot planets. One of the most important ones is photo-ionisation and photochemistry, which can strongly influence the chemical abundances in such highly irradiated planets (e.g. Moses et al. 2011). Photochemistry has started to be considered in the transmission spectra of cooler planets, though (Zahnle et al. 2009b; Shabram et al. 2011).

Furthermore, it is only recently that the effects of clouds have started to be included in models other than simply to cut off absorption features at a certain depth. High altitude clouds can cause inversion layers higher up in the atmosphere than the stratosphere, reduce fluxes in the IR emission spectrum, and can also increase the albedo of the planet and hence significantly affect its energy budget (e.g. Kitzmann et al. 2011; de Kok et al. 2011; Heng et al. 2012).

1.5.2 Observations of Well-Studied Targets

The hot Jupiters HD 209458b and HD 189733b have so far dominated characterisation studies because they orbit bright host stars ($V=7.6$ for HD 209458 and $V=7.8$ for HD 189733). The large number of photons enables high precision observations, and these two planets have been studied in some detail. HD 189733b is roughly Jupiter mass and size, but HD 209458b has a bloated radius and is less dense. HD 209458b has an equilibrium temperature of ~ 1450 K, while HD 189733b has an equilibrium temperature of ~ 1200 K. More recently, extensive observations have additionally focussed on GJ 1214b, a super-Earth of $6.55 M_{\oplus}$ transiting an M dwarf star. Although its atmospheric scale height is small, its host star is also small, at only $0.21 R_{\odot}$ (Charbonneau et al. 2009), meaning a deeper transit depth and hence larger detectable atmospheric signals than if the host star were sun-like.

This small sample of planets is currently the only source of detailed observations for exoplanets. Although exoplanet characterisation surveys are beginning, these favourable targets provide a framework in which to analyse the bulk properties that can be derived from other, less favourable targets. I will firstly discuss the current state of knowledge regarding HD 209458b, HD 189733b and GJ 1214b and then proceed to describe the rapidly increasing number of observations resulting from studying other targets.

HD 209458b

HD 209458b appears to have a cloudless upper atmosphere with many of the predicted atmospheric features present. The optical transmission spectrum shows that the atmosphere of HD 209458b contains sodium at the predicted level measured using the Na I feature, but no evidence of the predicted potassium K I feature (Charbonneau et al. 2002; Narita et al. 2005; Knutson et al. 2007b; Barman 2007; Snellen et al. 2008; Sing et al. 2008a,b). A benefit of such a bright target is that it provides high enough precision to enable the shape of the sodium feature as a function of wavelength to be well determined. In HD 209458b, the sodium absorption line profile shows a narrow absorption core and broader plateau-like shape rather than smoothly decaying wings (Sing et al. 2008a,b). As explained by Vidal-Madjar et al. (2011b), the absorption depth should be greater towards the core of the feature due to an increase of the absorption cross-section. A plateau region could indicate an abundance drop, where the increase in the cross-section is compensated for by the decrease in atomic sodium abundance in the altitude regions sensed. The observation of pressure-broadened line wings shows that the Na I feature is observed deep in the atmosphere, and suggests a relatively cloud-free and haze-free upper atmosphere.

There is also an extra absorber in the optical spectrum redward of the sodium lines, and Désert et al. (2008) show that this could be due to low levels of TiO and VO.

The UV spectrum shows large absorption signatures in the Lyman α H I line, O I and C II lines, which extend beyond the Roche lobe, demonstrating that atmospheric escape is occurring and that the blow-off of the hydrogen gas drags up heavier species (Vidal-Madjar et al. 2003, 2004; Linsky et al. 2010). Vidal-Madjar et al. (2003) estimated the escape rate to be $\geq 10^{10}$ g s⁻¹, consistent with predictions (Lammer et al. 2003; Lecavelier des Etangs et al. 2004). Absorption has also been observed around the H α feature, with a shallower transit depth than the Lyman α observations (Jensen et al. 2012; Astudillo-Defru & Rojo 2013). Additionally, the transmission spectrum shows a blueward slope of increasing absorption depth as a function of decreasing wavelength. While initially thought to be due to a Balmer jump (Ballester et al. 2007), Lecavelier Des Etangs et al. (2008b) showed that the spectrum is better fit by a Rayleigh scattering profile, which would be due to scattering by H₂ particles.

In the IR, high resolution spectroscopy by Snellen et al. (2010) detected CO in the atmosphere in the spectral range 2,291 to 2,349 nm with resolving power $R = 100,000$, despite not being detected at 2 μm with $R = 25,000$ by Deming et al. (2005). Additionally, Snellen et al. (2010) saw that the signal was blueshifted by approximately 2 km s⁻¹, suggesting strong east-west winds in the atmosphere.

There is still a discrepancy between the observed transmission spectra in the 1.1 to 1.6 μm range, where there should be prominent water features. Barman (2007) used the STIS data of Knutson et al. (2007b) to show evidence of water features in the near-IR which were consistent with their chemical equilibrium models. However, Deming et al. (2013) find muted water features in the spectrum of HD 209458b with WFC3, 0.57 times the expected amplitude from solar abundance models. Both instruments have proven reliable in the past for exoplanet transmission spectroscopy, so the source of the discrepancy is unknown. At longer wavelengths, the transit radius at 24 μm is consistent with clear atmosphere models and the radii measured in the optical (Richardson et al. 2006; Crossfield et al. 2012c). There is also a possibility that there is a water signature in the *Spitzer* IRAC¹² bands from 3.6 to 8.0 μm (Beaulieu et al. 2010), but the interpretation of the transmission spectrum in these bands is complicated since the variations in transit depth are larger than those predicted by many models (Shabram et al. 2011). Figure 1.15 shows a summary of the currently observed optical to near-IR transmission spectrum of HD 209458b.

¹²InfraRed Array Camera

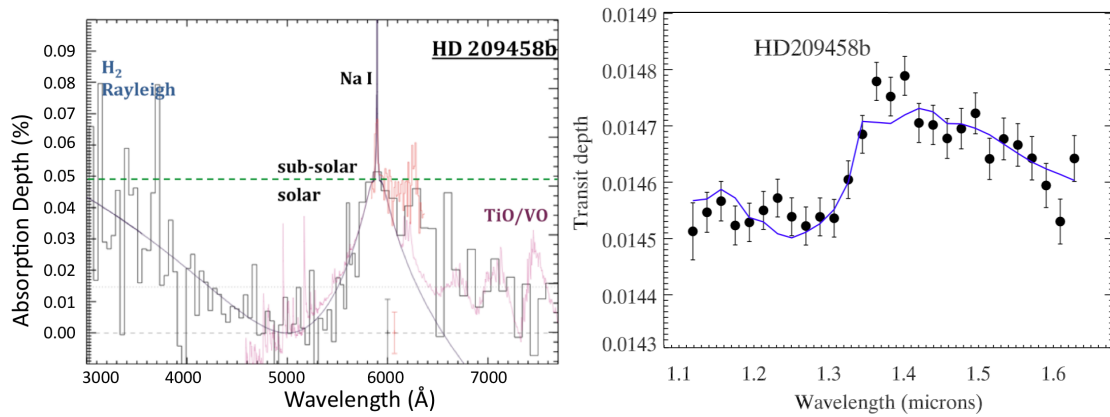


Figure 1.15: *Left*: Optical transmission spectrum of HD 209458b adapted from Sing et al. (2008b) showing the Na I doublet, Rayleigh scattering and possible TiO/VO absorption. *Right*: Near-IR transmission spectrum of HD 209458b adapted from Deming et al. (2013).

HD 209458b has also been observed extensively during its secondary eclipse, with *Spitzer* IRAC results showing that the planet has a temperature inversion and water emission (Knutson et al. 2008). Water, methane and CO were found to be present with NICMOS¹³ measurements, but it was later shown that the systematics¹⁴ of the NICMOS instrument were worse than previously thought and that it lacks the precision to detect atmospheric components in exoplanets (Swain et al. 2009; Gibson et al. 2011).

The measurements of secondary eclipse depth as a function of wavelength give the day side temperature profile as a function of altitude. Furthermore, temperature information on the upper atmospheric terminator can be gained by observing the sodium Na I doublet at high resolution, as done by Vidal-Madjar et al. (2011b,a). More detail on this technique is given in Chapter 3, but essentially, the atmospheric scale height is larger for a higher temperature, resulting in a more inflated atmosphere. A more inflated atmosphere results in an extended line profile shape, with the gradient of measured transit radius as a function of wavelength becoming steeper. Thus, one can identify regions of different atmospheric temperature by measuring the derivative of the transit radius as a function of wavelength around the sodium feature. Figure 1.16 shows the T - P profiles that produce the best-fitting model spectra for the secondary eclipse data, along with the observed terminator T - P profile of the upper atmosphere overplotted with models.

¹³Near Infrared Camera and Multi-Object Spectrometer

¹⁴A “Systematic” in this context means a contaminating flux variation as a function of some instrumental, Earth-based or astrophysical origin.

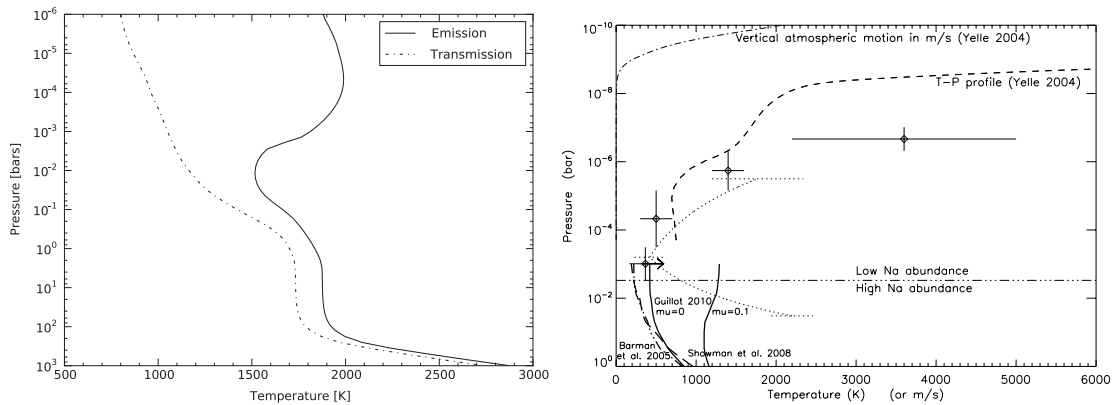


Figure 1.16: *Left:* Day side T - P profile for HD 209458b from Crossfield et al. (2012b) used to generate model spectra to match their data (24 μm) and that of Knutson et al. (2008) (3.6, 4.5, 5.8 and 8.0 μm). Also shown is the corresponding terminator T - P profile. *Right:* Measured terminator T - P profile for HD 209458b from Vidal-Madjar et al. (2011b,a), measured from observations of the Na I doublet using their analysis of medium resolution data and also the higher resolution results of Snellen et al. (2008) taken using Subaru. Overplotted are various models for the upper and lower atmosphere.

The day side T - P profile shows a temperature inversion, predicted by the model to be caused by TiO. The terminator T - P profile shows another inversion higher up, which is most likely the base of the thermosphere, the region where the temperature of the atmosphere starts to increase as a function of altitude due to the stellar irradiation. Models of the upper atmosphere and atmospheric escape predict that temperatures in the thermosphere could reach up to 10,000 K (Yelle 2004; Tian et al. 2005; García Muñoz 2007), and the observations are consistent with these predicted temperatures. The base of the thermosphere is not adequately modelled, which may explain why the observed thermosphere is at higher pressures than the models predict.

So far, no phase curve measurement exists for HD 209458b that can be used for any interpretation. The only attempt so far has been at 24 μm by Crossfield et al. (2012c), but long duration instrumental sensitivity variations over the course of the observations prevented any interpretation.

Overall, the picture that is emerging of HD 209458b is of a cloud-free atmosphere, with a stratosphere, possibly caused by TiO. There is evidence for absorption from Na I and Rayleigh scattering from H₂ in the transmission spectrum, along with water seen in the day side spectrum and in transmission. Atmospheric escape has been observed beyond the Roche lobe, and observations are able to detect the base of the thermosphere.

HD 189733b

The predicted equilibrium temperature of HD 189733b is only ~ 250 K cooler than that of HD 209458b assuming that both planets have zero albedo and totally efficient day-night heat transport. However, HD 189733b orbits a much cooler, more active star and the planet appears to have very different properties to HD 209458b. The most striking feature is that the whole optical transmission spectrum is dominated by a Rayleigh scattering signature, indicative of a small-particle haze high up in the atmosphere (Pont et al. 2008; Lecavelier Des Etangs et al. 2008a; Sing et al. 2011b). There is no evidence for the pressure-broadened line wings of the Na I lines as seen in HD 209458b or the K I lines, although the narrow cores of both features are found to be visible, meaning that atomic sodium and potassium are present, but that the wings are obscured by the high-altitude scattering haze (Pont et al. 2008; Redfield et al. 2008; Jensen et al. 2011; Huitson et al. 2012; Pont et al. 2013). Additionally, as with HD 209458b, the medium resolution HST¹⁵ observations show evidence of a thermosphere in the upper atmosphere of HD 189733b (Huitson et al. 2012). However, due to not knowing the species responsible for the scattering signature, the pressure level of the thermosphere base remains unknown (more details in Chapter 4).

In the near-IR to IR, the picture has been more complicated. Water has been detected in the day side spectrum (Grillmair et al. 2008) but spectroscopic observations in transmission have proved inconclusive. Water and methane features were observed in HD 189733b using HST NICMOS (Swain et al. 2008), but follow-up observations using the same instrument found results to be consistent with no water, or a high altitude haze obscuring water features (Sing et al. 2009). However, the most recent reductions (Gibson et al. 2011, 2012b) show that the results are very dependent on the de-correlation methods used to deal with systematic trends. Therefore the NICMOS observations do not have the precision to either confirm or deny the presence of molecular near-IR features, either in transmission or emission, when uncertainties due to de-correlation methods are taken into account. The HST WFC3¹⁶ has improved on the precision available using NICMOS, and new observations using WFC3 by Gibson et al. (2012a) suggest that in HD 189733b, the haze does extend into the near-IR, covering the predicted solar-abundance molecular features. The observations are not precise enough to rule out weaker features, but solar abundance features can be ruled out. By putting all the existing optical and IR observations together, Pont et al. (2013) also find results consistent with either haze or weaker than predicted molecular features redward of $1.1 \mu\text{m}$.

¹⁵Hubble Space Telescope

¹⁶Wide Field Camera 3

Transmission spectroscopy in HD 189733b is made more complicated than for HD 209458b because the star is very active, with optical stellar flux varying by $\sim 3\%$ over a stellar rotation period (Pont et al. 2007; Henry & Winn 2008; Pont et al. 2013; Aigrain et al. 2012). Although more significant at shorter wavelengths, Désert et al. (2009, 2011b) showed that even in the $3.6\ \mu\text{m}$ waveband, stellar activity can produce variations in the measured transit radius at different epochs comparable to the size of predicted features. Although water has been detected in transmission at 3.6 and $5.8\ \mu\text{m}$ with *Spitzer* (Beaulieu et al. 2008; Tinetti et al. 2007), Désert et al. (2011b) found that the effect of stellar activity variations on spectral features means that the water detection cannot be confirmed. Furthermore, Ehrenreich et al. (2007) also analysed the *Spitzer* data and found that the precision is not high enough to confirm the water features. Both Désert et al. (2009) and Knutson et al. (2012) found possible evidence for CO in the IR transmission spectrum, but again this is limited by stellar activity constraints. Variations of $6\ \text{mmag}^{17}$ were also seen in the $8\ \mu\text{m}$ transit depth when comparing 7 transits taken over ~ 590 days (Agol et al. 2010).

One advantage of observing the emission rather than the transmission spectrum is that it is not affected by stellar activity. Even so, observations require high precisions and are very challenging, meaning that many results remain controversial. For example, some studies found a significant emission feature at $3.25\ \mu\text{m}$, which could be due to non-LTE methane chemistry (Swain et al. 2010; Waldmann et al. 2012). However, the same feature was not found in other studies (Mandell et al. 2011). Also, while Charbonneau et al. (2008) found evidence in the spectrum at 3.6 , 4.5 , 5.8 , 8.0 and $24\ \mu\text{m}$ to confirm the water detection of Grillmair et al. (2008), this is inconsistent with the results of Grillmair et al. (2007). Additionally, Swain et al. (2009) detected absorption from H_2O , CO and CO_2 in the day side spectrum with NICMOS. However, there have been some difficulties discovered in interpreting NICMOS data, so these results should be confirmed by other instruments.

Some properties have been confirmed, however. For example, the day side lacks a temperature inversion (Deming et al. 2006; Charbonneau et al. 2008; Swain et al. 2009). Also, CO absorption has recently been detected using high resolution spectroscopy in the day side spectrum (Rodler et al. 2013; de Kok et al. 2013). There is also evidence that the brightness temperatures at wavelengths longer than $8\ \mu\text{m}$ are higher than predicted by clear atmosphere models and that the atmosphere looks isothermal at long wavelengths (Deming et al. 2006; Charbonneau et al. 2008; Knutson et al. 2012). Pont et al. (2013) suggest that the haze seen in transmission provides an explanation for these observations since the scattering and absorption caused by hazes means that the altitudes sampled by different wavelengths are closer

¹⁷Here, and in the rest of the thesis, mmag is used to mean 0.1% .

together than they would be in a clear atmosphere. Figure 1.17 shows a summary of the currently known properties of HD 189733b.

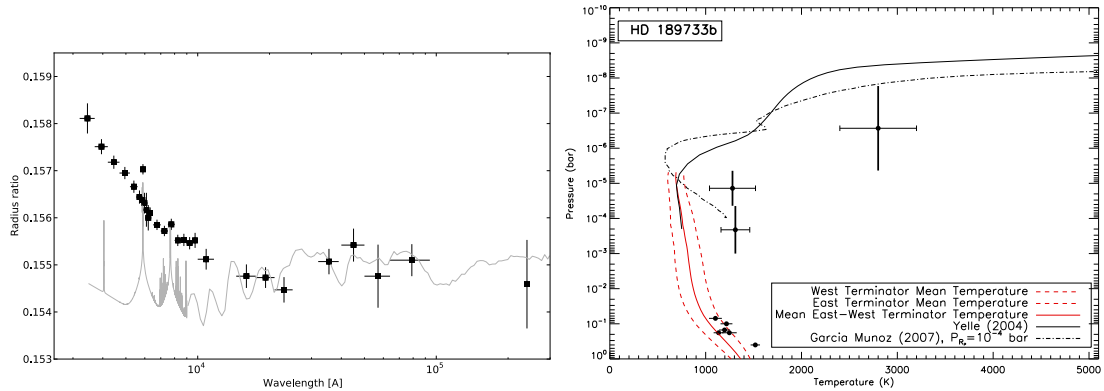


Figure 1.17: *Left*: Transmission spectrum constructed from existing literature by Pont et al. (2013) including stellar activity corrections. Where more than one measurement is available for the same wavelength, the results are averaged assuming no time variability in the transmission spectrum, after stellar activity is accounted for. The original data are from Pont et al. (2008); Swain et al. (2008); Sing et al. (2011b); Huitson et al. (2012); Gibson et al. (2012a); Désert et al. (2009, 2011b); Deming et al. (2006); Knutson et al. (2007a); Charbonneau et al. (2008); Knutson et al. (2009b, 2012). *Right*: Terminator T - P profile for HD 189733b from Huitson et al. (2012), based on the assumption that the Rayleigh scattering signature seen in the optical transmission spectrum is due to high-altitude atmospheric haze at a reference pressure of 10^{-4} bar. The thick vertical bars indicate isothermal atmospheric regions, and do not include the uncertainty in reference pressure. The data include the 1340 K temperature and pressure derived for the continuum by Lecavelier Des Etangs et al. (2008a) combined with the 1280 K temperature measured for the near IR continuum by Sing et al. (2009). The plot also shows lower altitude points from secondary eclipse observations of Knutson et al. (2007a, 2009b), Charbonneau et al. (2008) and Deming et al. (2006). The temperatures measured by Charbonneau et al. (2008) and Deming et al. (2006) were adjusted to the terminator temperature by Heng et al. (2012). T - P model profiles are shown for the lower altitude regions in red (Fortney et al. 2010). For the higher altitudes, models for the upper atmosphere of HD 209458b are shown for comparison, where the black solid line is the T - P profile from Yelle (2004) and the dot-dashed line is from García Muñoz (2007).

Unlike HD 209458b, several phase curves have been measured for HD 189733b, which shed further light on the planet's properties. Phase curves have been measured at 3.6, 4.5, 8.0 and 24 μm with *Spitzer* (Knutson et al. 2007a, 2009b, 2012). The first interesting observation is that the day side and night side temperatures are only ~ 250 K different in the 4.5, 8.0 and 24 μm bands, suggesting that thermal redistribution is efficient at the altitudes probed by these wavelengths, and also that the efficiency is similar at the three altitudes. Interestingly, the phase curve amplitude is higher at 3.6 μm , showing a temperature difference of ~ 500 K. The increased phase curve amplitude at 3.6 μm suggests that the 3.6 μm wavelength is sampling a

higher atmospheric layer than the 4.5 μm wavelength, where the radiative timescale is shorter. Clear atmosphere models predict the opposite, since they predict higher opacities at 4.5 μm than at 3.6 μm . The haze observed in transmission, however, has lower opacities for longer wavelengths and so would explain the observations. The second interesting observation is a smaller than expected hotspot offset. A small hotspot offset was initially explained by a non-synchronous¹⁸ rotation of the planet (Knutson et al. 2012). However, a more plausible explanation is that the high altitude haze moves the photosphere to lower pressures where the radiative timescale is shorter, which would lead to a smaller hotspot offset (Pont et al. 2013; Showman & Guillot 2002).

Finally, one thing that the two most-studied planets do have in common is their escaping atmospheres, although the best fit to the data for HD 189733b is an escape rate of $\sim 10^9 \text{ g s}^{-1}$, which is lower than that of HD 209458b. The escape rate was determined from resolved Lyman α observations of Bourrier et al. (2013); Lecavelier des Etangs et al. (2012) using STIS¹⁹, who also noticed evidence of temporal variability in the escape signature. The estimate is lower than that of 10^{10} g s^{-1} determined from unresolved ACS²⁰ observations of the Lyman α line observed by Lecavelier Des Etangs et al. (2010), which could be due to temporal variability or simply lack of resolution. Observations of the H α line suggest lower velocities of escaping material and, similar to HD 209458b, show a shallower transit depth than the Lyman α observations, suggesting that the two lines sample different atmospheric regimes and that ionisation is stronger than predicted (Jensen et al. 2012; Christie et al. 2013). There is also some evidence of blue-shifted absorption in the post-transit data, suggesting a cometary-like absorption tail. Ben-Jaffel & Ballester (2013) detected significant absorption from O I and obtained a possible detection of C II with early ingress. The broad shape of the line detected during transit suggests that there must be a very hot layer of O I high in the atmosphere, unless abundances are drastically super-solar (which would cause large observable line wings without excess line broadening). Additionally, Lecavelier des Etangs et al. (2012) provided contemporaneous X-ray observations using XMM-Newton and used this to estimate the total luminosity across the X-ray/EUV band and hence a 1% efficiency in the conversion of input energy into mass loss. The XMM-Newton observations are consistent with other X-ray observations (Pillitteri et al. 2010, 2011; Poppenhaeger et al. 2013). Interestingly, these latter authors also found evidence over multiple epochs that the planet affects stellar activity, by observing that flares appear to be linked to the planetary phase.

¹⁸A tidally locked planet usually rotates synchronously i.e. its rotation period is the same as its orbital period.

¹⁹Space Telescope Imaging Spectrograph

²⁰Advanced Camera for Surveys

In summary, HD 189733b displays a haze-dominated atmosphere, very different from that of HD 209458b. The Rayleigh slope observed over so many atmospheric scale heights suggests that particle sizes must be small, and of similar size throughout the upper atmosphere. Narrow line cores of the alkali features are detected, but no broad-band features. A high altitude haze can explain such otherwise puzzling features as an isothermal atmosphere up to the base of the thermosphere and a smaller than expected hotspot offset. Due to its proximity to its host star, the upper atmosphere of HD 189733b is escaping, with the detection of metals high in the exosphere suggesting a similar mechanism to that of HD 209458b.

GJ 1214b

GJ 1214b is the first intensively studied planet exploiting the ‘M dwarf’ opportunity, where planets orbiting small stars will give larger transit depths, rather than the ‘bright star’ opportunity, where large numbers of photons increase observational precision. GJ 1214 has a stellar radius of only $0.21 R_{\odot}$ and so presents a unique opportunity to study a super-Earth (or possibly a mini-Neptune) exoplanet. GJ 1214 has a V magnitude of 14.7 and an H magnitude of 9.1, making it ideal to observe in the IR. The planet has an equilibrium temperature of ~ 560 K and should therefore have a very different spectrum from a hot Jupiter, with methane dominating the near-IR and IR opacities rather than CO, and with the alkali metals condensed out of the gas phase, resulting in them not being present in the upper atmosphere. In this thesis, I have concentrated on observations and expectations for hot Jupiters. However, GJ 1214b has now been so extensively observed that it needs to be mentioned here. Furthermore, it is one of my long-term goals to eventually move towards characterising smaller exoplanets, and GJ 1214b will provide a useful well-studied comparison for such observations.

The picture of GJ 1214b has been somewhat controversial, although most results agree that the transmission spectrum is relatively featureless (Bean et al. 2011; Berta et al. 2012; Désert et al. 2011a; Crossfield et al. 2011; de Mooij et al. 2012). A featureless spectrum suggests either a high mean molecular weight, which reduces the atmospheric scale height and hence spectral features, or a global cloud or haze layer preventing observations from reaching deep into the atmosphere as in HD 189733b. There are, however, some observations which do suggest features in the transmission spectrum at the level expected if the atmosphere were cloud-free and dominated by light elements such as hydrogen (Croll et al. 2011a, *J* and *K* bands). The reason for the discrepancy is still unknown. Narita et al. (2013b) also performed narrow-band photometry in *J*, *H* and *K* bands, but found results consistent with a flat spectrum. Désert et al. (2011a) obtained results in the 3.6 and 4.5 μm *Spitzer* bands, from two light curves, which were later refined by Fraine et al. (2013), who measured

14 transits at 4.5 μm and 3 transits at 3.6 μm . The new observations eliminate cloudless H-dominated models. A summary of all the results is shown in Figure 1.18.

It is difficult to tell with only IR observations whether GJ 1214b has an atmosphere with a high mean molecular weight or whether it is less dense but has an obscuring cloud or haze layer. Optical observations can constrain this degeneracy by looking for possible Rayleigh scattering signatures. The observations of de Mooij et al. (2012) do suggest evidence of a Rayleigh scattering signature in optical g and r bands. However, further observations by de Mooij et al. (2013) and Teske et al. (2013) show that the conclusions are not yet certain. Observations by Narita et al. (2013a) in B band were also inconclusive with regard to the transit depth, although the authors also performed long-term monitoring of the star and found variability at the $2.1 \pm 0.4\%$ level in g' band with a period of 44.3 ± 1.2 days. They also found semi amplitudes of $0.56 \pm 0.08\%$ in R_c band and $0.32 \pm 0.04\%$ in I_c band, suggesting that caution should be employed when interpreting the photometric results. Figure 1.19 shows more clearly the transmission spectrum of GJ 1214b at optical wavelengths, although it does not include the results of Narita et al. (2013a). Another constraint on the atmospheric type could come from the detection of $H\alpha$ in the transmission spectrum, although so far results for this feature are inconclusive (Murgas et al. 2012).

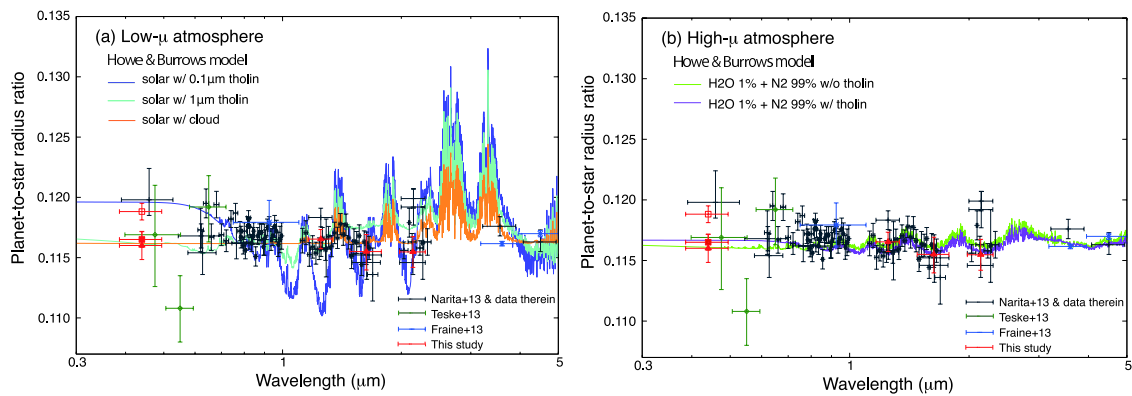


Figure 1.18: Summary of current results for the transmission spectrum of GJ 1214b from Narita et al. (2013a) compared to models for a low mean molecular weight atmosphere (left) and a high mean molecular weight atmosphere (right). The models are based on the formalism of Howe & Burrows (2012).

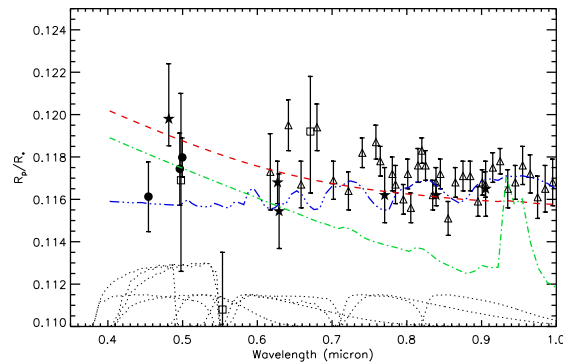


Figure 1.19: Summary of current optical results for the transmission spectrum of GJ 1214b by de Mooij et al. (2013). The filled circles are the observations from their work, the filled stars are from de Mooij et al. (2012), the open triangles are for data from Bean et al. (2011), and the open squares are for data from Teske et al. (2013). Overplotted are three models for the atmosphere of GJ1214b: a hydrogen-dominated atmosphere with solar composition (green line), a hydrogen-dominated atmosphere with clouds and low methane abundance (red line) and a water-dominated atmosphere (blue line). The dashed curves at the bottom are the transmission curves for the different filters. Note that for clarity the filter curves for the data from Bean et al. (2011) have been omitted, since they are effectively flat.

1.5.3 Further Observations of More Planets

Optical Transmission Spectra

Atmospheric surveys of multiple planets are now beginning, with understanding of the trends found anchored by the detailed properties of the most favourable cases. A large area of expansion has been transmission spectroscopy at optical wavelengths, where the blackbody spectrum from typical host stars peaks. Observations have now been carried out from both ground and space, searching for a variety of optical features. Some of the results are surprising when compared to predictions.

Firstly, the sodium feature has only been confirmed in three exoplanets besides HD 209458b and HD 189733b, which are WASP-17b, XO-2b and HAT-P-1b (Wood et al. 2011; Zhou & Bayliss 2012; Sing et al. 2012; Nikolov et al. 2013b), and the potassium feature has only been detected in two; HD 80606b and XO-2b (Colón et al. 2012; Sing et al. 2011a). The detection in HD 80606b is much larger than predicted and could be due to an escaping atmosphere. However, the detection is ~ 10 nm away from the rest-frame line centres and so is difficult to explain even with atmospheric escape. Only XO-2b has both sodium and potassium features confirmed in its atmosphere, while HAT-P-1b shows evidence of only the sodium feature but no potassium feature. For the other two planets, observations concentrated on one species alone, and so the presence or absence of the other cannot be ruled out or confirmed. In the case of XO-2b, the sodium feature is less than 50 \AA wide, suggesting

some haze or cloud cover obscuring the broader wings. Additionally, the observations of the sodium feature in WASP-17b tentatively suggest a lack of observable broad line wings. Conversely, the atmosphere of WASP-29b does not contain evidence of the predicted Na I feature at a resolving power of 430 (resolution of $\sim 14 \text{ \AA}$ at 6000 \AA). The observations suggest either a high altitude cloud or haze layer obscuring the unresolved line cores, or that Na I is not present in the upper atmosphere, and may have condensed into heavier compounds since the equilibrium temperature of the planet is 970 K. The transmission spectrum of WASP-23b, observed in 7 GROND²¹ passbands simultaneously is consistent with the clear atmosphere model, but further conclusions cannot be drawn from the data (Nikolov et al. 2013a). There is also tentative evidence to suggest sodium absorption in HD 149026b (Jensen et al. 2011).

The transmission spectrum of HAT-P-1b taken with HST STIS can be fitted just as easily by Rayleigh scattering or a high altitude cloud of larger grains (Nikolov et al. 2013b). There are also similar hints of a Rayleigh slope in the hot exoplanet WASP-12b (Sing et al. 2013), although the temperature required to fit the observations is much lower than expected for the planet, suggesting again, larger grains are important. Higher resolution observations around the predicted sodium and Rayleigh signatures could not confirm or rule out those features (Copperwheat et al. 2013).

One interesting result so far is that there has been no conclusive evidence for TiO features in an exoplanet transmission spectrum. Two planets at the required temperatures have been studied; WASP-19b, which has an equilibrium temperature of $\sim 2000 \text{ K}$, and WASP-12b, which has an equilibrium temperature of $\sim 2600 \text{ K}$. WASP-19b shows no evidence for predicted TiO features at the $2.7 - 2.9 \sigma$ significance level (Huitson et al. 2013, discussed in more detail in Chapter 6). Lendl et al. (2013) also find no evidence of TiO in r' , z' and $I+z'$ filters, although this is photometry taken over multiple epochs and could suffer from variability effects, since WASP-19 is a very active star. Mancini et al. (2013) also used photometric evidence to suggest a lack of TiO using simultaneous 7-band GROND observations. However, while the authors accounted for occulted starspots, the work has no correction for un-occulted starspots and the conclusions are based on absolute transit depths in the optical compared to the near-IR, which can be drastically affected by un-occulted starspots (see Chapter 6). WASP-12b also shows no signs of the predicted TiO features (Sing et al. 2013). These results are consistent with ground-based Gemini observations, which find the spectra inconsistent with cloud-free models but cannot confirm nor rule out TiO features (Stevenson et al. 2013). Knutson et al. (2010) showed a correlation between stellar activity and the lack of strong planetary thermal inversions, as measured by the $3.6 \mu\text{m}$ and $4.6 \mu\text{m}$ Spitzer occultation depths. They suggested that the cor-

²¹Gamma Ray burst Optical and Near-infrared Detector

relation might be caused by stellar activity breaking down the molecules responsible for strong thermal inversions. This may be the case for the atmosphere of WASP-19b. However, WASP-12 is a quiet star, suggesting that rainout²² could instead be responsible for the lack of observed TiO in the upper atmospheres of these planets. Observations which better constrain atmospheric dynamics, such as phase curves, would be a useful test of this hypothesis and I will observe the near-IR phase curve of WASP-19b with HST WFC3 for this purpose in 2014.

IR and Near-IR Transmission Spectra

After the difficulty of obtaining near-IR transmission spectra in the past, conclusive observations are finally starting to be made. It was confirmed by Crouzet et al. (2012) that extracting planetary spectra is at the limits of NICMOS' capability, and these authors confirmed that the NICMOS transmission spectrum of XO-2b is consistent with either a water detection or a flat spectrum. Recently, WFC3 has provided a dramatic improvement over NICMOS in reliability. Follow-up observations of XO-1b, where water was previously detected with NICMOS (Tinetti et al. 2010) and then shown to be inconclusive (Gibson et al. 2011), now show muted water features at an amplitude of 0.84 times the predicted level (Deming et al. 2013). Unlike any of the previously studied planets, the transmission spectrum of WASP-19b has been observed with WFC3 and Magellan to show the 1.4 μm water feature consistent with clear-atmosphere solar abundance models (Bean et al. 2013; Huitson et al. 2013; Mandell et al. 2013, Chapter 6). The Magellan spectrum could be consistent with muted features however, and fits well to both C-rich and O-rich models. Additionally, the observations are unable to confirm or reject the presence of water features at longer wavelengths. Similarly, HAT-P-1b has recently been observed to have a water feature in transmission in agreement with solar abundance clear-atmosphere models using WFC3 (Wakeford et al. 2013). Such results suggest a surprising diversity among the studied exoplanets, with the mechanisms behind the differences currently unclear.

Also, WASP-12b is now starting to be extensively studied. The radii in the 3.6 and 4.5 μm Spitzer bands are lower compared to the near-IR than predicted by clear-atmosphere models and the opacity appears greater in the 3.6 μm band than in the 4.5 μm band (Cowan et al. 2012; Stevenson et al. 2013). Furthermore, although the transmission spectrum in the near-IR obtained with WFC3 is inconclusive regarding the presence of molecular features, the transmission spectrum is best fit by a Mie scattering signature when optical STIS, near-IR and IR data are combined homogeneously (Sing et al. 2013; Stevenson et al. 2013; Cowan et al. 2012; Swain et al. 2013). Figure 1.20 shows a summary of the current transmission observations

²²Where a compound condenses and then falls out of the atmosphere due to gravity.

for WASP-12b except the optical STIS data, which is not yet published, and which provides a significant improvement on the precision obtained by Gemini.

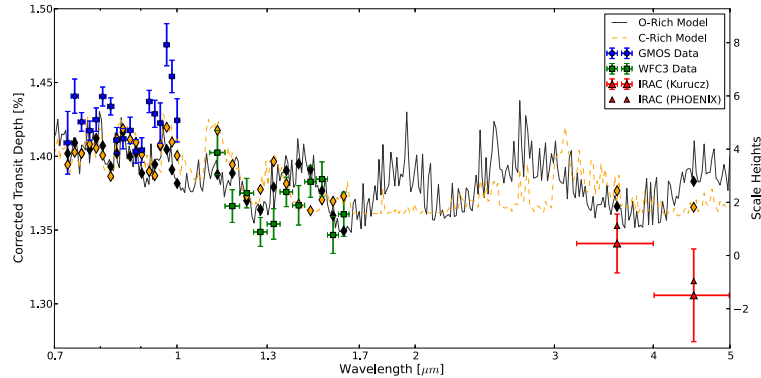


Figure 1.20: Summary of current results for the transmission spectrum of WASP-12b by Stevenson et al. (2013). The optical results are from their Gemini GMOS data. These authors re-analysed the WFC3 data first presented in Swain et al. (2013) and the Spitzer data first presented in Cowan et al. (2012).

UV Transmission Spectra

Due to low stellar fluxes, UV transmission spectroscopy is extremely challenging and only possible for bright targets. So far, the UV transits of only a few planets have been observed, including WASP-12b, 55 Cancri b and GJ 436. In the extended atmosphere of WASP-12b, Fossati et al. (2010) found evidence of Mg II at the 2.8σ level. They also found other 3σ deviations from the continuum in the planet's atmosphere, indicative of other metal lines, but the interpretation depends on the wavelength solution chosen. The authors also noted an early ingress, which is explained by Llama et al. (2011) as due to a magnetospheric bow shock. In GJ 436b, the Lyman α line has been observed in the planet's atmosphere with a signal of 11 %, implying an escape rate of 10^{10} g s^{-1} (Ehrenreich et al. 2011). Also a hint of an extended atmosphere has been observed around 55 Cancri b, a planet in possible grazing alignment with the star in a five-planet system (including the hot transiting super-Earth 55 Cancri e). Ehrenreich et al. (2012) found large Lyman α absorption at inferior conjunction of the planet, suggesting that the upper atmosphere of the planet produces a partial transit. No signal was detected from 55 Cancri e, placing an upper limit of $3 \times 10^8 \text{ g s}^{-1}$ on its upper atmospheric escape rate.

Emission Spectra

There are many planets for which one secondary eclipse depth has been measured, which constrains the temperature at one altitude. However, this thesis is focussed on transmission spectroscopy, which samples a higher altitude than those sampled by IR emission spectroscopy. Since determining a T - P profile from a transmission spectrum is currently only possible for the most favourable targets, the most useful constraints for my goals are cases where the eclipse depth has been measured in more than one band, constraining the temperature profile of one part of the atmosphere. Such results can help explain the features that are seen in transmission. Therefore, in this section I only discuss here one planet in detail, which is WASP-19b, since the measurement of its transmission spectrum forms the basis of Chapter 6. I will then briefly overview those planets which have been well studied and then discuss broad properties of the hot Jupiter exoplanet class as a whole.

WASP-19b is one of the most studied planets in secondary eclipse, apart from HD 189733b and HD 209458b, because it is one of the hottest known transiting exoplanets and has a very large eclipse depth. There have been photometric observations of the secondary eclipse of WASP-19b in the optical, z , H and K bands, and at 1.19, 3.6, 4.5, 5.8 and 8.0 μm (Anderson et al. 2010; Gibson et al. 2010; Burton et al. 2012; Lendl et al. 2013; Anderson et al. 2013; Abe et al. 2013). The results are consistent with no strong thermal inversion and also tentatively suggest an oxygen-dominated atmosphere when compared with the models of Madhusudhan et al. (2011b); Madhusudhan (2012). Figure 1.21 summarises the results for the emission spectrum. The optical signal could be due to either thermal or reflected components and Abe et al. (2013) find an upper limit for the geometric albedo of 0.27 ± 0.13 .

There are some other exoplanets which have been observed in detail in their secondary eclipse. One interesting case is that of WASP-12b. Initially, observations indicated a planet with a weak thermal inversion and inefficient thermal redistribution (López-Morales et al. 2010; Croll et al. 2011b; Zhao et al. 2012; Crossfield et al. 2012b). However, it was later found that the spectra were best fitted with a high C/O ratio and potentially efficient thermal redistribution due to shallow IR eclipse depths (Madhusudhan et al. 2011a). The picture then became more confusing when Cowan et al. (2012) measured eclipse depths in the Spitzer 3.6 and 4.5 μm bands which were too different to reconcile with either a solar or a high C/O ratio. A possible explanation was recently revealed by Crossfield et al. (2012a), who pointed out that WASP-12 has an M dwarf companion star initially reported by Bergfors et al. (2011, 2013). The companion star will cause eclipse depths to be underestimated, and since it is cooler than WASP-12, the effect will be more significant at longer wavelengths.

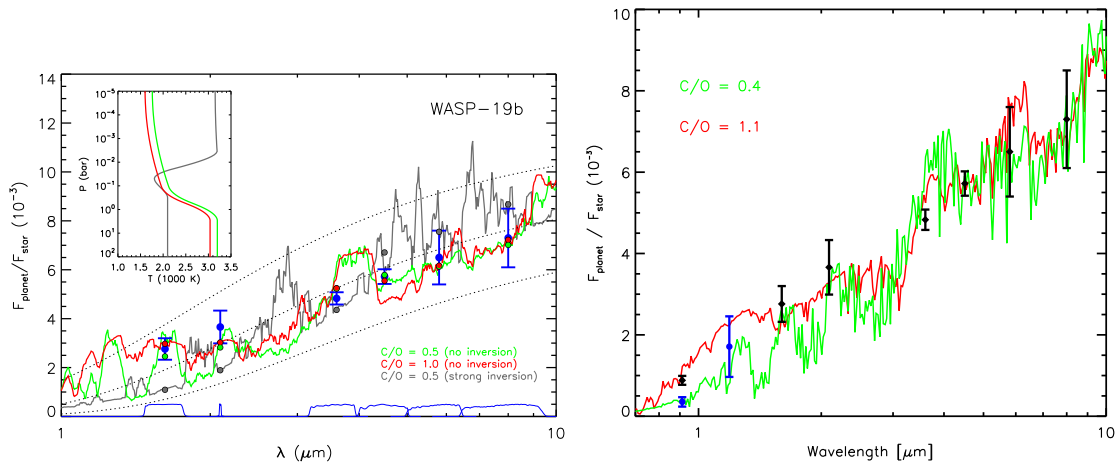


Figure 1.21: Emission spectra of WASP-19b. *Left*: Plot from Anderson et al. (2013) showing their results at 3.6, 4.5, 5.8 and 8.0 μm along with the results of Anderson et al. (2010) and Gibson et al. (2010). Overplotted are models with and without temperature inversions from Madhusudhan et al. (2011b). *Right*: Plot from Lendl et al. (2013) showing their results in z band and at 1.19 μm , along with the literature values from the left plot and another z band observation from Burton et al. (2012). Also shown are models from Madhusudhan (2012) with different C/O ratios.

After correcting for the effect of the companion star, Crossfield et al. (2012a) found that the emission spectrum is well approximated by a blackbody, and hence the planet lacks a stratosphere.

Other planets observed in multiple bands include CoRoT-1b, which has an inversion in the atmosphere deeper than the region sampled by Spitzer observations, a small but non-zero heat transfer from day to night side ($P_n = 0.1$) and a very low bond albedo consistent with zero (Rogers et al. 2009 and references therein). Another planet sampled in detail is HD 149026b, which has no indication of a temperature inversion, moderate thermal redistribution ($f = 0.5$) and large amounts of CO and CO₂ (Stevenson et al. 2012a and references therein). Finally, multi-wavelength analysis shows that TrES-3b is unlikely to have a temperature inversion (Christiansen et al. 2011 and references therein).

Such detailed analysis is not available for many planets. However, while the secondary eclipses of a greater number of planets have only been observed in a single band, or even two bands, the results can still be used to try to understand broad characteristics of the hot Jupiter class. For example, Knutson et al. (2010) used the difference in eclipse depth measured in Spitzer's 3.6 and 4.5 μm bands as a measure of whether an atmosphere contains a stratosphere. In a cloud-free atmosphere, the 3.6 μm wavelength should sample deeper into the atmosphere. Therefore, if the eclipse depth at 3.6 μm is greater than that at 4.5 μm then there is no inversion. If the eclipse depth at 4.5 μm is greater than the eclipse depth at 3.6 μm then there is

an inversion. Similar values at both wavelengths indicate an isothermal atmosphere. Knutson et al. (2010) found a correlation between the presence or absence of thermal inversions and the activity level of the star, quantified by the chromospheric Ca II H & K line emission ratios of $\log(R'_{\text{HK}})$. It is possible that radiation from stars with high activity levels could break down TiO, explaining the lack of observed stratospheres in planets which orbit active stars. Figure 1.22 shows the trend.

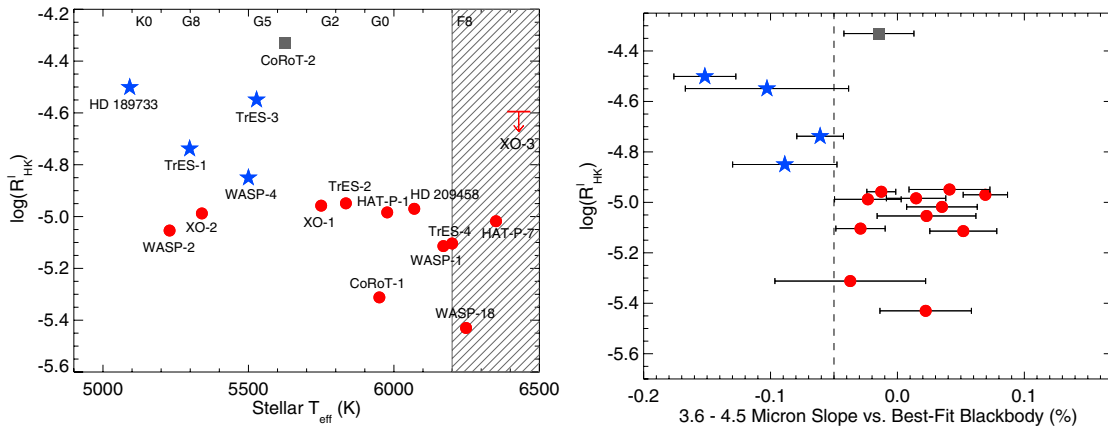


Figure 1.22: Figures from Knutson et al. (2010) showing the activity levels of various stars compared to whether or not their atmospheres are measured to host a thermal inversion. *Left*: Stellar effective temperature vs. activity index. The shaded region is where the calibration for $\log(R'_{\text{HK}})$ is uncertain (Noyes et al. 1984). *Right*: Their index for classifying temperature inversions vs. stellar activity index. In both plots, planets classified as having temperature inversions are shown as red circles and planets without are shown as blue stars. The spectrum of CoRoT-2b is unusual and is not described well by either model. XO-3b orbits a star with a high $\log(R'_{\text{HK}})$ ratio, but no emission visible in the Ca II H & K lines by inspection. The planet has a stratosphere. See Knutson et al. (2010) for the individual references for each observation.

Recent results since the paper of Knutson et al. (2010) are still relatively consistent with the trend. WASP-24b, WASP-43b, WASP-14b and WASP-5b have all been shown to lack strong temperature inversions (Blecic et al. 2011; Smith et al. 2012; Blecic et al. 2013; Baskin et al. 2013). Of these, WASP-24 is not chromospherically active ($\log(R'_{\text{HK}}) = -4.98 \pm 0.12$, Smith et al. 2012) and WASP-5b is moderately active ($\log(R'_{\text{HK}}) = -4.75$, Baskin et al. 2013).

Another interesting comparison that can be drawn between many planets with only one or a small number of secondary eclipse measurements is their thermal redistribution efficiencies. Knowing the distance of the planet from the star and the star's effective temperature, the day-side equilibrium temperature can be calculated from Equation (1.16) by assuming some recirculation efficiency, f , and some Bond albedo, A_B . If an assumption is made about the albedo of the planet, then the secondary eclipse depth can be used to infer the recirculation efficiency. Using the assumption of $A_B = 0$, Cowan & Agol (2011) compared redistribution efficiency as measured by

the secondary eclipse depth to the irradiation of the planet for many planets. A large secondary eclipse depth, and hence a high day side temperature would indicate inefficient thermal redistribution. They found that planets with equilibrium temperatures below ~ 2000 K display more efficient thermal redistribution than planets with equilibrium temperatures above ~ 2000 K, suggesting that the mechanisms responsible for thermal redistribution break down at hotter temperatures (see Figure 1.23).

There is so far no clear model explicitly explaining the mechanisms for thermal redistribution. Perna et al. (2012) computed 3D models with dual-band radiative transfer and found that recirculation starts to break down at temperatures of around 2000 K, consistent with observations. The efficiency of thermal redistribution is partly dependent on the ratio of radiative to advective timescales, but they found that opacity-driven effects (such as TiO causing irradiation to be deposited higher up) are secondary to the effects of irradiation. Figure 1.23 also shows some of their results.

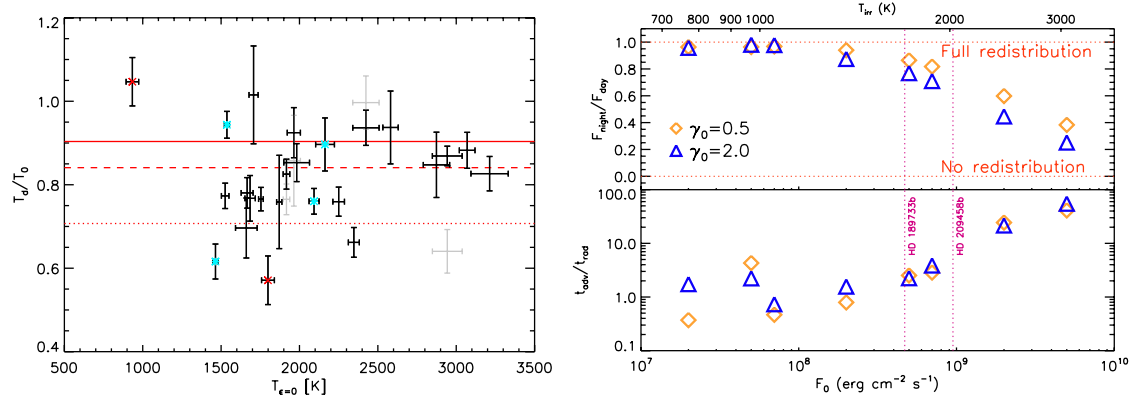


Figure 1.23: *Left:* Plot from Cowan & Agol (2011) showing dimensionless measured day side temperature (T_d/T_0) vs. the day side temperature that would be measured in the presence of no thermal redistribution ($T_{\epsilon=0}$). The red lines correspond to no recirculation (solid), uniform day hemisphere (dashed) and uniform planet (dotted). Planets should not lie above the solid red line. The points marked with red crosses are on eccentric orbits. The cyan asterisks denote planets which do not have a stratospheric temperature inversion. Some planets have both grey and black points, and these are planets for which the optical secondary eclipse has been measured. The grey points are using the default zero-albedo assumption and only data points for $\lambda > 0.8 \mu\text{m}$, and the black points are the day side temperatures measured when including the optical data. *Right:* Plot from Perna et al. (2012) showing the day-side to night-side flux ratio (top) and the advective to radiative timescale ratio (bottom) compared to irradiation. The γ_0 factor controls whether there is an inversion, with an inversion present if $\gamma_0 > 1$.

Phase Curves

The results quoted in Cowan & Agol (2011) rely on assumptions of the planetary albedos, since only day side temperature observations from secondary eclipse constrain the models. It is unclear whether the correlation is due to albedo differences or recirculation efficiency, and Figure 1.23 shows how important the albedo estimation can be. Thermal phase curves provide further information by measuring day-night contrast and recirculation rates independently of planet albedo. However, although highly useful, phase curve measurements require long duration observations which are challenging and difficult to schedule. Therefore, only 7 planets have thermal phase curves published so far including HD 189733b and HD 209458b (Knutson et al. 2007b, 2009b,a, 2012; Lewis et al. 2013; Agol et al. 2010; Cowan et al. 2012; Stevenson et al. 2012a,b; Maxted et al. 2013; Harrington et al. 2006; Crossfield et al. 2010, 2012b). One of the 7 planets, Upsilon and b, is not transiting and hence the interpretation of the phase curve amplitude requires an assumption of the system's inclination. The currently observed phase curves cover the extremes of the hot gas-giant equilibrium temperature range, from $T_{\text{eq}} \sim 700$ to 3000 K, and so far bear out the predictions and measurements from secondary eclipse observations of redistribution breakdown at hotter temperatures. The observations, which are measured at the IR photosphere, show day-night contrasts of only ~ 200 -500 K for the cooler planets, and a much stronger ~ 1900 K contrast for the hottest planet observed (WASP-12b). One important point to mention, though, is that these observations do occur at different wavelength ranges, and hence may not all be sampling the same altitude across the different planets. Furthermore, unless the dominant opacity sources are known (for example from the transmission spectrum) assumptions of the altitude sampled by each wavelength can be incorrect, as in the case of HD 189733b.

Recently, in order to try to explain current phase curve observations, Perez-Becker & Showman (2013) modelled atmospheric thermal redistribution by using a two-layer shallow-water (small atmosphere) model for synchronously rotating planets. They found that planets with weak friction and weak irradiation have strong zonal flow and hence small temperature differences between the day and night sides, whereas highly irradiated planets exhibit strong day to night temperature contrasts. They developed a theory which shows that the timescale for gravity waves²³ to propagate horizontally, τ_{wave} , is important in determining thermal redistribution efficiency. Figure 1.24 shows the models compared to current thermal phase curve observations.

²³Transverse waves caused by convection overshoot.

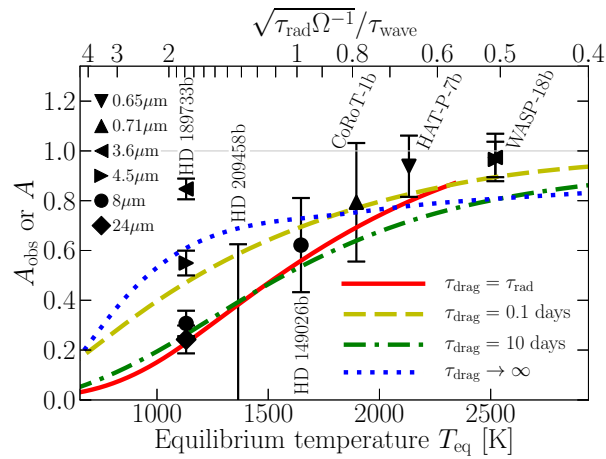


Figure 1.24: Plot from Perez-Becker & Showman (2013) showing their models of fractional day-night flux variations (A) vs. equilibrium temperature along with observed fractional day-night flux variations (A_{obs}). The models assume that the observed thermal emission comes from a layer at $P = 0.25$ bar. Most plotted solutions are in the weak-drag regime, so all curves lie close together and broadly reproduce the observational trend.

1.6 Challenges for the Future and My Contribution

What is emerging from observations is a large and unexpected diversity in studied planets, underlining a still significant gap in knowledge of hot Jupiters. I believe that hot Jupiters are important to study, both to obtain fundamental insights into underlying physics and as part of the path towards detecting habitable planets. With this in mind, this work has mainly sought to improve understanding of hot Jupiters by answering two complementary questions:

1. ***What are the detailed atmospheric properties of the most favourable targets?*** The demanding nature of exoplanet observations means that detailed atmospheric properties can only currently be obtained for a few most favourable cases (large atmospheric signals, bright stars etc.). Studying the most favourable targets in detail is important, since they can provide benchmarks for further studies of other planets.
2. ***Can we detect and understand different broad classes of hot Jupiters and the mechanisms behind the key differences?*** Another key type of observation is comparative exoplanetology. What we seek is an understanding of the physical mechanisms that operate in hot Jupiter atmospheres. Such knowledge cannot be gained from only a very small sample of planets. To have a true understanding, we need a large sample of planets, where we can link observed features with physical properties, such as stellar type, irradiation, and composition.

I believe that both goals are important and complementary, and have been involved extensively in trying to further them both.

Pushing the Boundaries of Observability

A strong advantage of studying exoplanet atmospheres now is that we develop vital new techniques for the future, with one eventual goal being the study and characterisation of potentially habitable planets. Although most studies now are concerning hot Jupiters, this work and my plans for the future are also designed to advance the precision of observations in two ways:

1. ***Testing and expanding the limits of ground-based transmission spectroscopy.*** Ground-based atmospheric characterisation is a rapidly developing and improving field. Since ground-based telescope time is much more easily available than space telescope time, it allows numerous targets to be studied, which is essential for comparative studies. Furthermore, the larger apertures available

from the ground also provide the ability to study fainter targets, and so increase the potential number of observable planets. I have been involved in certain developments in ground-based exoplanet observations including the first long-slit exoplanet transmission spectrum. I also plan to be involved in further work using very new techniques, which are detailed in Section 7.2.2.

2. **Beyond hot Jupiters.** It is important to extend atmospheric observations beyond hot Jupiters, to broaden our knowledge of atmospheric physics and to eventually lead to studies of Earth-like planets. Although the work in this thesis concentrates on hot Jupiters, I have had an HST proposal accepted to use similar methods for an eccentric warm Jupiter, in a different regime to the hot Jupiter class. Furthermore, after my PhD, I plan to be involved in a large *Spitzer* programme to observe cooler, smaller planets than those studied in this work.

Thesis Structure

- In Chapter 2, I provide an overview of the telescopes and instruments used in this project. I then outline the statistical and analysis methodology used in this work, and also some dominant methodology used in the field, which is only touched on briefly by my work. This chapter should serve as a reference point for techniques and nomenclature used throughout the thesis.
- Chapters 3 and 4 concentrate on answering the first question regarding hot Jupiters: attempting to reach a deeper understanding of the most favourable targets. These chapters detail medium-resolution observations of the Na I feature in HD 189733b and the determination of the upper atmospheric T - P profile.
- Chapters 5 and 6 concentrate on answering the second question regarding hot Jupiters. These chapters detail the first results from ground-based and space-based low-resolution spectroscopic surveys of hot Jupiters respectively. Simultaneously, Chapter 5 presents the first long-slit ground-based transmission spectrum of an exoplanet.
- In Chapter 7, I conclude and discuss my plans for the future. I outline how I will not only continue to observe hot Jupiters but how I will push the boundaries of observability towards other planets and other instrumental techniques with ongoing and future projects. I include here a brief description of my accepted telescope proposals for the future.
- In addition, Appendix A gives a list of constants, Appendix B gives a list of acronyms, Appendix C gives a list of definitions, and derivations can be found in Appendix D.

Chapter 2

Research Methodology

2.1 Instrumental and Observational Techniques

2.1.1 Spectroscopy

In spectroscopy, the light from a source is spatially dispersed across the detector depending on its wavelength, meaning that the intensity as a function of wavelength can be measured. The resolving power, R , of a spectrometer is defined as

$$R = \frac{\lambda}{\Delta\lambda}, \quad (2.1)$$

where λ is the wavelength being observed and $\Delta\lambda$ is the smallest wavelength difference that can be seen. The instrumental resolution is dependent on the resolving power of the disperser (see below), instrument optics and other factors such as slit width. For high resolution, the spectrum is imaged to a larger length at the detector. The disadvantage at higher resolution is that, because the spectrum is so extended at the detector, only a small wavelength range can be measured at any one time. Low resolution is required if many wavelengths are to be sampled at once.

The simplest form of a spectrometer is a prism, where light is dispersed due to the wavelength dependence of the refractive index of a material. Such devices can be positioned such that the central wavelength of interest passes straight through the prism with no refraction, meaning that the instrument can be used as both an imager or a spectrometer. However, such instruments are limited to the optical properties of transparent materials.

Gratings

Diffraction grating spectrometers work on the principle that constructive interference between components of light through multiple slits occurs at different phases depending on wavelength. A spectral grating is composed of many slits that produce a diffraction pattern, which has an envelope with constructive interference peaks at orders 0, 1, 2, etc. corresponding to 0, 1, 2 etc. wavelengths of retardation. The angular locations of the maxima in the interference pattern are governed by the grating equation (derived in Appendix D.6):

$$m\lambda = d \sin \theta, \quad (2.2)$$

where m is the diffraction or spectral order number, d is the distance between slits, λ is the wavelength of the observed light, and θ is the angle of emergence after passing through the slit. This equation assumes that the angle of incidence of radiation is perpendicular to the surface of the grating. The zeroth order is where light passes straight through the slit ($\theta = 0$) and so contains no wavelength dependence. Intensity decreases as θ increases, and so usually, the first order spectrum is used for primary analysis and the grating is positioned so that as much of the first order spectrum falls on the detector as possible.

Often, incoming light is deflected off grooves in the grating rather than passing through slits, and the setup resembles Figure 2.1 (θ now has a different meaning and is referred to as the “blaze angle”). The grating equation becomes (Appendix D.6)

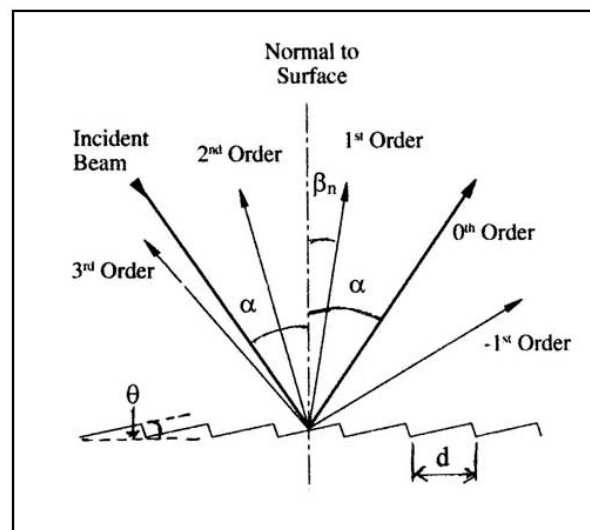
$$m\lambda = d(\sin \alpha + \sin \beta), \quad (2.3)$$

where α is the incident angle of radiation coming onto the grating and β is the angle of the radiation reflected from the grating, both relative to the grating normal. This equation is also valid for a transmission grating where the angle of incidence is α and angle of emergence is β . The spectral resolving power can be defined as (Palmer 2005)

$$R = mN, \quad (2.4)$$

where N is the total number of grooves illuminated on the surface of the grating. Using Equation (2.3), it can be seen that the resolving power can be defined as:

$$R = \frac{Nd(\sin \alpha + \sin \beta)}{\lambda}. \quad (2.5)$$



Reflection Grating Diffracted Orders

Figure 2.1: A schematic of a diffraction grating taken from <http://www.medwayoptics.com/> [accessed 01-Sep-2013].

Grisms

Some instruments are designed so that they can be used either as a camera or as a spectrometer, providing greater versatility. Since a spectrometer is usually positioned such that the first order spectrum falls on the detector and the zeroth order does not, the grating cannot simply be removed in order to take images. Instead, these instruments use a grism, which is a combination of a grating and a prism. The prism counteracts the deflection caused by the grating, allowing the light to be dispersed without being deflected and ensuring that the central wavelength passes straight through. In order to operate the instrument in imaging mode, the grism then simply has to be removed, allowing the image to fall on the centre of the detector.

Echelle

Echelle gratings operate at high resolution (high dispersion) by using a high incidence angle, and often using high spectral orders. They are usually used with a cross-disperser to get more than one order on the detector at the same time, and hence cover a reasonable wavelength range even with very high resolution. Such high resolutions are useful for detecting small Doppler shifts of spectral lines that could indicate the motion of a planet's atmosphere.

Multi-Object

Multi-object spectroscopy enables the spectra of more than one object to be obtained simultaneously, allowing removal of systematic trends that are common to all sources. There are three main techniques.

Firstly, long-slit spectroscopy uses a very long slit (typically a number of arcminutes in length), which is able to be rotated to any angle on the sky. The large slit length allows the observer to position the slit on the sky such that more than one star appears within the slit. The spectra are then separated on the detector in the direction perpendicular to the dispersion direction (for example Figure 5.1). The two stars need to be as close to one another as possible so that the effects of any small rotations of the slit on the sky during the long observations required to observe exoplanet transits are minimised.

Multi-slit spectroscopy is a variant on this, which uses many slits for many different objects. As well as allowing more comparison stars than long-slit spectroscopy, the field of view can be wider, allowing observations of a more similar comparison star or stars to the object of interest.

Integral field unit (IFU) spectroscopy is another variant, which uses many small lenslets or optical fibres, allowing the observer a very wide field of view and many comparison stars. Additionally, each fibre occupies a particular position on the detector in the cross-dispersion direction regardless of the location of the stars, meaning that multiple spectra do not overlap.

2.1.2 Detector Types Used in this Thesis

In this section, I will briefly overview the detector types which were used in this thesis. Basic information and phrases which are common to different types of detector are given in Appendix C.

The detectors used in this work all make use of doped semiconductor materials; one with extra electrons (n-type), and one with missing electrons or “holes” (p-type). The junction between the materials forms a “depletion region”, without free charge carriers. When a photon of high enough energy is absorbed by the material, it creates an electron-hole pair in the depletion region. The energy required for an incoming photon to produce an electron-hole pair is called the “band gap”. Silicon detectors are often used in the optical, while materials such as mercury cadmium telluride (HgCdTe) can be used in the IR, since the band gap can be altered and controlled by adjusting the relative amounts of Hg and Cd in the crystal.

In a CCD, a positive voltage is applied to the material, resulting in freed electrons being collected at one end of the cell. A barrier material prevents the electrons from leaving the cell. Once an exposure has finished, charge packets are read out from one point by moving the charge from each pixel along the whole array. The advantage of having all charges read out from one point is that there is less circuitry and hence less thermal noise, and the gain is the same for all pixels. It also allows the array to use very small pixels. The disadvantage is that, once read, charge cannot be returned to the pixel in which it originated and so a pixel can be read only once per exposure. CCDs are often made of silicon, with band gaps suitable for optical observations. All of the optical observations in this project made use of CCD detectors.

A photovoltaic detector uses the p-n junction as a capacitor, where the capacitance is determined by the voltage across the junction. Hilbert (2004)¹ describe the operation of the near-IR photovoltaic detector in HST WFC3 in the following way (the instrument is described in Section 2.2.1 and is the only photovoltaic detector used in this project). A negative reverse bias is applied across the junction at the start of an exposure. Incoming photons create photo-electrons in the p-n junction, which discharge the capacitance and reduce the voltage across the junction towards zero. Comparing the voltage at the end of the exposure with the bias voltage at the start of the exposure allows calculation of the number of photo-electrons generated (and hence the number of photons received) during the exposure.

Hilbert (2004) also discuss the reasons that the WFC3 detector exhibits non-linearity. They point out that the capacitance of the diode is a function of the voltage across the diode. Therefore, as more photons are received and the voltage decreases towards zero, the capacitance of the diode increases. Since $Q = C \times V$, where Q is charge, C is capacitance and V is voltage, the voltage measured is not a linear function of the charge induced by incoming photons. As the number of incoming photons increases, the voltage recorded decreases per photon. This non-linearity effect becomes significant for bright targets or long exposures and is significant long before saturation occurs.

An array of read-out amplifiers allows the possibility of “non-destructive reads”, which involves reading out a pixel and then leaving the charge in that pixel as it was before the read out. Multiple reads in a single exposure have the advantage of allowing the linearity of response to be tested, and also of driving down read noise. Testing the linearity of response in this way is sometimes referred to as sampling “up the ramp” because of the ramp-like shape of the response function as a function of increasing count level. The final signal value can be corrected to the value it should

¹Instrument science report WFC3-2004-06, available at www.stsci.edu/hst/wfc3/documents/ISRs/WFC3-2004-06.pdf [accessed 01-Sep-2013].

be if it is found to be in the non-linear regime, by comparing with a predicted linear response. Figure 2.2 shows an example of non-linearity observed with non-destructive reads for an exposure of the WFC3 detector, from Hilbert (2009)².

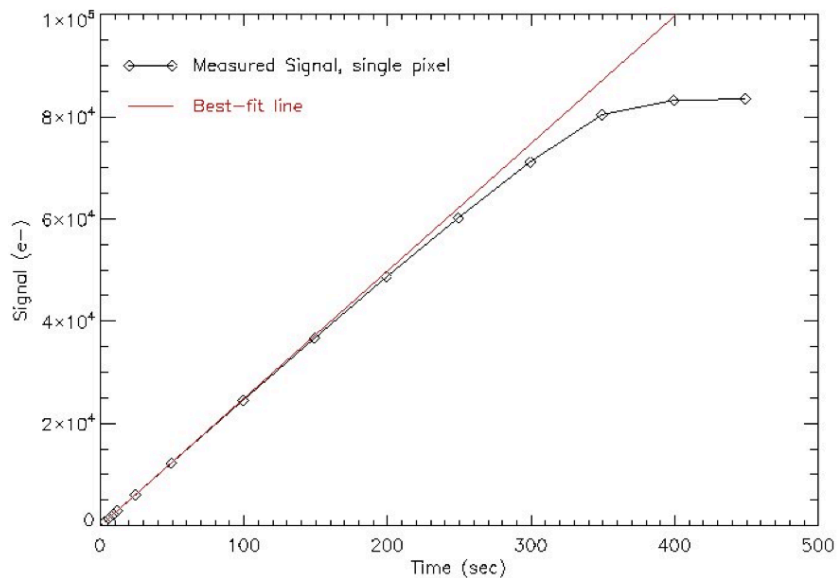


Figure 2.2: The WFC3 detector response as a function of increasing count levels for a single pixel from Hilbert (2009). Non-linearity is obvious from the multiple non-destructive reads within the exposure, and starts at relatively low count levels.

2.1.3 Sources of Noise

In this section, I will describe the main sources of noise for exoplanet characterisation observations, rather than providing a complete overview of all possible sources of noise. Additionally, some noise sources are dealt with in Section 2.1.4.

Photon Noise: Since photons are discrete particles, they are emitted from the source at random times. The probability of a photon arriving during a fixed time interval is small and arrival of successive photons can be considered independent. Thus, the fluctuation of the number of photons received over a given integration time will follow a Poisson distribution with variance $\sigma^2 = \mu$, where μ is the mean number of counts. Therefore, the signal-to-noise increases by the square root of the number of counts (see e.g. Wall & Jenkins 2009). For many samples of the mean flux (many exposures), the distribution of the means over time has a Gaussian distribution, which is very useful for modelling transit light curves using least-squares fitting.

²Instrument Science Report WFC3 2008- 39, available at www.stsci.edu/hst/wfc3/documents/ISRs/WFC3-2008-39.pdf [accessed 01-Sep-2013]

Read Noise: Read noise is produced by a small uncertainty in the conversion from analogue signal to digital number in the amplifier. There is also a small uncertainty in the current or voltage produced by photo-electrons. Typical values are a few electrons. In the presence of large numbers of photons, read noise becomes negligible (see e.g. Howell 2000).

Cosmic Rays: Cosmic rays are high-energy particles which can impact the detector during a long observation. Since they have very high energies, they record a large number of counts in the pixel or pixels on which they hit. For a spectrum, this produces a wavelength-dependent effect. Cosmic rays are transient events and can be detected and removed by comparing multiple exposures in an observation and looking for outliers.

Seeing: Seeing is caused by turbulence in the atmosphere, which causes the index of refraction where the telescope is looking to vary over time. The variation in the index of refraction integrated over the height of the atmosphere provides the characteristic scale for aberrations. The variation in index of refraction (seeing) worsens if there are smaller patches of turbulent atmosphere. The effect of large seeing is to effectively blur the images on the detector. It is not a significant problem for exoplanet observations unless there is blending of sources, the observations suffer variable slit losses³, or there is a significant difference in detector response for different pixels and the seeing varies. Defocussed images are often used in ground-based photometry to spread the light over many pixels in each observation and thus reduce the effects of non-uniform pixel response (e.g. Nikolov et al. 2013a).

Atmospheric Dispersion: Light from a source is refracted by the atmosphere between it and the telescope, with the degree of refraction dependent on wavelength, and worse for higher airmass. For spectroscopic observations, atmospheric dispersion causes slit losses. Usually, spectrometers are optimised so that the effects are smallest in the central wavelength used and worse towards the spectral edges.

Use of a wider slit can partially remove the problem and has the additional advantage of being less sensitive to seeing variations throughout an observing night. Additionally, some telescopes employ an atmospheric dispersion compensator (ADC), usually taking the form of one or more prisms which can be adjusted throughout the night to control the compensation.

³Light losses due to the point spread function (PSF) of the target not being properly centred within the telescope slit, or being too wide for the slit.

Other Correlated Noise: “Correlated noise” is a broad expression which means any form of instrumental, atmospheric or even astrophysical noise that varies as a function of time rather than being random. If such noise is also a function of wavelength, then the measurement of spectral features in transmission spectroscopy could be severely affected. For photometric measurements, absolute radii can be affected, preventing comparison of planetary radius ratios at multiple wavebands. Sources of correlated instrumental include thermal variations, drift of the source on the detector, varying inter-pixel and intra-pixel response, persistence, charge trapping, non-linearity and slit losses depending on telescope guiding. Further sources of noise could be astrophysical, such as intrinsic stellar variability.

For ground-based observations, there are atmospheric sources of noise such as airmass variations, seeing and sky brightness variations and variable telluric spectral features. Some methods of limiting atmospheric noise during observations have been discussed, but many sources of correlated noise cannot be avoided and must be dealt with in the data reduction and analysis stages. Since correlated noise is the most crucial to the long-duration measurements of transits and occultations where the critical measurement is relative brightness as a function of time, methods of dealing with it after observations are taken are discussed separately in Section 2.3.4. The individual sources of noise for the observations in this thesis are discussed separately in the relevant chapters.

2.1.4 Observational Techniques

Bias: Since an unexposed pixel will not give a value of 0 when read out, but will give a mean value with a small distribution around zero, it is necessary to introduce a bias to prevent negative values. The bias is a positive offset for all values read out and can be removed by subtracting a bias frame (image taken when no source illuminates the detector) or using a bias or “overscan” section (a region of the detector around the edge where no illumination occurs).

Dark Current: The detector material has a level of thermal noise depending on its temperature. If the thermal energy is high enough, it frees electrons from the semiconductor that contaminate the science signal. Dark noise has a Poisson distribution meaning that the noise level introduced into the signal is the square root of the number of electrons freed by thermal energy. Dark current can be removed by subtracting dark frames; images taken with the telescope shutter closed, but for the same duration as the science observation. The bias is also present in the dark images, and hence these can be removed together.

Flat Field: A flat field is a uniform exposure across all pixels, which the observer then normalises around 1 to remove from the science images. Flat-fields are designed to correct for the variation in gain or efficiency across different pixels. Flat-fielding can introduce noise into the high-precision observations required for exoplanet observations unless a large number of flat fields are co-added. To improve precision, exoplanet observations typically make use of “dome flats”, where the flat-field is obtained by illuminating the telescope dome, with the dome shut, rather than “sky flats”, which use the dawn or dusk light as an illumination source. Ideally, the illumination source should have the same spectrum as the incoming light that is observed because, typically, pixel response is a non-linear function of wavelength. Alternatively, flat-fields may not be as accurate as required and hence transit and secondary eclipse methods sometimes rely on a stable source position throughout the night, rather than using flat-fields. Provided that a source remains stable on the detector, flat-fielding errors are not time dependent, and so are cancelled out when in-transit or in-occultation data is compared to the stellar flux baseline.

2.2 Instruments Used for this Thesis

2.2.1 The Hubble Space Telescope (HST)

The HST is in orbit around the Earth with an orbital period of ~ 96 minutes (Figure 2.3). It has a 2 m primary mirror and instruments for UV to near-IR observations, both imaging and spectroscopic. The HST has proved very powerful for exoplanet atmosphere characterisation with very well-behaved systematics depending on the instrument. The two instruments that I have used for this project have well understood systematics and are introduced below.



Figure 2.3: The Hubble Space Telescope floating above Earth during servicing mission 3B, March 2002 (http://hubblesite.org/the_telescope/hubble_essentials/ [accessed 01-Sep-2013]).

Space Telescope Imaging Spectrograph (STIS)

I will provide a brief overview of only the instrument and setups that I used. Detailed information about STIS and observing instructions can be found in the instrument manual⁴.

STIS is a very versatile instrument. Among its abilities, some of the most important for exoplanet observations are that it is capable of measuring spectra from 1150 to 10,300 Å at low and medium resolution, and capable of high resolution echelle spectroscopy in the UV. The CCD provides a 52×52 arcsecond FOV, with a pixel

⁴Available at <http://www.stsci.edu/hst/stis/documents/handbooks/currentIHB/toc.html> [accessed 01-Sep-2013].

scale of ~ 0.05 arcseconds square per pixel. The full CCD is 1024×1024 pixels. Overheads are 45 seconds for full-frame readout, but can be reduced to 20 seconds for subarray readouts, which were used for all of the observations in this project. The detector can be operated with a gain of 4 or 1. The saturation limit is 120,000 electrons per pixel for a gain of 4, which is the full-well limit, and 33,000 electrons for a gain 1. One extremely useful aspect of the detector is that it has a very large dynamic range because its response is linear up until full-well saturation (with the exception of very small count levels, where non-linearity is observed but which is negligible here). Furthermore, if full-well saturation occurs, charge bleeds in the non-dispersion direction, which does not affect spectral measurements and still allows all photons to be collected and recorded at the correct wavelength. Such a feature is very valuable when high signal-to-noise observations are required, meaning that full-well saturation does not have to be considered when trying to optimise the duty cycle unless the number of counts is extremely high and a small subarray is being used. I did not notice any persistence effects for any of the observations taken for this project. Within the instrumental capabilities of STIS, there are many different settings and gratings. Those which were used to obtain data for this project are listed in Table 2.1.

Grating	Wavelength Range (\AA)	Resolving Power (R)
G750M	5450-10,140	5000
G430L	2900-5700	530
G750L	5300-10,300	530

Table 2.1: STIS gratings used in this project. The letter “G” denotes first order gratings. Note that, although the wavelength coverage of the G750M grating is 5450-10,140 \AA , this only represents the available range of possible wavelengths that can be observed. The wavelength coverage that can be simultaneously observed with one observation is only 570 \AA at $R = 5000$ and depends on the tilt of the grating used. To obtain observations over the full spectral range, 9 different settings must be used. For use in this project, a single tilt was used, which allowed observations in a wavelength range of 5808-6380 \AA . The first order “L” gratings have only one setting and cover their whole wavelength range simultaneously. Also note that resolving powers are approximate and also do change with the tilt angle. The resolving powers quoted here are the ones for the settings used in this project.

Wide Field Camera 3 (WFC3)

Again, I will provide only a brief overview of the instrument and relevant setups. Detailed information about WFC3 and observing instructions can be found in the instrument manual⁵.

WFC3 is an imaging instrument which also has gratings for spectroscopic mode observations. IR spectroscopic data was used for this project, with the G141 grating, covering a wavelength range of 10870-16870 Å. For IR observations, the filter wheel, which also houses the gratings, and the detector package are housed in a cold shroud maintained at -30 °C to reduce background emission onto the detector. The detector is a 1024 × 1024 pixel HgCdTe photovoltaic array. The pixel scale is 0.135 × 0.121 arcseconds per pixel with a total field of view of 136 × 123 arcsec. The instrument is operated with a gain of 2.5. The saturation threshold is defined to be where the detector response deviates by more than 5 % from linear, and occurs at ~ 31,000 DN (data number), or 78,000 electrons. However, the detector response has been observed to start becoming non-linear at around 18,000 DN. In order to account for non-linearity, exposures taken with WFC3 include a number of non-destructive reads chosen by the observer for up-the-ramp fitting.

Overheads are ~ 40 seconds per exposure, but for observations such as planetary transit or secondary eclipses, which require many exposures per orbit, the most significant overhead is the WFC3 buffer dump. For very few long exposures, buffer dumps occur parallel to the exposure. This is not the case for a series of short exposures, where a lot of information needs to be stored, which leads to non-simultaneous buffer dumps. To reduce the number of buffer dumps, the observer can read out sub-arrays rather than the full frame, with a 128 × 128 subarray sufficient to hold the length of a first order spectrum. Alternatively, the number of non-destructive reads per exposure can be reduced, which is reasonable if count levels remain low enough that non-linearity is not a problem. Finally, WFC3 now also offers a new mode, called “spatial scan”, where the spectrum is smeared across the detector in the non-dispersion direction during an exposure. Spatial scanning allows for lower count levels per pixel and longer exposure times, meaning an improved duty cycle. I have observations scheduled using this mode, which has proven useful for bright targets, such as HD 209458b (Deming et al. 2013).

⁵Available at <http://www.stsci.edu/hst/wfc3/documents/handbooks/currentIHB/toc.html> [accessed 01-Sep-2013].

2.2.2 The Grand Telescopio Canarias (GTC)

The GTC is the world's largest optical telescope with a 10 m primary mirror, providing valuable high-precision measurements for exoplanet observations (Figure 2.4). The primary mirror is segmented to prevent flexure. Currently, two instruments are available at the GTC, positioned at the two Nasmyth foci of the telescope; OSIRIS and CanariCam. CanariCam can perform imaging and long-slit spectroscopy with spectral resolving power $R = 175 - 1300$. OSIRIS provides imaging in broad, medium and narrow bands, tuneable filter imaging, long-slit and multi-object spectroscopy. Spectral resolving power is $300 - 2500$. Several more instruments are under development and consideration, some of which may be installed in the Cassegrain focus.



Figure 2.4: Image of the GTC at La Palma taken by the Universidad Complutense de Madrid group of Extragalactic Astrophysics and Astronomical Instrumentation, as part of the Survey for High-z Absorption Red and Dead Sources (SHARDS) European Southern Observatory/GTC Large Program. Available at <http://guaix.fis.ucm.es/node/1480> [accessed 01-Sep-2013].

Optical System for Imaging and Low-Resolution Integrated Spectroscopy (OSIRIS)

For this project, I made use of the OSIRIS long-slit mode. Multi-object spectroscopy was not available at the time of the observations. The slits are 7.4 arcmin in length and up to 10 arcseconds in width. Note that a 5 arcsecond slit width was used for this project, since that was all that was available at the time. The gratings used to obtain the data in this project are given in Table 2.2.

Grism	Wavelength Range (Å)	Resolving Power (R)
R500B	3750-8586	540
R500R	5000-9300	590

Table 2.2: GTC OSIRIS grisms used to obtain data for this project, along with their wavelength ranges and resolving powers.

The OSIRIS detector is composed of two 2048×4096 pixel CCDs, with a variety of read-out speeds. The spectroscopic standard mode uses a gain of 1.15 but can also be operated with higher gain. The CCD response is within 1 % of being linear up to 90 % of the A-to-D saturation limit (65,536 DN). The readout time for a spectroscopic exposure is 42 seconds with 2×2 binning (standard). The unvignetted field of view is 7.8×7.8 arcmin. There is no ADC, but this is being considered. Further information about GTC OSIRIS can be found on the GTC website⁶.

2.2.3 Cerro Tololo Inter-American Observatory (CTIO)

The CTIO is a complex of telescopes and instruments located approximately 80 km east of La Serena, Chile, and is part of the National Optical Astronomy Observatory (NOAO) and the Kitt Peak National Observatory (KPNO). Information about the telescopes at the site can be found at <http://www.ctio.noao.edu/noao/>, and some of the larger telescopes are shown in Figure 2.5.



Figure 2.5: Photograph of the SMARTS (Small and Moderate Aperture Research Telescope System) 1.5 m, 1.3 m, 1.1 m and 0.9 m telescopes at the CTIO, available at <http://www.ctio.noao.edu/noao/content/smarts-consortium> [accessed 01-Sep-2013].

⁶<http://www.gtc.iac.es/instruments/osiris/osiris.php> [accessed 01-Sep-2013].

The 1.3 m Telescope and ANDICAM

The data used in this project made use of the 1.3 m telescope, which is equipped with ANDICAM (A Novel Double-Imaging CAMera). The 1.3 m telescope was previously the 2MASS southern telescope. It is a Cassegrain that has been modified to include a beam splitter, allowing IR light and optical light to reach different detectors. ANDICAM is therefore capable of simultaneously recording images in the optical and near-IR. Figure 2.6 shows a schematic of the light path inside the instrument.

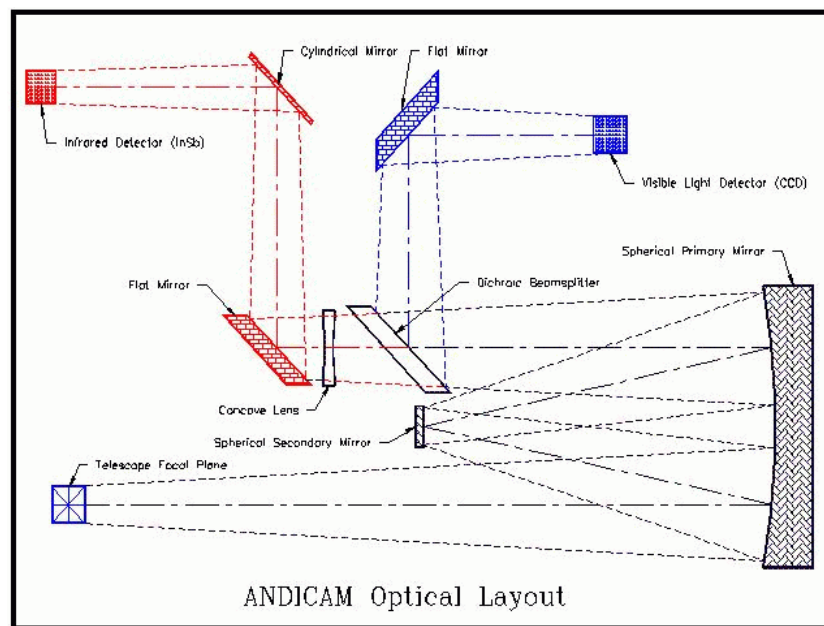


Figure 2.6: Schematic of the light path for the ANDICAM instrument, available at <http://www.astronomy.ohio-state.edu/~depo/research/instrumentation/andicam/andicam.html> [accessed 01-Sep-2013].

However, only the optical instrument, along with the CCD detector, was used for this project. The programme used the V filter, which has a central wavelength of 5386.76 \AA and a FWHM⁷ of 948.66 \AA . Overheads are around 47 seconds per image using 2×2 binning and acquisition takes 3 minutes. The CCD detector is 2048×2048 pixels, with a scale of 0.3 arcsec per pixel. The CCD response is less than 1% non-linear up to count levels of 45,000 DN, with A/D saturation occurring at 65,536 DN.

⁷Full Width at Half Maximum

2.2.4 Summary

Although the observing programmes and principal investigators (P.I.s) for data used in this project are given in the relevant chapters, along with more detailed observational information than given here, Table 2.3 provides a summary of the programme IDs and principal investigators associated with the data used in this project.

Telescope	Instrument	Setting	Target	ID	P.I.
HST	STIS	G750M	HD 189733b	11572	D. K. Sing
HST	STIS	G750M	HD 209458b	8789	T. M. Brown
GTC	OSIRIS	R500R	XO-2b	182.C-2018	D. K. Sing
GTC	OSIRIS	R500B	XO-2b	182.C-2018	D. K. Sing
HST	STIS	G430L	WASP-19b	12473	D. K. Sing
HST	STIS	G750L	WASP-19b	12473	D. K. Sing
HST	WFC3	G141	WASP-19b	12181	D. Deming
CTIO 1.3 m	ANDICAM	V filter	WASP-19	2011A-0209	D. K. Sing
CTIO 1.3 m	ANDICAM	V filter	WASP-19	2012A-0432	P. A. Wilson

Table 2.3: Summary of observations used in this project listing the instrumental settings, target, run IDs and P.I. for each observation. The observations are listed in order of when they were analysed by me, rather than the order in which they were taken, to be consistent with the order of chapters in this work.

2.3 Analysis Techniques

2.3.1 Least Squares Fitting

The Chi Squared Statistic

For a Gaussian distribution of mean μ and variance σ^2 , the probability of observing a value z is

$$P = \frac{1}{\sqrt{2\pi\sigma^2}} \exp\left[-\frac{(z - \mu)^2}{2\sigma^2}\right]. \quad (2.6)$$

This principle can be used in model selection where it can be assumed that the data have a Gaussian distribution around the true model value. The probability that a data point, y_i with uncertainty σ_{y_i} is drawn from a given model m_i is given by

$$P = \frac{1}{\sqrt{2\pi\sigma_{y_i}^2}} \exp\left[-\frac{(y_i - m_i)^2}{2\sigma_{y_i}^2}\right]. \quad (2.7)$$

The model with the highest probability is that which minimises the exponent. For N data points, this means that observers seek to minimise the expression:

$$\chi^2 = \sum_{i=1}^N \frac{(y_i - m_i)^2}{\sigma_{y_i}^2} \quad (2.8)$$

This expression is referred to as the χ^2 statistic, and is a measurement of how well the model describes the data. Here, σ_{y_i} is the uncertainty on each data point y_i , and characterises the deviation from the model that is expected due to known noise sources. For example, in my work, usually this value is assumed to be dominated by photon noise in the initial analysis, before other sources of noise are quantified. The best fitting model is the one that gives the lowest χ^2 . Models have free parameters, such as baseline stellar flux or planetary radius contrast, and a fitting routine is employed to find the parameters which give the lowest χ^2 for each model considered.

To quantify the goodness of fit, the deviations from the model must be compared to the expected values assuming that the model is correct and deviations are due to expected random scatter (e.g. photon noise). The ratio of the variance of the fit compared to the variance of the parent distribution can be approximated by χ^2/ν , where $\nu = N - M$ and M is the number of free model parameters (Bevington & Robinson 2003)⁸. If the fitting function accurately predicts the values of the parent distribution, then this number, called the reduced χ^2 or χ_ν^2 , should be close to 1. The quantity ν is

⁸Note that in some cases, $\nu = N - M - 1$ is used, where the data are normalised around the mean value before the χ^2 statistic is computed. Since the mean value itself is a free parameter, it must also be included in ν (Press et al. 2007).

known as the number of degrees of freedom (DOF). A larger number of free parameters allows the model to vary in more different ways to fit the data, and thus a larger number of free parameters should decrease the value of χ^2 if the model is correct. Whether a more complex model is justified over a simpler one depends on how much χ^2 decreases and how many extra parameters are required, and methods for deciding between models in this way are discussed in Section 2.3.4.

The likelihood that the model describes the data is then given by the probability that the χ^2_v obtained from randomly sampling N observations from a normal distribution would exceed the value of χ^2_v obtained by the deviations from the model fit. Such probabilities have been tabulated by many researchers (e.g. Bevington & Robinson 2003) and are used by observers to assess the goodness of fit of a model. A probability value close to 0.5 means that the deviations between the data and the model match what is expected statistically, and the χ^2_v values are close to 1. If the probability is poor (and χ^2_v large) then random deviations explain the data better than the model. If the probability is close to 1 (and $\chi^2_v \ll 1$) then this would suggest that the uncertainties on the data points in the fit are overestimated, since these govern the random deviations expected.

The χ^2 statistic is used in exoplanet science to determine the best model for transit data, usually including systematic trends. It must be noted that the χ^2 statistic assumes that the distribution is Gaussian around the model, which is not necessarily true for small numbers of datapoints. In many of my cases, the χ^2 statistic should only be used to compare models, and not to obtain any further information, e.g. how close the model is to representing the data plus photon noise scatter only. With this caveat in mind, I still use the χ^2 statistic in the majority of this work because it performs the task of choosing between models and finding the best one.

Model Fitting Techniques

It can be shown that the value of χ^2 varies as the square of distance from the minimum. An increase of 1 standard deviation (σ) in a parameter from its value at the minimum χ^2 would increase χ^2 by 1. Uncertainties on fitted parameters can therefore be computed from the variation in χ^2 as a function of changing that parameter value in the case where parameters are independent (not covariant).

There are various techniques used for minimising χ^2 for a given model with free parameters. The simplest is a grid search, where values for the fitted parameters are run through manually. This can be very time-consuming, especially when starting values are not even approximately known. Alternatively, a gradient search (steepest descent) calculates the direction in which χ^2 decreases most rapidly and incrementally adjusts parameters in that direction at each step (Bevington & Robinson 2003).

Although faster than the grid search, the gradient search may have trouble converging on the actual minimum where the gradient becomes small. Another method is the expansion method, which finds an analytical solution to describe the χ^2 hypersurface approximately around a local area rather than mapping the χ^2 hypersurface with parameters to determine the direction of minimisation. The analytical function is then minimised with respect to increments in the parameters. The expansion method can be very useful close to a minimum, but harder to compute further away where the hypersurface is more complicated. Bevington & Robinson (2003) give the full method for this implementation.

Levenberg-Marquardt (L-M) Method

In this work, I make use of the Levenberg-Marquardt (L-M) method, which combines both the expansion method and the gradient search method, using the gradient search when far away from a solution and the expansion method when close by, to enable it to converge more easily. Using the expansion method only close to the minimum means that only the linear terms in the analytical solution need to be considered:

$$\chi^2 \approx \chi_o^2 + \sum_{j=1}^m \left(\frac{\partial \chi_o^2}{\partial a_j} \delta a_j \right). \quad (2.9)$$

The method then minimises χ^2 with respect to the increments, δa_j of the m fitted parameters, and solves for the optimum values of the increments:

$$\frac{\partial \chi^2}{\partial a_k} \approx \frac{\partial \chi_o^2}{\partial a_k} + \sum_{j=1}^m \left(\frac{\partial^2 \chi_o^2}{\partial a_j \partial a_k} \delta a_j \right) = 0. \quad (2.10)$$

The results can be written as

$$\beta_k - \sum_{j=1}^m (\delta a_j \alpha_{jk}) = 0 \quad k = 1, m \quad (2.11)$$

where

$$\beta_k \equiv -\frac{1}{2} \frac{\partial \chi_o^2}{\partial a_k} \quad \text{and} \quad \alpha_{jk} \equiv \frac{1}{2} \frac{\partial^2 \chi_o^2}{\partial a_j \partial a_k} \quad (2.12)$$

$$\text{or } \beta = \delta \mathbf{a} \alpha, \quad (2.13)$$

where β and $\delta \mathbf{a}$ are row matrices and α is a symmetric matrix of order m . The factors of $\pm 1/2$ are included so that these definitions correspond to conventional definitions (Bevington & Robinson 2003). The matrix α is the curvature (Hessian) matrix and measures the curvature of the χ^2 hypersurface (Bevington & Robinson

2003). Marquardt (1963) defined a new matrix α' by increasing the diagonal terms in the curvature matrix α by a factor $1 + \lambda$:

$$\beta = \delta a \alpha' \quad \text{with} \quad \alpha'_{jk} = \begin{cases} \alpha_{jk}(1 + \lambda) & \text{for } j = k \\ \alpha_{jk} & \text{for } j \neq k \end{cases} \quad (2.14)$$

If λ is very large, then the matrix α' is forced into being diagonally dominant, giving m separate equations (one for each parameter), which can be used to determine the direction of decreasing χ^2 (gradient method). If λ is small, then the equation is similar to that derived from the Taylor expansion Equation (2.13). The solution for parameter increments, δa_j comes from matrix inversion of Equation (2.14):

$$\delta a_j = \sum_{k=1}^m (\beta_j \epsilon'_{jk}), \quad (2.15)$$

where ϵ' is the inverse of the matrix α' , with elements given by Equation (2.14). The initial value of λ should be small enough to use the analytical solution, but large enough that χ^2 decreases (Bevington & Robinson 2003). The procedure for a fitting routine is:

1. Compute the initial χ^2 from starting parameters ($\chi^2(a)$).
2. Begin with a small λ (usually 0.001).
3. Using this λ value, compute the step size, δa and the new chi squared $\chi^2(a + \delta a)$.
4. If $\chi^2(a + \delta a) > \chi^2(a)$, then increase λ by a factor of 10 and repeat the previous step.
5. If $\chi^2(a + \delta a) < \chi^2(a)$ then decrease λ by a factor of 10 and consider $a' = a + \delta a$ to be the new starting point. Go back to step 3 using $a = a'$.

For each iteration, steps 3 and 4 may need to be performed several times to optimise λ . In practice, the process can be stopped on the first or second occasion that χ^2 decreases by a negligible amount. This is especially useful in the case of a flat valley near the minimum, where the minimum is not well defined.

Once the minimum has been found, λ is set to zero and the error matrix (covariance matrix of standard errors) is computed, $\epsilon = \alpha^{-1}$. The errors in parameters are obtained from the square roots of the diagonal terms. For this reason, it is important that all fitted parameters are fitted simultaneously so that the covariance matrix can be properly computed. Final parameter errors will be underestimated if, for example, a fit is performed using the L-M technique which removes systematic trends from a light curve, and then the cleaned light curve is fitted using the L-M technique to find

transit parameters. The fitting algorithm will have no knowledge of the degree of covariance between the magnitude of the parameters describing the systematic trends and the magnitude of the parameters describing the transit. Furthermore, uncertainties on fitted parameters can be underestimated if the uncertainties on the data points are underestimated, because the covariances between parameters are not measured properly. Methods for testing uncertainties and obtaining accurate uncertainties are discussed later, in Section 2.3.4.

In my work here, I make use of the `MPFIT` package developed by Markwardt (2009). Aside from the original algorithm, this `IDL` package offers several improvements, including the ability to constrain parameter values, manually set the parameter step sizes, and return the full covariance matrix.

2.3.2 Markov Chain Monte Carlo (MCMC)

In this work, I use the L-M method to analyse data, but in the later chapters, I also make use of the MCMC `EXOFAST` written by Eastman et al. (2013) to check for consistency with the results of the L-M method. Therefore, I will briefly explain the key principles of the MCMC method here.

The MCMC method is designed to thoroughly explore the χ^2 space but in a more efficient manner than the grid search method. A Monte Carlo calculation means that randomness is included in some way. For example, Monte Carlo simulations can be used to check experimental results by using the fitted model to generate simulated datasets (e.g. the bootstrap technique, described in Section 2.3.4). They can also be used in theoretical calculations. A Markov Chain is a memoryless random chain, in which the next state does not depend on previous states. The procedure for an MCMC is described by the following steps (the Metropolis-Hastings algorithm, see e.g. Young & Smith 2010):

1. The MCMC chain starts off at one point in parameter space where the likelihood, \mathcal{L} , is calculated.
2. Step randomly in parameter space
3. Compute the new likelihood at this new position in parameter space
4. Draw a random number between 0 and 1
5. If the random number drawn is less than the ratio of the new likelihood to the old likelihood then accept the step and add the new parameters to the chain. If the random number drawn is greater than the ratio of the new likelihood to the old likelihood, then reject the step and add the old parameters to the chain.

Once these steps have been performed once, repeat steps 2-5 many times. For a large number of parameters, the optimal acceptance rate is $\sim 23\%$ (Roberts et al. 1997). While running an MCMC takes more time than the L-M method, the advantage is that the MCMC method produces posterior probability distributions for the model parameters rather than just a single set of best fitting parameters. Bayes' formula is used to calculate the posterior probability (likelihood) at each step:

$$P(B | A) = \frac{P(A | B)P(B)}{P(A)}, \quad (2.16)$$

where A is typically the data and B is the model. $P(B)$ is the prior information that may be known (flat priors are used in the case of no knowledge). $P(A)$ is a normalisation constant, which does not need to be computed unless different models are compared. The posterior probability is usually calculated assuming that the model is correct and that the deviations from the model follow a Gaussian distribution:

$$p(y_i | m_i) = \frac{1}{\sqrt{2\pi\sigma_{y_i}^2}} \exp\left(-\frac{(y_i - m_i)^2}{2\sigma_{y_i}^2}\right) \quad (2.17)$$

and

$$\mathcal{L} = \prod_{i=1}^N p(y_i | m_i) \quad (2.18)$$

More details of `EXOFAST` and how it works are discussed in Eastman et al. (2013), including choices on where to start the chain, step size, how many steps to perform and the priors. Also see Gelman et al. (2003); ter Braak (2006); Ford (2006); Hogg et al. (2010) for more information, including conditions for stopping the MCMC process without specifying a particular number of steps and how to obtain final parameter uncertainties from the posterior distributions.

2.3.3 Nelder-Mead Simplex Algorithm

The Nelder-Mead simplex algorithm is introduced by Nelder & Mead (1965) as a method for the minimisation of a function with free parameters. It is otherwise known as the downhill simplex method, or sometimes known as `AMOEBA`. It has the advantage that it does not require derivatives, but only requires function evaluation, and so can be better at finding the best fit than χ^2 fitting techniques. However, it can be computationally expensive for a model fit with many parameters. `EXOFAST` makes use of `AMOEBA` to find an initial starting position.

A simplex is a geometric figure in N dimensions, which consists of $N + 1$ points and their interconnecting line segments and polygonal faces (Press et al. 2007). In two dimensions, a simplex is a triangle, and in three dimensions it is a tetrahedron

(the shape does not have to be regular). Essentially, if $f(x, y)$ is the function to be minimised, the process starts with 3 vertices of a triangle, $\mathbf{V}_k = (x_k, y_k)$, $k = 1, 2, 3$. The function $f(x, y)$ is evaluated at each of the three points, and a new simplex drawn based on the differences between the three evaluations. The process is then repeated many times. The detailed process of using the Nelder-Mead simplex algorithm to minimise a function is outlined in Press et al. (2007) and Mathews & Fink (2004).

2.3.4 Quantifying Uncertainties and the Goodness of Fit

Akaike Information Criterion (AIC) and Bayesian Information Criterion (BIC)

When fitting different models to data (for example modelling systematic trends), it is not always known what the dominant causes are of observed trends (e.g. airmass, seeing, position of the source on the detector etc.). The systematic trends could also be non-linear functions of the physical variables with an unknown order of dependence. To distinguish between different physically-motivated models using χ^2 fitting techniques such as the L-M method, more than just the χ^2 statistic for each model must be used. For example, fitting a linear function of airmass as a de-trending model makes sense, but what is to stop an observer fitting a higher order model? A very high order polynomial function of many variables could over-fit the data by giving the model so much freedom that it can fit white noise. Such a model would give a lower χ^2 value, but could be removing real information from the data, and may give results that are incorrect. Both the AIC and BIC aim to weight the likelihood of different models by how many free parameters they have, and it is thus useful to use the AIC and BIC as well as simply looking at the reduced χ^2 of different model fits to the data.

The AIC was introduced by Akaike (1974b,a), and is given by

$$\text{AIC} = 2k - 2 \ln L, \quad (2.19)$$

where k is the number of free parameters in the model and L is the maximum likelihood for that model. The BIC was introduced by Schwarz (1978) and is defined as

$$\text{BIC} = \chi^2 + k \ln n, \quad (2.20)$$

where k is the number of free parameters in the model, and n is the number of data points. The change in BIC or AIC for two models is an approximation of the Bayes factor, where the Bayes factor is the ratio of likelihoods of two different models:

$$B = \frac{p(x | M_1)}{p(x | M_2)}, \quad (2.21)$$

where x is the data and M_1 and M_2 are two different models (for more details see Young & Smith 2010). The Bayes factor can be approximated by the AIC or BIC as

$$B \approx \exp\left(-\frac{1}{2}\Delta\text{AIC}\right) \quad \text{or} \quad B \approx \exp\left(-\frac{1}{2}\Delta\text{BIC}\right), \quad (2.22)$$

allowing models to be rejected with confidence intervals. The advantage is that the AIC and BIC do not depend on the priors on the parameters of the two models, which the true Bayes factor does. Although the AIC and BIC are only strictly valid for large numbers of data points (as is the χ^2 statistic), the real limits of experiments are such that an ideal experiment cannot be performed, and the AIC, BIC and χ^2 statistic are some of the most useful tools available for comparing models. Note however, that the AIC and BIC should be applied to physically motivated models and the results checked, especially for parameters correlated with the parameter of interest (e.g. planetary radius contrast). It is possible that an unphysical combination of parameters could produce the best statistics.

Correlation Coefficients

A useful statistic is a test of whether different datasets, or different parts of datasets, are correlated. For example, subtracting white light residuals⁹ from the light curves of spectral bins can remove trends which are common to all wavelengths without removing information about the relative transit depths as a function of wavelength (although the absolute transit depths are lost). Correlation coefficients are also calculated in MCMC routines to search for degeneracies between fitted parameters. The correlation coefficient (also called Pearson's correlation coefficient) for two parameters x and y is defined as the covariance between parameters over the scatter in the distribution for each parameter:

$$\rho = \frac{\text{COV}(x, y)}{\sigma_x \sigma_y}. \quad (2.23)$$

The correlation coefficient can be estimated directly from the data:

$$\rho = \frac{\sum_i (x_i - \bar{x})(y_i - \bar{y})}{\sqrt{\sum_i (x_i - \bar{x})^2 \sum_i (y_i - \bar{y})^2}}. \quad (2.24)$$

The value of the correlation coefficient varies from 1 in the case of perfect correlation to -1 in the case of perfect anti-correlation. A value of zero means that the datasets are completely uncorrelated. In practice, random noise in the datasets means that a value of zero is unlikely, and I found values of $\pm 0.3 - 0.4$ when comparing simulated

⁹Throughout this work, I use the term "residuals" to mean the data after subtracting the best-fitting model.

datasets made from an array of a single number with random photon noise added in each case.

Underestimated Uncertainties and Correlated Noise

When the best physically motivated model is fitted to a dataset and remaining deviations from the model are higher than predicted, it is most likely that there are sources of noise that are not included in the model. Such un-modelled noise sources mean that the uncertainties on the data points are inaccurate and hence the uncertainties on the fitted parameters will be underestimated. To account for unknown noise sources, the best model is chosen via some fitting routine and the resulting ratio between the deviations from that model and the predicted uncertainties are used either to re-scale the final uncertainties on the derived parameters, or to re-scale the uncertainties on the fitted data points and fit the model again. The larger error bars allow the covariances of the fitted parameters to be higher and thus the resulting error bars on the fitted parameters of interest are higher, and more realistic than using the original data point uncertainties. In most cases, re-scaling the initial parameter uncertainties is equivalent to re-scaling the photometric error bars and performing the fit again. However, if some parameters are strongly covariant with one another, re-scaling the parameter uncertainties rather than the photometric uncertainties can lead to a difference in the best fitting parameters (see Chapter 6).

For uncorrelated (white) noise above the predicted level, parameter uncertainties may be underestimated, but the derived parameter values themselves are not largely affected. In order to obtain realistic uncertainties, the re-scaling described above can be performed using the ratio of the standard deviation of the data from the best-fit model compared to the predicted deviation. This process makes two assumptions; firstly, that the model used is correct, and secondly that the uncertainties on each data point are the same (Bevington & Robinson 2003). The latter assumption may not be valid for ground-based data where one part of an observing night or season may contribute significantly worse data quality than others. The approximation, however, is usually reasonable for space based data.

In the case of correlated (“red”) noise, the effects on the results are more significant because they can drastically affect measured parameter values, and need to be treated more carefully. Unlike white noise, the effects of red noise do not reduce with binning many exposures over time. Since the aim in transit and occultation observations is to measure atmospheric properties based on the variation of the flux from the system over time, such variations of an instrumental origin can skew the results significantly. Re-scaling photometric uncertainties with the standard deviation in this case would underestimate the uncertainty on the measured properties, such as planetary

radius, because it does not take into account the structure of the noise. For example, all the points before the transit may be high compared to the model, and all the points within the transit could be low. Such a noise structure would artificially increase the measured transit depth, but would have the same standard deviation as a case where high and low points are randomly distributed amongst the before-transit and during-transit data points. Thus observers require methods to characterise the presence and degree of red noise in observations, rather than simply re-scaling the error bars with standard deviation or reduced χ^2 . Once the level of red noise is determined, the error bars can then be re-scaled by the appropriate amount, similar to above.

Jackknife and Bootstrapping

The jackknife method was invented by Quenouille (1949) to estimate properties of a sample by repeatedly removing one or more observations from the sample at random to create many simulated datasets. This method preserves the time-correlated nature of the data and so measures red noise to an extent. However, I found that the prayer bead and binning techniques (below) produced larger and more realistic error bars when compared to how much fitted transit radii changed depending on model parameter choice.

Bootstrapping was first introduced by Efron (1979) and can be performed by firstly subtracting a model and then creating simulated datasets where each new data point y_i is equal to the corresponding model value, m_i , plus one of the data residuals taken at random, r_j . Although a good method in the case of white noise, the bootstrap method has the effect of not preserving the time-dependent structure of the noise, and so underestimating the uncertainties.

Prayer-Bead Method

The prayer-bead method (Moutou et al. 2004; Gillon et al. 2007; Désert et al. 2009) is a residual permutation method which is meant to characterise red noise. The principle is similar to the bootstrap technique, but with significant differences that make it much more reliable for characterising red noise. In the prayer-bead method, the initial fit to the data is performed and the residuals calculated. Then, more fits are performed, equal to the number of exposures. In each iteration, i , the fitted data is replaced with $y_i = m_i + r_{i+n}$, where y_i is the new i^{th} exposure to be fitted, m_i is the model value from the first fit for the i^{th} exposure, and r_{i+n} is the residual for the $i+n^{\text{th}}$ exposure. For each fit n is increased by 1, until the residuals have completely cycled around. The advantage of the prayer-bead technique is that the order of residuals remains the same, and so the structure of the correlated noise is not altered. Nonetheless, depending on the timescale of correlated noise, there could be points during the prayer-bead analysis

where certain simulated datasets look the same as one another, thus also underestimating the uncertainties. The advantage of the prayer-bead method is that it can be used in the case of datasets with only few exposures in the light curve and does not require the timescale of red noise to be long.

Binning Technique

The binning technique was first introduced by Pont et al. (2006) and is expanded on by Winn et al. (2008). The binning method is based on the idea that, if a light curve is binned into time bins of N points, uncorrelated noise should reduce by a factor of \sqrt{N} . The levels of red noise are therefore measured using $\sigma_N^2 = \sigma_w^2/N \left(\frac{M}{M-1}\right) + \sigma_r^2$, where σ_N^2 is the variance of binned fluxes in M time bins of N points, σ_w is the white noise component (uncorrelated), and σ_r characterises the red noise. The value of N to use is typically the timescale that is important for transit observations, for example the timescale of the transit. However, since it is possible to have trends that occur over an entire transit, I perform the beta method for all possible different binning increments, and look for the case where σ_r is the highest. To measure the level of red noise, since σ_w is not known beforehand, the standard deviation in the binned light curve, σ_N , is compared to the standard deviation expected if the deviation of the raw light curve from the model is due to white noise alone, i.e. $\sigma_1^2/N \left(\frac{M}{M-1}\right)$, where σ_1 is the standard deviation of the unbinned residuals. So, $\sigma_r^2 = \sigma_N^2 - \sigma_1^2/N \left(\frac{M}{M-1}\right)$ is used.

In order to incorporate red noise into the resulting uncertainties on physical parameters, such as transit depth, the β factor is suggested by Winn et al. (2007), where $\beta = \sigma_N/(\sigma_w/\sqrt{N})$. Here, σ_w is used rather than σ_1 because it is possible that correlated noise can be seen in the unbinned residuals, and β could be underestimated. In practice, the difference is negligible. The white noise component of the unbinned residuals is worked out from the red noise, by $\sigma_w^2 = \sigma_1^2 - \sigma_r^2$.

Wavelet Method

The wavelet method was introduced by Carter & Winn (2009) as a method for estimating parameters from datasets that contain correlated noise. It is assumed that there are two Gaussian noise processes; uncorrelated noise and correlated noise which has a power varying as $1/f^\gamma$. The wavelet method is therefore most suited to modelling long-duration correlations, and as such I was not able to make use of it in this work. Briefly, the wavelet method transforms the residuals into wavelet space (analogous to a Fourier transform except localised in time rather than frequency). It then calculates the wavelength coefficients and scaling coefficients.

Gaussian Processes

Although not used in this project, GP regression can be used to interpret exoplanet data (Gibson et al. 2012b). The joint probability of a set of N observations is treated as a multivariate Gaussian described by an array of N mean values and an $N \times N$ covariance matrix. Such a process can be used to include noise terms as well as terms describing the parameters of interest, such as transit parameters. The GP uses a kernel (functional form of the covariance) and covariance parameters (“hyperparameters”), discussed in Pont et al. (2013). Since the GP is specified by a covariance matrix, it predicts the difference in flux at two times, rather than an absolute flux value. The advantage of the GP technique is that it can model noise sources simultaneously with the transit fit and it does not require a specific parameterised de-trending model to interpret data.

Re-Scaling Uncertainties

Many of the methods of measuring red noise discussed in this section use the residuals for the calculation. This means that a fit has already been performed, and that it is assumed that the de-trending model used is correct (i.e. that it may not completely describe all the systematic trends, but that it does not add any trends, and does describe real trends). If the initial model is assumed to be correct, then re-scaling can be used to take into account any red noise not included in the model, in the same way as re-scaling for white noise. For STIS and WFC3 data, I can be reasonably confident that the model describes the systematics well, since the dominant systematic trends of these instruments are well known and understood (Sing et al. 2008a, 2011b; Huitson et al. 2012; Deming et al. 2013).

Note that re-scaling with β only takes into account long-term systematic trends. It is possible that the scatter may be higher than the photometric error bars after re-scaling because of systematic noise on very short timescales and white noise. In such a case, β_w can be used, which is defined as the ratio of σ_w to the formal photon noise uncertainty (Lendl et al. 2013). In this case, parameters or photometric uncertainties are re-scaled with $\beta \times \beta_w$. In cases where β is measured to be ≤ 1 , observers can re-scale only with β_w , which is the same as re-scaling with the standard deviation of the residuals.

Chapter 3

Transmission Spectroscopy of Sodium in HD 189733b with HST STIS

3.1 Aims and Introduction

This chapter is based around the goal of improving understanding of the most favourable targets. Here, I will detail observations of the sodium Na I doublet observed in the transmission spectrum of HD 189733b with the medium resolution HST STIS grating G750M.

Observations previous to my work suggested that the transmission spectrum of HD 189733b is dominated by a Rayleigh scattering signature. However, absorption from Na I was detected in the atmosphere from the ground, with a relative absorption depth of $(67.2 \pm 20.7) \times 10^{-5}$ (Redfield et al. 2008) compared to the continuum. This detection was later revised to $(52.6 \pm 16.9) \times 10^{-5}$ by Jensen et al. (2012).

Aside from confirming the ground-based detection, the further aim is to use the increased resolution and high signal-to-noise of my spectra compared to the ground-based detection to resolve the spectral absorption depth profile of the doublet, which shows the characteristic shape of the sodium absorption feature. From this, it is possible to retrieve properties of the atmosphere, such as abundances and the presence or absence of high-altitude clouds and hazes. The results are published in Huitson et al. (2012).

3.2 Observations and Data Reduction

3.2.1 Observations

The transits were observed using the HST STIS G750M grating (HST Proposal GO 11572. Cycle 17, PI: David Sing). In total, 7 primary transits of HD189733b were observed. Three of these transits obtained data of high quality. Of the others, two suffered from a positioning error of the spectrum when using sub-arrays on the CCD, as also noted in Brown (2001). Two further visits obtained no data as those visits suffered from guide star problems. Table 3.1 gives details of the 7 visits.

Visit	Calendar Date	JD	Notes
1	31 st October 2009	2455135.31	Positioning error. Spectrum blueward of 6000 Å used in part of the analysis
2	6 th November 2009	2455141.42	No data acquired
3	13 th November 2009	2455148.62	Whole spectrum useable
51	18 th December 2009	2455184.11	No data acquired
52	15 th August 2010	2455423.72	Positioning error. Spectra were unuseable.
54	1 st October 2010	2455470.31	Whole spectrum useable
55	30 th November 2010	2455530.22	Whole spectrum useable

Table 3.1: Table of HST STIS visits, showing observation dates and data quality.

Each dataset consists of a series of 144 spectra, each covering a wavelength range of 5808-6380 Å. There are 30 spectra in the initial HST orbit (before the transit), another 38 spectra before the transit, 38 during and 38 after the transit. Each individual spectrum is taken at a slightly different time of the planet's orbit so that the flux and the spectrum can be measured before, during and after transit. This essentially gives the light curve of the planetary transit at each spectral wavelength measured. The G750M grism has a resolving power of $R = 5000$, which gives a resolution of ~ 1.2 Å or ~ 2 pixels at 5890 Å. The observations were made with a slit of width $52'' \times 2''$ to minimise light loss. The data were then bias-subtracted, dark-subtracted and flat-fielded using the `CALSTIS` pipeline¹. The pipeline also provides a wavelength solution. I then used a custom routine to remove cosmic ray contamination, by comparing each pixel in each image with the same pixel in all other images and removing significant (5σ) outliers by replacing them with the mean value for that pixel. Approximately 0.25 % of pixels were affected by cosmic ray events compared to the total number of pixels on the subarray, consistent with the number expected from the STIS manual. A potentially more robust method could be to exclude bad pixels from further analysis

¹Details available at:
http://www.stsci.edu/hst/stis/documents/handbooks/currentIHB/c15_pipeline2.html.

rather than interpolating over them. Although this was not tried here, I did test the difference between removing and interpolating over bad (saturated) pixels in Chapter 6 and did not find a significant difference between the two methods.

3.2.2 Extracting Spectra

When the data are received from the telescope, one exposure appears as a 2-dimensional image outputted from the CCD in which the spectrum is the bright horizontal line, as seen in Figure 3.1. The two dark lines towards the left-hand side of the spectrum are the sodium Na I doublet absorption lines.



Figure 3.1: Image showing a CCD output of one of the exposures using the HST STIS G750M grating that was used to analyse sodium in HD189733b. The Na I lines are to the left of the image.

These data were then extracted as an array of flux versus wavelength for each exposure using IRAF². IRAF defines an aperture around the bright line corresponding to the spectrum and then extracts the flux values within this aperture for each pixel in the dispersion direction. Since each pixel corresponds to a different wavelength, a spectrum can be constructed. During the extraction process, the spectral trace needs to be measured and accounted for, which is the position of the spectrum on the CCD. It can be seen that the line slopes downward towards the right in Figure 3.1. IRAF measures this slope and moves the aperture it is using during the extraction process to compensate. The aperture used for the extractions here was 13 pixels wide, and was determined by measuring the red and white noise in the extracted light curves of a variety of different aperture sizes. The spectra were then shifted to a common wavelength scale by cross-correlating with the mean of the shifted spectra, and were then corrected to a rest frame by comparison with a model spectrum.

²Image Reduction and Analysis Facility.

3.3 HST STIS Light Curve Fitting

A light curve of photon flux against time was created by summing the photon flux over the full spectrum in each exposure (each individual spectrum). Plotting this flux against time gives the ‘white’ light curve. Since the HST orbits the Earth, it can only spend some time out of each orbit observing the target. Therefore the transit light curve over time contains gaps in the observations due to Earth occultation.

The light curves exhibit instrumental effects, which are described by Brown (2001). The dominant systematic trends are over an orbital timescale and are due to PSF³ variations caused by the thermal expansion and contraction of the HST optical assembly as the HST is heated and cooled during its orbit⁴. The orbital PSF variations are referred to as the “breathing” trends. The breathing effects are worse during the first orbit of any visit, as the HST thermally settles into its new pointing position. Many programmes therefore do not use the first orbit for primary analysis (e.g. Brown 2001; Charbonneau et al. 2002; Sing et al. 2008a). Figure 3.2 shows the raw white light curves which exhibit the dominant systematics.

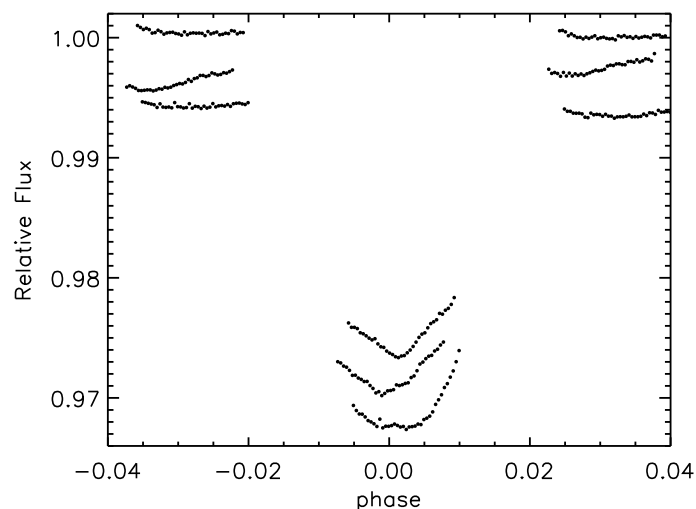


Figure 3.2: Raw white light curves for (top to bottom) visit 3, visit 54 and visit 55, excluding the first orbit of each visit. Arbitrary flux offsets have been applied for clarity.

There are two orbits before the transit, one during transit and one after transit. The systematics were corrected for by discarding the first orbit, and then discarding the first exposure of the retained orbits. The first exposure in each STIS orbit is usually unreliable (Sing et al. 2011b). After this, the remaining systematics were removed by fitting a fourth-order polynomial dependence of the fluxes on HST orbital phase to the light curve, whilst simultaneously fitting for the transit radius using the analytical transit

³Point Spread Function

⁴See instrument science report ACS 2008-03 for more details, available at www.stsci.edu/hst/acs/documents/isrs/isr0803.pdf [accessed 01-Sep-2013]

models of Mandel & Agol (2002). The Levenberg-Marquardt least-squares technique was used for the fit, using the `MPFIT` package (Markwardt 2009), using the unbinned data. The sections of the in-transit light curve obviously crossing stellar spots were not included in the fits. The effect of stellar spots on the transmission spectrum is further discussed in Section 3.4.3. Figure 3.3 shows the resulting light curves and residuals once systematics have been removed. Fitting the light curve with models from Mandel & Agol (2002) gives the radius of the planet from the depth of the transit, using Equation (1.2) and knowing the stellar radius.

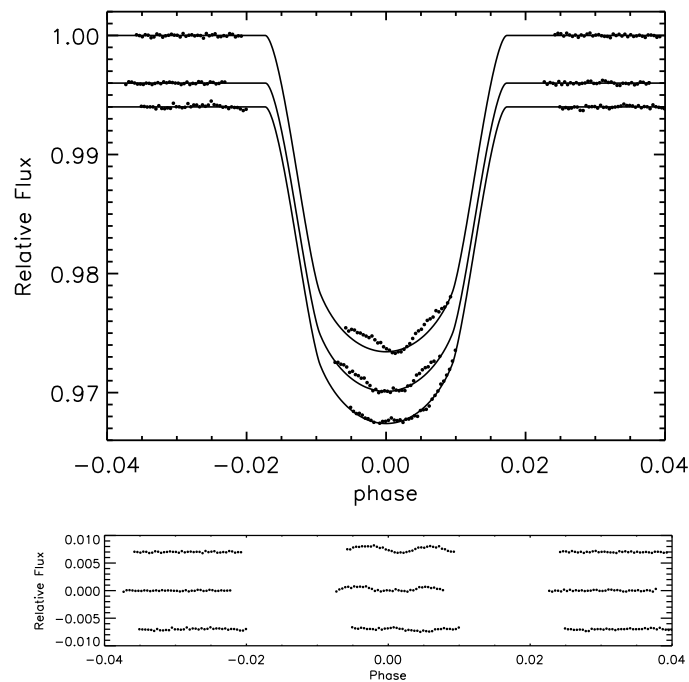


Figure 3.3: White light curves for (top to bottom) visit 3, visit 54 and visit 55 with the systematic effects removed. Arbitrary flux offsets have been applied for clarity. For each visit, the best fitting analytical transit model of Mandel & Agol (2002) is over-plotted. Plotted underneath are the residuals for (top to bottom) visit 3, visit 54 and visit 55. Arbitrary flux offsets have been applied for clarity. The regions where the planet crosses stellar spots can be clearly seen.

Visits 54 and 3 still exhibit structure in the transit due to occulted starspots, where the flux is higher than the transit model predicts. The effect of starspots on the results is discussed in Section 3.4.3. I observed that the transit depth for visit 54 was shallower than the other two visits. This could be due to an occulted starspot in the centre of the transit in addition to those at the edges, so that the planet would cover part or all of at least one starspot during the whole transit.

3.3.1 Limb Darkening

Correcting for the effects of stellar limb darkening on the transit light curves and the spectral absorption depth profiles is important at visible wavelengths, so this was also included in the light curve fits. Two limb darkening corrections based on two stellar models were compared: the Kurucz (1993) 1D ATLAS model⁵ and a fully 3D time-dependent hydrodynamic stellar atmospheric model (Sing et al. 2011b; Hayek et al. 2012). The models were compared using visit 55, where there are no visible occulted spots at the limbs of the transit. The other two complete visits do not have enough data at the limbs of the transit light curve to constrain the fits.

In the 1D case, I followed the method of Sing et al. (2009) and Sing (2010), and used a 3-parameter law:

$$\frac{I(\mu)}{I(\mu = 1)} = 1 - c_2(1 - \mu) - c_3(1 - \mu^{3/2}) - c_4(1 - \mu^2), \quad (3.1)$$

The stellar parameters used were $T_{\text{eff}} = 5000$ K, $\log(g) = 4.5$, and $[\text{Fe}/\text{H}] = 0.0$, along with the response function of the G750M grating and STIS detector. The resulting coefficients for white light from the models were $c_2 = 0.8918$, $c_3 = 0.0515$ and $c_4 = -0.1930$. This fit gave a reduced χ^2 of 2.65 and BIC of 282. I did not fit the transit light curves for the limb darkening coefficients.

In the 3D case, the stellar limb darkening was fitted with a 4 parameter law, as it appears to perform well at small μ :

$$\frac{I(\mu)}{I(\mu = 1)} = 1 - c_1(1 - \mu^{1/2}) - c_2(1 - \mu) - c_3(1 - \mu^{3/2}) - c_4(1 - \mu^2). \quad (3.2)$$

The parameters for the white light curve were $c_1 = 0.7043$, $c_2 = -0.4493$, $c_3 = 1.0538$, and $c_4 = -0.4569$. I found that the fits and the magnitudes of red noise improved significantly over the 1D case. The reduced χ^2 when using the 3D models was 1.94, with a BIC of 211. Despite this, however, the measured planet to star radius ratio changed by less than 1σ , in contrast to results at bluer wavelengths from Sing et al. (2011b). These authors give an in-depth discussion of the comparison between 1D and 3D models for broadband G430L transit observations (2900-5700 Å) and find that the fits to their data are significantly better using the 3D model than the 1D model. They find that the 1D model does not perform as well at shorter wavelengths where limb darkening is stronger.

I also simultaneously investigated whether fitting for any x and y offset of the spectra and the slope on the detector (such as due to target motion within the aperture) with linear functions was justified by improvement in the fit, as done by Sing et al.

⁵See <http://kurucz.harvard.edu/stars/hd189733> [accessed 01-Sep-2013].

(2011b). These corrections improved the reduced χ^2 and significantly improved the BIC. Table 3.2 shows the results of different fits for the 3D limb darkening case. Both the χ^2 values quoted above for the different limb darkening prescriptions are in the case where the additional parameters have been fitted.

Fit Position Parameters?	Visit 3		Visit 54		Visit 55	
	no	yes	no	yes	no	yes
DOF	69	66	79	76	86	83
NFree	8	11	8	11	8	11
χ^2_v	1.948	1.751	5.705	1.958	2.522	1.936
BIC	176	167	447	183	268	211
R_p/R_*	0.15734	0.15720	0.15505	0.15499	0.15638	0.15628
σ_{R_p/R_*}	0.00016	0.00014	0.00036	0.00012	0.00023	0.00017

Table 3.2: Fitting statistics depending on whether the x and y offsets of the spectra were included in the fit. “NFree” is the number of free parameters. It can be seen that there are significant improvements for all the visits when these parameters are fitted. Note that the three visits give different absolute radii from one another. This is most likely due to differences in un-occulted spot level. However, this chapter makes use only of radius variations as a function of wavelength rather than absolute measurements, and so the actual R_p/R_* values do not affect the conclusions. It is also interesting to note that the absolute R_p/R_* level obtained from visit 55, which contains no occulted spots, matches well with the level determined independently from ACS data by Pont et al. (2013).

Fitting the systematic trends in this way produced S/N values for the white light curves between 10,000-11,000 (precision levels of 90-100 ppm), which are 78-86 per cent of the Poisson-limited value. These per exposure precision levels are an improvement on the results when not fitting for these additional position-dependent parameters (130-160 ppm).

I checked for red noise by using the binning technique described in Pont et al. (2006), by observing whether residuals binned in time followed a $N^{-1/2}$ relationship, where N is the number of points in the time bin. There was no significant evidence of red noise in visit 54 or visit 3. For visit 55, the magnitude was 3×10^{-5} for the white light curve, which corresponds to a S/N of $\sim 33,000$. It translates into an error in depth measurement in the planet’s atmosphere of ~ 50 km, which is less than 1/3 of a scale height in the lowest regions (smallest scale height) probed by these measurements. Since the final uncertainties are $\sim 100 - 300$ km in altitude, these low levels of systematic trends do not dominate the uncertainties. Smaller bandwidths are generally closer to Poisson-limited, and I found that the red noise in a 20 Å band centred on the sodium doublet was negligible ($< 1 \times 10^{-5}$).

3.4 Analysis

3.4.1 Spectral Absorption Depth Profile of the Na I Doublet

A resolved spectral profile can tell observers much more than simply that an element is present in an exoplanetary atmosphere. Very narrow lines could indicate high-altitude obscuring material. A smooth, Eiffel-tower shape would indicate fairly constant abundance, whereas sharp changes in the line could indicate sharp abundance changes in Na I, or changes in temperature (see Chapter 4).

Charbonneau et al. (2002) measured the absorption depth (AD) of sodium by comparing the flux in transit of a band centred around the sodium wavelengths to bands either side of it, defined as ‘blue’ and ‘red’ bands. Each spectral exposure was integrated over the defined band around the sodium lines and then normalised to the out of transit flux in the same band. The in-transit portion of the resulting light curve was then compared to the in-transit portions of the light curves for the blue and red bands (also normalised), to observe the excess absorption from the Na I doublet. The difference in absorption in the centre (sodium) band compared to the blue and red bands is given by Charbonneau et al. (2002) as

$$n_{\text{Na}} = n_c(t) - [n_b(t) + n_r(t)]/2, \quad (3.3)$$

where $n_c(t)$, $n_b(t)$ and $n_r(t)$ are the normalised light curves in the centre (sodium), blue and red bands respectively. The sodium AD is found by comparing the excess absorption in the centre band during transit with that out of transit, where the only absorption features should be from the star:

$$\Delta n_{\text{Na}} = \overline{n_{\text{Na}}(t_{\text{in}})} - \overline{n_{\text{Na}}(t_{\text{out}})}. \quad (3.4)$$

The difference in the out-of-transit region, $\overline{n_{\text{Na}}(t_{\text{out}})}$, should be close to zero, since the light curve at each wavelength has been normalised to its out-of-transit flux. Charbonneau et al. (2002) defined three different width central bands: ‘wide’, ‘medium’ and ‘narrow’, and corresponding blue and red bands which are just outside the limits of the centre band. The ‘narrow’ centre band is 12 Å wide.

In this current work, the spectral AD during transit in a band centred within the Na I doublet was compared to bands on either side of the doublet following this method. For the bands outside the sodium wavelengths, I used the ‘wide’ bands defined by Charbonneau et al. (2002), which is a combination of a blue (5818-5843 Å) and a red (5943-5968 Å) band. The difference between this work and previous work is that I measured the spectral absorption depth profile by using a ‘centre’ band of fixed size, and measured the differential AD in the sodium feature by moving this ‘centre’

band across the feature in wavelength. The ‘centre’ bands were 1.2 Å wide, which is the instrument resolution.

The three complete visits were used for this analysis, as was visit 1, since only wavelengths up to 5968 Å were required. Visit 1 was only used for this differential method, and so was not discussed in Section 3.3. I tested the effect of using different reference bands by using the ‘medium’ reference band as defined by Charbonneau et al. (2002), as well as a reference band closer to the doublet. The choice of reference band shifts the profile in altitude by less than $\frac{1}{2}\sigma$ and does not change the shape of the AD profile as a function of wavelength.

This differential method has the advantage that systematic errors largely cancel out, as they are largely wavelength independent over the small wavelength range studied, giving a robust way to measure Na I absorption. It also averages the blue and red background components, giving an average that largely compensates for the effects of limb darkening in the sodium bands. This method is also particularly useful here due to the presence of occulted starspots at the limbs of two of the visits, as the flux variations due to transiting in front of occulted spots are similar in the Na band and the ‘wide’ bands, and thus cancel out when comparing the bands.

However, this method does not account for differential limb darkening in the sodium line core wavelengths. The limb darkening is weaker at the line core compared to the continuum, because the core of the stellar Na I line is produced above the photosphere, further away from the centre of the star than where the continuum is produced. At these altitudes, the temperature gradient becomes smaller (see Hayek et al., 2012). The differential limb darkening leads to a slight underestimation of the absorption depth in the line core, since the limb darkening effects are not fully cancelled out by the differential method. This effect was corrected by comparing limb darkening models for each of the evaluated sodium wavelengths with that of the ‘wide’ band. The transit models were given a fixed planetary radius, to evaluate the difference in model limb darkening alone, and then the differences were added to the sodium absorption depths (see Figure 3.4 for an example of the difference in limb darkening between the line core and the wings). The greatest effect was in the innermost line cores, with a magnitude of $\sim 2 \times 10^{-4}$ or $\frac{1}{2}\sigma$. The effects were found to be negligible for wavelengths greater than 3 Å away from the line cores.

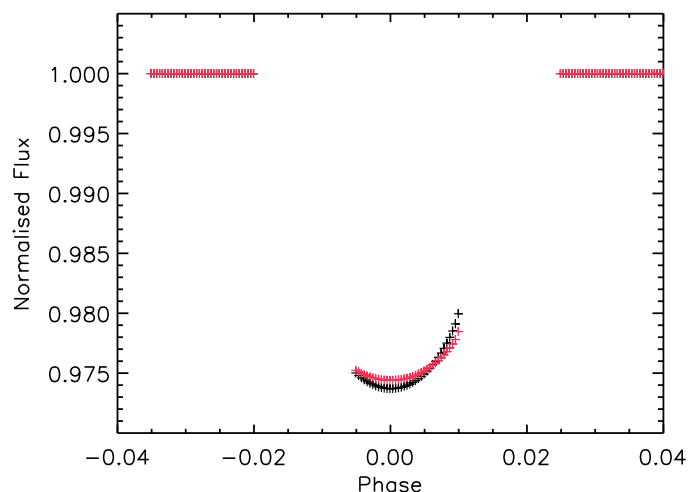


Figure 3.4: An example of the differential limb darkening in the sodium line core for visit 55. The red line shows the transit model with limb darkening for the core of the line and the black line shows the transit model with limb darkening for the reference band (blue+red band).

Figure 3.5 shows the spectral absorption depth profile around the Na I feature and Table 3.3 lists the differential absorption depths for each wavelength bin. In Section 3.4.3, I find that the effects of starspots on this profile are minimal and within the observational uncertainties. Error bars were computed from the standard deviations of the ‘centre’ and ‘reference’ light curves and scaled with red noise when red noise was detected. The spectrum is composed of the spectra from the individual visits weighted by their uncertainties. Comparing Figure 3.5 to the equivalent spectrum for HD 209458b from Sing et al. (2008a) shows that the measured differential Na I absorption for HD 189733b is deeper in the line cores. There is one data point in the centre of the two doublet lines which appears to have an unexpectedly low absorption. This is due to one pixel in the centre of the doublet showing low absorption. It is not associated with any excess red noise, and so I could not scale the uncertainty any higher. This anomaly was also observed in the HD 209458b spectrum from Sing et al. (2008b) using the same instrument, but there are no obvious defects on the CCD that could account for this effect. The differences in velocity frame for the two stars is sub-pixel for these data, and so the same wavelength should fall on the same pixel for both datasets.

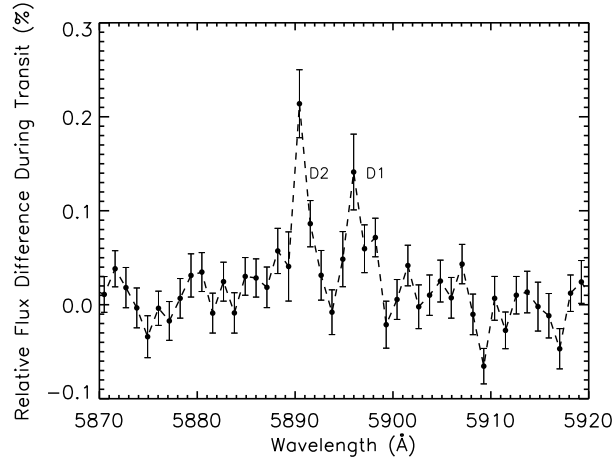


Figure 3.5: Spectral AD profile at each wavelength in the sodium region with 1σ error bars, binned to the STIS resolution of 2 pixels. The Na I D1 and D2 doublet lines are resolved, as shown by the largest two peaks. The absorption depths for the doublet are greater than the equivalent profile for HD 209458b (Sing et al. 2008a).

λ (Å)	AD ($\times 10^{-5}$)	Error ($\times 10^{-5}$)	λ (Å)	AD ($\times 10^{-5}$)	Error ($\times 10^{-5}$)
5870.50	10.95	19.04	5871.61	38.27	19.24
5872.71	18.20	21.41	5873.82	-3.38	21.21
5874.93	-34.05	22.34	5876.04	-3.78	18.22
5877.15	-17.25	20.63	5878.25	6.80	21.09
5879.36	31.16	23.01	5880.47	34.76	20.70
5881.58	-8.91	21.23	5882.69	24.54	20.73
5883.79	-8.71	21.49	5884.90	30.13	20.06
5886.01	28.46	20.34	5887.12	18.51	21.61
5888.23	57.24	24.06	5889.33	40.69	36.82
5890.44	213.89	36.17	5891.55	86.23	24.62
5892.66	31.31	26.42	5893.77	-7.95	23.81
5894.87	48.48	29.33	5895.98	141.22	40.31
5897.09	59.56	25.44	5898.20	71.53	20.53
5899.31	-21.23	25.01	5900.41	5.60	21.23
5901.52	41.71	21.60	5902.63	-2.19	23.29
5903.74	10.17	21.49	5904.85	25.18	22.27
5905.95	7.36	21.65	5907.06	43.25	20.97
5908.17	-10.27	21.61	5909.28	-65.38	18.88
5910.39	6.79	23.31	5911.49	-27.29	19.54
5912.60	10.12	19.95	5913.71	13.50	22.14
5914.82	-2.03	26.01	5915.93	-11.71	23.66
5917.03	-46.86	21.42	5918.14	12.27	19.40
5919.25	24.25	22.80			

Table 3.3: Weighted average of spectral absorption depth (AD) in each wavelength (λ) around the Na I doublet compared to absorption in adjacent bands. The data are binned to the STIS instrument resolution of 2 pixels.

3.4.2 Integrated Absorption Depth Profile of the Na I Doublet

In order to allow direct comparison with the previously published Na I profiles of HD 209458b and WASP-17b (Sing et al. 2008a; Wood et al. 2011), I also computed the differential integrated AD profile as a function of bandwidth. Using the method described by Charbonneau et al. (2002), the absorption depth during transit in a band centred on the Na I doublet was compared to the same blue and red reference bands as used for the spectral absorption depth profile. To make the integrated AD profile, I used two ‘centre’ bands, one centred on each sodium doublet line (5896 and 5890 Å). These bands were then increased in size from 3 to 80 Å, with a single ‘centre’ band being used where the centre bands were large enough to encompass both lines together (bandwidth ≥ 12 Å). This gives a profile of absorption depth vs bandwidth (total width of the ‘centre’ band or bands), and is hereafter referred to as the integrated absorption depth (IAD) profile.

Figure 3.6 shows the resulting IAD profile averaged for the 4 visits (weighted by the uncertainties of each visit) and Table 3.4 lists the absorption depths for each band. The mean IAD profile gives a depth of $(51.1 \pm 5.9) \times 10^{-5}$ for a bandwidth of 12 Å, which was the bandwidth used by Redfield et al. (2008) and Jensen et al. (2011) for their ground-based measurements. This result is within 1σ of these previous results, confirming the absorption depth found with an increased S/N of almost a factor of 3.

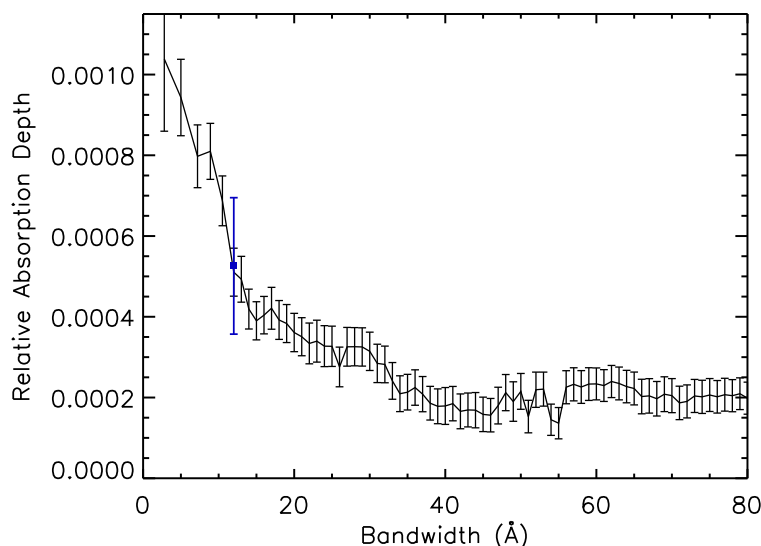


Figure 3.6: The IAD profile defined by the depth in a band centred on the Na I doublet compared to absorption in adjacent bands, weighted with uncertainty in absorption depth for 4 visits averaged. The increasing band sizes show the IAD profile, which flattens out at bandwidths larger than 45 Å, showing that the line wings broader than this are obscured. The point from Jensen et al. (2012) is shown in blue with a filled square. My more precise results agree with their measurement at the 1σ level.

Band width Å	Absorption depth ($\times 10^{-5}$)	Error ($\times 10^{-5}$)	Band width Å	Absorption depth ($\times 10^{-5}$)	Error ($\times 10^{-5}$)
2.8	103.9	17.9	5.0	94.3	9.5
7.2	79.8	7.8	8.9	81.0	6.9
10.5	68.7	6.2	12.0	51.1	5.9
13.0	49.3	5.7	14.0	41.9	4.9
15.0	39.0	4.7	16.0	40.4	4.6
17.0	42.1	5.2	18.0	39.2	4.8
19.0	38.3	4.7	20.0	36.1	4.7
21.0	35.1	4.7	22.0	33.4	5.1
23.0	34.0	5.2	24.0	32.7	5.1
25.0	32.7	5.0	26.0	27.6	4.9
27.0	32.6	4.8	28.0	32.6	4.7
29.0	32.5	4.7	30.0	31.4	4.7
31.0	28.5	4.8	32.0	28.2	4.5
33.0	24.1	4.5	34.0	20.9	4.4
35.0	21.3	4.4	36.0	22.5	4.4
37.0	20.8	4.4	38.0	18.6	4.2
39.0	17.8	4.3	40.0	17.9	4.6
41.0	18.5	4.3	42.0	16.6	4.3
43.0	16.9	4.2	44.0	16.9	4.4
45.0	15.8	4.3	46.0	15.6	4.1
47.0	18.0	4.5	48.0	21.2	4.5
49.0	19.0	4.9	50.0	21.5	4.4
51.0	15.3	4.0	52.0	21.9	4.4
53.0	22.1	4.2	54.0	14.5	3.9
55.0	13.6	3.9	56.0	22.5	4.1
57.0	23.3	4.1	58.0	22.6	4.1
59.0	23.3	4.1	60.0	23.4	3.9
61.0	23.0	3.9	62.0	24.0	4.0
63.0	23.5	4.1	64.0	22.7	4.0
65.0	22.2	4.1	66.0	20.2	4.3
67.0	20.4	4.3	68.0	19.7	4.3
69.0	20.8	4.3	70.0	20.5	4.2
71.0	18.7	4.1	72.0	19.0	4.1
73.0	20.4	4.1	74.0	20.2	4.1
75.0	20.6	4.1	76.0	20.2	4.0
77.0	20.7	4.1	78.0	20.5	4.0
79.0	20.9	3.9	80.0	19.8	4.0

Table 3.4: Weighted average of integrated absorption depth in each band centred on the Na I doublet compared to absorption in adjacent bands. “Bandwidth” refers to the total width of the ‘centre’ band or bands.

One disadvantage of the IAD method is that the line appears wider than in reality due to a dilution effect of increasing the bandwidth, weakening the sodium absorption signature confined to smaller bandwidths. Furthermore, another disadvantage is that noise at small bandwidths can have an effect on measurements at wider bandwidths. For example, noise at 50 Å can be seen to affect the IADs measured at wider bandwidths in Figure 3.6, producing an unphysical measurement. Since the method of calculating the absorption depth requires integrating over all the points within the bandwidth centred on the sodium doublet, each point has a dependence on the last, and so these errors propagate to wider bands. The IAD profile is not used for primary analysis and is only used for comparison with other work, and to test the effects of stellar spots on the transmission spectrum in Section 3.4.3.

3.4.3 The Effect of Occulted Starspots

The local flux increases seen as bumps in the light curves in Figure 3.3 are most likely due to occulted starspots. HD 189733 is a very active star, showing large periodic flux variations over time at the few per cent level in the optical, and starspots are clearly seen in other transit light curves as well (Sing et al. 2011b; Pont et al. 2008; Henry & Winn 2008). As discussed in Chapter 1, occulted spots decrease the inferred planetary radius. What needs to be assessed for my goals is whether there is a significant wavelength dependence to the effect of occulted starspots over the spectral regime studied. I also need to determine the likely effect of un-occulted spots, which will artificially increase measured transit radii.

The differential method of measuring the spectral AD profile should mostly cancel out the effects of both occulted and un-occulted stellar spots, since the studied wavelength range is small. However, it is not a priori known how much the level of stellar spots affects the stellar sodium signature, and hence the effect on the inferred planetary AD as a function of wavelength. This effect could be greater in the line cores than in the broad regions of the lines and could be significant if the sodium signature is strongly dependent on the spot temperature.

The sodium data here are used to determine empirically the effect of occulted spots on the differential Na I spectral AD profile, and then to infer the likely effect of un-occulted spots. This analysis is performed on the IAD profile because the effects will be more severe in this profile than in the spectral AD profile, since they will be most pronounced in the line cores. Figure 3.7 shows the mean IADs versus bandwidth for the 4 visits compared with the mean IADs evaluated using only the exposures that appear to occult stellar spots, and also only those that do not.

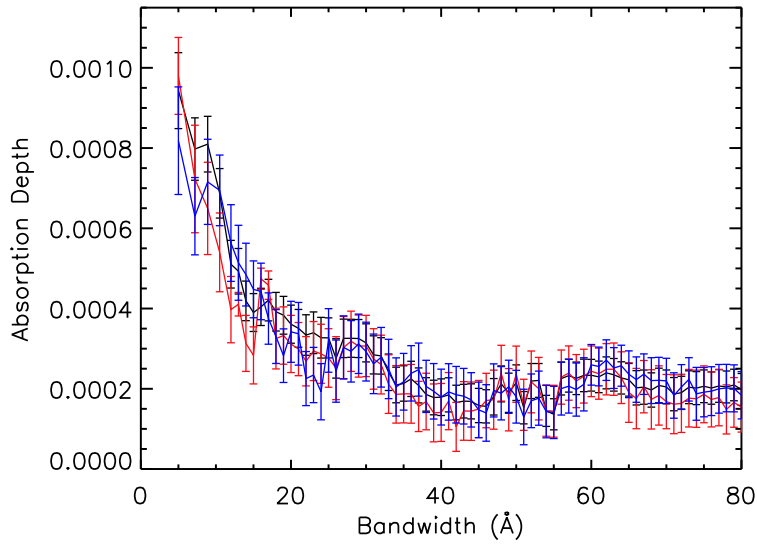


Figure 3.7: Weighted average of IAD in a band centred on the Na I doublet compared to absorption in adjacent bands. *Black*: using all exposures, *blue*: using only exposures clearly not contaminated by occulted starspots, *red*: using only exposures that appear to contain occulted starspots. This shows that the starspots do not have a significant effect on the Na I AD profile measurement at my level of precision.

As expected, the absorption depth decreases when using only the spotted exposures and increases when using only the non-spotted exposures. The mean absorption depth in a 12 \AA band is $(39.7 \pm 8.2) \times 10^{-5}$ when using only the spotted regions and $(56.3 \pm 9.6) \times 10^{-5}$ when using only the non-spotted regions. The effect at even smaller bandwidths, where the difference is expected to be more noticeable, is around $5 - 15 \times 10^{-5}$. However, these effects are within the error bars. There does not appear to be a significant effect on the differential Na I absorption due to spectral features in the spots at the level of precision of the observations, although an effect can be seen. For my purposes, I can therefore assume that the spots have a similar spectrum to the non-spotted surface. In this case, un-occulted starspots are expected to have a less significant effect than occulted starspots, so I can assume that these effects are also smaller than the uncertainties in absorption depth. It has, however, been noticed that at both longer and shorter wavelengths, the effects become more significant (Sing et al. 2011b), especially when considering the spectrum over wider spectral domains.

3.4.4 Broadband 5808-6380 Å Spectrum

The G750M data can also be used to look for other spectral features and to determine the shape of the overall spectrum from 5808 to 6380 Å. Spectra were created by binning the spectral time series into 5 wavelength bins of ~ 110 Å for visits 3, 54 and 55. Each band was fitted individually in the manner described for the white light curve. The fitted planet to star radius ratios were then used to construct a binned transmission spectrum. The inclination, a/R_\star and central transit time were fixed to the values given in Hayek et al. (2012) and Agol et al. (2010), which were $i = 85.71$ deg, $a/R_\star = 8.8564$, $T_0 = 2454279.436714$. Using the same orbital parameters for each bin ensures that differences in the best fitting R_p/R_\star values between bins are due only to radius variations as a function of wavelength.

Determining accurate radii required the occulted stellar spots in the light curves to be taken into account. The fluxes of each exposure contaminated by occulted spots in visits 3 and 54 were measured with the white light curve, producing the shape of the features. These were then used to model the spots in each of the wavelength bands, by fitting the features in each band with the shape measured from the white light curve and an amplitude parameter. This assumes that the shape of the spots is roughly the same in all the different bands and that the spectra of the spots are constant. Figure 3.8 shows the spotted exposures overplotted with the best fitting spot amplitudes for each wavelength band. Figure 3.9 shows the data residuals once the spots, systematic trends and transit have been removed. Comparison with Figure 3.3 shows that the spots have been effectively removed.

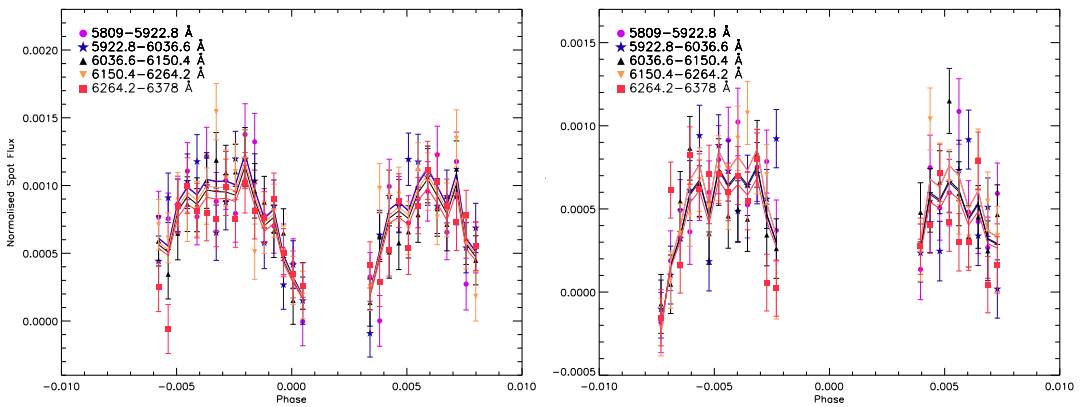


Figure 3.8: Spotted exposures overplotted with the best fitting spot models for visits 3 (left) and 54 (right). A non-spotted transit model has been subtracted from both so that the magnitude of the spots can be seen more easily.

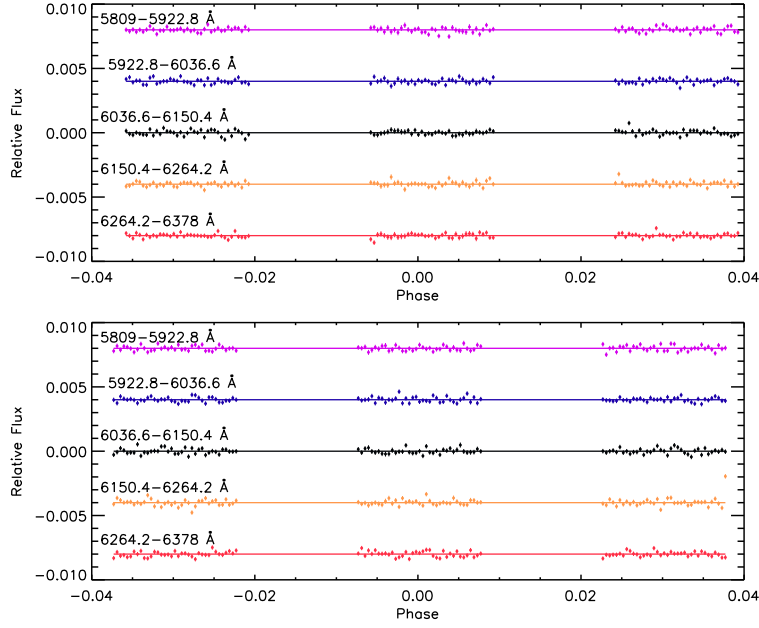


Figure 3.9: Residuals of the data minus spotted models for visit 3 (top) and visit 54 (bottom) for the G750M band divided into 5 ~ 110 Å bins. Arbitrary flux offsets have been applied for clarity. The colours and bands are the same as in Figure 3.8. The flatness of the residuals show that the occulted starspots have been effectively removed.

Occulted spot features are more severe at blue wavelengths than at red depending on their temperature contrast with the non-spotted surface (e.g. Pont et al. 2007). Figure 3.10 shows the best-fit spot amplitude parameters along with a predicted slope for spots of temperature 4000 K. Sing et al. (2011b) found that this temperature best matched their data over a broad wavelength range. The spot amplitude was defined to be 1 for white light. My measured slope is in agreement with this model, but cannot be used to constrain the spot temperature further than the constraints provided by previous work. It can be seen that the amplitude increases slightly towards blue wavelengths as expected, although this is only a 1σ effect over my wavelength range.

The planetary radius and spot amplitude parameter were initially fitted together and then fitted one at a time iteratively until the solutions converged, allowing the radii in each wavelength band to be fitted while taking into account the shape of the spots in the light curve. The transmission spectrum was then corrected for un-occulted spots by reducing the measured radii by 1% (see Sing et al. 2011b), and averaged for the 3 visits. Red noise values were negligible for visits 54 and 55 in all bands. For visit 3, $\beta = 1.3$ for the central wavelength band and 1.2 for two of the other bands, and was negligible elsewhere. These values were incorporated into the measurement uncertainties for that visit, giving the value less weight when I took the mean of all visits.

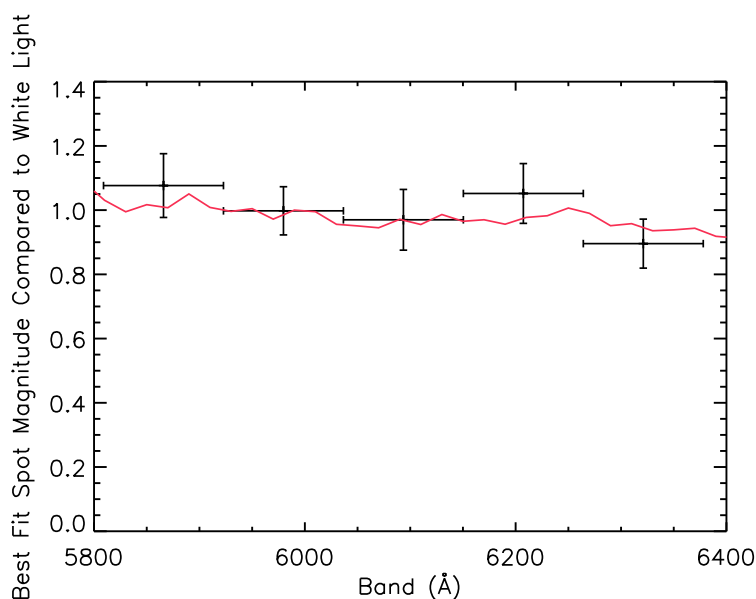


Figure 3.10: Average best fitting spot amplitudes from the models for visit 54 and visit 3, plotted against wavelength. It can be seen that there is a wavelength-dependent slope, but this is within the errors of the measured parameters. Overplotted in red is a model spectral signature of occulted spot amplitude, assuming that the spots have a temperature of 4000 K. The measured slope is in agreement with this model, but cannot be used to constrain the temperature any further.

Figure 3.11 shows the resulting spectrum and Table 3.5 shows the fitted values of R_p/R_* . Figure 3.11 also shows a Rayleigh slope for an atmospheric temperature of 1340 ± 150 K determined from previous observations (Lecavelier Des Etangs et al. 2008a). The data are consistent with Rayleigh type scattering, but I cannot further constrain the uncertainty on the measured temperature with my data, although the observations do reach precisions of approximately one atmospheric scale height for each of the binned spectral points. Additionally, a flat spectrum is seen with spectral bins narrower than those of either of the two previously observed broad-band spectra, which is consistent with the conclusion that the Na I line wings are absent. It also indicates that there are no other broad spectral features in the G750M wavelength range. In contrast to the flat spectrum measured here, the spectrum of HD 209458b showed significant excess absorption at 6200 Å (Sing et al. 2008a; Désert et al. 2008). The non-detection of significant excess absorption at 6200 Å in HD 189733b suggests that either this feature is real or any systematics responsible for the feature vary with time.

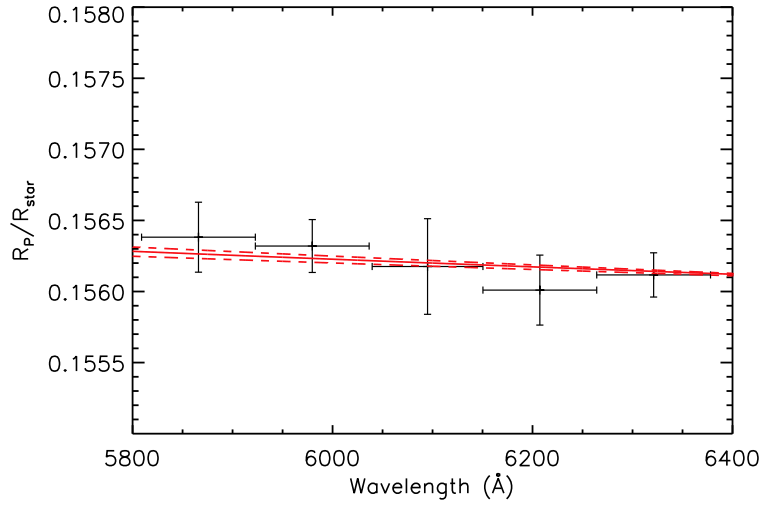


Figure 3.11: The STIS G750M broad spectrum overplotted with a Rayleigh scattering prediction from previous broad-band ACS data (Pont et al. 2008; Sing et al. 2011b) at the temperature of 1340 K determined by Lecavelier Des Etangs et al. (2008a) (solid line) with a range of ± 150 K (dashed lines). It can be seen that the G750M data is consistent with this slope.

Wavelength (Å)	R_p/R_\star	Error
5809-5922	0.15638	0.00025
5923-6037	0.15632	0.00019
6040-6150	0.15618	0.00034
6150-6264	0.15601	0.00025
6264-6378	0.15612	0.00016

Table 3.5: Fitted planet-to-star radius ratios for ~ 110 Å bands, used to construct the broad-band transmission spectrum over the G750M band.

In Figure 3.11, there is a slight dip around 6200 Å, which appears to coincide with a bump in Figure 3.10, both in the data and the predicted model spot spectrum. This suggests that, again, starspots are having an effect on the observations, but that the effect is within the observational errors. The spectrum here is used only to show that there are no other broad features in the spectrum, and as such, the small deviation potentially caused by occulted starspots is not corrected for as it will not change this conclusion.

3.5 Discussion

3.5.1 The Optical Transmission Spectrum of HD 189733b

An important goal of this study is to make the most complete picture of the atmosphere of HD 189733b that is currently possible. This means adding together all the transmission observations, including broad-band spectra and the sodium measurement here. Although the sodium spectral AD measurements are differential absorption depths compared to the continuum, they can also be written in terms of planetary radius, if the transit radius of the continuum is known. The planetary radius at each wavelength is given by

$$\frac{R_P}{R_\star} = \frac{R_{P(\text{white})}}{R_\star} + \Delta \frac{R_P}{R_\star}, \quad (3.5)$$

where $\Delta \frac{R_P}{R_\star}$ is the sodium AD relative to the continuum (“white”), expressed in units of R_P/R_\star . Converting AD to $\Delta(R_P/R_\star)$ can be done by considering the change in observed flux during the planet’s passage, which is given by

$$\frac{\Delta F}{F} = \text{AD} = \left(\frac{R_P}{R_\star} \right)^2, \quad (3.6)$$

where ΔF is the change in flux due to the planetary transit and F is the out-of-transit flux. For a small change in AD, this can be written:

$$\Delta(\text{AD}) = 2 \left(\frac{R_P}{R_\star} \right) \Delta \frac{R_P}{R_\star} \Rightarrow \Delta \frac{R_P}{R_\star} = \frac{\Delta(\text{AD})}{2 \left(\frac{R_P}{R_\star} \right)}. \quad (3.7)$$

Doing this enables the differential ADs to be compared with other datasets from other observations, which are usually quoted in terms of R_P/R_\star . A spectral AD profile can be found directly from fitting the transit at each wavelength around the sodium feature for R_P/R_\star and comparing it to the continuum fit, but the differential method is more reliable for that purpose. There are large differences between the measured R_P/R_\star values for each visit when fitting the white light curves, whereas the differential ADs are very similar between visits for the method used by Charbonneau et al. (2002). For that reason, the differential AD values are clearly more reliable. The reason for this is that un-occulted spots affect the absolute transit depth more significantly than they affect the relative transit depths, which are what is measured when calculating the differential AD values. The differential AD values can then be combined with a well known value of $R_{P(\text{white})}/R_\star$ from broad-band datasets, in order to convert the differential ADs to a spectrum. I used $R_{P(\text{white})}/R_\star = 0.15628$, which is the radius from my visit 55, and which agrees well with the literature values in Pont et al. (2008).

Figure 3.12 shows the results of comparing my data with that in the literature.

3.5.2 Interpretation of the Narrow Absorption Lines

The blue-rising continuum absorption observed in the atmosphere of HD 189733b by Pont et al. (2008) and Sing et al. (2011b) was attributed to a high-altitude haze in the atmosphere of the planet, which would obscure most of the Na I doublet. Figure 3.12 shows the previously observed broad-band spectrum (Pont et al. 2008; Sing et al. 2011b) compared to a model spectrum assuming a haze-free atmosphere (Fortney et al. 2010) and a solar Na I abundance. The observed spectrum lacks the broad alkali line wings and H₂O signatures. The broadband data are binned to $\sim 500 \text{ \AA}$, showing that the equivalent widths of those bins are not significantly higher than the featureless spectrum. Figure 3.12 also shows my measured spectrum for the G750M band, as well as points from the medium resolution spectrum at 2, 5, 12, and 18 \AA from the centre of the doublet, confirming a narrow Na I feature. The previous broad-band spectroscopy would not have had sufficient spectral resolution to resolve such a narrow feature unambiguously. The 3 observations from STIS G750M, STIS G430L (Sing et al. 2011b) and ACS HRC (Pont et al. 2008) all independently agree that there are no observable broad Na I line wings.

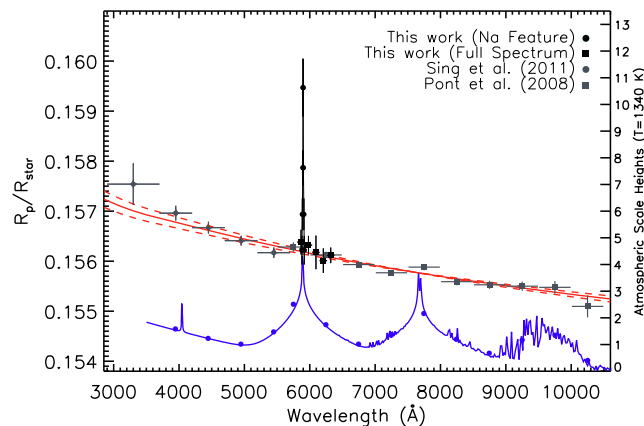


Figure 3.12: Spectrum over the G750M band (black squares) compared with previous work. Also shown are points from the G750M spectrum at 2, 5, 12 and 18 \AA from the centre of the doublet (black circles). The red lines show the Rayleigh scattering prediction from the ACS data (Lecavelier Des Etangs et al. 2008a). The blue line shows a model assuming a haze-free atmosphere from Fortney et al. (2010) at solar Na I abundance, normalised to the radius at IR wavelengths from Agol et al. (2010). Blue circles show model values binned to the G430L and ACS resolution.

The species responsible for the Rayleigh scattering signature observed in HD 189733b is unknown, but the signature should place constraints on the composition of the scattering species (Lecavelier Des Etangs et al. 2008a; Sing et al. 2011b).

Rayleigh scattering dominates only for particle sizes much smaller than the wavelength ($2\pi a \ll \lambda$) and where the scattering efficiency is dominant over the extinction efficiency. H_2 , which is abundant in the atmosphere, is much smaller than the observed wavelengths. A narrow Na I doublet profile can be explained by a low sodium abundance ($\sim 0.1 \times$ solar) which can hide the Na I line wings beneath the H_2 Rayleigh signature. Although there is no reason not to expect a low abundance of atomic sodium, such a conclusion would also suggest low abundances of other constituents such as atomic potassium or water, since these features are also not apparent in the transmission spectrum at predicted levels. I therefore believe that the scattering signature is due to a high-altitude haze.

A high-altitude scatterer could obscure spectral signatures from lower altitudes, allowing only the upper regions to be observed, where pressures are low and there is no observable pressure broadening of the Na I feature. Thus, the transmission spectrum will not show the sodium line wings, even for a solar or above-solar Na I abundance. If the Rayleigh scattering signature is due to a haze of condensate particles, then the condensate must be transparent enough for the absorption to be negligible relative to scattering, which rules out many condensates such as MgSiO_4 and oxygen-deficient silicates (Lecavelier Des Etangs et al. 2008a). One possible species is MgSiO_3 , which fits the observed spectrum from Sing et al. (2011b), Pont et al. (2008), and also the 1.66 and 1.87 μm points from Sing et al. (2009). Assuming a uniform haze layer with a single size component, the observed broad-band data from STIS and NICMOS constrain the particle size to be in the range 0.01-0.03 μm , by requiring that the molecule scatters at all observed wavelengths.

The narrow range of particle sizes needed to be consistent with the observations shows that it is potentially difficult to explain the broad-band Rayleigh signature over the 4000-18700 \AA range with scattering by a haze of condensates. Rayleigh scattering has a $a^6\lambda^{-4}$ dependence, meaning that the observed slope suggests only a small variation in particle size over the observed range of atmosphere (providing that the atmospheric temperature remains similar over most of the broad-band optical spectrum, which fits with observations). It is expected that a condensate would vary in grain size with depth, making the observations hard to explain. However, the mechanics of keeping dust grains aloft in such atmospheres are not well understood, and there could be more than one absorber. The properties and even species responsible for the scattering signature are therefore not well constrained.

The Relative Atomic Sodium Abundance

Since there is more than one species that could be responsible for the Rayleigh scattering signature, the abundance of the scattering species is unknown. Equation 1.9 demonstrates that, for a given differential planetary radius (corresponding to a differential AD), there is a degeneracy between the continuum pressure level observed and the abundance of the observed species (in this case Na I). However, it is still possible to place constraints on the relative abundances of species. Comparison with the near-IR measurements gives the relative abundance of atomic sodium compared to water, and has the advantage that the Rayleigh scattering reference pressure of the AD = 0 level does not need to be known.

Abundance measurements of identified spectral features can be determined from transmission spectra by re-arranging Equation (1.9). The relative abundance of two species is given by (also shown by Désert et al. 2009):

$$\frac{\xi_1}{\xi_2} = \frac{\sigma_2}{\sigma_1} e^{(z_1 - z_2)/H}, \quad (3.8)$$

where ξ_1 and ξ_2 are the abundances, σ_1 and σ_2 are the wavelength-dependent cross-sections at λ_1 and λ_2 , and z_1 and z_2 are the altitudes of the observed spectral features at λ_1 and λ_2 of species 1 and 2 respectively. The atmospheric scale height is represented with H . All other constants cancel out assuming that both spectral features occur in the same temperature regime. I compared my measured sodium absorption depth with the radius observed at 8 μm by Agol et al. (2010), assuming that this feature is due to absorption from atmospheric water. The results from secondary eclipse observations have detected a water absorption signal at this wavelength (Grillmair et al. 2008), meaning that water is likely to be the source of the 8 μm feature seen in transmission (as already envisaged by Désert et al. 2009).

I used Equation (3.8) along with $\sigma_{\text{H}_2\text{O}} = 2 \times 10^{-20} \text{ cm}^2$ at a wavelength of 8 μm (Désert et al. 2009) and a radius for the water feature at 8 μm of $R_p/R_\star = 0.15531$ (Agol et al. 2010). This was compared to the radius in the region 10-18 \AA away from the centre of the Na I doublet, which was $R_p/R_\star = 0.1572 \pm 0.0002$. This wavelength region was measured to have a similar temperature to the continuum (see Chapter 4) and has absorption cross-section $\sigma_{\text{Na}} = 3.5 \times 10^{-20} \text{ cm}^2$. Since this is not a differential measurement, I used only the fitted radius from visit 55, which has the smallest contamination from occulted stellar spots of all the visits, rather than an average of all 3 visits. The un-occulted spot correction used for the G750M band was 1 per cent, and the un-occulted spot correction used for the 8 μm band was 0.2 per cent (see Sing et al. 2011b).

The solar abundance ratio of sodium to water is $\xi_{\text{Na}}/\xi_{\text{H}_2\text{O}}[\text{solar}] = 6.63 - 9.95 \times 10^{-3}$ or $\ln(\xi_{\text{Na}}/\xi_{\text{H}_2\text{O}}[\text{solar}]) = -5.0$ to -4.6 (Lodders 2003; Lodders & Fegley 2002; Sharp & Burrows 2007). For HD 189733b, I calculated values of $\xi_{\text{Na}}/\xi_{\text{H}_2\text{O}}[189]$ which were ~ 100 times higher ($\ln(\xi_{\text{Na}}/\xi_{\text{H}_2\text{O}}[189]) = +1.3 \pm 0.75$), indicating a super-solar abundance ratio. This range includes the errors due to uncertainty in z , the uncertainty in the correction for un-occulted starspots at both visible and IR wavelengths, and also the uncertainty in the solar ratio of sodium to water.

Since EUV radiation ionises Na I, but depressed NUV can diminish ionisation, it is unclear which effects dominate, and whether there should be more ionisation of atomic sodium in HD 189733b compared to HD 209458b or less. It is also possible that these different wavelengths penetrate to different distances in the atmospheres. Understanding the atmospheric physics at these pressure levels requires much further work, but it is hoped that these initial observations can provide some constraints to theoretical work. Additionally, one abundance ratio between two features is insufficient to draw any conclusions about the actual abundances of the elements responsible, but this could be improved with additional comparisons with other features.

3.6 Summary and Conclusions

This work has detected sodium in the atmosphere of HD 189733b with 9σ confidence, confirming the previous ground-based measurement, and has improved the precision of the measured absorption level by almost a factor of 3. The improved resolution has enabled me to measure the sodium doublet absorption profile. I can confirm the presence of a very narrow Na I doublet feature, which can be explained by a high-altitude haze obscuring broad Na, K and H₂O features, or a low Na I abundance hiding the wings beneath an H₂ scattering signature. I do not detect any other spectral features in the 5808 – 6380 Å range.

It is not possible to constrain the absolute Na I abundance without knowing the species responsible for the continuum signature and hence the reference level, but comparison with a feature at 8 μm indicates that the relative abundance of sodium compared to water is much greater than solar.

From this and other measurements, it is clear that the two most well-studied hot Jupiters are very different. It is thought that there are at least two types of hot Jupiter, depending on whether stratospheres are present, but more measurements are required to determine whether HD 189733b and HD 209458b are representative of the different types. The case of WASP-17b, which has even narrower Na I line profiles, suggests a range of properties across the hot-Jupiter class.

With regard to HD 189733b, there needs to be further investigation as to what is causing the Rayleigh signature in order to place constraints on its possible abundance. Since this work, an optical secondary eclipse measurement has been published which does not show a high albedo, and so suggests that the haze seen in transmission is not optically thick when observed in emission, or that the terminator has different properties to the day side (Evans et al. 2013). Ideally, the albedo needs to be measured at more wavelengths to obtain a reflection spectrum, and this needs to be combined with optical phase curve observations to determine the uniformity of cloud cover. Such observations are very challenging, however.

Chapter 4

Measuring Atmospheric Temperature Profiles from Transmission Spectroscopy

4.1 Aims and Introduction

The following chapter describes how alkali lines can be used to measure the temperature structure in upper planetary atmospheres at the terminator by measuring the line profile shape seen in transmission. The derivative of absorption depth as a function of wavelength is characteristic of the atmospheric temperature profile, with higher temperatures increasing the scale height and thus causing a steeper line slope. The aim is to measure the upper-atmospheric terminator T - P profile for HD 189733b using the observed sodium lines from the previous chapter, which will further constrain the specific properties of the favourable target HD 189733b.

Prior to this study, only one planet had a measured terminator T - P profile, which was HD 209458b, where Vidal-Madjar et al. (2011b) and Vidal-Madjar et al. (2011a) calculated a T - P profile from 10^{-3} to 10^{-6} bar from optical high- and medium-resolution transmission spectra. Vidal-Madjar et al. (2011b) found an isothermal atmospheric layer of ~ 1500 K from 10^{-4} to 10^{-5} bar, where above this layer, the temperature rose again to 3600 ± 1400 K at $\sim 10^{-6}$ bar, a sign of the planet's thermosphere. A further aim is to compare the two exoplanets and look for differences and similarities. HD 209458b and HD 189733b are interesting to compare directly because they are in many respects at opposite ends of the spectrum of hot Jupiters. HD 209458b has a bloated radius, displays a stratospheric temperature inversion and has a star that is much less active than HD 189733. In contrast, HD 189733b does not have a bloated radius, does not display a stratospheric temperature inversion, and orbits one of the most active extrasolar planet hosting stars, although cooler than HD 209458.

Additionally, the optical transmission spectrum of HD 209458b is similar to clear atmosphere predictions with broad Na I line wings, whereas that of HD 189733b appears comparatively flat. This makes HD 189733b an ideal planet to study in detail for comparison with HD 209458b.

The T - P profile depends on many factors, such as IR and visible opacities in the atmosphere, the presence of clouds or condensates that can cause heating of the lower atmosphere and scattering in the upper atmosphere, the efficiencies of horizontal and vertical advection, and the intense incoming radiation from the star which can cause the upper atmosphere to heat up significantly. Since so many factors can affect the energy budget of the planetary atmosphere, it is difficult to say in advance how incoming stellar radiation on HD 189733b affects the atmospheric temperature profile. For this reason, the key differences between HD 209458b and HD 189733b make them even more interesting to compare. For example, it is not clear how the high-altitude haze observed in HD 189733b will affect the atmospheric temperature profile, since Heng et al. (2012) demonstrate that the presence of clouds and hazes can have very different effects on the temperature-pressure profile depending on their thicknesses and opacities. IR absorption due to a haze layer can heat the lower atmosphere and cool the upper atmosphere, whereas optical scattering will have the opposite effect, warming the upper atmosphere. The differing levels of radiation from the host stars will likely have a significant effect on the upper atmospheric chemistry as well, such as breaking down certain compounds (Knutson et al. 2010).

Furthermore, the model framework developed here can be used to measure the T - P profiles for other planets if the data is available. It was also used to re-evaluate the existing T - P profile of HD 209458b after I discovered an error in the literature. The work described in this chapter is published in Huitson et al. (2012) and it also contributed to a publication by Vidal-Madjar et al. (2011a).

4.2 The Model Spectral Absorption Depth Profile

Rybicki & Lightman (1979) define the optical depth as $d\tau_\nu = \alpha_\nu ds$, where α_ν is the absorption coefficient defined by $dI_\nu = -\alpha_\nu I_\nu ds$. Integrating the optical depth over the observer's line of sight in transmission gives:

$$\tau_\nu = \int_{-\infty}^{\infty} \alpha_\nu ds, \quad (4.1)$$

where τ_ν is the optical depth along the path of travel of photons across the terminator (the x direction, which is horizontal in the planet's atmosphere). For the x direction, I define $x = 0$ to be where the terminator is i.e. where the transmission spectrum is measured. Rybicki & Lightman (1979) define:

$$\alpha_\nu = n\sigma_\nu \quad (4.2)$$

where n is the number of particles per unit volume and σ_ν is the absorption cross section at frequency ν . Figure 4.1 shows a schematic of the path of light during a planetary transit. The x direction is the direction of the blue arrow. The horizontal column density, N_H is then:

$$N_H = \int_{-\infty}^{\infty} n(x) dx \quad (4.3)$$

where $n(x)$ is the number density of particles as a function of position x . The barometric equation relates a pressure at a given altitude, $P(z)$, to a pressure at a reference altitude, $P(z_0)$, and is derived in Appendix D.3 as

$$P(z) = P(z_0) \exp\left(-\frac{z - z_0}{H}\right), \quad (4.4)$$

where z is the measured transit radius, I define z_0 to be the height of the continuum where the planetary disc is opaque ($z_0 = R_p$), and H is the atmospheric scale height. As in Section 1.3.2, I define the atmospheric scale height assuming hydrostatic equilibrium and an atmosphere composed of an ideal gas, where $H = k_B T / \mu g$ and k_B is Boltzmann's constant, T is the local temperature, μ is the mean molecular weight of the atmospheric composition and g is the surface gravity (derivation in Appendix D.2). The following derivation is summarised partly by Fortney (2005) and partly by Lecavelier Des Etangs et al. (2008a) but, for clarity, I will write it here in more detailed form in the notation used in this chapter. I define Δz to be the altitude, z , measured in transmission spectroscopy minus that of the continuum level, z_0 . It can be thought of as the wavelength-dependent observed height of the exoplanet's translucent atmosphere.

The horizontal distance, x , from the edge of the atmosphere to the terminator makes a right-angled triangle with the vertical distance R_P and the distance from the centre of the planet to the outer edge of the atmosphere ($R_P + \Delta z$) as shown in Figure 4.1. From Pythagoras' theorem, this gives $x^2 = (R_P + \Delta z)^2 - R_P^2$. Expanding this and cancelling out R_P terms gives $x^2 = 2R_P\Delta z + \Delta z^2$. Assuming that $2R_P\Delta z \gg \Delta z^2$ means that the Δz^2 term is negligible, so $2R_P\Delta z \approx x^2$. Substituting into Equation (4.4) gives

$$n(x) = n_0 e^{-\frac{\Delta z}{H}} = n_0 e^{-\frac{x^2}{2R_P H}}, \quad (4.5)$$

where also, pressure has been replaced by number density, which is valid for an atmosphere in hydrostatic equilibrium. Then, the above expression can be substituted into Equation (4.3) to give

$$N_H = \int_{-\infty}^{\infty} n(x) dx = \int_{-\infty}^{\infty} n_0 e^{-\frac{x^2}{2R_P H}} dx. \quad (4.6)$$

The result can be obtained from a standard integral: $\int_{-\infty}^{\infty} e^{-x^2/a} dx = \sqrt{\pi a}$. Therefore, the result can be written as $N_H = n_0 \sqrt{2\pi R_P H}$. For an exoplanet atmosphere, n_0 will depend on the altitude, z , in the atmosphere and so I will use the symbol $n(z)$ rather than n_0 for clarity. This means that $n(z)$ is the number density at the terminator (so a fixed x) but is a function of altitude.

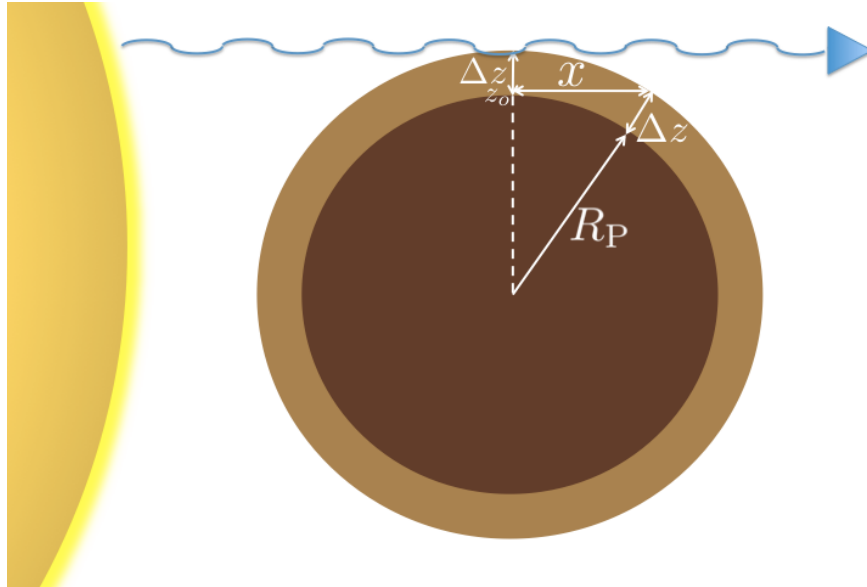


Figure 4.1: Schematic to illustrate the path of light through the planet's terminator during transit. The blue arrow is the light from the star passing through the atmosphere and moving in the x direction. R_P denotes the opaque planetary disc, which is opaque at all wavelengths. The radius R_P is defined as being at $\Delta z = 0$ for transmission spectroscopy (z_0). The transit radius as a function of wavelength is then given by $R_P + \Delta z(\lambda)$.

Equation (4.1) can then be written as follows:

$$\tau_v = \int_{-\infty}^{\infty} \sigma(\lambda) n dx = \sigma(\lambda) n(z) \sqrt{2\pi R_p H}. \quad (4.7)$$

Transmission spectroscopy aims to detect atmospheric species by detecting variations in z in order to infer the absorption cross-section, $\sigma(\lambda)$, in the atmosphere and detect specific atmospheric species. By definition, the optical depth at the measured transit radius must be such that atmospheric absorption can be detected. Lecavelier Des Etangs et al. (2008a) show that, at the transit spectral radius, $\tau_v = 0.56$ for a wide range of atmospheric temperatures. They name the optical depth at the transit radius τ_{eq} . Therefore, if z is the measured transit radius (i.e. the observer sees an occulting disc of radius $z = R_p + \Delta z$), then Equation (4.7) can be written as

$$\tau_{\text{eq}} = \sigma(\lambda) n(z) \sqrt{2\pi R_p H}. \quad (4.8)$$

Re-arrange Equation (4.8) to get $n(z)$ in terms of τ_{eq} , $\sigma(\lambda)$ and H :

$$n(z) = \frac{\tau_{\text{eq}}}{\sigma(\lambda) \sqrt{2\pi R_p H}}. \quad (4.9)$$

Using the Barometric formula again, but this time keeping it in terms of z , gives

$$\frac{n(z)}{n_{z=0}} = e^{-\Delta z(\lambda)/H} \Rightarrow \frac{\tau_{\text{eq}}}{\sigma(\lambda) \sqrt{2\pi R_p H} n_{z=0}} = e^{-\Delta z(\lambda)/H}. \quad (4.10)$$

Re-arranging Equation (4.10) gives the expected excess transit radius as a function of wavelength-dependent cross-section and number density of the atmosphere:

$$\Delta z(\lambda) = H \ln \left(\frac{\sigma(\lambda) n_{z=0}}{\tau_{\text{eq}}} \sqrt{2\pi R_p H} \right). \quad (4.11)$$

Equation (4.11) can also be written in terms of atmospheric pressure by assuming the ideal gas equation of state. At the reference altitude, $\Delta z = 0$, $P = P_o$ and the ideal gas equation can be written: $P_o V = N k_B T \Rightarrow P_o = N k_B T / V = n_{z=0} k_B T$. Then, $P_o / k_B T = n_{z=0}$ can be substituted into Equation (4.11).

However, Equation (4.11) gives the expected differential transit radius as a function of wavelength for the total atmosphere, where $n_{z=0}$ is the total number density of all species and $\sigma(\lambda)$ is the wavelength-dependent absorption cross-section for all species. In reality, it is difficult to compute the wavelength-dependent cross-sections for all possible species. In this study, I consider Δz as a function of wavelength due to absorption from only one species: atomic sodium, and measure the excess absorption of the Na I doublet compared to the continuum. In this case, the number density in Equation (4.11) becomes $\xi_{\text{Na}} n_{z=0}$ where ξ_{Na} is the abundance of sodium relative to

the total atmospheric abundance. Putting this into Equation (4.11) and writing $\sigma_{\text{Na}}(\lambda)$ rather than $\sigma(\lambda)$ to indicate that I am dealing with only sodium gives

$$\Delta z(\lambda) = H \ln \left(\frac{\sigma_{\text{Na}}(\lambda) P_o \xi_{\text{Na}}}{\tau_{\text{eq}} k_B T} \sqrt{2\pi R_p H} \right) = \frac{k_B T}{\mu g} \ln \left(\frac{\sigma_{\text{Na}}(\lambda) P_o \xi_{\text{Na}}}{\tau_{\text{eq}}} \sqrt{\frac{2\pi R_p}{k_B T \mu g}} \right), \quad (4.12)$$

where I have also expanded H and consolidated terms of k_B and T .

4.3 Determining Upper Atmospheric Temperatures from an Absorption Profile

It can be shown that the atmospheric temperature can be derived from the planetary transmission spectrum. Differentiating Equation (4.12) with respect to wavelength and re-arranging gives

$$\frac{\partial z(\lambda)}{\partial \lambda} = \frac{k_B T}{\mu g} \frac{\partial(\ln \sigma_{\text{Na}}(\lambda))}{\partial \lambda} \Rightarrow T = \frac{\mu g}{k_B} \left(\frac{\partial(\ln \sigma_{\text{Na}}(\lambda))}{\partial \lambda} \right)^{-1} \frac{\partial z(\lambda)}{\partial \lambda}. \quad (4.13)$$

The first term on the right in Equation (4.13), $\mu g/k_B$, is known for a gas giant atmosphere because the atmosphere is dominated by molecular hydrogen. It can also be assumed that the atmosphere is shallow and hence g and μ are constant. For the sodium doublet, the second term, $[\partial(\ln \sigma_{\text{Na}}(\lambda))/\partial \lambda]^{-1}$, is calculated from known cross sections. The third term, $\partial z/\partial \lambda$, is then measured from the transmission spectrum to give the atmospheric temperature. Higher temperatures cause the atmospheric scale height to increase, and so the feature becomes more extended, with a greater slope, as shown in Figure 4.2 for the sodium Na I doublet. To determine $\sigma_{\text{Na}}(\lambda)$, I modelled each line as a Voigt profile, which is a convolution of a Gaussian and Lorentz profile:

$$H_v = \frac{a}{\pi} \int_{-\infty}^{\infty} \frac{e^{-y^2} dy}{(u-y)^2 + a^2}. \quad (4.14)$$

I refer to the Voigt function as H_v rather than the usual H to avoid confusion with the atmospheric scale height. The Voigt profile includes Doppler broadening (Gaussian component) and natural and collisional broadening (Lorentz component). Two terms, a and u control the shape of the Voigt function. I made use of the IDL routine VOIGT.PRO to calculate the Voigt profile using the terms a and u as input parameters. The variable y is equal to $\sqrt{mv^2/2k_B T}$, where m is the atomic mass, v is the velocity component of the atom along the line of sight to the observer, and T is the atmospheric temperature. This quantity does not have to be known since it is integrated over infinity whilst computing the Voigt profile. More details of the Voigt function are given in Rybicki &

Lightman (1979). The first term is given by $a = \Gamma/4\pi\Delta\nu_D$, where Γ includes the natural decay rate, γ , and the atomic collision rate, ν_{col} . The total decay rate is given by $\Gamma = \gamma + 2\nu_{\text{col}}$. It can be assumed, due to the observed lack of pressure-broadened Na I line wings, that pressure broadening is negligible and hence I set the collision rate, $\nu_{\text{col}} = 0$. Indeed, including pressure broadening had very little effect on the calculated T - P profile that resulted. The second term is given by $u = (\nu - \nu_o)/\Delta\nu_D$, where $\Delta\nu_D$ is the Doppler width, ν_o is the central frequency of the line being computed, and ν is the frequency over which the profile is to be generated. The Doppler width is calculated separately for each line using

$$\Delta\nu_D = \frac{\nu_o}{c} \sqrt{\frac{2k_B T}{\mu_{\text{Na}}}}, \quad (4.15)$$

where μ_{Na} is the mean molecular weight of sodium and c is the speed of light in a vacuum. As well as investigating the effect of including pressure broadening, I also performed the analysis using a Lorentz function containing only natural broadening. I found that the derived T - P profile was similar to that calculated using the Voigt profile with natural and Doppler broadening, indicating that Doppler broadening is also negligible. The frequency-dependent absorption cross-section for a Voigt profile is given as (Rybicki & Lightman 1979)

$$\sigma(\nu) = \frac{\pi e^2}{m_e c} \frac{f}{\Delta\nu_D \sqrt{\pi}} H_\nu, \quad (4.16)$$

where σ_o is the absorption-cross section at the centre of the relevant line, e is the electronic charge, m_e is the mass of the electron, and f is the absorption oscillator strength¹. Knowing the absorption cross-section, the atmospheric temperatures can be derived from high and medium resolution spectral AD profiles where $\frac{\partial z}{\partial \lambda}$ can be measured. From the transit radius itself, z can be measured, meaning that a profile of atmospheric temperature as a function of altitude can be calculated.

¹The term ‘‘oscillator strength’’ comes from a classical description of quantum mechanics (see Rybicki & Lightman 1979).

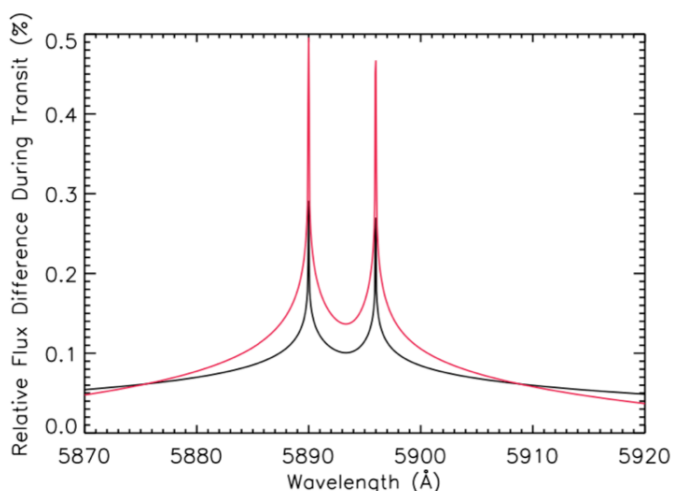


Figure 4.2: Two example Voigt profiles of the sodium doublet calculated for different temperatures (black = 1300 K, red = 2500 K). This illustrates the effect of temperature increasing the atmospheric scale height.

4.3.1 Reference Pressure and Pressure Scales

The goal of this chapter and this method is to measure the terminator T - P profile using an observed atmospheric feature such as the sodium Na I doublet. The above method describes how to measure the temperature profile as a function of altitude in the atmosphere, or a T - z profile. In order to measure a T - P profile, the pressure corresponding to each measured altitude needs to be determined. Re-arranging Equation (4.12) gives

$$e^{-\Delta z(\lambda)/H} = \frac{\tau_{\text{eq}}}{\xi_{\text{Na}} P_0 \sigma_{\text{Na}}(\lambda)} \sqrt{\frac{k_B T \mu g}{2\pi R_P}}. \quad (4.17)$$

From the Barometric formula again ($e^{-\Delta z/H} = P/P_0$) this can be written:

$$\frac{P(\lambda)}{P_0} = \frac{\tau_{\text{eq}}}{\xi_{\text{Na}} P_0 \sigma_{\text{Na}}(\lambda)} \sqrt{\frac{k_B T \mu g}{2\pi R_P}} \Rightarrow P(\lambda) = \frac{\tau_{\text{eq}}}{\xi_{\text{Na}} \sigma_{\text{Na}}(\lambda)} \sqrt{\frac{k_B T \mu g}{2\pi R_P}}, \quad (4.18)$$

where $P(\lambda)$ is a function of wavelength because $\Delta z(\lambda)$ is a function of wavelength, since it depends on absorption cross-section.

In most cases, however, the abundance of the species being studied (e.g. sodium) is not known. Therefore, the alternative method of working out the pressure scale is to use the Barometric law with a known reference pressure level, P_0 , corresponding to the point $\Delta z = 0$. Equation (4.17) can be used to calculate the reference pressure for a molecule with known abundance. In the case of a cloud-free atmosphere, the spectrum blueward of 4000 Å is predicted to be dominated by Rayleigh scattering from H_2 . If that is the case, then the reference pressure at an altitude measured blueward of 4000 Å can be derived because the abundance of hydrogen can

be considered to be ≈ 1 . Equation (4.17) then becomes

$$e^{-\Delta z(\lambda)/H} = \frac{\tau_{\text{eq}}}{\xi_{\text{H}} P_{\text{o}} \sigma_{\text{H}}(\lambda)} \sqrt{\frac{k_{\text{B}} T \mu g}{2\pi R_{\text{P}}}}, \quad (4.19)$$

and the reference pressure can be obtained by setting Δz equal to zero and the abundance equal to 1 (as also done by Vidal-Madjar et al. 2011b):

$$1 = \frac{\tau_{\text{eq}}}{P_{\text{o}} \sigma_{\text{H}}(\lambda)} \sqrt{\frac{k_{\text{B}} T \mu g}{2\pi R_{\text{P}}}} \Rightarrow P_{\text{o}} = \frac{\tau_{\text{eq}}}{\sigma_{\text{H}}(\lambda)} \sqrt{\frac{k_{\text{B}} T \mu g}{2\pi R_{\text{P}}}}. \quad (4.20)$$

Here, $\sigma_{\text{H}}(\lambda)$ can be assumed to be the Rayleigh scattering cross-section for H_2 molecules. For HD 189733b, the reference pressure, P_{o} , at the centre of the sodium doublet is ~ 150 mbar (see Section 4.4.1). Equation (4.20) gives an upper limit for reference pressure, since it is possible that high-altitude clouds or hazes could obscure the H_2 Rayleigh signature and raise the altitude of the spectral continuum, as seen in HD 189733b. This possibility is discussed in more detail in Section 4.4.1.

4.4 Applications to Specific Planets

To determine the temperature at a given altitude region in a planet's atmosphere, model AD profiles are generated for the measured spectral feature (in this case the Na I doublet). The model AD profiles are then fitted to transmission spectral data with temperature as a free parameter. The temperature is fitted at different parts of the observed line profile, and thus temperatures are derived for different altitudes where the absorption takes place: deeper in the atmosphere from the broader parts of the line and at higher altitudes from the narrower parts of the line. The fits also use a free z_0 parameter to enable the profile to shift up and down, to ensure that the fit is not degenerate with the local abundance. This method is independent of absolute absorption depth and depends only on the absorption profile slope, which means that knowledge of the reference pressure scale or the abundances is not required to measure the local temperatures and hence to obtain a T - z profile. Conversions to T - P profiles are discussed when I present the results. In Section 4.4.1, I apply the models to the data for HD 189733b described in Chapter 3 and in Section 4.4.2, I apply the models to data for HD 209458b given to me by A. Vidal-Madjar (priv. comm.).

Constant sodium partial pressure is assumed. This assumption could be invalid if the sodium abundance is not constant with altitude over the range in which a single temperature is fitted. For this reason, I have attempted to measure temperatures over only one scale height each and hence measure local regions of the atmosphere, where the assumption should be valid. However, the spectral resolution

of the HD 189733b data detailed in the previous chapter prevented such a measurement over only one scale height in the narrow line cores, where I had to measure a single temperature over a greater altitude. Additionally, I assume a value for the mean molecular weight, μ , which could change if the composition is drastically different from my assumption (unlikely) or if photodissociation occurs high up in the atmosphere, meaning that H rather than H₂ is the dominant hydrogen-bearing species. These caveats are discussed further when I present the results of the analysis.

4.4.1 Applying the Models to Sodium Observations of HD 189733b

I firstly calculated the T - P profile for HD 189733b, using the data described in Chapter 3. Measured differential transit depths can be converted into differential altitudes, Δz , in km in the planet's atmosphere, so that the spectrum can be fitted for temperature. In Section 3.5.1 I showed how to convert AD into a measurement in terms of $\Delta \frac{R_p}{R_\star}$. This can be converted into ΔR_p by simply multiplying by R_\star .

Visible transmission spectroscopy and the sodium D doublet in particular should probe the upper atmosphere, at pressures below 150 mbar to as low as 10^{-9} bar, where the atmosphere could be at very high temperatures (Lecavelier des Etangs et al. 2004; Yelle 2004; García Muñoz 2007; Moses et al. 2011). Vidal-Madjar et al. (2011b,a) measured a temperature of 3600 ± 1400 K for the upper atmosphere of HD 209458b, using the narrowest bands (highest altitudes) of the exoplanet's sodium AD profile. Here, I use the models generated above to determine the temperature ranges covered by the measurements of HD 189733b.

The value I used for R_\star was $0.756 R_\odot$. Figure 4.3 shows the G750M AD profile converted to km. For HD 189733b, I assume a shallow atmosphere with constant surface gravity of $g = 2141$ cm/s. Since the measured ADs in the sodium line cores reach altitudes above the continuum of ~ 4000 km, the assumption of a shallow atmosphere may not be valid. The potential effect of a non-constant surface gravity over the measured region would be to increase the atmospheric scale height as a function of altitude, and hence cause measured temperatures to be overestimated at higher altitudes. I discuss the magnitude of the potential effect when I present the derived temperatures. For an atmosphere composed of mainly hydrogen and helium (85 per cent H, 15 per cent He), $\mu = 2.3 \times 1.6726 \times 10^{-24}$ g. The sodium abundance, ξ_{Na} , planetary radius, R_p , and the reference pressure, P_o , do not affect the slope of the model profiles and hence the fitted temperatures. I arbitrarily set these values to a solar abundance, $\xi_{\text{Na}} = 1.995 \times 10^{-6}$ relative to the abundance of hydrogen (Lodders 2003), $R_p = 1.138 R_{\text{Jup}}$, and $P_o = 410$ mbar.

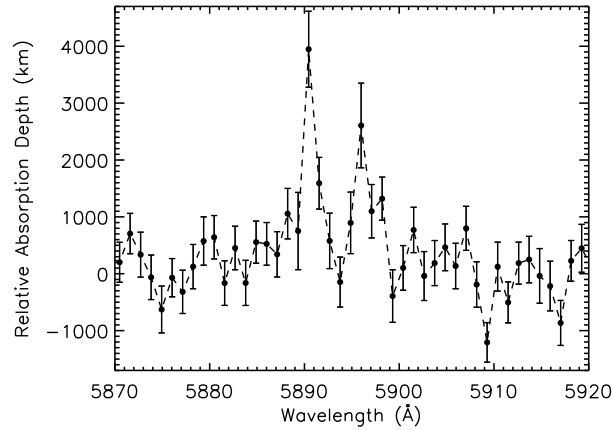


Figure 4.3: The transmission spectrum around the sodium Na I feature in terms of differential height in the atmosphere, where the continuum level is given as $\Delta z = 0$. The heights for each wavelength correspond to the transit radius above the continuum at that wavelength.

I used the central wavelengths from Steck (2010)², with $\lambda_0(D_1) = 5895.98 \text{ \AA}$ and $\lambda_0(D_2) = 5890.00 \text{ \AA}$. I used $\Gamma = 61.542 \times 10^6 \text{ s}^{-1}$ and $f = 0.3199$ for the D_1 line, and $\Gamma = 61.353 \times 10^6 \text{ s}^{-1}$ and $f = 0.6405$ for the D_2 line (Steck, 2010). I assumed $\mu_{\text{Na}} = 23 \times 1.6726 \times 10^{-24} \text{ g}$. The functions a , u and then H_v were computed separately for the D_1 and the D_2 lines of the sodium doublet. Then the wavelength-dependent absorption cross-section was calculated separately for the D_1 and D_2 lines, and the combined profile was worked out using $\sigma_{\text{Na}}(\lambda) = \sigma_{D_1}(\lambda) + \sigma_{D_2}(\lambda)$.

The Doppler Effect of the Planet's Motion on the Observed Na D Doublet Lines

During the transit, most of the planet's orbital velocity is in a direction perpendicular to the observer's line of sight. However, at the edges of the transit, there may be some component acting towards or away from the observer that will affect the observed absorption features. Here, I calculate the expected Doppler broadening of the Na I doublet during a transit due to the planet's orbital motion, which can affect the observed line shape and hence the derived temperatures if the effect is large enough. To work out the effect, I first calculated the component of the planet's orbital velocity towards or away from the observer. The period, P , of the orbit is 2.2 days and the radius of the orbit is $r = 0.03 \text{ AU}$ ($1 \text{ AU} = 1.496 \times 10^{11} \text{ m}$). The radius of the orbit was assumed to be constant due to the low eccentricity of the system (Agol et al. 2010). The angular velocity is given by $\omega = (2\pi)/P = 3.28 \times 10^{-5} \text{ rad s}^{-1}$. The linear velocity at any point in the orbit is then given by $v = \omega r$, and I obtain $v = 148 \text{ km s}^{-1}$.

²Available at <http://steck.us/alkalidata> [Accessed 02-Sep-2013]

The velocity actually observed will be a function of the position of the planet along its orbital path and of the inclination of the system, so that the observed velocity, v_{obs} , is given by

$$v_{\text{obs}} = v \sin i \cos \theta, \quad (4.21)$$

where i is the orbital inclination with respect to the observer and θ is the angle of the planet's motion compared to the observer's line of sight to the star (i.e. when the planet is adjacent to the star from the observer's point of view and all of the planet's velocity is directed towards the observer, then $\theta = 0$). The value v_{obs} was calculated for each point in the planet's orbit for half a complete orbit, starting with the planet moving directly towards the observer and ending with the planet moving directly away. The Doppler shift, z_D , is then given by $z_D = v_{\text{obs}}/c$, where c is the speed of light in a vacuum. Figure 4.4 shows the Doppler shift for each point in the planetary phase for the half-orbit. Positive values are redshifts and negative values are blueshifts. However, the planet was not observed for this duration. It was only observed for a short time around the primary transit. Figure 4.5 shows the Doppler shift as a function of phase for the phases at which the planet was observed in each HST visit.

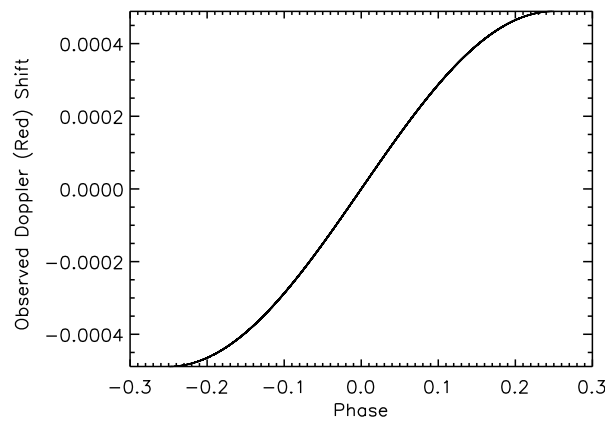


Figure 4.4: Doppler shift, z_D , as a function of planetary phase due to the component of the planet's orbital velocity towards or away from the observer. Negative values correspond to blueshifts and positive values correspond to redshifts.

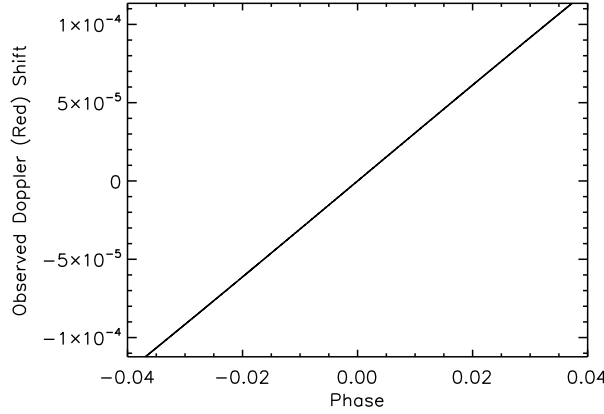


Figure 4.5: Doppler shift, z_D , as a function of planetary phase as in Figure 4.4, but only for the phases when the observations were taken. The phases observed for each visit are very slightly different but this plot covers the total range observed over all visits. Negative values correspond to blueshifts and positive values correspond to redshifts. The effects are minimal over the duration of one HST visit.

The broadening of the sodium line can be worked out from the Doppler shifts by using

$$z_D = \frac{\lambda_{\text{obs}} - \lambda_o}{\lambda_o} \Rightarrow \lambda_{\text{obs}} = \lambda_o + \lambda_o z, \quad (4.22)$$

where λ_{obs} is the observed (Doppler shifted) wavelength, and λ_o is the rest-frame wavelength (non-Doppler shifted). Since z_D changes with time, λ_{obs} was computed for each wavelength in the sodium feature for each phase during the observation. In order to ascertain whether the effects are important for the analysis, the difference in wavelength can be compared between the most blueshifted case (lowest phase observed) and the most redshifted case (highest phase observed). The total shift during the planet's orbit (180°) is around 6 \AA , but the total shift for the observed part of the orbit (transit + baseline) was only $< 0.7 \text{ \AA}$ per transit, which is lower than the instrumental resolution. Therefore, the broadening effects on the observed line profiles due to the planet's orbital motion do not need to be considered when fitting for atmospheric temperatures.

Atmospheric Temperatures for HD 189733b

When fitting the models to the data, I found two temperature regions. Fitting the whole Na I profile with a sodium doublet model at one temperature gave a χ^2 of 48.4 and $T = 2000 \text{ K}$ for 35 DOF with a BIC of 51.7. However, fitting for two temperature regimes, one at low altitudes probed by the 'line wings' and one at high altitudes probed by the 'line cores', resulted in a superior fit, with a χ^2 of 37.4 and BIC of 44.6 for 34 DOF. The signal in the 'line wings' ($5874\text{-}5886 \text{ \AA}$ and $5899\text{-}5912 \text{ \AA}$) of the Na I

lines is significant at the 2.9σ level added over the whole wavelength region for all visits, indicating a likely detection separate from the ‘line cores’ (5887-5898 Å).

The best fit to the ‘line wings’ of the Na I feature was 1280 ± 240 K, with $\chi^2 = 28.0$ (24 DOF). This region approximately covers altitudes of less than 500 km above the continuum, which is within the same altitude region in the atmosphere as the blueward rise in absorption depth observed in the near-UV by Sing et al. (2011b), who found a temperature of 2100 ± 500 K. This marginally suggests that another mechanism may be required to explain the excess absorption in the blue region of the spectrum, though the temperatures agree at the 1.5σ level. The best fitting temperature for the Na I ‘line cores’ was found to be 2800 ± 400 K, with $\chi^2 = 11.0$ for 11 DOF. This region corresponds approximately to altitudes of 500-4000 km above the continuum. The best fits are shown in Figure 4.6, with the heights in km being relative to the continuum.

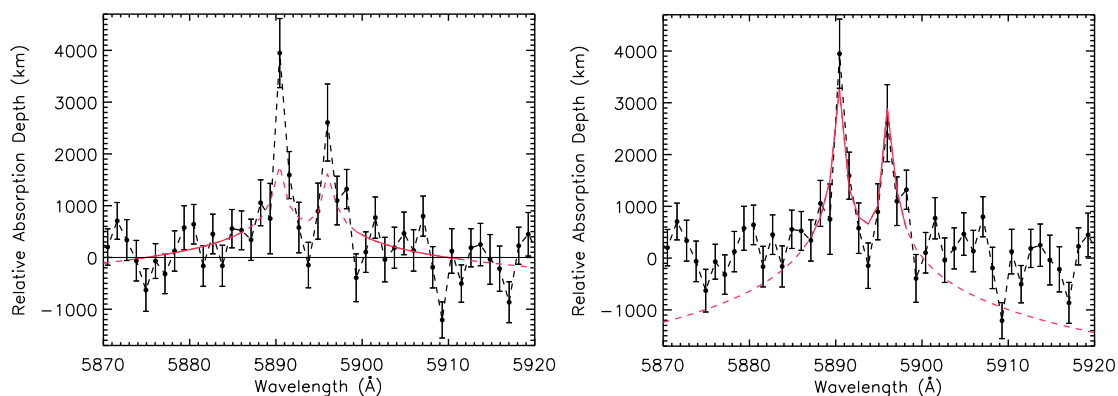


Figure 4.6: Plots showing isothermal model fits to the different wavelength regions of the data. The best fitting models are shown in red, binned to the instrument resolution. *Left:* Fit to the ‘line wings’ (5874-5886 Å and 5899-5912 Å), which probes atmospheric regions less than ~ 500 km above the reference altitude. The best fitting temperature is 1280 ± 240 K, a temperature that is similar to the temperature obtained by fitting the broad-band continuum absorption with Rayleigh scattering at the same wavelength range (Lecavelier Des Etangs et al. 2008a). *Right:* Fit to the ‘line cores’, at 5887-5898 Å. This wavelength region probes higher atmospheric regions, greater than ~ 500 km above the continuum. The temperature is found to increase to 2800 ± 400 K.

I fitted the data omitting pressure broadening. Including pressure broadening in the fit (Iro et al. 2005) with pressures of 60-150 mbar for the line wings had very little effect, with the best fitting line wing temperature increasing by ~ 20 K and the χ^2 increasing to 32.6 for 24 DOF. Pressure broadening does not affect the innermost cores of the lines. In order to consider the spectral dispersion in the fits, I moved the centres of the fitted sodium model by one pixel (0.54 Å) bluewards and redwards of the centre values and found that the ‘line core’ temperatures changed by only ~ 200 K.

I further tested whether the ‘line wing’ signal is due to a Rayleigh signature rather than sodium absorption. This was tested by combining the cross-sections for the sodium doublet and a Rayleigh signal, and placing the Rayleigh signal at the altitude level of the ‘line wings’. Keeping the ‘line core’ temperature fixed at 2800 K and fitting the ‘line wings’ with a sodium and Rayleigh signal gave a χ^2 of 35.6, instead of 28.0 in the sodium-only case, indicating that a Rayleigh component to the signal is likely to be negligible. Fitting a model with a sodium line core with temperature free to vary and a Rayleigh signal gave a χ^2 of 55.5 and a BIC of 59.0 when fitted to the ‘line core’ and ‘line wing’ regions together. Table 4.1 summarises the statistics of the different fits.

Since the temperature derived from the Rayleigh slope by Lecavelier Des Etangs et al. (2008a) is very similar to the fitted temperature obtained here by assuming that the whole signal in the ‘line wings’ is due to sodium, the conclusions do not change depending on whether the signature in the lower atmospheric regions is due to sodium absorption or a Rayleigh signature. In either case, two temperature regimes are required to explain the observations, with the derived temperatures also being similar in both cases for the ‘line wings’. The line core measurement is clearly due to sodium absorption and is not affected at all.

Model	χ^2	DOF	BIC
One temperature sodium only	48.4	35	51.7
Two temperatures sodium only	37.4	34	44.6
One temperature + Rayleigh	55.5	35	59.0
Line ‘core’	11.0	11	16.0
Line ‘wings’ sodium only	28.0	24	34.4
Line ‘wings’ assuming Rayleigh	35.6	24	42.0

Table 4.1: Fitting statistics for different atmospheric models fitted to the spectrum around the Na I feature in the atmosphere of HD 189733b. The top three rows are fits for the whole profile (‘line core’ and ‘line wings’ together) whilst the bottom three rows describe fits to the different profile sections independently. Here “sodium only” indicates models where it is assumed that all of the observed signal fitted is due to absorption by Na I with no Rayleigh component, and “Rayleigh” indicates models where it is assumed that the ‘line wing’ signal is due to Rayleigh scattering.

It should be pointed out here that although I binned the fitted data to the instrument resolution, it is potentially possible to fit the spectrum at full resolution if the model is convolved with the instrument response (e.g. as done by Kaspi et al. 2001). In the case here, the reduction in S/N resulting from decreasing the bin size would limit the improvement to a factor of $\sqrt{2}$. However, for lower resolution data with higher S/N, this option could provide a significant improvement on the accuracy of measured

atmospheric temperatures.

The resulting T - z profile is shown in Figure 4.7, where the altitudes correspond to the atmospheric height ranges above the continuum probed by each of the fitted wavelength regions of the doublet. This profile includes the previously measured temperature of 1340 ± 150 K found by Lecavelier Des Etangs et al. (2008a) for the Rayleigh continuum slope in the sodium region, at altitudes of $\Delta z = 0$ -200 km.

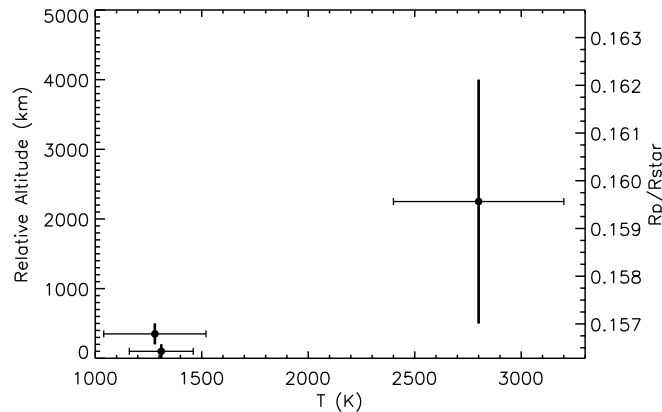


Figure 4.7: Temperature-altitude profile for HD 189733b. The altitude values shown are relative to the continuum level and are binned to the HST STIS resolution. The thick vertical lines indicate isothermal atmospheric layers. The horizontal error bars show the range of temperatures that match the spectral AD profile for the given atmospheric region. The lowermost point is the temperature derived from the Rayleigh continuum slope by Lecavelier Des Etangs et al. (2008a). The temperature rise with increasing altitude that is observed occurs much higher in altitude than the stratosphere.

The Terminator Temperature-Pressure Profile for HD 189733b

The temperatures of the upper atmosphere probed by the optical observations increase with increasing altitude. The measurements probe atmospheric regions well above the stratosphere, which could indicate that I am observing the base of the atmospheric thermosphere. To compare my calculated temperature profile with theoretical models, I generated a T - P profile. Firstly, I used the derived temperatures to work out the corresponding atmospheric scale heights, and hence the pressure structure of the atmosphere relative to the reference level using Equation (4.18). I assume a well-mixed atmosphere where the scale heights derived from the sodium line will be representative of the atmosphere. The fact that the temperature derived from the line wings is similar to that derived from the broad-band Rayleigh signature by previous work suggests that such an assumption is valid.

The spectral ADs measured here are only relative to the AD in the reference bands defined in Section 3.4.1 and, as discussed in Section 4.3.1, the derived T - z pro-

file can only be converted into an absolute T - P profile if the pressure at the reference altitude is known (also discussed by Lecavelier Des Etangs et al. 2008b). Determining the reference pressure requires the species responsible for the continuum absorption in the reference bands and its abundance to be known. In the case of HD 209458b, the identification of Rayleigh scattering by H_2 provided the required abundance information (Vidal-Madjar et al. 2011b). Since the continuum absorption in HD 189733b is due to an unknown species of unknown abundance, the inferred pressure-altitude relationship is not well constrained and can shift up or down in terms of pressure depending on the reference pressure.

The way to proceed is first to use a reference pressure based on the assumption that the continuum signature is due to Rayleigh scattering by H_2 molecules, with a temperature of 1340 K (Lecavelier Des Etangs et al. 2008a), meaning that I can use Equation (4.20). Lecavelier Des Etangs et al. (2008a) found $\sigma_H = 2.52 \times 10^{-28} \text{ cm}^2$ for hydrogen at 7500 Å, which gives a reference pressure of ~ 150 mbar in the wavelength region around the Na I feature. This reference pressure is an upper limit, since it corresponds to the dominant H_2 molecule to explain the broad-band absorption signature, and thus to the lowest altitude (highest pressure) level possible. The pressure profile calculated from Equation (4.18) can then be linked to the reference pressure of 150 mbar at $\Delta z = 0$ ($R_p = 0.15628$) to enable calculation of a pressure-altitude relationship. Figure 4.8 shows the pressure-altitude profile calculated using the fitted temperatures, and hence scale heights, from the Na I spectral AD profile.

Any other Rayleigh scattering species will be at higher altitudes, meaning that the pressure profile based on H_2 as the scattering species is an upper limit. The T - P profile was shifted to lower pressures to consider T - P profiles that result from different possible scattering species at different reference pressures. Figure 4.9 shows an example for an isothermal atmosphere and a high-altitude scatterer with an arbitrary reference pressure level of 25 mbar. As stated in Chapter 3, I believe that the scattering signature is most likely due to a high-altitude haze rather than due to H_2 . I therefore discuss the high-altitude haze scenario in greatest detail, but I also provide the corresponding upper-limit pressure values for the terminator T - P profile assuming H_2 scattering for comparison. Since the scattering species is so unknown, this is a first step, and I present only a representative T - P profile based on constant grain sizes for a single absorber, $MgSiO_3$.

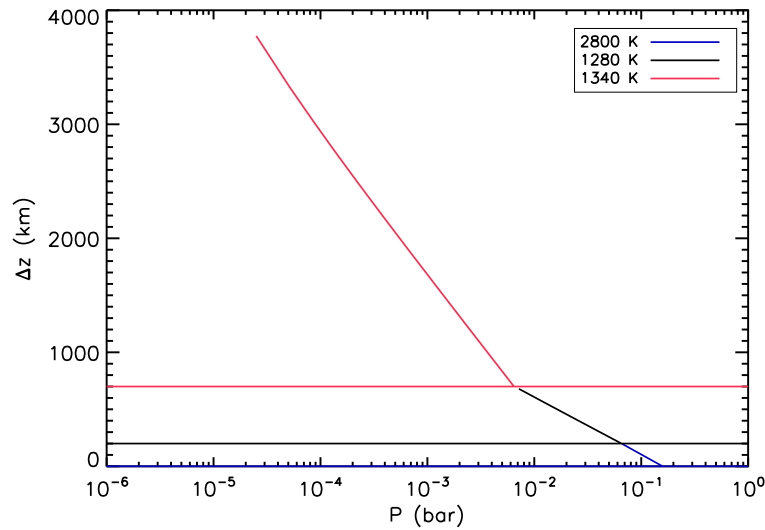


Figure 4.8: Pressure versus altitude in the atmosphere of HD 189733b, based on the regions sampled by the Na I line, using the derived temperatures for each region. The plot also includes the temperature derived for the 0-200 km region above the continuum by Lecavelier Des Etangs et al. (2008b). The coloured horizontal bars indicate the bottom of each isothermal region. This pressure profile places the $\Delta z = 0$ point at 150 mbar, and hence the whole profile shows the pressures for the case assuming that H_2 scattering defines the reference altitude. This profile will move downwards in pressure for the case of a high-altitude haze.

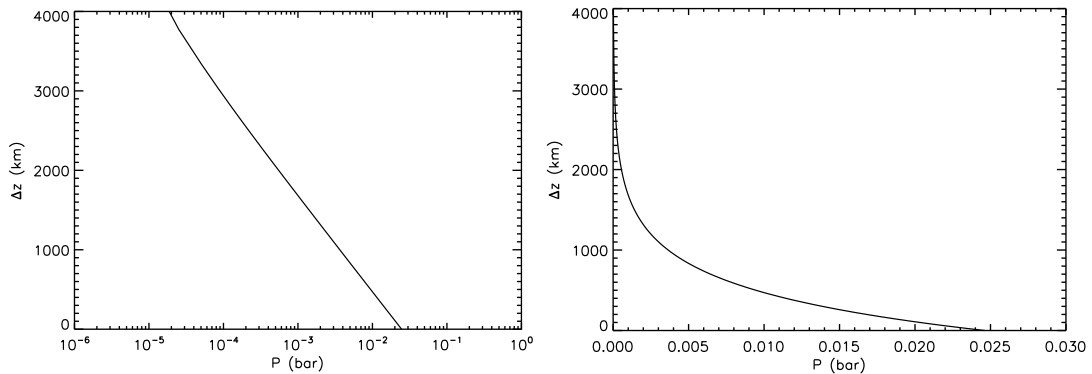


Figure 4.9: *Left*: Pressure versus altitude in the atmosphere of HD 189733b, based on the regions sampled by the Na I line and assuming a constant temperature of 2800 K. The reference pressure is arbitrarily set to 25 mbar for illustration. *Right*: The same plot on a linear scale for illustration of how the pressure varies in the planet's atmosphere as a function of altitude.

Lecavelier Des Etangs et al. (2008a) show that, for MgSiO_3 grains of particle sizes between 0.01 and 0.03 μm and a temperature of 1340 K, the haze should be at pressures between $10^{-3} > P > 10^{-5}$ bar. This assumption is based on the abundance of MgSiO_3 grains being limited by Mg abundance, and the assumption of solar Mg abundance. The reference pressure that I adopted was 10^{-4} bar, representative of the $10^{-5} - 10^{-3}$ bar range that fits the broad-band observations. Depending on the

species, this reference pressure could shift significantly. Figure 4.10 shows the T - P profile derived assuming that the Rayleigh signature is due to a high-altitude silicate haze. The vertical bars in Figure 4.10, which indicate pressure ranges, do not include the uncertainty in the pressure reference level. They indicate the altitude range over which each temperature is fitted. In the case assuming instead that H_2 is the scattering species, the derived pressures would be 150 mbar for the reference level, 65 to 6.6 mbar for the lower region of the observable doublet at 1280 ± 240 K, and 6.5 to 0.02 mbar for the upper region of the doublet at 2800 ± 400 K. This scenario places the sodium very low down in the atmosphere where the pressures are high, and hence it requires low sodium abundance.

I also show the temperatures and pressures observed for lower altitudes (higher pressures) from the secondary eclipse observations of Knutson et al. (2007a, 2009b), Charbonneau et al. (2008) and Deming et al. (2006). The temperatures in the last two works were adjusted to the terminator temperature by Heng et al. (2012) and these are the values that I use. I also combined the temperature measurement from Sing et al. (2009) with that from Lecavelier Des Etangs et al. (2008a) since they are both derived from fits to the broad-band Rayleigh slope in transmission. The models shown for comparison to HD 189733b are from Fortney et al. (2010), Yelle (2004) and García Muñoz (2007). Both upper atmospheric models (pressures below 10^{-6} bar) were computed for HD 209458b. These upper-atmospheric models are only approximations in the regions of interest here, since the region of the transition from the lower to upper atmosphere is difficult to simulate with existing models. Additionally, the upper-atmospheric models use a solar-type spectrum as input. The models of Moses et al. (2011) make allowances for the reduced emission at wavelengths longer than 2830 \AA , but the thermosphere is placed at a specific pressure, based on the models of García Muñoz (2007). Since it is currently not possible to predict the effect of the increased stellar activity on the high-atmosphere T - P profile, I have not attempted to scale these models for HD 189733b.

The pressures where the strong temperature rise occurs are at least an order of magnitude higher than the pressures at the base of the thermosphere found in the models of the upper atmosphere of HD 209458b, assuming a high-altitude haze as a reference level. This difference increases even further, by 3 orders of magnitude, if I assume H_2 as the scattering species. The discrepancy between the data and the models could indicate that the observations measure a lower-altitude temperature rise rather than the temperature rise characteristic of the base of the thermosphere, although the mechanism for such a deeper temperature rise is unknown. Alternatively, the discrepancy could be because the scattering species is higher in the atmosphere than my $MgSiO_3$ example case. My calculated pressures can shift by an order of

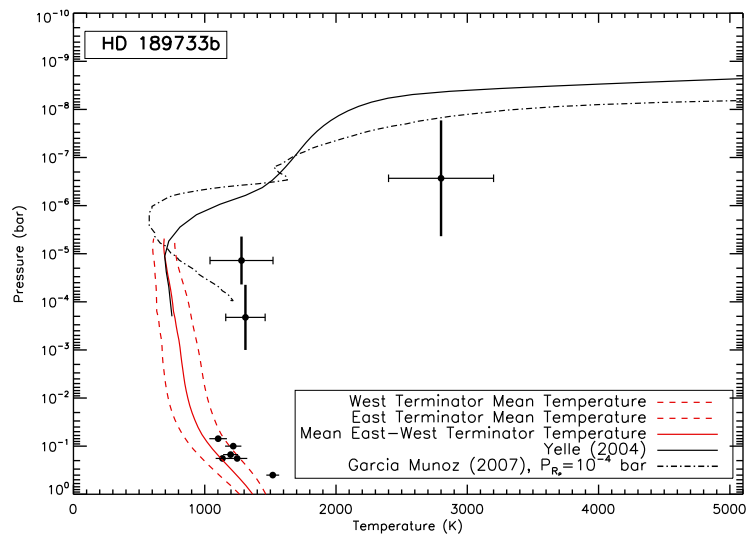


Figure 4.10: T - P profile for HD 189733b based on the assumption that the Rayleigh scattering signature is due to high-altitude atmospheric haze at a reference pressure of 10^{-4} bar. The temperatures are plotted in black for each pressure range (thick vertical bars). The thick vertical bars do not include the uncertainty in reference pressure. The data include the 1340 K temperature and pressure derived for the continuum by Lecavelier Des Etangs et al. (2008a) combined with the 1280 K temperature measured for the near IR continuum by Sing et al. (2009). The plot also shows lower altitude points from Knutson et al. (2007a, 2009b), Charbonneau et al. (2008) and Deming et al. (2006). The temperatures measured by Charbonneau et al. (2008) and Deming et al. (2006) were adjusted to the terminator temperature by Heng et al. (2012). T - P model profiles are shown for the lower altitude regions with red dashed lines (Fortney et al. 2010), and for the higher altitudes I show models for the upper atmosphere of HD 209458b for comparison, where the black solid line is the T - P profile from Yelle (2004) and the dot-dashed line is from García Muñoz (2007).

magnitude assuming an MgSiO_3 haze, and could shift even more if another species is responsible for the scattering continuum.

It is important to note that, if the reference pressure and hence pressure scale height in the measured regions shifts significantly, the assumption that H_2 is the dominant atmospheric species may become invalid. At higher altitudes, Yelle (2004) suggested that the scale height could increase due to the change in dominance of hydrogen from H_2 to H , which would decrease the mean molecular weight, μ . A lower mean molecular weight would increase the scale height without having to increase the temperature, and in this case, the 2800 K temperature would be an overestimate. However, the observed Na I line cores (highest altitudes) are observed in my data at $r/R_p \sim 1.06$, where H_2 should dominate according to that study. Furthermore, García Muñoz (2007) show that H dominates over H_2 only for pressures lower than $P = 10^{-8}$ bar.

I still investigated the temperatures that resulted from increasing the mean molecular weight and found that, in the extreme case of μ being half of what I previously assumed, the derived temperature of the line cores is similar to that of the line wings. However, such a temperature would imply firstly that thermal dissociation would be negligible, and also would suggest that the observations are not reaching such low pressure regimes as previously thought. This, in turn, would mean that H_2 must be adopted as the dominant atmospheric species. Such a circular argument does suggest that the observations could be probing some transition region in the atmosphere. Furthermore, sodium ionisation would occur at such low pressure regimes, at least partially counteracting the effect of the decrease in mean molecular weight and flattening the line profiles. Finally, the assumption of an H_2 -dominated atmosphere was the same as used for the T - P profile of HD 209458b by Vidal-Madjar et al. (2011b,a), meaning that such an assumption is required in order to compare the two results. Further theoretical work is required to better understand the overall properties of the atmosphere, especially as the models for the upper atmosphere of HD 209458b may not adequately describe HD 189733b, and that is why I use the assumptions of H_2 dominance and negligible ionisation.

Additionally, in creating the model AD profiles, I also assumed constant surface gravity. For absorption depths of ~ 4000 km (approximately 5% of the radius of Jupiter) the assumption may not hold. However, the effect on the results in my case is most likely negligible, since a height of 4000 km translates to a decrease in surface gravity of $\sim 10\%$, which affects the measured atmospheric scale height by ~ 25 km. Such a change is not significant when compared to the observed rise in temperature, for which a doubling of the scale height is required.

4.4.2 Applying the Models to Sodium Observations of HD 209458b

Since there is no work at present that is able to model all of the factors at the base of the thermosphere or at low pressures for HD 189733b, I cannot draw any meaningful comparisons with existing models. While it is hoped that these observations will be able to constrain future theoretical work, the most useful comparison now is to compare the calculated T - P profile with that of HD 209458b.

During the analysis of the T - P profile of HD 189733b, I compared my model AD profiles to those of Vidal-Madjar et al. (2011b) and detected an error in their analysis of HD 209458b. In the conversion of the absorption depth into altitude, their altitude measurements were systematically over-estimated. In order to verify a recalculated T - P profile which was afterwards published in Vidal-Madjar et al. (2011a), I independently calculated a T - P profile from the absorption depths given to me by A. Vidal-Madjar (priv. comm), which come from HST programme GO-8789 (P.I. T.M.

Brown). The original paper determined the T - P profile from the IAD profile, as described in Section 3.4.2, and so I also adopted that method. In order to calculate model IAD profiles, I took the model Voigt profiles generated around the sodium doublet and then performed the integrated analysis on them, as done on the data. For example, the model IAD value at 12 \AA is the mean of the model spectral AD values within a 12 \AA band around the Na I feature. Figure 4.11 shows an example IAD model profile along with the IAD profile data converted to differential altitude.

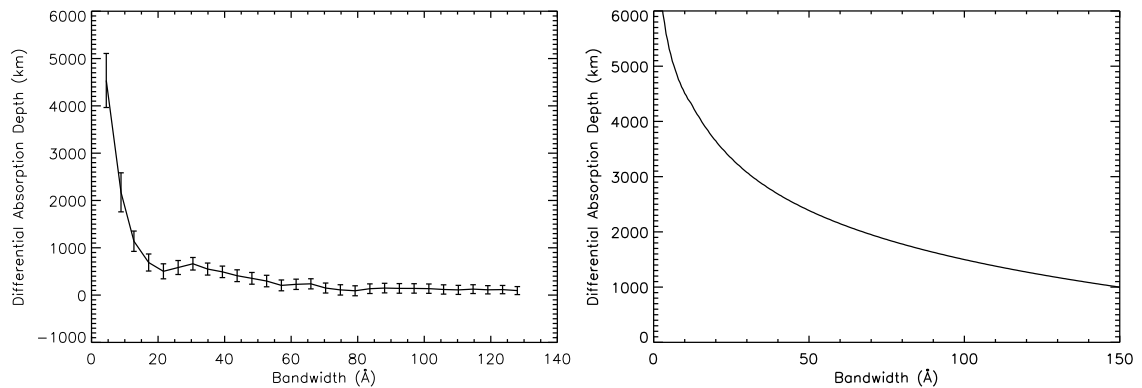


Figure 4.11: *Left*: IAD profile of the absorption around the Na I doublet in HD 209485b from STIS (A. Vidal-Madjar, priv. comm.) along with the high-resolution data point at a bandwidth of 0.75 \AA from Snellen et al. (2008). *Right*: A model IAD profile calculated using the Voigt profile with a temperature of 1500 K. This averages the two lines together, and was the method used by Vidal-Madjar et al. (2011b).

Table 4.2 gives the resulting altitudes, temperatures and pressures derived for the different regions of atmosphere. These are slightly different from the ones shown in Vidal-Madjar et al. (2011a) since they were measured independently. Furthermore, the final T - P profile which appears in Vidal-Madjar et al. (2011a) is calculated using the spectral AD profile rather than the IAD profile (the problems mentioned in Section 3.4.2 were pointed out by Ignas Snellen during the referee process of Huitson et al. (2012), which is why I changed my method to use the spectral AD profile, as did other authors). Furthermore, some of the temperature regions measured for HD 209458b were later combined since they were smaller than one atmospheric scale height. I therefore compare the published T - P profile of HD 209458b with that of HD 189733b rather than using my calculated profile. One thing to note is that, despite the caveats in Section 3.4.2, temperatures derived from an IAD profile are reliable and consistent with those derived from the spectral AD profile provided that it is certain that the studied regions of the line are resolved and detected. It must be known that the fitted wavelength regions far away from the line cores display a decreasing absorption depth as a function of bandwidth due to real absorption rather than due to a dilution of a narrow signal as the bandwidth is increased. Error estimates on the temperatures are less trivial, however, and the errors on fitted temperature values

quoted in Table 4.2 are therefore likely underestimates.

z (km)	T (K)
0-250	400 ± 100
250-400	600 ± 100
400-600	850 ± 150
600-800	550 ± 150
800-3000	1500 ± 100
3000-5000	3250 ± 1000

Table 4.2: The values for the HD 209458b T - P profile derived using the IAD values and using similar atmospheric regions to the original paper of Vidal-Madjar et al. (2011b).

Comparing the T - P Profiles of HD 209458b and HD 189733b

Figure 4.12 shows a comparison of the T - P profiles for both HD 189733b (this work) and HD 209458b, (from Vidal-Madjar et al. 2011a). For comparison to the HD 209458b data, the models of Showman et al. (2009) are shown for the lower atmosphere, and the models of Yelle (2004) and García Muñoz (2007) are shown for the upper atmosphere. All the models are specifically calculated for HD 209458b. Comparing the calculated T - P profiles to the models shows that the models predict lower pressures at the thermobase than those derived from the observations for HD 209458b (assuming that the observed temperature rise is indicative of the thermobase).

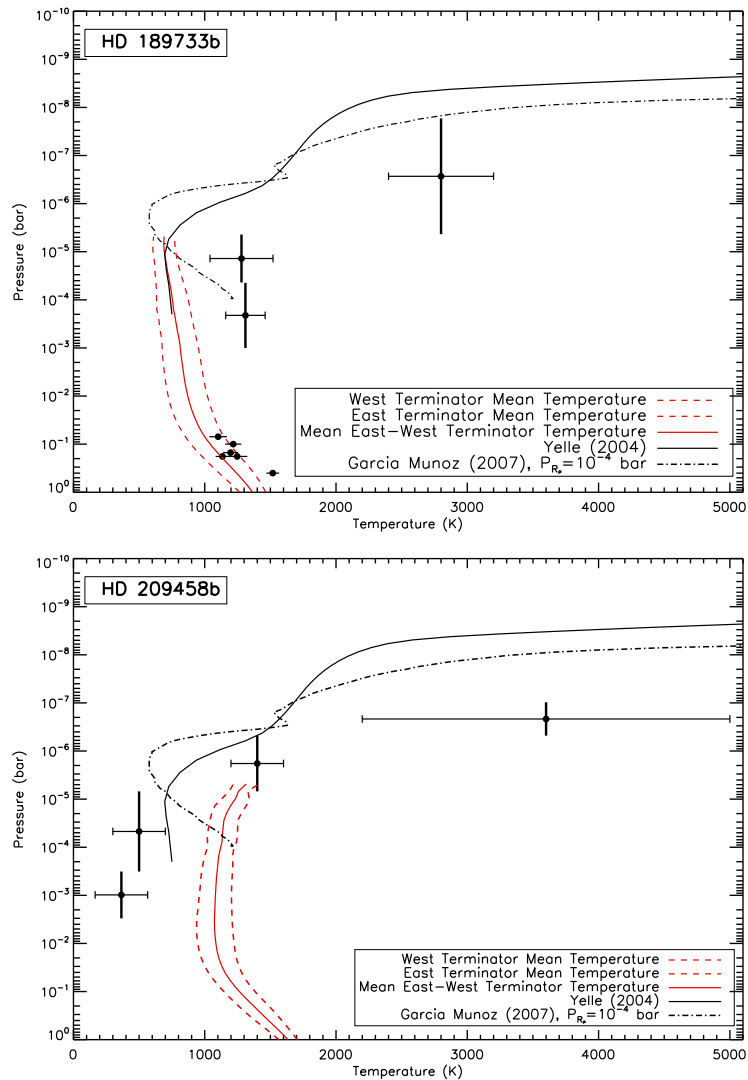


Figure 4.12: *Top*: T - P profile for HD 189733b, the same as Figure 4.10. *Bottom*: T - P profile for HD 209458b using the measurements from Vidal-Madjar et al. (2011a), plotted as black points using the same plotting scheme as for HD 189733b. Shown with red dashed lines are models for the lower atmosphere (Showman et al. 2009). The solid black line is a model from Yelle (2004) and the dot-dashed line is a model from García Muñoz (2007).

Since there are no models specifically for the upper atmosphere of HD 189733b at pressures below 10^{-6} bar, the most useful comparison to draw currently is between the two T - P profiles calculated from observations of both planets. To compare the two planets, I assume that, for each planet, the observed temperature rise indicates a detection of the base of the thermosphere, although I cannot be sure that the temperature continues to rise above the observed altitude regions. Both planets have measured escaping atmospheres (Vidal-Madjar et al. 2003; Lecavelier Des Etangs et al. 2010), which should be associated with extremely high temperatures at high altitudes.

The shape of the derived T - P profile for the uppermost regions of HD 189733b looks similar to the HD 209458b profile. The conclusion that the profiles appear similar has to be tentative as the IR data points are not tied to the pressure scale of the upper-atmospheric measurements for HD 189733b, so the overall T - P profile would look different if only the upper atmospheric region of the profile were shifted in pressure. Also, although the hottest point for HD 209458b appears hotter than that for HD 189733b, it should be remembered that this was measured using high-resolution data, which is not available for HD 189733b. Therefore, the hottest point for HD 189733b is actually more directly comparable to the second hottest point for HD 209458b. It would be very interesting to resolve the spectral absorption depth profile further and determine more accurately the shape of the T - P profile. The speed with which the upper atmosphere heats up with increasing altitude could give clues about any absorbing or reflecting material high in the atmosphere.

4.5 Summary and Conclusions

I have used the Na I spectral AD profile to determine the temperature as a function of altitude in the atmosphere of HD 189733b and have found that two temperature regimes are required to explain the observations. The temperature rises with increasing altitude over the regions measured, indicating a likely detection of the planet's thermosphere. A hot thermosphere is expected from models and has been detected in HD 209458b, a finding which I have also confirmed in this work. So far, only two planets have measured upper-atmosphere terminator temperature profiles, but it is reasonable to assume that most hot Jupiters will exhibit hot thermospheres, due to their closeness to their host stars and the amount of radiation they receive in their upper atmospheres.

I calculated the T - P profile for HD 189733b assuming that Rayleigh scattering from a high-altitude haze defines the reference level, based on MgSiO_3 as the scattering species. It is possible that condensates such as MgSiO_3 could sublime at temperatures of ~ 1300 K or even lower temperatures at the low pressures sensed with the visible data (e.g. Moses et al. 2011), which could indicate that another species is responsible for the observed signature. The calculated pressures are 3 orders of magnitude higher if I assume that H_2 Rayleigh scattering defines the continuum reference level, indicating how uncertain the pressure scale is. Additionally, the pressure scale as a function of altitude will change if the sodium abundance is not constant throughout the atmosphere.

This work measures only the second upper-atmospheric temperature profile for an extrasolar planet, as well as confirming findings for the first. Despite their large

spectroscopic differences, the upper atmospheric temperature profiles of HD 209458b and HD 189733b appear similar, showing that these temperature measurements are valuable additions to existing observations. As the method described here has now been demonstrated to be possible and reliable for more than one exoplanet, it could be applied to other planets, leading to further understanding of their upper atmospheres and how they interact with their host stars. High and medium resolution observations of individual spectral lines are valuable for determining the temperature structure of a planet's upper atmosphere. Therefore, I have taken observations with the high-resolution IFU spectrograph FLAMES³ GIRAFFE at the VLT⁴ to attempt to measure the upper-atmosphere terminator T - P profiles of WASP-31b and WASP-39b in a similar manner. The data are still being analysed. With regard to HD 189733b specifically, the temperature-altitude profile could also be improved with further observations of the sodium line core at high resolutions, which would constrain the hottest temperatures more accurately.

³Fibre Large Array Multi-Element Spectrograph

⁴The European Southern Observatory (ESO) Very Large Telescope at Paranal, Chile. For more information, see <http://www.eso.org/public/teles-instr/vlt.html> [accessed 02-Sep-2013].

Chapter 5

GTC Long-Slit Transmission Spectroscopy of XO-2b

5.1 Aims and Introduction

The following chapter describes the first published long-slit exoplanetary transmission spectrum, and is the first part of my thesis to focus on expanding knowledge to a large number of exoplanets by measuring broad properties. This observation is the first in a planned survey of 10 hot-Jupiter exoplanets using ground-based long-slit spectroscopy to cover a wide spectral range of 3800 to 9300 Å at low resolution with GTC OSIRIS (ID 182.C-2018, PI D.Sing). At the time of these observations, almost all of the detections in transmission had been for HD 209458b and HD 189733b, and so the aim is to try to put the differences that are observed between these most favourable targets into a wider context. The target list for the survey is given in Table 5.1.

Name	Mass (M_{Jup})	Radius (R_{Jup})
GJ 1214b	0.02	0.24
HAT-P-1b	0.53	1.24
HAT-P-4b	0.68	1.27
HAT-P-6b	1.06	1.33
HAT-P-12b	0.21	0.96
HAT-P-18b	0.20	1.00
TrES-2b	1.28	1.24
TrES-4b	0.93	1.78
WASP-21b	0.30	1.07
XO-2b	0.57	0.98

Table 5.1: List of targets for the GTC transmission spectral survey. Masses and radii are from <http://exoplanets.org/> and references therein [accessed 02-Sep-2013].

As a ground-based survey making use of a technique not used before for exoplanet characterisation, these observations are also an important step in developing ground-based exoplanetary characterisation techniques. The challenge of exoplanet characterisation is the requirement for high precision observations but without compromising spectral resolution significantly. For this reason, the large apertures provided from the ground may be an advantage over space-based platforms. At the time of this work, advances were being made towards broad-band ground-based transmission spectroscopy using integral field spectroscopy (Arribas et al. 2006) and multi-object spectroscopy (Bean et al. 2010), and this work was the first to use the long-slit technique.

The specific aims of this chapter are to characterise the broad-band transmission spectrum of the hot Jupiter XO-2b, the first planet to be observed in the survey. With an equilibrium temperature of ~ 1500 K, it is unknown whether the atmosphere of XO-2b should be clear or cloudy and it would be interesting to compare XO-2b to HD 189733b. So far, the only observations of this planet reveal a K I feature in the atmosphere using narrow-band photometry (Sing et al. 2011a).

The observations detailed here simultaneously measured the spectrum of a comparison star, allowing for differential spectrophotometry. The data covered two transits, one of which I analysed and so the majority of this chapter focuses on that transit. At the end of the chapter, the results from both transits are combined and I analyse them with the models derived in Chapter 4. It was found that sub-mmag level slit losses between the target and reference star prevented the full optical transmission spectrum from being constructed, limiting the analysis to differential absorption depths over ~ 1000 Å regions. However, sodium was detected in the planet's atmosphere, with a lack of broad line wings observed. A wider slit has now been commissioned for the telescope based on this observation, significantly improving the data quality. The work in this chapter contributed to the publication by Sing et al. (2012).

5.2 Observations

These observations used GTC OSIRIS (Cepa et al. 2000, 2003) and were taken with the 2×2 binning mode with a full frame readout at a speed of 500kHz, which produces a readout overhead time of 17 seconds. The readout speed of 500kHz has a gain of $1.46 \text{ e}^-/\text{ADU}$ and a readout noise of 8 e^- . While 500kHz is the noisiest readout speed (100 and 200kHz are available), it allows for the most counts per image to be obtained due to a higher gain.

The observations were made using a long slit of length $8.67'$ in the spatial direction with a $5''$ width (the widest available slit at the time of the observations) to minimise slit losses. Two transit events of XO-2b were observed, one with the R500B grism and one with the R500R grism. The R500B grism covers a spectral range from 3750 to 8586 \AA and has a dispersion of about 3.7 \AA per binned pixel. The R500R grism covers a spectral range from 5000 to 9300 \AA and has a dispersion of about 4.7 \AA per binned pixel. Both grisms have spectral resolving power $R \sim 500$. The reference star used was XO-2B, the stellar companion of XO-2. The two stars are separated by only $31''$ and both have the same spectral type (K0V) and similar magnitudes, making this an ideal case. The FOV was orientated such that both stars were centred in the slit. Figure 5.1 shows a resulting CCD image.

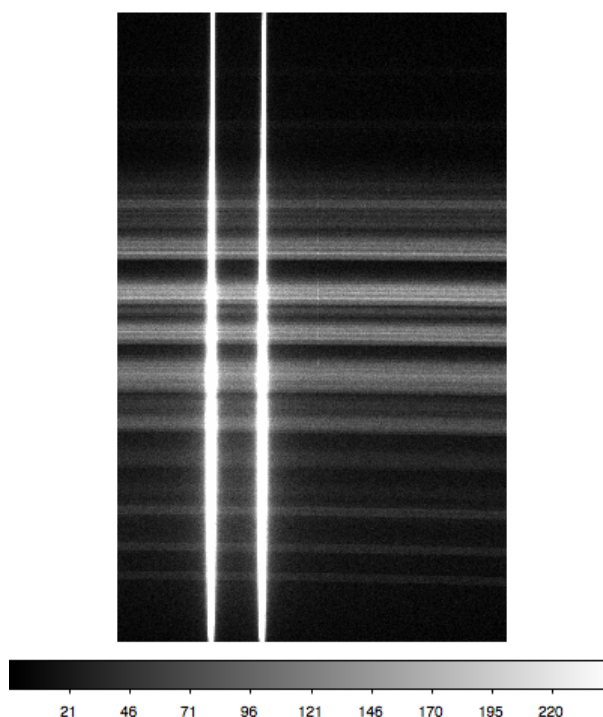


Figure 5.1: GTC Osiris CCD frame of XO-2A and XO-2B from 23rd Dec 2011 taken with the R500R grism and a $5''$ wide long slit. The image shown is after bias subtracting and flat-fielding the image. Horizontal lines show spectral features in the sky.

XO-2A and XO-2B were observed during the XO-2b transit events of 23rd December 2011 and 3rd February 2012. The first transit was observed with the R500R grism using 10 s exposure times, meaning that 770 exposures were obtained during the night, between UT 01:01 and UT 06:56. Seeing varied from 0.8'' to 0.9'' under photometric conditions and airmass ranged from 1.07 to 1.54. The second transit was observed with the R500B grating with 22 second exposure times, meaning that 519 exposures were obtained during the night between UT 20:32 and UT 02:15. Seeing ranged from 0.8'' to 2.0'' and airmass ranged from 1.07 to 1.4.

Exposure times were kept constant for a given night, maintaining the peak counts between 25000-40000 ADUs for both the reference and target stars. Defocusing was used to avoid saturation in improved seeing conditions. For each night 100 bias and 100 well-exposed dome flat-field images were taken ($\sim 30,000$ ADU/pixel/image). As is standard for exoplanet characterisation studies, the programme uses dome-flats, as opposed to sky-flats.

The observations were all specified to occur at the same pixel location, to help suppress flat-fielding errors. Through ESO GTC program 182.C-2018, D. Sing (priv. comm) used 12 transit light curves taken with narrowband imaging to estimate the guiding performance during a typical 4.5 hour long transit observation. They found the guiding performance of GTC OSIRIS to be quite stable, with measured drifts of 1.4 ± 1.0 pixels ($0.18 \pm 0.13''$) in the CCD X-direction and 1.0 ± 0.6 pixels ($0.13 \pm 0.06''$) in the Y-direction over a 4 hour period.

5.2.1 Reduction

The bias frames and flat fields were combined and used to correct each image through standard IRAF routines. The wavelength calibration was determined from HgAr, Xe and Ne arc lamps. There is one image for each lamp, and so the three images first had to be added together using the `IMARITH` task in IRAF to create a master lamp image (Figure 5.2). Once a combined image was created, the `IDENTIFY` task was used to manually match individual spectral peaks at known wavelengths to image pixels. The wavelength solution is non-linear, and the best solution was found by fitting a 4th order polynomial to the measured values of wavelength and pixel for each feature found in `IDENTIFY`. The fitted polynomial of pixel number was used as the wavelength solution, rather than directly applying the output from `IDENTIFY` to the spectral images. This calibration was checked by ensuring that stellar features of known wavelengths appeared in the correct place using the measured wavelength solution. With a low-resolution grism in conjunction with a wide slit, the spectra are inherently of low spectral resolution, limiting the narrowest useable bandwidth to around 50 Å and so small inaccuracies in the wavelength solution are insignificant.

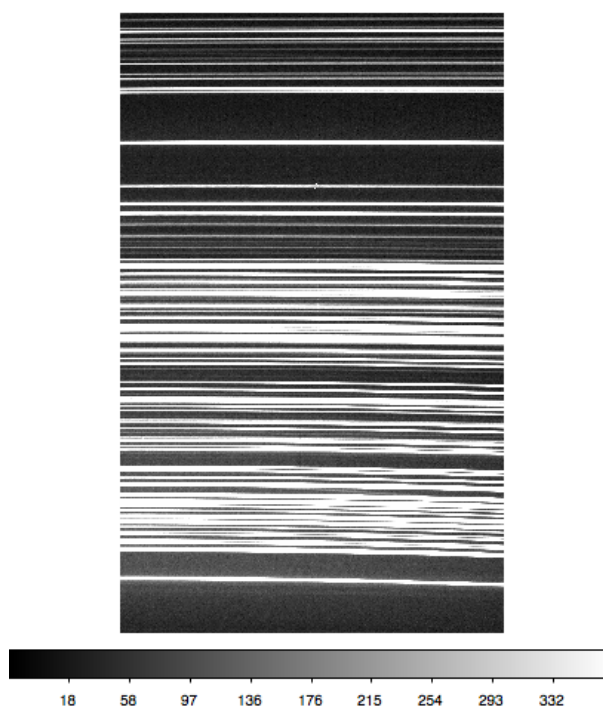


Figure 5.2: GTC Osiris CCD frame of the combined HgAr, Xe and Ne lamp images, used for wavelength-calibrating the spectra.

Aperture extraction for both the target and reference spectra was done for the R500R spectrum using `IRAF APALL` with a wide 42 pixel aperture, background subtraction, and no weights applied to the aperture sum (Figure 5.3 shows the spectra from one exposure along with one exposure from the transit observed with the R500B grism). For both nights, the appropriate aperture size was chosen to minimise the out-of-transit light curve dispersion. The aperture sizes were very similar for both nights (although I did not extract the R500B spectrum, which was reduced by D. Sing).

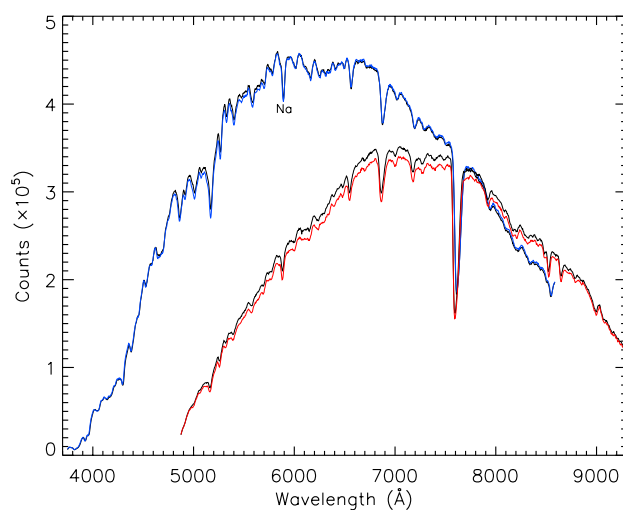


Figure 5.3: Extracted R500R (red) and R500B (blue) grism spectra of XO-2A and both corresponding spectra of the reference star, XO-2B (black). The plot is taken from Sing et al. (2012) and was constructed by D. Sing using my R500R data and his R500B data.

5.3 Analysis

To extract the planetary transmission spectra, I analysed the R500R spectrum, while the R500B spectrum was analysed by D. Sing. Here I will discuss the methods used to analyse the R500R spectrum, and also give results for the R500B spectrum for comparison. To check consistency, I also ran my analysis routines on the R500B data and obtained the same results as D. Sing.

The extracted spectra were used to create differential spectrophotometric light curves, by summing the spectra over wavelength regions of interest, and dividing the flux of the target star by that of the reference star in the same wavelength region. Firstly, the spectra were summed over the whole wavelength range to produce the white light curves. Figure 5.4 shows the extracted white light curves for both grisms, with only errors from photon noise.

Each of the white light curve points has a very high total count rate, typically 2×10^8 counts per exposure for R500R and 3×10^8 counts per exposure for R500B. This gives a theoretical limiting photon noise per exposure of 14,000 for R500R and 17,000 for R500B. The observed transit light curves, however, display clear mmag-level systematic trends. These are most likely due to differential slit losses between the target and reference star. In discussions with the GTC staff, the probable cause of the systematics is due to the telescope guiding (A. Cabrera-Lavers priv. comm.).

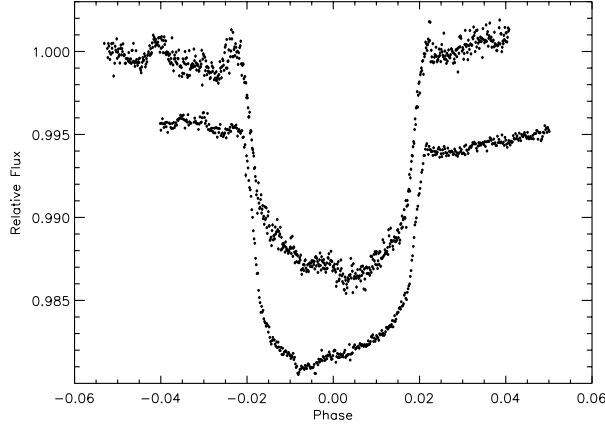


Figure 5.4: Extracted white light curves for R500R (top) and R500B (bottom). An arbitrary flux offset has been applied for clarity. Note the greater scatter on the R500R points, which have shorter exposure times and a lower signal per exposure.

The guiding is performed with respect to the target, and the guiding corrects via linear displacements in the focal plane. Thus, the lack of rotator correction causes small positional displacements of the reference star in the slit, which produces light losses seen as trends in its light curve. Light curves for the target star were extracted without using the reference star, but the systematics in this case were even worse since larger trends such as airmass and sky variations were not removed. I therefore performed the rest of the analysis on the differential light curve for the R500R spectrum, and the R500B spectrum was also extracted using the differential light curve.

The transit light curves were modelled with the analytical transit models of Mandel & Agol (2002), fitting for the central transit time, planet-to-star radius contrast, inclination, a/R_* , baseline flux and a systematics model (see Section 5.3.1) using the `IDL` implementation of the Levenberg-Marquardt least-squares algorithm, `MPFIT` (Markwardt 2009). To account for the effects of limb darkening on the transit light curve, I adopted the three parameter limb darkening law, calculating the coefficients from the stellar models of Kurucz (1993) following Sing (2010):

$$\frac{I(\mu)}{I(\mu = 1)} = 1 - c_2(1 - \mu) - c_3(1 - \mu^{3/2}) - c_4(1 - \mu^2). \quad (5.1)$$

5.3.1 Parameterised Slit Losses

The first method that I tried in order to remove the slit-loss trends was to create a model for the behaviour of the trends as a function of time. The best fitting model for the R500R data was found to be a linear function of planetary phase (ϕ), a quadratic function of FWHM (δ_w) and a linear trend with x position on the detector:

$$f(\phi, \delta_w, x) = f_0 \times (a_1\phi + 1) \times (a_2\delta_w + a_3\delta_w^2 + 1) \times (a_4x + 1), \quad (5.2)$$

where f_0 is the baseline flux and a_1, a_2, a_3 and a_4 are constant fitted parameters. A FWHM dependence is expected for slit losses, as wider PSFs lead to wider wings and larger slit losses.

I also looked for correlations with other parameters, such as airmass, sky brightness, y position on the CCD, altitude, azimuth and telescope rotation angle, but found that these did not improve the fit. The best fit was determined from using the reduced χ^2 and the BIC, to prevent over-fitting the data. The resulting fit is very unsatisfactory, with $\chi^2_v = 37.963$ and $\text{BIC} = 28981$, suggesting that this parameterisation does not fully capture the behaviour of the systematics. Figure 5.5 shows the full model for systematics and transit overplotted on the R500R white light curve. Clear mmag-level trends are still apparent in the residuals. The real physical parameter required to properly remove the slit-loss systematic is the position of each star on the slit, which is not recorded, and hence any parameterisation will most likely be insufficient.

Interestingly, the oscillations in the R500B light curve were more periodic, and were well-fitted with a series of sine and cosine terms in addition to a linear term in phase and a linear term with FWHM. These terms did not improve the fit to the R500R data. See Sing et al. (2012) for more details of the model used to fit the R500B data.

The standard deviation was 4.5×10^{-4} for the R500R white-light curve and the standard deviation was 2.3×10^{-4} for the R500B white-light curve. These deviations are dominated by the residual slit-loss trends and are a factor of 6 above the theoretical photon noise limit for the R500R transit and a factor of 4 above the theoretical photon noise limit for the R500B transit. Following Pont et al. (2006), I assessed the levels of residual red noise by using the binning technique described in Section 2.3.4. I then re-scaled the fitted parameter uncertainties to incorporate the measured red noise values by using the $\beta \times \beta_w$ factor described by Winn et al. (2008) and Lendl et al. (2013).

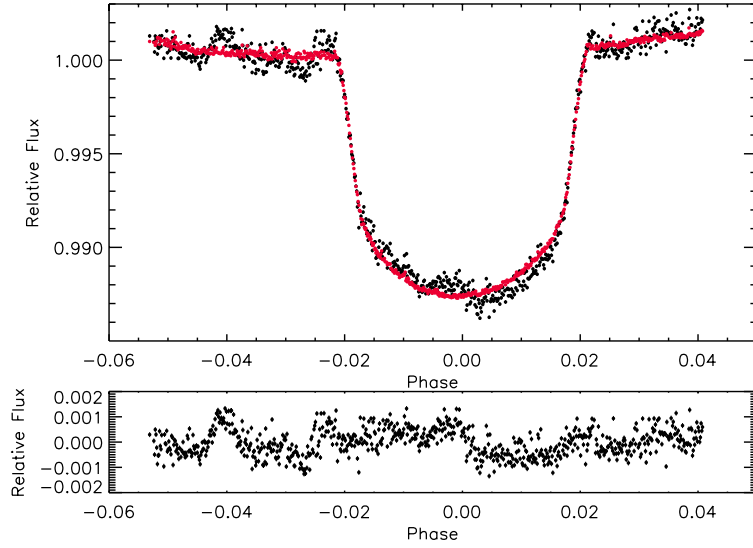


Figure 5.5: White light curve from the R500R grism, overplotted with the transit model from Mandel & Agol (2002) multiplied by the trend model in Equation (5.2). Plotted underneath are the residuals, with mmag-level trends still apparent.

Despite having different systematic trends, the best fitting planetary system parameters match well between the two GTC observations. The best fits give a system inclination of 88.4 ± 1.7 deg and a/R_\star of 8.07 ± 0.15 for the R500R transit, and $i = 88.8 \pm 0.9$ deg, $a/R_\star = 8.17 \pm 0.08$ for the R500B transit. These values match well with previous determinations, including values obtained over three years from 10 transits by Kundurthy et al. (2013), who found $i = 88.79 \pm 0.15$ deg and $a/R_\star = 8.14 \pm 0.06$.

To obtain the transmission spectrum, light curves summed over different spectral bins were fitted for radius contrast. All system parameters (inclination, central transit time, a/R_\star) were fixed to the best fitting white light values and only the radius contrast, baseline flux and de-trending coefficients were allowed to vary. If the removal of systematics is successful, then obtaining the transmission spectrum by measuring R_p/R_\star in different wavelength bins is the most preferable method, because absolute transit depths are obtainable. However, the systematics are still present at an unacceptable level, meaning that differential spectroscopy is the only option (see below).

5.3.2 Common-Mode Slit Losses and Differential Transmission Spectra

Systematics which have the same structure in each waveband are “common mode”. Common mode systematics can be removed by subtracting the white light trends from the spectral wavebins. For systematics which are similar in each wavelength, common-mode subtraction can remove the bulk of the contaminating signal. The advantage of removing the slit losses by common-mode subtraction rather than using the parameterised method is that the higher order frequencies are naturally subtracted. The disadvantage is that absolute transit depth information is lost. Relative transit depths as a function of wavelength, however, are still able to detect specific spectral features as the shape of the transmission spectrum is preserved.

The common mode technique was investigated for the XO-2b data to determine how much of the contaminating signal could be effectively removed. Different techniques were employed to remove the common-mode trends including using the transit-removed white light slit losses as an external decorrelation parameter in the transit light curve fits, which allows for the same systematic structure but with a scaling parameter. Fig. 5.6 shows the resulting de-trended light curves for spectral bins of $\sim 380 \text{ \AA}$ for the R500R data. A similar plot is shown in Sing et al. (2012) for the R500B data.

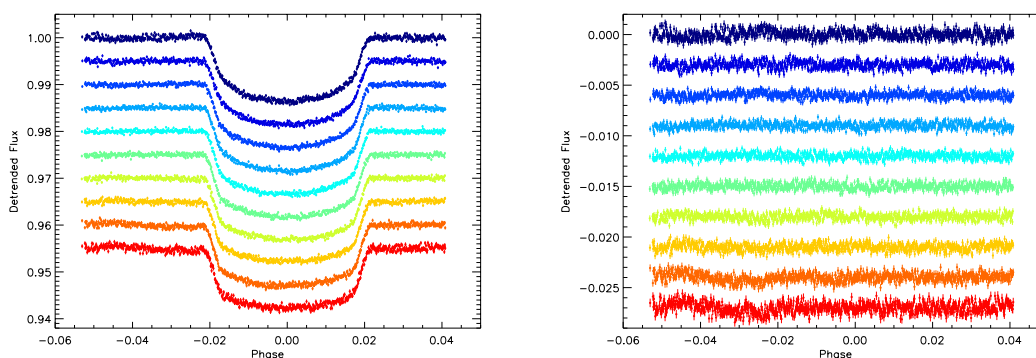


Figure 5.6: *Left*: Light curves for different spectral bands of width $\sim 380 \text{ \AA}$ after correcting for systematics using the white-light residuals. The bluest wavelength bin is at the top and the reddest at the bottom. Arbitrary flux offsets have been applied for clarity. It can be seen that there are small differences in the systematics as a function of wavelength. *Right*: Residuals of each lightcurve minus the models including transit, to better show any wavelength dependence. Arbitrary flux offsets have been applied for clarity. The light curves have precisions ranging from 500 ppm at the spectral edges to 350 ppm nearer the centre.

It is clear that there are small wavelength dependencies. The residuals are much flatter closer to the centre of the full spectral range than at either of the spectral edges. Additionally, there is a small slope as a linear function of phase, which appears at the edges of the spectrum. Some wavelength-dependence in light losses is expected, since atmospheric dispersion will not be the same at all wavelengths. The wavelength dependence is better illustrated in Figure 5.7, which shows variations in the light curve as intensity variations in shades of grey. These variations are plotted vs phase along the horizontal axis and wavelength along the vertical axis. There are clear variations with time, and clear variations with wavelength, but the plots show that there is very little variation as a function of both wavelength and time (which would manifest itself as diagonal features). Only such diagonal features significantly affect the shape of the transmission spectrum (relative transit depth as a function of wavelength).

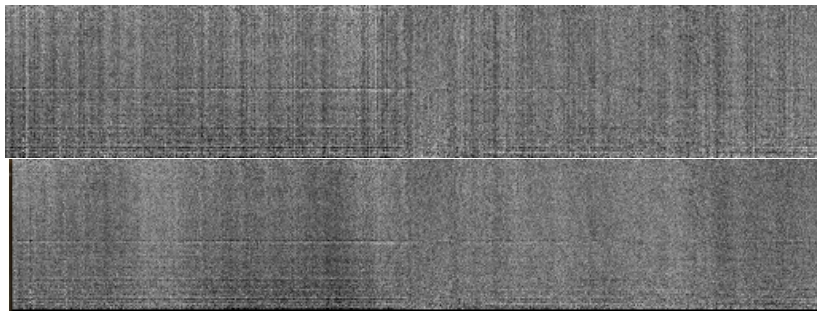


Figure 5.7: Plots to illustrate the wavelength and time dependence of systematics. The top plot shows the raw light curves, and the bottom plot shows the light curves de-trended using the white light residuals.

I also subtracted the normalised white light curve from the spectral transit light curves, fitting for the differential planetary radius, rather than using the white-light residuals as a de-trending parameter. In this method, the majority of the transit is subtracted, leaving only the differences in limb darkening and planetary radius, but the slit losses are also largely removed. Both methods produced similar results, though results are quoted and conclusions drawn from the subtracted transit light curve fits, as these were able to be fit with a minimum number of free parameters.

5.3.3 Extracting the Planetary Transmission Spectrum

Due to the presence of small visible wavelength dependences in the trends, it is important that the common-mode technique is not used over too wide a wavelength range. For this reason, I focussed on specific spectral features and, rather than subtracting the white light trends, I subtracted the trends in a ‘reference’ bin, centred within the wavelength region of interest. The spectral extent to which the slit losses of a given reference bin could be used was assessed quantitatively by measuring the linear Pearson correlation coefficient between the residuals of each wavelength bin and the residuals of the reference bin once a transit model had been subtracted from each (leaving only the systematic trends). It was found for the R500B data that well-correlated slit losses produced red noise values below 1×10^{-4} , and produced correlation values of 0.8 and higher (D. Sing, priv. comm.). I therefore also considered residuals to be well-correlated with those in the reference bin if the correlation coefficient was 0.8 or higher, which produced red noise values below 2×10^{-4} for the R500R spectral bins. Spectral ranges were limited to no larger than $\sim 500 \text{ \AA}$ away from the centre of any particular reference bin before correlation values dropped significantly (see Figure 5.8). Such small spectral ranges confirm that the analysis is indeed limited to searches for specific expected spectral features, including sodium, potassium, and $H\alpha$. Potassium was unfortunately compromised by large telluric O_2 lines (also see Crossfield et al. 2012b), and $H\alpha$ did not show significant absorption.

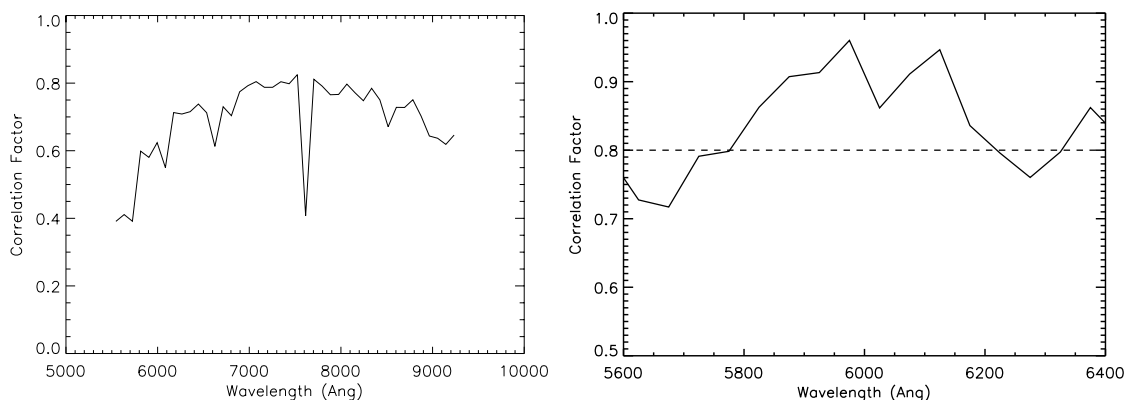


Figure 5.8: *Left*: Linear Pearson correlation coefficients for the residuals of different wavelength bins relative to the white light residuals for the R500R transit. *Right*: Linear Pearson correlation coefficients for the residuals of different wavelength bins relative to the residuals for the ‘reference’ light curve, summed over the 5850-6150 \AA range, again for the R500R transit. In both cases, only a transit model has been subtracted to obtain the residuals, not a model including systematic trends.

In the sodium search, the extracted spectrum was restricted to the small region around the sodium feature, where it is safe to use the common-mode technique for removing trends. The wavelength ranges were 5450-6150 Å for the R500B spectrum and 5850-6150 Å for the R500R spectrum. The efficiency of the CCD introduces significant errors in the R500R spectrum blueward of 5800 Å, where the efficiency is less than half of that at the peak response. The light curves were fitted adopting the stellar model limb darkening values as well as fixing the inclination and a/R_\star to the best-fitting values found previously. The fits included three free parameters: one parameter for the differential planet to star radius ratio, $\Delta R_p/R_\star$, and two parameters for the baseline flux allowed to vary in time linearly. The resulting combined spectrum is shown in Figure 5.9, using bin sizes of 50 Å.

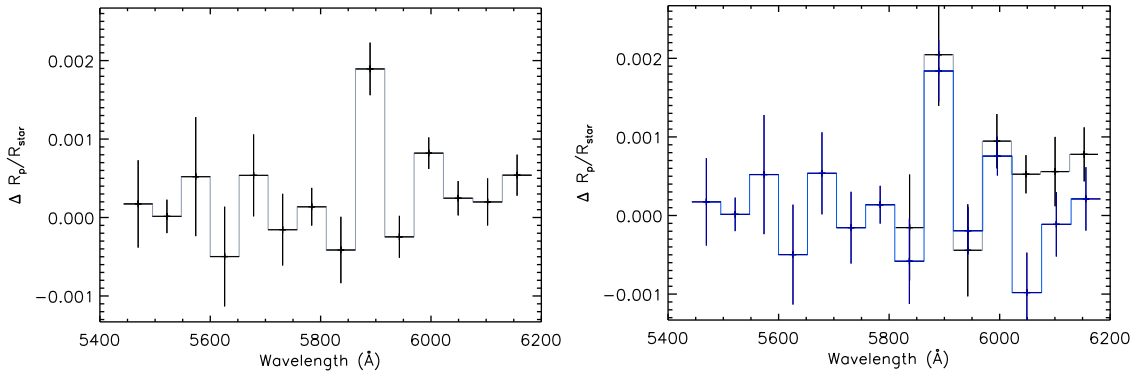


Figure 5.9: *Left:* The differential spectrum around the sodium feature, using a weighted mean of both the R500R and R500B observations where the wavelengths overlap (5850-6150 Å). The X-axis error bars indicate the spectral bin sizes, while the Y-axis error bars indicate the $1-\sigma$ uncertainty in differential radius ratio. *Right:* The differential spectrum around the sodium feature shown separately for both the R500R (black) and R500B (blue) transits.

For the R500R observation, I investigated the effect of changing the spectral binning on the resulting differential spectrum in increments of 12 Å. Including the variance of each point from this method had a negligible effect on the error bars, except in the sodium feature, where the absorption depth decreased if the band was moved more than 25 Å away from the central wavelength of the feature, consistent with a positive detection. The red noise was seen to vary by up to $\sim 20\%$ depending on the particular bins used, and I selected the binning which resulted in the lowest red noise. I also found that changing the reference wavelengths by 50-100 Å made no difference to the shape of the relative spectrum. The results from these investigations are shown in Figure 5.10.

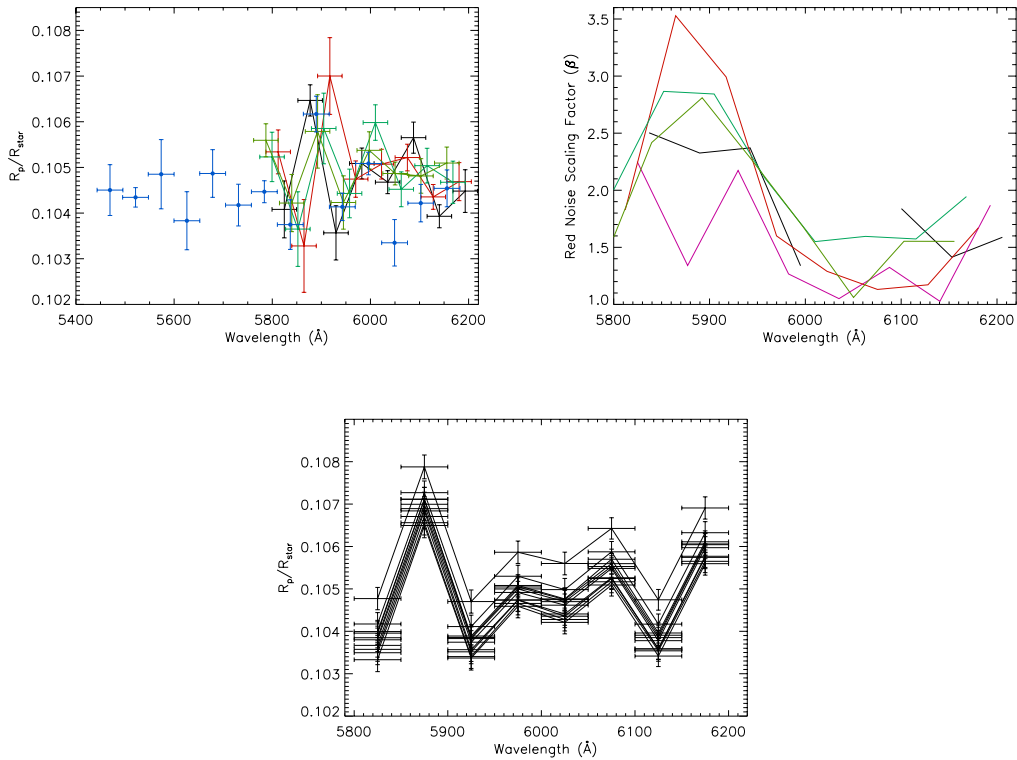


Figure 5.10: *Top Left:* The XO-2b spectrum extracted using different binnings for the spectral wavebands in the R500R spectrum (each colour of joined points represents a different binning). The unconnected blue points are the R500B spectrum. *Top Right:* Red noise scaling factors for each bin (using the same colours for different binnings as the top left plot). These indicate the contribution of red noise to the overall uncertainties for each spectral bin. Note that the gap for one of the spectra is where the red noise became unmeasurable. *Bottom:* For the best spectral binning (lowest red noise) this illustrates the effect of changing the reference band. It can be seen that the spectrum moves up and down, but the shape remains the same. Therefore, the differential spectrum, which the conclusions are drawn from, remains unaffected.

In addition to measuring the differential transmission spectrum, I also measured the differential absorption depth of just the sodium feature compared to adjacent bands blueward and redward of the feature, using the method described in Charbonneau et al. (2002) and Chapter 3. To do this, I used a 50 Å band centred on the sodium doublet, and 50 Å blue (5812-5862 Å) and red (5917-5967 Å) bands. There was significant differential absorption in the sodium region, with differential absorption depths of $49 \pm 17 \times 10^{-5}$ for the R500R observation and $47 \pm 11 \times 10^{-5}$ for the R500B observation. The combined relative absorption depth of the Na I feature using the weighted mean spectrum is $47 \pm 9 \times 10^{-5}$, consistent with the spectral results, which gives a 5.2σ detection of sodium in the atmosphere of XO-2b. Figure 5.11 shows the differential light curve around the sodium region compared to a combination of the two adjacent bands, illustrating the excess absorption depth.

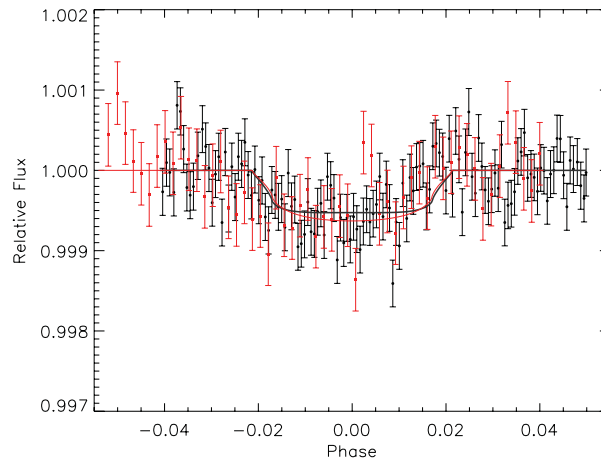


Figure 5.11: Differential transit light curves of a 50 Å band centred on the sodium doublet compared a reference band composed of bands either side of the sodium feature (5812–5862 Å and 5917–5967 Å). The R500R transit is shown in red and the R500B transit is shown in black with the corresponding models in the same colours. The figure is from Sing et al. (2012) and I produced only the R500R transit in this work. The R500R data are binned by 14 points and the R500B data are binned by 4 points. The R500R light curve has stronger differential limb darkening due to the weaker spectral response in the blue reference band.

5.4 Discussion

5.4.1 Atmospheric Model Fits

The spectrum appears featureless except in a single bin around the sodium feature, suggesting that the doublet must be unresolved in the data, and narrower than the 50 Å bins used for this study. Such a narrow feature could be indicative of high-altitude haze or clouds, which obscure the lower regions of the atmosphere by scattering signatures, as seen in HD 189733b (Chapter 3, Pont et al. 2008, Lecavelier Des Etangs et al. 2008a, Sing et al. 2011b, Huitson et al. 2012). Alternatively, in cloud-free upper atmospheres dominated by alkali-metal absorption, flat spectral regions can be observed where the abundance drops suddenly as altitude increases, which counteracts the increase in absorption cross-section toward the line core. This behaviour is seen in HD 209458b (Sing et al. 2008b; Vidal-Madjar et al. 2011b). Abundance drops could be attributed to processes such as ionisation, or condensation if the temperature profile crosses the condensation curve. I fitted the spectrum of XO-2b with different models to assess the significance of the observed lack of line wings (this process is detailed in Sing et al. 2012, with this section worked on essentially only by me).

I first used a model transmission spectrum developed specifically for XO-2b by J. Fortney from Sing et al. (2011a) which is based on the formalism of Fortney et al. (2010) and Shabram et al. (2011). This model includes a self-consistent treatment of radiative transfer and chemical equilibrium of neutral species; however the formation of hazes and photo-ionization are both neglected. Broad sodium and potassium line wings are seen in the model, each over 1000 Å wide. The model was binned to the transmission spectral resolution of 50 Å and fitted to the data with z_0 as a free parameter, as shown in Figure 5.12. The best fit gives $\chi^2 = 37.6$ for 13 DOF.

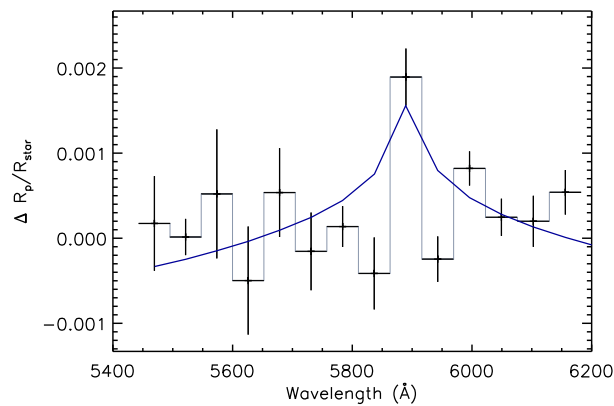


Figure 5.12: The mean differential transmission spectrum from the R500R and R500B spectra around the sodium feature (black). Also plotted is a model from Fortney et al. (2010), assuming a haze/cloud free atmosphere dominated in the optical by alkali metal absorption, fitted to the data with only a vertical offset as a free parameter (blue solid line).

I then modelled the feature using an analytic isothermal model transmission spectrum for the sodium feature as described in Chapter 4 and Huitson et al. (2012), based on the formalism of Lecavelier Des Etangs et al. (2008a) and Vidal-Madjar et al. (2011b), with temperature and the reference level, z_0 , as free parameters. Fixing the isothermal model temperature to an average temperature of 800 K produced a fit very similar to the full model, with $\chi^2 = 38.3$ for 13 DOF. Adding pressure broadening to this model produced no noticeable difference in the fits. Allowing the temperature parameter to vary freely produced a temperature of ~ 390 K ($\chi^2 = 31.6$ for 12 DOF), showing that the model has to flatten the line wings to fit the data. Neither model provides a satisfactory fit. The fits are shown in Figure 5.13

For an alternative model, I assumed that the sodium feature is unresolved at a resolution of 50 Å with the line wings either obscured by scattering from clouds or hazes, or flat due to a sudden abundance change as a function of altitude. I choose a width of 12 Å for the unresolved feature, which must be less than 50 Å, and then artificially set the regions of the high-resolution model outside this wavelength range to be flat with a constant radius. The flat regions of the model were set to the zero

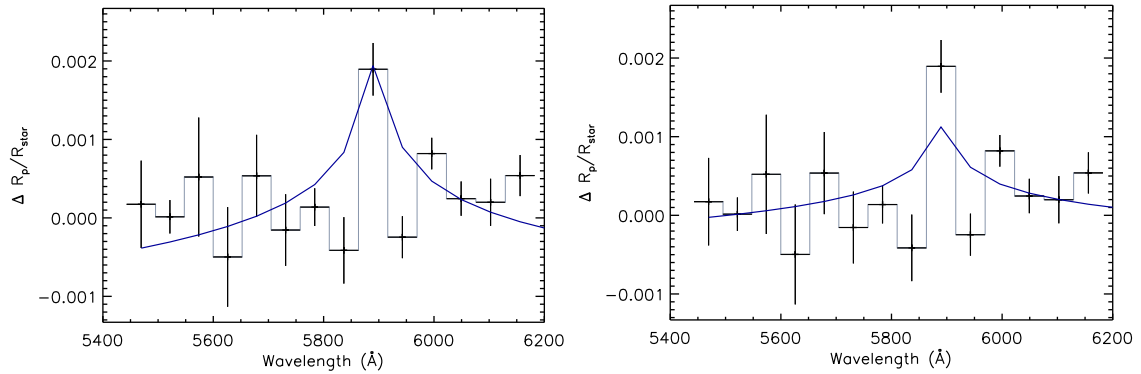


Figure 5.13: *Left*: The mean differential transmission spectrum from the R500R and R500B spectra around the sodium feature (black) overplotted with a model fit based on the formalism of Huitson et al. (2012) described in Chapter 4, assuming a haze/cloud free atmosphere at 800 K (solid blue line). *Right*: The mean differential transmission spectrum overplotted with the same model, but with the temperature as a free parameter.

reference level and fit with a free parameter, meaning that all regions outside the 12 Å feature have the same radius, which is allowed to move up and down relative to the sodium feature. This is equivalent to adjusting the height of the cloud deck/haze layer, or adjusting the sodium abundance at the lower altitudes probed by the sodium line wings. Additionally, the z_0 parameter is still free, allowing the model spectral profile to freely move up and down as a whole. The resulting fits are the same when this procedure is employed on both the analytic isothermal models from Huitson et al. (2012) and the numerical Fortney et al. (2010) models, as the narrow sodium feature is only detected in one 50 Å bin, providing no temperature information. The fit is shown in Figure 5.14. The best fit gives a $\chi^2 = 19.2$ for 12 DOF, which is a better fit than the standard models at the $3.5 - 4 \sigma$ level.

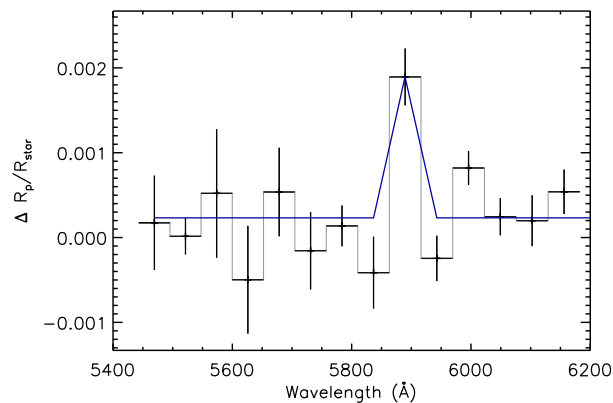


Figure 5.14: Fit assuming an unresolved feature narrower than 50 Å wide, either due to a cloud or haze layer obscuring the line wings or an abundance drop with increasing altitude. Fitted data points are shown in black, and the model is shown with a blue solid line.

Changing the width of the unresolved feature (wider or narrower than 12 Å) did not change the best fit, since the free parameter for the altitude of the line wings adjusted to compensate. Additionally, I tried adding a Mie or Rayleigh scattering cross-section to the sodium line cross-section in the isothermal models, to compare with the completely flat model, to try to distinguish between the two cases of an obscuring haze or a sudden abundance decrease from photo-ionization or condensation. I used the `BHMIE` IDL routine to compute the Mie scattering efficiencies. I then used various grain sizes and the optical properties of MgSiO_3 given by Lecavelier Des Etangs et al. (2008a) to determine the scattering cross-sections. I found that I could not differentiate with any significance between the cases of Mie scattering, Rayleigh scattering and an abundance drop, with the resulting χ^2 values only 1σ different. Changing the grain size changes the expected cross-section as a function of wavelength, so it is possible to fine-tune the grain size in the model to best fit the data. This method, however, would likely over-fit the data, and so the conclusion has to be that there is not enough information to decide between the different scenarios. Also there are other factors that affect the grain scattering efficiency, such as the optical properties of the grains and hence their real and imaginary refractive indices. Both condensation and ionisation have been inferred in hot Jupiter atmospheres (Sing et al. 2008b; Vidal-Madjar et al. 2011a), although in the case of XO-2b the expected T - P profile does not cross the condensation curve of Na I into Na_2S (Figure 5.15).

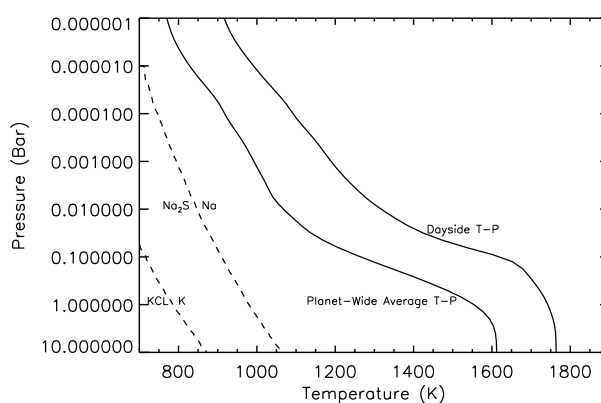


Figure 5.15: T - P profiles for the day side and global average atmosphere of XO-2b adapted from Fortney et al. (2010) shown with solid lines. Also plotted with dotted lines are the temperatures and pressures at which atomic sodium and potassium are predicted to condense out of the gas phase (Morley et al. 2012).

5.4.2 Comparison with Previous Observations of Potassium

I compared my spectral data and models to the photometric data taken with the OSIRIS tuneable filters in 2009/2010 around the potassium feature (Sing et al. 2011a). I fixed my analytic isothermal models to 1500 K to match the models in Sing et al. (2011a). The shape of the observed potassium feature suggests that there are visible K I line wings. However, the transmission spectrum around the sodium feature is not on an absolute radius scale and thus the two datasets can move up or down in altitude relative to one another, complicating the analysis. For example, a Rayleigh continuum slope with a λ^{-4} dependence could cover the wings of sodium but not potassium. Alternatively, the abundance of potassium could be more enriched relative to its solar value than the sodium abundance. By adjusting temperature, abundance in the lower altitudes (corresponding to the line wings) and haze or cloud altitude, any of the models can be consistent with the combined sodium and potassium data. Thus, the potassium data are not able to constrain the atmospheric properties further than the spectroscopic data alone.

5.4.3 Future Observations

In order to differentiate between the possible explanations of why the sodium feature is narrower than predicted by current models, it would be useful to resolve the doublet. Accurately measuring the shape of the absorption feature may enable observers to determine whether there is a specific region in the atmosphere where abundance of Na I drops (as in HD 209458b) or whether hazes or clouds obscure the Na I line wings (as in HD 189733b). Observations in narrower bands may also be able to place constraints on atmospheric temperatures and hence what species of condensates may be present in the atmosphere.

Assuming that the Na I doublet is only just unresolved at a resolution of 50 Å enables me to place a lower limit on the absorption depth in smaller bands. Assuming a 50 Å wide feature means that all of the absorption seen in the Na I feature is spread over 50 Å. If the feature is narrower, then the absorption will be concentrated in the narrower bands and the absorption depth in those bands will be even greater. The best fitting relative absorption depth in the Na I feature from the model is 37×10^{-5} compared to the continuum. The model value is lower than the measured absorption depth from the data, because the reference band in the model case is the best fit to the continuum absorption depth over the whole measured spectral range, which is not specific to the region just either side of the Na I doublet, and instead includes other wavelengths in the average. Using this value gives a predicted relative absorption depth of 60×10^{-5} in a 12 Å band using the isothermal model at 800 K, and 54×10^{-5}

using the full model from Fortney et al. (2010). If the feature is even narrower, then the absorption depth will be greater.

A minimum absorption depth of 54×10^{-5} in a 12 Å band means that the light curves for the reference and Na I bands must have a combined co-added precision of at least 1.8×10^{-4} for a 3 σ detection. Assuming that the signal-to-noise level is the same for each band (reference and sodium), this requires a precision of 1.27×10^{-4} for each band co-added over all exposures and all observations at that wavelength.

5.5 Conclusions

Absorption from the sodium Na I doublet was detected in the atmosphere of XO-2b at the 5.2 σ level using long-slit spectroscopy. This makes XO-2b the first extrasolar planet to have both atmospheric sodium and potassium detected, features which have both been long predicted for hot Jupiter atmospheres. While more data points are required to confirm the presence of K I line wings conclusively, the current observations suggest that the two detected features appear quite different, with absorption likely seen in the wings of the K I lines, but not in the wings of the Na I lines.

Such differences could be due to a difference in abundance of the two species, since Na I condenses out of the gas phase at higher temperatures than K I. Also, if potassium line wings are present in the transmission spectrum, it could rule out ionisation of sodium, because potassium should be ionised before sodium. XO-2b could also be another example of a hazy planet, or a planet with a high cloud deck. Rayleigh scattering by small grains could hide the absorption from sodium in the lower atmosphere, but leave the potassium line wings observable. If the grains do not vary much in size throughout the upper atmosphere, the scattering cross-section will be smaller at longer wavelengths, which is what has been seen in HD 189733b. None of these scenarios can be ruled out or confirmed with the two datasets. Low-resolution spectroscopy over the whole spectrum could confirm the presence of K I line wings, and place constraints on potential scattering species. Additionally, high resolution spectroscopy around the Na I and K I line cores can help constrain atmospheric temperatures and abundances.

The detection demonstrates the feasibility of using ground-based long-slit spectroscopy for detecting features in transiting extrasolar planets. While this analysis was limited to measuring differential transmission spectra due to slit losses, adopting wider slits should substantially increase the photometric precision and allow full broad-band transmission spectra to be obtained. A 10 arcsecond slit has now been constructed for the GTC for this reason, and Figure 5.16 shows preliminary results from that slit

for XO-2b, which shows great improvement over the previous light curves (A. Cabrera Lavers, priv. comm). The majority of the GTC survey will be able to make use of this new, wider, slit.

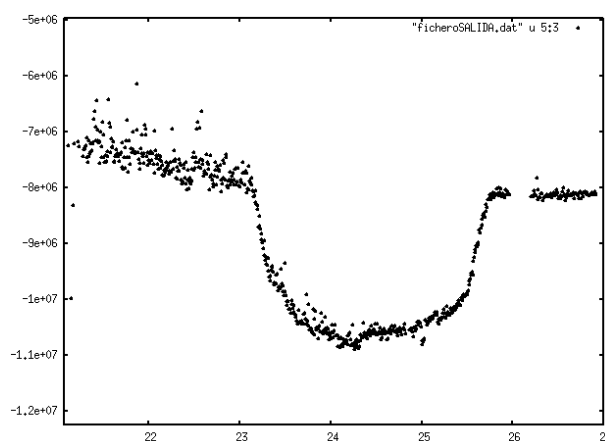


Figure 5.16: Preliminary GTC OSIRIS R500B white light curve of the transit of XO-2b from A. Cabrera Lavers (priv. comm), on an arbitrary flux scale, using the new 10'' slit. The start of the observation was at high airmass, and there was a specific instrumental problem towards the end, which resulted in a gap in the observations. However, the systematics have clearly significantly improved over the previous observations.

Of the well-studied planets so far, the emerging picture is far from simple, with the observations of XO-2b different yet again from those of HD 189733b and HD 209458b. The move towards comparative exoplanetology, of which this thesis is a part, is important in understanding current observations. Meaningful understanding of the causes of observed properties is only possible with a large sample. It will be very interesting to compare XO-2b to other planets as the survey continues.

Chapter 6

The First Results from the Optical HST Transmission Spectral Survey of Hot Jupiters

6.1 Aims and Introduction

Last year, the Exeter group was awarded 124 orbits of HST time to conduct transmission spectroscopy of 8 hot Jupiters over the entire optical to near-IR range (3000 Å to 1.7 μm, GO-12473, PI: D.Sing). The aims are to cover a sample representative of the hot Jupiter exoplanet class (with equilibrium temperatures ranging from 1000 to 2600 K) and look for broad trends and similarities. More specific goals are to determine the prevalence of clouds and hazes and look for signatures of stratosphere-causing molecules, to directly identify them. Specific features which can be detected are TiO, Na I, K I, Rayleigh signatures in the optical, and H₂O in the near-IR. The near-IR transmission spectrum can also place constraints on the planet's C/O ratio, which is useful in interpreting results at longer wavelengths (e.g. from *Spitzer*). This is the first space-based large sample of hot Jupiters to be studied homogeneously across the optical range. An existing survey provides near-IR data for most of the targets, with the Exeter programme obtaining additional near-IR data for those planets not covered. The results will be the complete optical to near-IR transmission spectra of all 8 planets at high precision, providing the first opportunity to begin comparative exoplanetology in conjunction with the GTC survey. The target list is complementary with the large GTC programme target list (only 2 targets are in both programmes), which, with the new 10 arcsecond slit, will also now be capable of producing very high precision observations. Table 6.1 shows the list of targets for the HST programme.

Name	Mass (M_{Jup})	Radius (R_{Jup})
HAT-P-1b	0.53	1.24
HAT-P-12b	0.21	0.96
WASP-6b	0.52	1.22
WASP-12b	1.36	1.79
WASP-17b	0.51	1.93
WASP-19b	1.13	1.39
WASP-31b	0.48	1.54
WASP-39b	0.28	1.27

Table 6.1: List of targets for the HST transmission spectral survey. Masses and radii are from <http://exoplanets.org/> and references therein [accessed 03-Sep-2013].

In this chapter, I present the first results of the HST survey: the optical to near-IR transmission spectrum of the hot Jupiter WASP-19b. WASP-19b has an equilibrium temperature of ~ 2000 K and so could be a possible candidate for upper-atmospheric TiO, which should be very obvious in the optical transmission spectrum but has not yet been conclusively observed. However, the star WASP-19 is very active, with chromospheric Ca II H & K line emission ratios of $\log(R'_{\text{HK}}) = -4.660$, compared to -4.501 for the active star HD 189733 and -4.970 for the inactive star HD 209458 (see Noyes et al. 1984, Knutson et al. 2010 and references therein). As shown by Knutson et al. (2010) it is possible that strong stellar activity breaks down the molecules responsible for causing stratospheres.

The strength of water features observed in the near-IR transmission spectrum can constrain elemental abundances but can also give an indication of potential cloud or haze cover. Prior to these observations, the transmission spectra of all planets observed in the near-IR had no or muted water features, suggesting some cloud or haze cover. It was unclear at the start of these observations whether a haze would be expected in the upper atmosphere of WASP-19b since it is not known whether the high altitude haze seen in HD 189733b has a photochemical origin, and what condensates could survive at temperatures above 2000 K. The results presented below show a planet unlike any previously observed, hinting at a large diversity in the hot Jupiter class which warrants further survey-style exploration. The results are published in Huitson et al. (2013).

6.2 Observations and Data Reduction

Three transits of WASP-19b were observed using HST STIS for programme GO-12473 (P.I. D. Sing), with two transits observed with the G430L grating (2900-5700 Å) and one transit observed with the G750L grating (5300-10300 Å). Details are shown in Table 6.2. I also analysed near-IR archival data from programme GO-12181 (P.I. D. Deming). One transit of WASP-19b was observed using the HST WFC3 in spectroscopic mode with the G141 grism (1.087-1.687 μm). The dates of the WFC3 observation are also given in Table 6.2.

Visit	Instrument Setup	Date of Observation (JD)
3	STIS G430L	2456047.584236 - 2456047.826377
4	STIS G430L	2456051.517847 - 2456051.769039
18	STIS G750L	2456057.041354 - 2456057.297512
WFC3	WFC3 G141	2455743.874347 - 2455744.105609

Table 6.2: Dates of the HST STIS visits (top three rows) and the archive WFC3 visit. This STIS visits are referred to by their visit numbers in following sections. As there is only one WFC3 visit, I do not refer to it by visit number.

Each STIS transit contains 38 spectra, with the first orbit containing 8 spectra and the three subsequent orbits containing 10 spectra, giving 10 in-transit and 28 out-of-transit exposures for each observation. Both gratings have a resolving power of $R = 530$, resulting in a resolution of ~ 8.1 Å at 4300 Å and a resolution of 14.6 Å at 7750 Å (the centre of the G750L band). The scale is ~ 2.75 Å per pixel for G430L and ~ 4.88 Å per pixel for G750L. The 1024×128 subarray was used to reduce overheads. Exposure times were 293 seconds with 21 second overheads.

The WFC3 observations used the 128×128 pixel subarray to reduce overheads. The dataset consists of 274 spectra, covering the wavelength range 1.087-1.687 μm with a scale of 0.00465 μm per pixel and a resolving power of $R = 130$. This gives a spectral resolution ~ 0.01 μm at 1.4 μm . Each exposure contains a zero read, then 4 non-destructive reads, with the first after 0.1 seconds and the next three every 7 seconds after that. Each exposure has a 19 second overhead. There are 70 exposures taken during the transit event. There is also one useable orbit before transit, which contains 70 exposures, and one after transit, which contains 70 exposures.

As with many past transit studies with HST, for both the STIS and WFC3 observations, I did not use the first orbit, since the HST thermally settles into its new pointing position during this time, and the systematics are considerably worse during this orbit (see Chapter 3 for more details). The data were bias-subtracted, dark-subtracted and flat-fielded using the `CALSTIS` and `CALWF3` pipelines. The data are not corrected with wavelength-dependent flat-fields in the pipelines. This can be a problem if a spectrum

shifts in the dispersion direction during the observation, meaning that a given pixel will not always be receiving the same wavelength in each exposure and as such its response may vary from exposure to exposure. However, by cross-correlating with the spectrum from the first exposure, I found that these shifts were sub-pixel over the whole transit for each observation.

For WFC3, both the `_ima` and the `_flt` files are corrected by the pipeline for non-linearity in the pixel response by fitting a 3rd order polynomial to the differences in counts per second between the non-destructive reads for each image. This is a potential problem for exposures with a small number of reads, since the fitting algorithm will be sensitive to noise. However, the values are fitted per CCD quadrant rather than per pixel, so any variation in the correction should be common-mode (see Chapter 5) rather than wavelength-dependent. There is a possibility of there being an offset in flux between the two halves of the spectrum if the spectrum is spread over two quadrants (as is the case for WASP-19b). However, the first and second reads are assumed to be in the linear regime, and hence are not corrected. I found that extracting the spectrum using the second read (with an exposure time of ~ 7.3 seconds and maximum count level of 10,560 DN, well within the linear regime) is very similar to the spectrum extracted using the final read, which contains a linearity correction. This suggests that the pipeline up-the-ramp fitting did not introduce any significant wavelength-dependent errors.

Cosmic rays were subtracted from the images using custom routines. Previous studies of the bright targets HD 209458b and HD 189733b with STIS used the whole timeseries per pixel to flag outliers which are significantly different in flux from the mean value for that pixel after correcting for the transit (e.g. Sing et al. 2008a, 2011b; Huitson et al. 2012, Chapter 3). WASP-19 is much fainter than HD 189733b (12.6 vs 7.7 V magnitude), meaning that, for this STIS data, much longer exposures were required to obtain enough counts for each measurement. Longer exposure times meant that the number of exposures per orbit in the WASP-19b data was nearly 3.5 times lower than for the HD 189733b observations detailed in Chapter 3. The smaller number of exposures per visit meant that the cosmic ray removal routines used previously were insufficient, since remaining outliers in the light curves dominated the transit fitting. A new routine was developed at Exeter, by N. Nikolov, which uses the difference image of one exposure compared to the next and compares this with a batch of exposures to detect transient events, with the drop in flux due to the transit also taken into account. Using difference images has the advantage of subtracting almost all of the stellar spectrum in the images that are analysed for cosmic ray events. The affected pixel values are then interpolated from the profiles of columns either side of the bad pixel. This is the procedure that I made use of, and more details about it are given in

Nikolov et al. (2013b).

Pixels flagged as bad by the HST pipeline were also interpolated over by using the same procedure as for removing cosmic rays for STIS. For WFC3, I also interpolated over pixels which had been marked by the pipeline as “unstable detector response” and “unstable zero value”. I discarded columns containing pixels flagged as “saturated”. Only the saturated pixels affected the spectrum by greater than 1σ . The reason for this is that the pipeline does not correct pixels that it measures to deviate from linear response by more than 5 % (the threshold for the “saturation” flag), and so these pixels then become very different in flux from the rest of the pixel values. Since a given pixel reaching this threshold does not occur for every exposure, this produces an effect that is both time dependent and wavelength dependent. I therefore neglected the columns containing saturated pixels altogether if they were saturated in even one exposure. Figure 6.1 shows the variation in electrons/second between the final two reads before and after removing saturated columns. Four columns show clear evidence of saturated pixels, which show up as dark horizontal bands, although 6 pixels in the spectrum were flagged by the HST pipeline as saturated and were omitted from the analysis (two of these were not saturated in many exposures and so are difficult to see in Figure 6.1).

Note that the difference in value between the pixels flagged as saturated in the final read and the previous read, shown in Figure 6.1, is not at the 5 % level (the largest difference between the second and final read is $\sim 3 \%$), suggesting that the pipeline flagged these pixels due to having only a small number of non-destructive reads per exposure and the fits being noisy, rather than the pixels being genuinely saturated. Since photon noise requires that I use large spectral bins for the final WFC3 spectrum, removing a small number of saturated pixels does not significantly affect the measurements. However, if one observed a brighter star and wished to use smaller spectral bins and hence all of the pixels, it may be worthwhile to re-run the WFC3 pipeline with the up-the-ramp correction omitted, as long as count levels are sufficiently low.

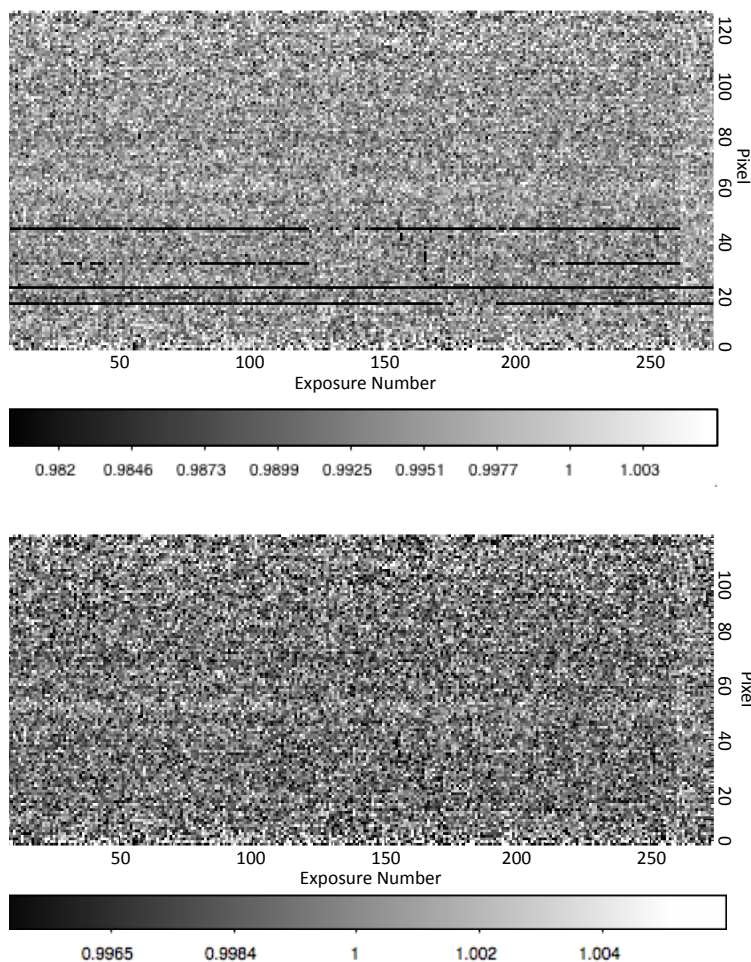


Figure 6.1: Residual plot of each spectral element in the final read divided by the same spectral element in the previous read, in counts per second for each exposure, including all the pixels (top), and after removing the columns with pixels flagged as “saturated” (bottom). On the vertical axis, increasing pixel numbers correspond to increasing wavelength, with the shortest wavelength being $1.087 \mu\text{m}$ and the longest wavelength being $1.687 \mu\text{m}$. The pixel scale is 46.5 \AA per pixel. The saturated regions are clearly seen as dark streaks corresponding to a low value of counts/second in the final read, where the pipeline has not corrected for the effects of non-linearity. The increase in flux with increasing exposure number in the final few exposures is due to the ramp effect (discussed in Section 6.4.1). Although visible by eye, the flux jump is beneath the white noise level when examined quantitatively. When using larger wavelength bins, the effect becomes more significant compared to photon noise, but is effectively removed by my de-trending procedures, and in the spectral light curves other trends become more important (Section 6.4.1). Furthermore, since the flux increase is time-dependent but not wavelength-dependent, relative transit depths as a function of wavelength (and hence spectral features) will not be affected.

After cosmic ray and flagged-pixel removal, the spectra were extracted using the IRAF APALL task. Transit light curves were produced by summing the photon flux over the full spectral range in each exposure. The spectral extraction was performed with and

without background subtraction, using a range of background regions and different polynomial orders of background subtraction. The extraction was performed using a large range of aperture sizes. The best aperture size and background subtraction were selected from measuring the white noise and the correlated noise in the out of transit exposures. For the low-cadence STIS observations, I used the out-of-transit standard deviation as a measure of noise. I used the `_flt` files and found the optimum apertures for spectral extraction to be 13 pixels wide.

For the WFC3 observation, I measured the correlated noise using the binning technique described in Pont et al. (2006) and Winn et al. (2008) as well as measuring the white noise. I extracted both the `_flt` and the `_ima` files, but used the `_ima` files for the analysis since the out-of-transit standard deviation was found to be lower than for the `_flt` files. The difference between the `_ima` and the `_flt` files is that the `_flt` files combine all the reads in an exposure to give a mean value of electrons/second in each exposure, rather than containing an image for each non-destructive read. It is likely that the increased noise in the `_flt` files is due to the high photon noise in the first and second reads being included in the average. The optimum aperture for the `_ima` files was determined for each non-destructive read. The optimum aperture size changes with different reads, as the source gets brighter on the detector, the significance of the wings of the PSF increases and a wider extraction aperture is needed for later reads. For the final read of each exposure, the best spectral extraction aperture was found to be 26 pixels wide.

I then tested further for possible residual non-linearity in the WFC3 data by checking for any pixels that deviated from photon noise significantly and which were not flagged by the HST pipeline. To do this, I divided the extracted spectrum from the final read of each exposure by that of the reads before, and then compared these differential values to the expected photon noise value. Figure 6.2 shows the results for each spectral element, where different colours in the image represent different exposures. A differential value higher than photon noise in a single exposure would indicate a random event such as a cosmic ray, whereas having a significant number of exposures showing noise above the photon level in one column would indicate a systematic effect in that column, which could be problematic (single events do not present a problem since the WFC3 light curve has a large number of datapoints per orbit). The five obviously deviant pixels in the plot correspond to five of the six pixels flagged by the pipeline as non-linear in at least one exposure (the 6th occurs in only one exposure and so is not flagged here). The four most prominent peaks correspond to the dark streaks seen in Figure 6.1. There was one column flagged as bad by my routine in addition to those flagged by the HST pipeline, which I also excluded from further analysis (in total removing 7 columns). It should be pointed out, however,

that this additional flagged point had an insignificant effect on the final transmission spectrum. The plot includes the first orbit. Variations in electrons/second between the two final reads were at the photon noise level once the saturated pixels were removed.

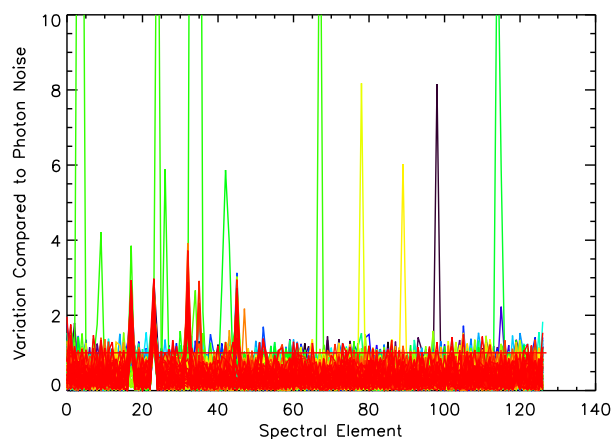


Figure 6.2: Extracted spectrum from the final read in counts/second divided by the extracted spectrum of the previous read in counts/second for each exposure, compared to the photon noise level for each spectral element. Shorter wavelengths are on the left and longer wavelengths are on the right. Each colour represents one exposure in the transit timeseries, and the plot includes the first orbit. Deviations from photon noise in a single exposure are cosmic rays or other random events and do not present a problem in interpreting the transmission spectrum since there are many datapoints in the transit light curves. Five columns can be seen where pixels clearly deviate from the photon noise level in many exposures. These correspond to pixels flagged as “saturated” by the WFC3 pipeline. One more pixel was also flagged by my routine which was not flagged by the HST pipeline, but excluding this column had a negligible effect on the transmission spectrum.

A final check was then made for non-linearity far from the saturation limit, which may not be so obvious with the methods above. According to the instrument manual¹, $> 5\%$ non-linearity (the threshold for the “saturation” flag) is observed with counts above 31,000 DN (or 78,000 electrons with a gain of 2.5), and I had saturation flags in 6 pixels of the spectrum. However, non-linearity begins at count levels of around 18,000 DN, well below this threshold, as shown by Hilbert (2009)². Figure 6.3 shows the brightest extracted spectrum in counts and counts per second for each non-destructive read except the first, both after removing columns with pixels flagged as saturated. The variations in counts per second between one read and another are at the photon noise level.

¹<http://www.stsci.edu/hst/wfc3/documents/handbooks/> [accessed 03-Sep-2013].

²Instrument Science Report WFC3 2008-39, available at www.stsci.edu/hst/wfc3/documents/ISRs/WFC3-2008-39.pdf [accessed 03-Sep-2013].

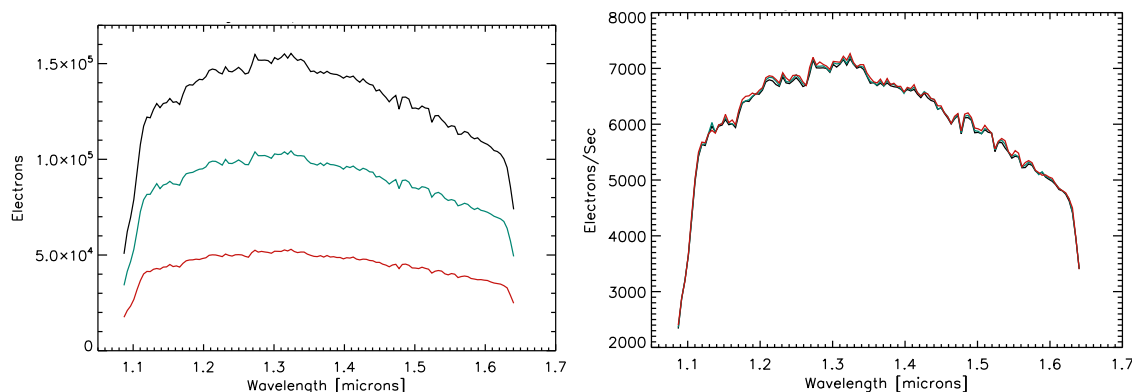


Figure 6.3: The brightest spectrum extracted using each of the 3 last reads in counts (left) and counts per second (right). The different reads are shown in different colours. These are the spectra summed over the whole 26 pixel wide aperture. Photon noise error bars are not plotted for clarity, but the difference in counts per second between any two reads does not exceed the photon noise level.

I used the extracted `_x1d` spectra from the `calstis` pipeline for the STIS wavelength solution (which was very similar to using a linear solution, with differences of the order 1 \AA). The wavelength solution for the WFC3 spectrum has to be calibrated from the direct image taken at the beginning of the observation. This means measuring the x and y position of the target in the image, and then locating what wavelength this corresponds to. The information of pixel location vs. λ_0 was taken from Kuntschner et al. (2009)³, which notes the different starting wavelengths for different pixel locations. The observer can then measure the number of pixels between the source in the direct image and the start of the spectrum on the detector in the spectral images to get the starting wavelength for the spectrum. The reference pixel from the direct image is at $\lambda_0 = 0.9005 \text{ \mu m}$, and the start of the spectrum is 40 pixels higher in the x (dispersion) direction. Using the scale of 0.00465 \mu m per pixel, a 40-pixel offset means that the spectrum begins at 1.087 \mu m . For the 128 subarray, the image is sometimes moved between the direct image and the spectrum to ensure that as much of the first order spectrum as possible lands on the subarray. I checked that this was not done by referring to the reference pixel information in the header.

³Instrument Science Report WFC3-2009-17, available at www.stsci.edu/hst/wfc3/documents/ISRs/WFC3-2009-17.pdf [accessed 03-Sep-2013]

6.3 STIS Analysis

6.3.1 Un-occulted Spot Correction

Figure 6.4 shows the white light curves for each STIS visit. Systematic trends over an orbital timescale due to the “breathing” effect described in Chapter 3 can clearly be seen, which are dealt with in Section 6.3.2. The transits firstly need to be corrected for stellar activity as WASP-19 is known to be a very active star, and the stellar flux varies significantly over time due to this activity.

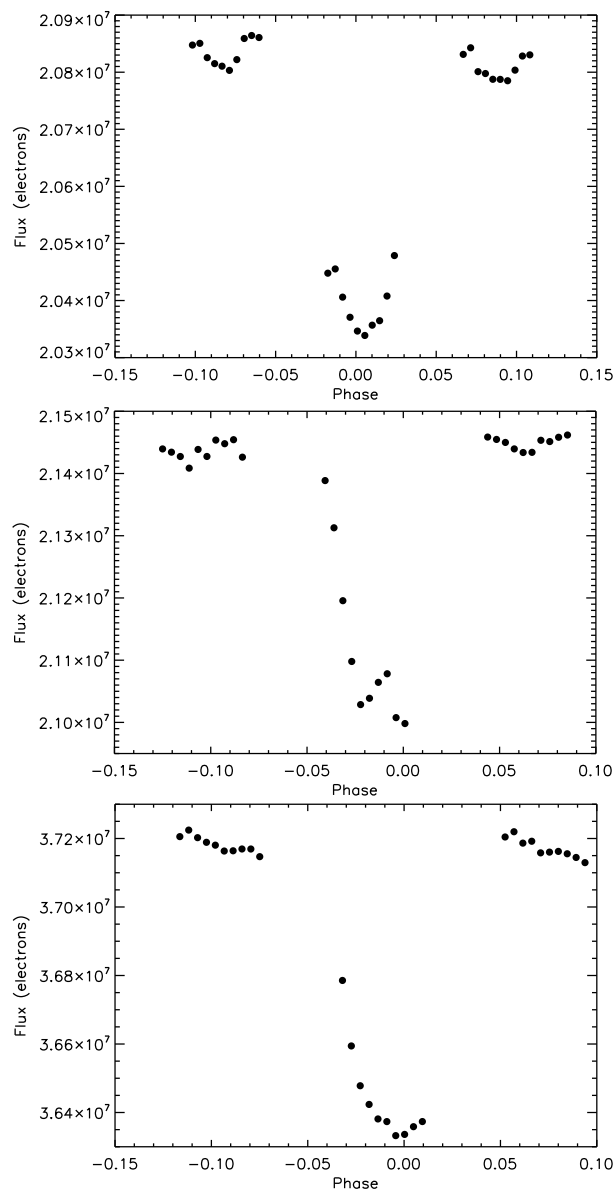


Figure 6.4: STIS white light curves before any correction for systematics, and before correcting for un-occulted starspots. From top to bottom: visit 3, visit 4, visit 18.

The stellar flux variations over time occur because the number of starspots on the surface of the star changes with time, and also, as the star rotates, spots come into and out of the view of the observer. Both of these effects cause the stellar flux to fluctuate quasi-periodically. The effects of dark stellar spots on the interpretation of planetary transits were discussed in Chapter 1, where un-occulted spots cause an overestimation of the planetary radius and occulted spots cause an underestimation of the planetary radius. The effect on the measured planetary radii is wavelength dependent because the stellar spots have a different temperature and spectrum from the non-spotted stellar regions, and this may affect the transmission spectrum if the number of spots on the stellar surface is large. The effect of un-occulted stellar spots needs to be accounted for before the planetary radii are fitted.

In Chapter 3, I was able to analytically measure the effect of starspots on the detected sodium feature by using the parts of the transits where starspots were obviously occulted. Such an analysis is not possible for WASP-19b, however, since there are no occulted starspots obviously visible in the red grating, and none of the points between 2rd and 3rd contact in either of the two blue visits are clearly free of starspot crossing signatures. It is therefore not possible to directly compare the spectra obtained from the spot-crossing exposures compared to the other exposures in a given transit as done for HD 189733b. Furthermore, I want to obtain absolute transit radii here rather than a differential measurement, which means also correcting for the absolute un-occulted spot level rather than just considering the wavelength-dependence of stellar spots on the transmission spectrum. I therefore use stellar models and stellar modelling to correct the transit light curves before they are fitted for planetary radius contrast.

Previous studies have done the correction after obtaining the transmission spectrum, but doing the correction beforehand slightly changes the shape of the limb darkened transit, since the limb darkening models assume a non-spotted star at the temperature of the non-spotted surface. I neglected the limb darkening of the spots, which should be negligible at my level of precision, and also did not consider the effects of bright active stellar regions. The extensive data on the HD 189733 system shows no significant effects of bright active stellar regions (Pont et al. 2013).

Variability Monitoring

WASP-19 was monitored from the ground for 135 days using the CTIO 1.3 m telescope with ANDICAM and the V filter (5400 Å with FWHM \sim 1200 Å), giving a light curve of flux over time with one exposure approximately every 2 days (programme 2011A-0209, P.I. D. Sing). The HST team then obtained a second season of monitoring with the same instrument, which covered a further 120 days, to better estimate the maximum stellar flux level (programme 2012A-0432, P.I. P.A. Wilson). The photometric data were reduced and analysed by P.A. Wilson, to give the resulting long-duration light curve (Figure 6.5). All three of the HST STIS transit observations took place during the first season of this monitoring. Since there are ANDICAM photometric data points very close to the transit observations, I simply used these photometric data points themselves to give the flux dimming values for the times of my transit observations, using the rest of the light curve to normalise these points.

All of the monitoring data were used to normalise the light curve after data points that were taken during transit events were removed. The flux values measured during the stellar monitoring need to be relative to the non-spotted reference level in order to be used to correct spectroscopic data. Assuming that there are always some spots on the stellar surface, the maximum flux observed during monitoring does not correspond to the non-spotted star. Aigrain et al. (2012) found that the non-spotted flux can be estimated as $F_{\star} = \max(F) + k\sigma$, where F is the variability monitoring light curve, k is a fitted value, and σ is the scatter of the light curve. They also found that $k = 1$ is a good value to use for active stars, based on data for HD 189733 and simulated test cases. I did not have enough data to further constrain the factor, so I fixed $k = 1$. To determine percentage dimming, I normalised the photometric measurements to $F_{\text{norm}} = F/F_{\star}$.

It should be pointed out that the number of starspots on the stellar surface can change over long timescales. Since the amount of dimming is obtained by normalising the monitoring light curve using its maximum flux value and scatter, observing over multiple seasons increases the accuracy of the spot corrections. Upon obtaining the second \sim 120 day season of variability monitoring for WASP-19b, re-analysis of the ANDICAM data caused the flux levels measured for the first season to change by \sim 0.6 – 0.9 %. Although this did not affect the relative radii determined (and hence spectral features) from the transits that occurred during the variability monitoring, their absolute level was affected by \sim 0.0004 R_{P}/R_{\star} for wavelengths around the ANDICAM V band. Although small, such an absolute correction could be larger if the stellar flux were observed for several years. Additionally, the effect will be larger in shorter wavelength bands. In comparing multiple datasets, variability monitoring is most useful if it is continuous throughout all transit observations, allowing the radii to be compared relative to one another on the same scale. Furthermore, the shift in normalised flux

level obtained when using the second monitoring season illustrates that longer-term monitoring is useful to accurately determine the non-spotted stellar flux level, F_{\star} , for example as done for HD 189733b (Pont et al. 2013).

Table 6.3 gives the dimming values corresponding to each of the STIS visits and Figure 6.5 shows the ANDICAM photometry along with a Lomb-Scargle periodogram⁴ showing a clear peak at 10.48 days, very close to the expected 10.5 day stellar rotation period (Hebb et al. 2010; Abe et al. 2013). The other significant peaks in the periodogram are likely due to noise in the data and are less than 2 days different from the main peak. With data sampled only every 2 days, I cannot draw any conclusions from these periodicities about possible spot configurations. I am not attempting to constrain the stellar periodicity here, but rather just to show that the variability monitoring photometry has the precision required to correct the STIS data for un-occulted stellar spots.

Visit	F_{norm}	Error
3	0.949	0.0014
4	0.964	0.0013
18	0.961	0.0014

Table 6.3: Values for the stellar fluxes as a fraction of the non-spotted flux, F_{\star} , for each STIS visit.

⁴Calculation of the probabilities of different periodicities in the data via Fourier analysis but modified to allow evaluation of data unevenly spaced in time. This method is equivalent to least-squares fitting of sinusoids. At a given frequency, ω , the height of the peak at this point, Y , gives the significance level of the peak: $P = 1 - (1 - e^{-Y})^n$. The value n is the number of independent frequencies inspected, and is roughly equal to the number of points for evenly spaced data and the number of ‘clumps’ for unevenly spaced data. It is included as a statistical penalty, since the probability of spurious peaks occurring increases with n (see Lomb 1976, Scargle 1982, Horne & Baliunas 1986 and Wall & Jenkins 2009 for more information). The Lomb-Scargle periodogram in this work was calculated using the `IDL` procedure `SCARGLE.PRO` written by J. Wilms.

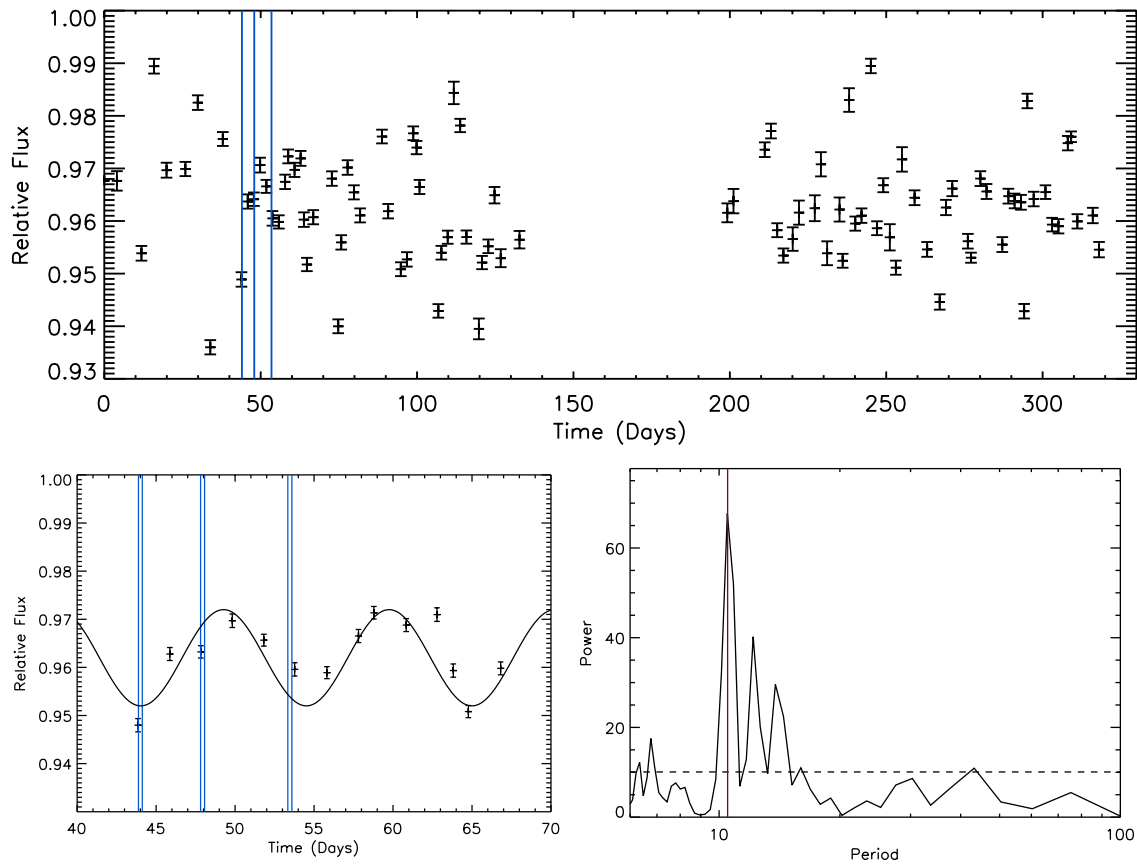


Figure 6.5: *Top*: ANDICAM variability monitoring data for both seasons, with all data points included, even those during transit events. The data are normalised to the assumed non-spotted stellar flux. Vertical (blue) lines show the starts and ends of the three STIS transits. The transits occur at days 44.0, 47.95 and 53.45, with a duration of ~ 1.5 hours. The Julian date of the first ANDICAM observation is 2456003.70253. *Bottom Left*: Zoom-in on the variability monitoring data around the STIS transits, with a sine wave overlotted with period of 10.5 days. The sine wave model is more simplistic than reality and it can be seen that the real photometry, and hence spot coverage, is more complex. Additionally, in the top plot, the amplitude clearly changes over periods longer than 10.5 days, most likely due to spot evolution. *Bottom Right*: Lomb-Scargle periodogram showing dominant periodicities in the variability monitoring data. A vertical (red) line shows the stellar rotation period of 10.5 days determined in the literature (Hebb et al. 2010; Abe et al. 2013), which matches well with the strongest periodicity observed in the ANDICAM data (10.48 days). Two other strong periodicities are seen, less than 2 days from the main peak, but these must be spurious because they are so close to the main peak. There are not enough data to detect longer period modulations at higher than 3σ confidence level (the dotted line shows the 99.8 % confidence level).

Correcting the Light Curves for Un-occulted Stellar Spots

I define the flux dimming correction at the variability monitoring wavelength as $\Delta f_o = 1 - F_{\text{norm}}$. So, for example, if the star is at 99 % brightness of the non-spotted flux, this is a 1 % dimming, or $\Delta f_o = 0.01$. The flux dimming at the V-band wavelength then has to be extrapolated to other wavelengths, since the brightness contrast of spots compared to the non-spotted surface will be more severe in the blue and less severe in the red because the spots are cooler than the non-spotted surface. This wavelength-dependent correction factor is derived by Sing et al. (2011b) as

$$f(\lambda, T) = \left(1 - \frac{F_{\lambda, T_{\text{spot}}}}{F_{\lambda, T_{\text{star}}}}\right) / \left(1 - \frac{F_{\lambda_o, T_{\text{spot}}}}{F_{\lambda_o, T_{\text{star}}}}\right), \quad (6.1)$$

where $F_{\lambda, T_{\text{spot}}}$ is the stellar flux at a temperature T_{spot} and at the wavelength of the transit observations, $F_{\lambda, T_{\text{star}}}$ is the stellar flux at a temperature T_{star} and at the wavelength of the transit observations, $F_{\lambda_o, T_{\text{spot}}}$ is the stellar flux at a temperature T_{spot} and at the variability monitoring reference wavelength (λ_o), and $F_{\lambda_o, T_{\text{star}}}$ is the stellar flux at a temperature T_{star} and at the variability monitoring reference wavelength. T_{spot} and T_{star} are the temperatures of the spotted and non-spotted stellar surface respectively. I use the models of Kurucz (1993) to determine the stellar fluxes at each temperature and wavelength as done by Sing et al. (2011b).

Therefore, the flux dimming correction at each wavelength becomes $\Delta f = \Delta f_o \times f(\lambda, T)$, for a given T_{spot} . Errors in Δf_o do not significantly affect the wavelength-dependence of the transmission spectrum, but rather the absolute baseline⁵ radius of the spectrum. For the wavelength-dependent correction, I set T_{spot} to be 5000 K, which seems to fit the occulted spot amplitude as a function of wavelength in the G430L data (see Section 6.3.3). The occulted spot temperatures were determined by splitting the G430L data into 5 bands and assuming that the occulted spot has a constant shape in each band and varies only in amplitude. I fitted for this amplitude in each band along with R_p/R_\star . However, the spot amplitude is very degenerate with fitting for the planetary radius and HST systematic trends, and so I discuss differences in the transmission spectra that could result from assuming different temperature spots in Section 6.5. The fits to the G430L data are discussed in Section 6.3.3. The factor $f(\lambda, T)$ varies from ~ 1.2 over the mean of the G430L band to ~ 0.82 over the mean of the G750L band for $T_{\text{spot}} = 5000$ K. The flux dimming Δf is then applied to each of the transits at each band, and then the radii are fitted. It is applied using the following method.

⁵Throughout this chapter, I use the word “baseline” to refer to the absolute R_p/R_\star level of a spectrum rather than the differential radius variation characteristic of the transmission spectrum. Thus, a shift in “baseline” does not affect the shape, wavelength and size of spectral features.

The observed flux of the star (when not being crossed by the planet) is

$$F_{\text{obs}} = (1 - \Delta f) \times F_{\star} \Rightarrow F_{\star} = \frac{F_{\text{obs}}}{(1 - \Delta f)}, \quad (6.2)$$

where F_{\star} is the true brightness of the star if it were unspotted. I need to know $F_{\star} - F_{\text{obs}}$, which is the flux dimming, so that I can add this value onto each exposure in the transit light curve. The flux dimming can be written as:

$$F_{\star} - F_{\text{obs}} = F_{\star} - (1 - \Delta f)F_{\star} = \Delta f \times F_{\star}. \quad (6.3)$$

I do not know F_{\star} explicitly, and so I write the dimming as a function of F_{obs} only:

$$\Delta f \times F_{\star} = \frac{\Delta f}{(1 - \Delta f)} F_{\text{obs}} \quad (6.4)$$

Finally, the correction was added to the transit in the following way:

$$y_{\text{corrected}} = y + \frac{\Delta f}{(1 - \Delta f)} \overline{y[\text{OOT}]}, \quad (6.5)$$

where $y_{\text{corrected}}$ is the corrected light curve, y is the original, uncorrected, light curve and $\overline{y[\text{OOT}]}$ is the mean of the out of transit exposures and should be equivalent to F_{obs} .

This model was tested on a non-limb darkened transit. A transit was produced using the analytical transit models of Mandel & Agol (2002) with all the limb darkening coefficients set to zero, and a fixed radius. The change in depth, $\Delta d/d$ should equal the flux dimming, Δf . I applied the un-occulted spot correction to the model transit, and then used the L-M least-squares technique, using the `IDL MPFIT` package (Markwardt 2009) to fit for the new transit radius. I tried several different values for Δf and in each case, the new fitted depth, $(R_p/R_{\star})^2$, was a factor Δf smaller than the starting depth (e.g. $\Delta d/d$ was 1 % smaller for an inputted Δf of 1 %).

6.3.2 De-Trending the STIS White Light Curves

The main systematic in the STIS light curves is the “breathing” effect discussed in Chapter 3 and by Brown (2001). The breathing effect was accounted for by fitting a 4th order polynomial dependence of the fluxes on HST phase simultaneously with transit depth. The fit also included a linear slope with time. The HST team scheduled the first exposure of each orbit to be very short (1 second) and I discarded this first exposure as well as the first orbit, due to problems with the first exposure of each orbit in the past (e.g. Sing et al. 2011b, Chapter 3). I used the L-M technique and the `IDL MPFIT` package, using the unbinned data to perform limb darkened transit fits. I also

found that fitting for linear dependences of the fluxes on x and y offsets of the spectra on the detector improved the fit, and improved the BIC. Higher order corrections with x and y offsets did not improve the BIC, and neither did higher order or lower order breathing corrections. Figure 6.6 shows the de-trended light curves and the residuals overplotted with the best-fitting transit models of Mandel & Agol (2002). I fixed the central transit time, orbital inclination, and a/R_\star to the parameters measured using the much higher cadence WFC3 data, which match well with literature values (see Section 6.4.2). The orbital parameters determined from free fits to the STIS data also match the literature values well within 1σ but have much larger error bars than the WFC3 parameters, most likely due to the lower cadence during the observations compared to the WFC3 dataset.

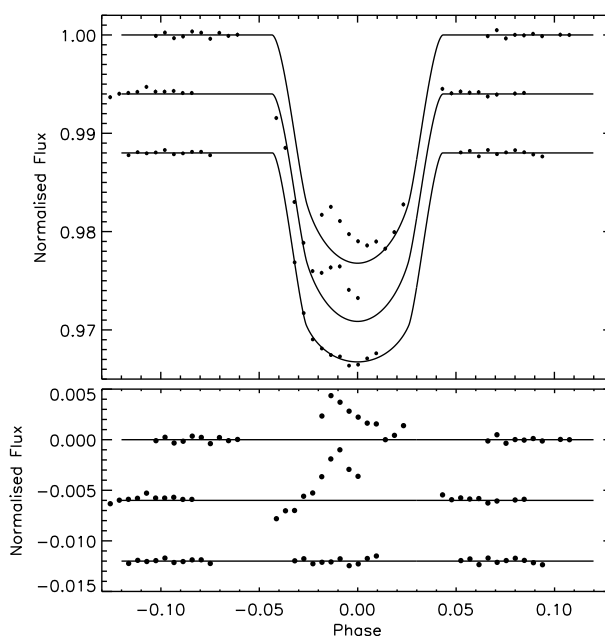


Figure 6.6: STIS white light curves after de-trending, overplotted with the best-fitting transit models of Mandel & Agol (2002). From top to bottom: visit 3, visit 4, visit 18. The two G430L light curves clearly show stellar spot crossings. Residuals are shown underneath in the same vertical visit order. The light curves and residuals have arbitrary flux offsets for clarity.

The two blue transits clearly show the occultation of starspots as ‘bumps’ in the light curves where the flux in transit is higher than the non-spotted model predicts. When performing the fits for the systematics, I did not include the points obviously crossing starspots. Starspot occultations can still clearly be seen in the residuals. For visit 4, the middle visit in Figure 6.6, the residuals drop below the predicted transit model during the start of ingress. Since the slope of data in ingress is different from the transit model, allowing the central transit time to be free did not allow this region to be fitted better by the transit models. Only a change in inclination or a/R_\star can

allow this region to be fitted well, but such a fit deviates significantly from the transit parameters measured using the WFC3 data and literature values. I conclude that this shape is most likely due to residual systematic trends. Although there is a possibility of the planet crossing a bright region on the star, such crossings have not been observed with the more active system HD 189733b (Pont et al. 2013) and I find in Section 6.3.3 that for 1000 Å spectral bins, these deviations from the expected transit model are not correlated with wavelength as would be expected for a bright spot crossing.

As in Chapter 5, I used the the Kurucz (1993) 1D ATLAS stellar atmospheric models and a 3-parameter limb darkening law of the form

$$\frac{I(\mu)}{I(\mu = 1)} = 1 - c_2(1 - \mu) - c_3(1 - \mu^{3/2}) - c_4(1 - \mu^2) \quad (6.6)$$

as described in Sing (2010). I used the closest match to the known information about WASP-19, with $T_{\text{eff}} = 5500$ K, $\log g[\text{cgs}] = 4.5$ and $[M/H] = 0$. I then fixed the limb darkening coefficients to the model values when fitting for planetary radii. The white light R_p/R_* value for the G750L light curve is measured to be 0.1402 ± 0.00053 . For this light curve, the residuals have a standard deviation of 2.4×10^{-4} and the best fit gives $\chi^2_{\nu} = 2.2$ and $\text{BIC} = 74$ assuming only photon noise uncertainties on the data points. Due to having no nonspotted points in the transits apart from during ingress and egress, I do not attempt to determine absolute radii for the two blue transits.

I do not know the variation in stellar brightness due to activity between my observations and previous observations. However, Table 6.4 shows that my measured G750L white light radius is in agreement with the R band literature value of Hellier et al. (2011). My measured radius ratio is larger than that measured by Dragomir et al. (2011), but smaller than those measured by Tregloan-Reed et al. (2013) and that measured in z band by Hebb et al. (2010). The lightcurves of Tregloan-Reed et al. (2013) were fitted with a transit model that includes occulted spots, but were not corrected for un-occulted spots due to there being no variability monitoring data available. All other literature radii are not corrected either for occulted or un-occulted stellar spots.

The maximum dimming observed at the ANDICAM monitoring wavelength of 5400 Å that does not coincide with a transit event is 5.7 %. Table 6.4 gives the dimming at each wavelength used in the literature that a 5.7 % dimming at 5400 Å corresponds to, calculated using Equation (6.1). The maximum dimming values for each wavelength quoted in Table 6.4 are the maximum overestimation of depth as a per cent of the measured depth due to dimming from un-occulted starspots. Apart from the measurements of Tregloan-Reed et al. (2013), occulted starspots may reduce this effect. Using the values given in Table 6.4 means that the radii could change relative to one another by up to $0.0035 R_p/R_*$.

Band	Radius	Reference	Maximum Flux Dimming (%)
G750L	0.1402 ± 0.00053	This work	4.7
z band	0.1425 ± 0.001	1	4.0
Gunn r	0.1407 ± 0.0043	2	4.9
Cousins R	$0.1342^{+0.0052}_{-0.0048}$	3	5.0
Gunn r	0.1435 ± 0.0014	4	4.9
Gunn r	0.1417 ± 0.0013	4	4.9
Gunn r	0.1430 ± 0.0008	4	4.9

Table 6.4: A comparison of the STIS G750L white light radius with literature values. The maximum flux dimming values are the maximum flux dimming observed during the WASP-19b variability monitoring at 5400 Å (5.7 %), scaled for each wavelength using Equation (6.1). Assuming that similar variations continue over long timescales, this constitutes the greatest dimming expected due to stellar spots. Literature references are: 1.Hebb et al. (2010), 2.Hellier et al. (2011), 3.Dragomir et al. (2011), 4.Tregloan-Reed et al. (2013). The three values from Tregloan-Reed et al. (2013) are from three transits observed only four days apart.

All the measured radii are consistent with one another within the limits of the unknowns on stellar variability and stated measurement uncertainties. It should also be pointed out that the differences in absolute radii between transits measured at different epochs could be even larger than the values quoted here due to long-term evolution of the number of starspots on the stellar surface. Alternatively, variations could be smaller, if observations are taken at similar periods in the variability cycle and the starspot configurations have not had long to evolve. Comparing the sample of measurements shows that the variation between the different datasets taken over a period of 2 years is indeed smaller than the maximum variation observed during the variability monitoring for the datasets that were not corrected for either occulted nor un-occulted spots. The difference between the radii observed by Tregloan-Reed et al. (2013) and Dragomir et al. (2011) is larger than the difference expected due to un-occulted spot variation, although the 1σ error bars of both observations overlap within the expected range.

The initial uncertainties on my fitted parameters are from a fit assuming photon noise uncertainties on the data points. I tried to scale the parameter uncertainties resulting from the fits with remaining red noise, by using the binning technique to determine σ_r and then re-scaling the fitted parameter uncertainties from the fits with β (Pont et al. 2006; Winn et al. 2008). As there are only 10 exposures per orbit for the STIS data, it is hard to estimate β for large bin sizes, and I find $\beta = 1$ for the G750L white light curve. For this reason, I was unable to re-scale the parameter uncertainties with red noise using this method. I also used the prayer-bead method to quantify how any remaining systematics could affect the measured transit depth and found that the

variances from the prayer-bead method were below the white noise level, indicating low levels of red noise.

Deviations from the ideal transit model are therefore on short timescales and act like white noise. In order to take into account residual white noise above the photon noise level, I re-scaled the parameter uncertainties in the fits by only β_w (Lendl et al. 2013). In other fits in this chapter, I do not always find $\beta = 1$, so in this case, I re-scale with $\beta_w \times \beta$. Note that if either β or β_w is less than 1, I set it equal to 1 to avoid any shrinking of the error bars. The value of β_w for the G750L white light curve was 1.68.

In case of unusual correlations between fitted parameters, I also tested re-scaling the photometric error bars in the fitted data with $\beta_w \times \beta$ rather than re-scaling the resulting parameter uncertainties from fits using photon noise error bars for the data. The results were equivalent, here and in all the other fits performed in this chapter, except when measuring the G430L transmission spectrum. Although the systematics of the STIS instrument are well-known and so the de-trending model can be considered reliable, I did also test that the choice of de-trending model does not significantly affect the transmission spectrum for the G750L data.

6.3.3 Optical Transmission Spectra

G750L

The spectra were split into 4 spectral bins $\sim 1000 \text{ \AA}$ wide, except the reddest bin, where the instrument response and stellar flux are lower, which was $\sim 2000 \text{ \AA}$ wide. The light curves were corrected for un-occulted spots in each band using Equation (6.5) and the Δf_o values corresponding to the measured stellar fluxes are given in Table 6.3. The wavelength dependent un-occulted spot correction is shown in Figure 6.7 for the STIS G750L wavelengths for different T_{spot} values ranging from 3500 to 5250 K, which is 250 K cooler than the non-spotted surface. I used the Kurucz (1993) model stellar spectra at different temperatures to work out the correction. The Δf spot correction values used for each G750L band are given in Table 6.5, assuming a spot temperature of 5000 K, with a non-spotted stellar surface temperature of 5500 K. The limb darkening parameters were fixed to the model values, and are given in Table 6.6.

Band (\AA)	Δf
5300 - 6300	0.037
6300 - 7300	0.033
7300 - 8290	0.030
8290 - 10300	0.027

Table 6.5: Spot correction factors used for each STIS G750L spectral band, assuming $T_{\text{spot}} = 5000 \text{ K}$. From Table 6.3, the value for Δf_o at the CTIO wavelength is 0.039.

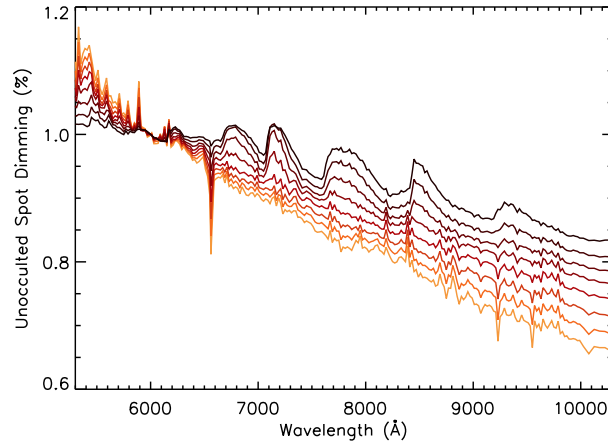


Figure 6.7: Model wavelength-dependent un-occulted spot dimming over the STIS G750L wavelength range for spot temperatures of 5250-3500 K in increments of 250 K, assuming a 1 % dimming at 6000 Å. Hotter temperatures are shown in lighter reds, with decreasing temperatures shown with darker reds. The stellar spectrum models are from Kurucz (1993).

Band (Å)	c_2	c_3	c_4
5300 - 6300	1.2332	-0.6132	0.1399
6300 - 7300	1.3703	-0.9688	0.2774
7300 - 8290	1.3557	-1.1067	0.3560
8290 - 10300	1.3514	-1.2060	0.4061

Table 6.6: Limb darkening coefficients from the Kurucz (1993) stellar atmosphere models used for each band in the STIS G750L transit light curve fits.

The transit radius was then measured for each bin. The inclination, a/R_\star and central transit time were fixed to the values measured from the WFC3 white light curve. I use the orbital parameters from the WFC3 white light curve since this represents the most constraining dataset that I have, and the derived values match well with those in the literature.

I fitted a 4th order polynomial function of HST phase to all orbits, including the in-transit orbit, at the same time as fitting for the transit depth and linearly-varying baseline flux. In the bands with the highest signal-to-noise, linear trends with x and y position of the spectrum on the detector could also be fit. It was determined separately for each band whether x and y correlations should be fit or not, by calculating the BIC. Higher order corrections than linear with x and y position were not justified in any of the bands. I also noticed a small quadratic trend with planetary phase. Fitting for this changed the measured planetary radii by much less than 1σ but increased the BIC, so the parameter was kept fixed to zero. In all cases, the systematic trends were fitted jointly with the planetary radius to enable covariances to be accounted for.

I do not see any distinctive occulted stellar spots in the G750L light curves. All the deviations from a flat line that are seen in the residuals do not behave like spots as a function of wavelength (they are not of greater amplitude in bluer wavelengths). Without being sure that a correlated trend is due to a spot there is no justification to treat it like a spot, and therefore I treated all remaining deviations in the residuals as noise (using the same method as for the white light curve, I used β_w to re-scale the parameter uncertainties from the L-M algorithm in each band, and the prayer-bead and binning techniques to test for red noise, finding $\beta = 1$ for all light curves). I checked that the choice of fitted model describing the systematic trends had an insignificant effect on the measured radii.

Additionally, in case small occulted starspots could affect the fitted parameters, I also tried using only the out-of-transit orbits to fit for the systematic trends. Once the fit to the out-of-transit exposures was performed, I fixed the parameters describing the systematic trends and then fitted the whole corrected light curve for only the planetary transit depth. I also tried using the “divide-out” method (described in Section 6.4), fitting for only a linear slope in phase and the planetary radius. The spectra from each method agree to well within 1σ .

I also tried binning the spectrum into only two bands (5300-7300 Å and 7300-10300 Å), and the results from this agree very well with the results from using 4 bands. Fitting the white light radius as a whole is consistent as well. This indicates that using 4 bands has not introduced any new systematics from having less signal in each band. There is fringing in the reddest part of the G750L spectrum on the CCD. The bands were chosen deliberately to lie between fringes, but a test using bands deliberately in the middle of fringes produced the same spectrum. It is likely that the effect of fringing on the transmission spectrum is negligible as I am using very large bins covering many fringe features.

I tried both cosmic ray removal routines; the ‘difference’ method described at the start of this chapter, and the original method of flagging outliers using the whole timeseries as used in Chapter 3. I found that both methods produced similar spectra, although the spectrum produced with the ‘difference’ method was marginally flatter. The variance from the prayer-bead method and the white noise in the light curves were both lower for the ‘difference’ cosmic ray removal routine, and so this is the routine that I adopted.

For the new (‘difference’) routine, I used a conservative 5σ clipping in the cosmic ray removal and compared this with the results from using a 3.75σ clipping. In other similar datasets of the large HST STIS programme, 3.75σ is the level where the residuals start to deviate significantly from Gaussian. For the WASP-19b dataset, the measured R_p/R_* value in the reddest bin changed the most, by $\sim 0.5 \sigma$, with the

extracted light curve looking noticeably less noisy when using 3.75σ clipping. Figure 6.8 shows the light curves determined from the 3.75σ cosmic ray clipping and Table 6.7 gives the corresponding radii. Figure 6.9 shows the resulting transmission spectrum for both clipping levels in the cosmic ray removal routine. It can be seen that the lower level clipping produces a marginally flatter spectrum than the higher level clipping, suggesting that un-removed cosmic rays can mimic spectral features in light curves with few exposures.

The measured radii were obtained by fitting the systematic trends and R_p/R_\star simultaneously. I also tried subtracting the white light residuals from each spectral light curve before performing any fits, to remove common-mode trends, but found no significant change in noise level, indicating that the most significant trends are not common mode over the observed large wavelength range.

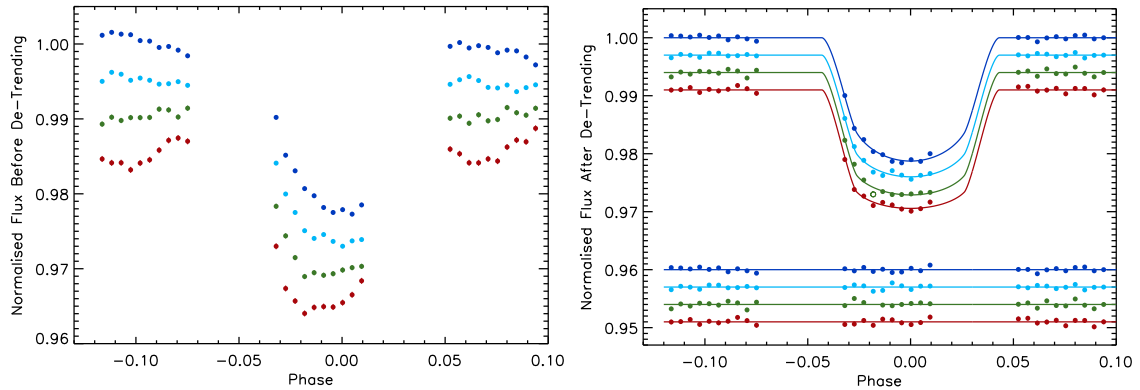


Figure 6.8: *Left:* Raw light curves for each of the G750L spectral bins, each normalised to their out-of-transit flux. The bluest bands are at the top and the reddest are at the bottom. Each light curve has an arbitrary flux offset for clarity. Wavelength-dependent trends as a function of HST orbital phase can clearly be seen. *Right:* De-trended light curves for each of the G750L spectral bins with the bluest at the top and the reddest at the bottom, overplotted with the best-fitting analytical transit models of Mandel & Agol (2002). Underneath are the residuals with bluest at the top and reddest at the bottom with arbitrary flux offsets for clarity. One $> 3\sigma$ outlier was clipped during the fit in the second reddest band (shown as an open circle), but the fit was performed again with this point not clipped and the measured R_p/R_\star value was not significantly affected. For all plots, photon noise error bars are shown and are within the point symbols.

Band (\AA)	R_p/R_\star	χ^2	σ_w	σ_r	β_w
5300 - 6300	0.1407 ± 0.0007	25.3	0.00028	0	1.4
6300 - 7300	0.1395 ± 0.0006	26.1	0.00027	0	1.5
7300 - 8290	0.1406 ± 0.0008	24.6	0.00033	0	1.4
8290 - 10300	0.1403 ± 0.0008	21.6	0.00036	0	1.2

Table 6.7: Fitted planetary radii with respect to stellar radius for each STIS G750L band. Red and white noise values were determined using the binning technique. The χ^2 values are based on the fits using only photon noise for the photometric uncertainties. Each fit has 18 degrees of freedom except the light curve where an outlier was clipped, which has 17 degrees of freedom.

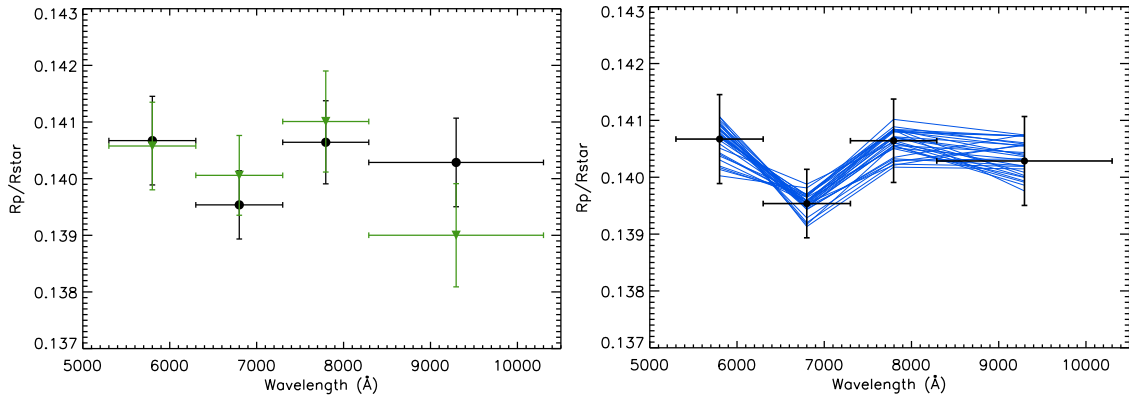


Figure 6.9: *Left:* STIS G750L transmission spectrum of WASP-19b. The black points show the spectrum extracted using 3.75σ clipping in the cosmic ray removal routine, and the green points show the spectrum extracted using 5σ clipping of cosmic rays. *Right:* Prayer-bead analysis for the transmission spectrum extracted using 3.75σ cosmic-ray clipping. The black points are the fitted transmission spectrum and each of the blue lines represents a simulated transmission spectrum from one of the prayer-bead loops. The variance suggests that the error-bars are well estimated.

G430L

I tried to construct the transmission spectrum in the G430L wavelength range, but the shape and the conclusions were significantly dominated by systematics due to the presence of severe occulted starspots. For this reason, I was not able to obtain the transmission spectrum of WASP-19b in the G430L wavelength range. It was possible to obtain the differential transmission spectrum for HD 189733b by measuring the shape of the spot in the white light curve and then fitting jointly for a spot amplitude parameter and the planetary radius in each wavelength (Chapter 3, Huitson et al. 2012; Sing et al. 2011b). However, fitting for the occulted spot amplitude was not possible for WASP-19b, as no exposures between 2nd and 3rd contact were “spot-free”.

Furthermore, the necessary low cadence for the WASP-19b observations presents a problem when trying to disentangle the effects of stellar spots, differential

planetary radii, systematic trends and any remaining low-level cosmic rays. I found that I could not construct a transmission spectrum because the measured planetary radii as a function of wavelength were very sensitive to the treatment of stellar spots, the de-trending model used, and to which exposures were used. Removing random single exposures from the transit changed the measured planetary radii by over ± 3 scale heights, which is larger than any spectral feature I hope to detect in a given band. The parameter for the amplitude of the spot was very degenerate with the R_p/R_* parameter in the fits. If I fit the data using the MCMC package `EXOFAST`, developed by Eastman et al. (2013), it reports linear Pearson correlation coefficients of $\sim 0.5 - 0.6$ for some bands. The high correlation values are most likely due to not having any non-spotted exposures between 2nd and 3rd contact to anchor the transit model, and so I cannot measure the departures from the non-spotted transit shape independently from the transit depth. To avoid unphysical results, I limited the radius variation across the wavelength range in the fits to 4 scale heights, which is the maximum predicted by current atmosphere models.

The correlation of the spot amplitude parameter with the HST-phase de-trending parameters was even higher than the correlation with fitted radius, with some linear Pearson correlation coefficients above ± 0.9 . To try to avoid the shape of the occulted spots affecting the de-trending for the structure of the systematics, I tried fitting only the two out-of-transit orbits for systematics and then fitting the transit and spot amplitude only, using the corrected light curve. However, it is still possible that the spot amplitude measurement could be affected by the instrumental systematics in each band. I re-scaled the photometric uncertainties with β and β_w and re-fit for parameters, rather than re-scaling the parameter uncertainties from fits assuming photon noise, because I found small differences between the two methods in this case.

Additionally, fitting the spot amplitude was not only very degenerate with fitted parameters, but also very sensitive to noise. Since the white light spot includes noise, so does the model for the spot shape. I therefore smoothed my spot shape with a Gaussian function before fitting it for amplitude in each band. Figure 6.10 shows fits to the spectral light curves using the spot shape from the data, with uncertainties scaled with $\beta \times \beta_w$. The light curves shown have been de-trended and so should only contain the transit and occulted spot shapes. Figure 6.11 shows the resulting spot amplitude parameter for each wavelength, and Table 6.8 gives the spot amplitude parameters for each wavelength band along with statistics of the fits. It is clear that, especially in the bluest bands, not all trends have been removed.

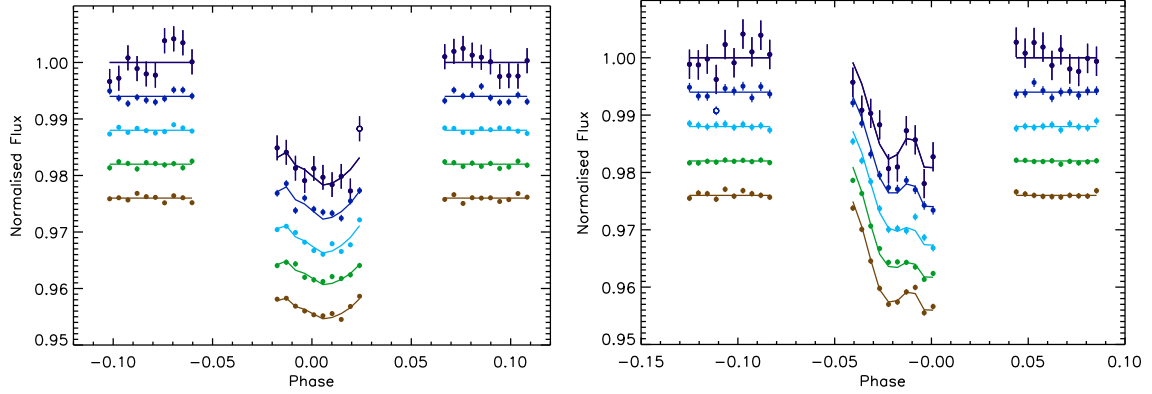


Figure 6.10: STIS G430L light curves for each spectral bin, going from shorter wavelengths at the top of each plot to longer wavelengths at the bottom of each plot, after de-trending. The left plot shows visit 3 and the right plot shows visit 4. The transit models including the occulted spot are shown with lines. The last point in the transit was not fitted in the bluest band of visit 3, and one outlier in the orbit before transit was not fitted for the second bluest band of visit 4. The points not fitted are shown with open symbols. The error bars on the individual data points have been re-scaled with $\beta \times \beta_w$ to show the level of uncertainty in the data due to noise above the photon noise level.

Band (\AA)	spot amplitude (%)	error (%)	σ_r	σ_w
2900-3700	2.15	0.75	0.0015	0.0017
3700-4200	2.10	0.21	0	0.00091
4200-4700	1.70	0.14	0	0.00060
4700-5200	1.56	0.16	0.00013	0.00050
5200-5700	1.31	0.13	0	0.00050
Band (\AA)	spot amplitude (%)	error (%)	σ_r	σ_w
2900-3700	1.58	0.48	0.00034	0.0023
3700-4200	1.11	0.11	0.00006	0.00075
4200-4700	0.74	0.12	0	0.00063
4700-5200	0.70	0.06	0.00009	0.00039
5200-5700	0.93	0.09	0	0.00049

Table 6.8: Fitted spot amplitude parameters for each band of G430L visits 3 (top) and 4 (bottom), where these are the relative amplitude values compared to the reference wavelength. Assuming a 1 % flux dimming at 6000 \AA , the spot amplitude parameters and errors are in units of %.

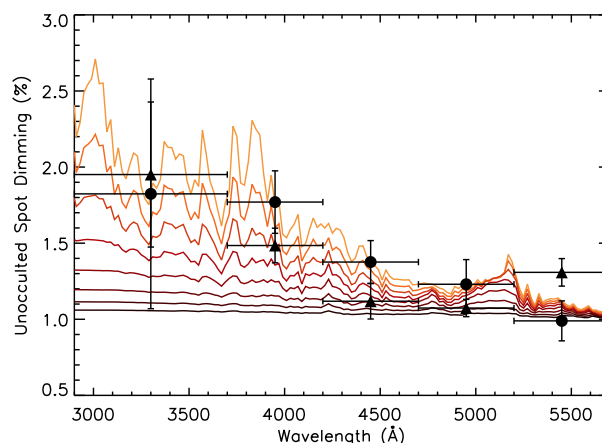


Figure 6.11: Model wavelength-dependent un-occulted spot corrections over the STIS G430L wavelength range, with measured occulted spot magnitudes as a function of wavelength shown as circles (visit3) and triangles (visit4). Horizontal error bars show the data bin sizes. The model spot temperatures range from 5250-3500 K in increments of 250 K. Hotter temperature spot models are shown in lighter reds, with decreasing temperatures shown with darker reds. The stellar spectrum models are from Kurucz (1993).

I fitted different model stellar spot spectra to the measured spot amplitudes using an amplitude offset constant across all wavelengths as a free parameter and using the weighted mean of the two datasets together. The fits suggest that higher spot temperatures in the plausible range of 5250-3500 K give the best fits, with the best fitting temperature being 5000 K and with the fit using the lowest temperature of 3500 K worse by 2σ . The fits using each visit individually gave results within ± 250 K of the value when using the mean of both visits. I found that the fitted spot magnitudes in each band were slightly different than when performing the fits using only photon noise uncertainties and re-scaling fitted parameters compared to re-scaling the photometric uncertainties, but the best fitting occulted spot temperature did not change.

I adopt a 5000 K temperature for all spots on the stellar surface for the rest of the analysis. The fits suggest that the spots are likely in the range from 4000-5250 K. Due to the presence of obvious remaining systematic trends in the blue light curves, I still consider the possibility of different temperatures in Section 6.5 and discuss the spectra resulting from assuming different temperatures for the un-occulted spot correction. Interestingly, a paper published after I completed this work found similar spot temperatures to the ones I obtained from the G430L data, with the authors finding plausible spot temperatures to be in the range 500-800 K cooler than the stellar surface from different photometric bands (Mancini et al. 2013).

I found a suggestion of higher transit depths in the G430L wavelengths compared to the G750L prediction. If I fixed the G430L radii to be at the measured G750L level, the fits were $\sim 2\sigma$ worse than allowing the fit radius to be free, which gave a deeper transit. Deeper radii could indicate spectral features, however they could also be the result of unseen occulted stellar spots in the G750L data. Since I see spot crossings in the G430L transits, I can account for them. In the redder wavelengths, spots that are not easily visible by eye are not accounted for except as a source of correlated noise and, if present, these can still make the measured planetary radii shallower. For this reason, and due to the dependence of the G430L radii on the detrending methods used and occulted spot amplitude as a function of wavelength, I do not draw any conclusions from the measured deeper transit radii in the blue.

6.3.4 Searching for Specific Optical Features

Differential Measurements

Since the spectral bins required in the optical transmission spectrum are large, it is possible that potential features could be washed out and that the atmospheric properties could be better constrained by searching for specific spectral features in narrow bands where signals are high. I looked for specific features using differential light curves, measuring differential transit depths between specific bands. Using differential light curves has the advantage that common-mode systematic trends naturally cancel out, meaning that detections could be more significant. For bands that are close together, this may provide an improvement over subtracting the white light residuals, since the systematics may be more similar in bands which are not very far apart in wavelength (as shown in Chapter 5).

I defined several indices, which are composed of a differential transit depth in an “in” band compared to the transit depth in an “out” band. The “in” band is composed of a wavelength or wavelengths where there should be significant excess absorption due to a specific spectral feature, while the “out” band is composed of a wavelength or wavelengths where the absorption is expected to be at the continuum level.

I defined two indices to look for the presence of TiO features. Firstly, I defined a “red edge” index to measure the very strong slope of decreasing planetary radius with increasing wavelength characteristic of TiO in red wavelengths. I refer to the differential transit depth measurement of two bands across this slope as $[\text{TiO}]_{\text{red}}$. Secondly, I defined a “comb”⁶ index, where the “in” band is comprised of many small bands corre-

⁶I use the word “comb” to refer to the comb-like shape of the many small TiO bandheads across the predicted visible transmission spectrum.

sponding to the locations of narrow features within the large TiO feature and the “out” band is comprised of bands between these narrow features. I refer to the differential measurement of the mean transit depth in the “in” band compared to the mean transit depth in the “out” band as $[\text{TiO}]_{\text{comb}}$. I restricted the TiO comb filter to the flat region of the broad TiO feature, to ensure that it is a separate measurement from the red edge measurement, and is not sensitive to spectral slopes.

I also defined bands around the alkali line features, with an “in” band centred around each doublet core and the corresponding “out” band composed of a band either side of this. I refer to the differential “in” minus “out” transit depth measurements as $[\text{Na}]$ and $[\text{K}]$ indices for the sodium Na I doublet and the potassium K I doublet respectively. I used a band either side of each alkali feature as the “out” band to avoid the measurements being skewed by any slopes in the spectrum.

All of the defined indices were then applied to theoretical models of WASP-19b both with and without TiO opacities and the model index values used to compare with the differential measurements from the data. The models are based on the formalisms of Fortney et al. (2010, 2008) and Burrows et al. (2010); Howe & Burrows (2012) and are described in Section 6.5.1. The wavelength ranges for each index and the predicted TiO-containing and TiO-free model values for the WASP-19b models are given in Table 6.9. I give the model values in units of scale heights so that more than one planet can be directly compared using the index measurements.

The models containing TiO have very similar values in my index measurements except for the $[\text{TiO}]_{\text{comb}}$ index value. The two models have different resolution, and it is reasonable to suppose that the contrast between small “in” and “out” TiO bands will decrease in a lower resolution model, which is the case. Additionally, there are differences between the TiO-free models. In my defined wide bands, the $[\text{Na}]$ and $[\text{K}]$ signals are smaller in the models based on Burrows et al. (2010); Howe & Burrows (2012) than the models based on Fortney et al. (2010, 2008). The reason for lower $[\text{Na}]$ and $[\text{K}]$ signals in the Burrows et al. (2010); Howe & Burrows (2012) models is that these models contain opacities that are not included in the models of Fortney et al. (2010, 2008), and which obscure the broad Na I and K I line wings. The reason for the $[\text{TiO}]_{\text{red}}$ signal being less negative in the TiO-free models of Burrows et al. (2010); Howe & Burrows (2012) than in the TiO-free models of Fortney et al. (2010, 2008) is the same, because the bands used for the $[\text{TiO}]_{\text{red}}$ measurement intersect with the potassium feature, which will cause a negative differential absorption depth measurement in a TiO-free atmosphere and a positive measurement in an atmosphere containing TiO opacities.

Band Name	[TiO] _{red}	[TiO] _{comb}	[Na]	[K]
“in” bands (Å)	6616 - 7396	5443 - 5543	5597- 6190	7280-8080
		5608 - 5700		
		5839 - 6002		
		6150 - 6348		
		6641 - 6929		
“out” bands (Å)	7396 - 8175	5346 - 5443	5300-5597	6880-7280
		5543 - 5608		
		6190-6486		
		5700 - 5838		
		6002 - 6150		
		6348 - 6641		
	6929 - 7046			
WASP-19b	-0.71 ^[1]	0.09 ^[1]	1.15 ^[1]	0.60 ^[1]
Model Value (no TiO)	-0.07 ^[2]	0.27 ^[2]	0.40 ^[2]	0.36 ^[2]
WASP-19b	1.75 ^[1]	1.39 ^[1]	-0.10 ^[1]	-0.60 ^[1]
Model Value (TiO)	1.71 ^[2]	0.82 ^[2]	0.10 ^[2]	-0.57 ^[2]

Table 6.9: Wavelength ranges for differential bands and predicted differential model values. The model values are in scale heights, where I take the scale height to be ~ 490 km for WASP-19b. The models are made specifically for WASP-19b, but using units of scale heights has the advantage that the model values will be similar between different planets of the same atmospheric type. Model values with [1] next to them are based on the formalism of Fortney et al. (2010, 2008) and model values with [2] next to them are based on the formalism of Burrows et al. (2010); Howe & Burrows (2012).

I also defined some indices in the blue G430L wavelengths to see if it was possible to distinguish spectral slopes characteristic of hazes from spectral slopes induced by the occulted spots using the differential method. However, the results that I obtained varied significantly (by ± 3 scale heights) for a given index depending on how I chose to treat the systematics. I therefore do not quote values from these data.

I measured the differential transit depths for each index by first normalising the light curve in each band to its out-of-transit flux, and then subtracting the “out” light curve from its corresponding “in” light curve. I corrected for differential limb darkening by using the Kurucz (1993) stellar models to predict the limb darkening coefficients for each wavelength, and found the differential limb darkening coefficients. These were then subtracted from the differential light curves. I then measured the differential absorption depth in transit compared to out of transit, as previously done for alkali line features (e.g. Chapter 3, Charbonneau et al. 2002). The differential light curves are shown in Figure 6.12 and Table 6.10 lists the results. I used the out-of-transit regions of the light curves to de-trend with remaining wavelength-dependent systematics based on time, HST phase and the position of the spectrum on the CCD. I found that de-trending using only a linear slope with time produced differential absorption depths that agree to within $\sim 6\%$ (less than $1/20\sigma$) with the results obtained using the

more complete de-trending model. Additionally, I tried fitting for the differential transit (one limb darkened transit minus the other) simultaneously with the systematics and found similar results with differences of less than $1/2\sigma$ for all bands other than sodium. The uncertainty on each mean “in” minus “out” value is the standard deviation of the differential light curve. For bands other than sodium, I found that fitting different models for the systematics gave similar results. Therefore, it can be assumed that white noise mostly dominates in the differential light curves.

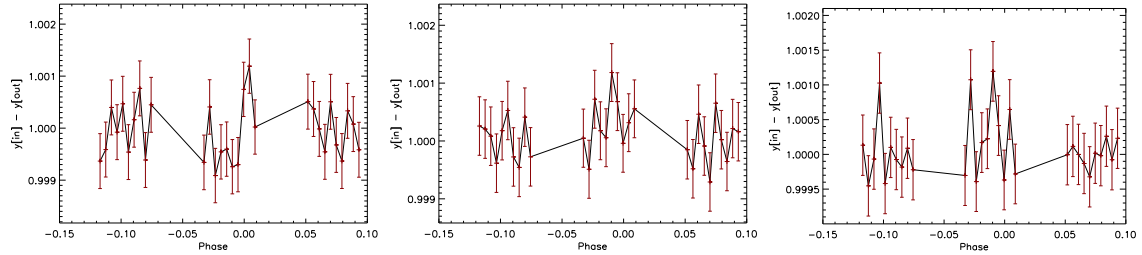


Figure 6.12: Differential light curves. *Left:* K minus continuum ([K]), *middle:* TiO “red edge” ([TiO]_{red}), *right:* TiO “comb” ([TiO]_{comb}). Each differential light curve is the “in” - “out” light curve + 1. Uncertainties on the data points are from photon noise.

Index	$\Delta z/H$	model $\Delta z/H$ value	
		TiO / no TiO [1]	TiO / no TiO [2]
[K]	0.71 ± 1.32	-0.6 / 0.6	-0.57 / 0.36
[TiO] _{red}	-1.73 ± 1.59	1.75 / -0.71	1.71 / -0.07
[TiO] _{comb}	-1.42 ± 1.37	1.39 / 0.09	0.82 / 0.27

Table 6.10: Measured differential absorption depth values scaled with scale height, H (where I take $H \sim 490$ km). Model values in column [1] are based on the formalism of Fortney et al. (2010, 2008) and model values in column [2] are based on the formalism of Burrows et al. (2010); Howe & Burrows (2012).

There was a more significant dependence on fitted parameters for the sodium feature, however, which indicates that wavelength-dependent systematics dominate in this band, and so I was not able to use this measurement. The measured [Na] value changed by ± 2 scale heights depending on the model chosen. It is well known that STIS exhibits wavelength-dependent breathing trends, which are worse at the spectral edges (e.g. Sing et al. 2011b). While I had hoped that the differential measurements would alleviate this problem to some extent by using bands relatively close together, it was not sufficient for the [Na] measurement. Wavelength-dependent trends clearly remain and the method of their removal significantly affects the differential [Na] measurement.

The $[\text{TiO}]_{\text{red}}$ and $[\text{TiO}]_{\text{comb}}$ measurements show a tentative lack of predicted TiO features, assuming solar TiO abundance. The $[\text{TiO}]_{\text{red}}$ measurement is 1σ away from the model values for a TiO-free atmosphere and 2σ away from both model values assuming an atmosphere with a solar abundance of TiO. The $[\text{TiO}]_{\text{comb}}$ measurement is 2σ away from the TiO-containing model value from Fortney et al. (2010, 2008) but only 1.6σ away from the lower resolution TiO-containing model value from Burrows et al. (2010); Howe & Burrows (2012). The $[\text{TiO}]_{\text{comb}}$ measurement is $1.1\text{-}1.2 \sigma$ away from the TiO-free atmosphere model values. The $[\text{K}]$ measurement is within 1σ of the TiO-free and TiO-containing model values, and as such the precision is not high enough to distinguish between the cases of whether the potassium feature is present or whether it is not.

It is possible that features in the transmission spectrum can change depending on the assumed stellar spot temperature, and hence assumed features in the stellar spectrum, meaning that any of the band measurements could be affected by which temperature I use for the un-occulted spot correction. I investigated possible spot temperatures in increments of 250 K from 5250 K to 3500 K, which is 2000 K cooler than the non-spotted stellar surface. I found that altering the spot temperature to the extremes of this range, from 3500 to 5250 K, affected the measured index measurements by ≤ 0.05 scale heights.

The Search for Alkali-Metal Features

The tentative lack of TiO features could suggest either a cloud or haze obscuring the predicted TiO features or an atmosphere free of clouds and hazes but where TiO is not present or under-abundant. In this latter case, the alkali lines should be prominent, and hence I conducted a more thorough search for the Na I and K I features, since the current measurements are inconclusive.

As the K I measurement appears more stable than the Na I measurement, I searched for the K I feature first. I tested whether the measured differential AD around the K I feature became stronger when using smaller “in” bands but retaining the same “out” bands as defined in Table 6.9 (a similar process to producing the IAD profiles in Chapter 3). Using an “in” band 50 \AA wide gave a differential radius of 2.0 ± 3.5 scale heights, while the corresponding model values were 3.0-3.4 scale heights. The measurement when using a 100 \AA width for the “in” potassium band is 1.9 ± 2.8 scale heights, where the corresponding model values were 2.1-2.8 scale heights. The differences between the model values as a function of “in” bandwidth used to measure the K I feature are within the uncertainties of the measurements, and so I cannot confirm or reject the hypothesis that K I is present in abundance in the upper atmosphere of WASP-19b. Figure 6.13 shows the absorp-

tion depths as a function of “in” bandwidth for various band sizes compared to model predictions.

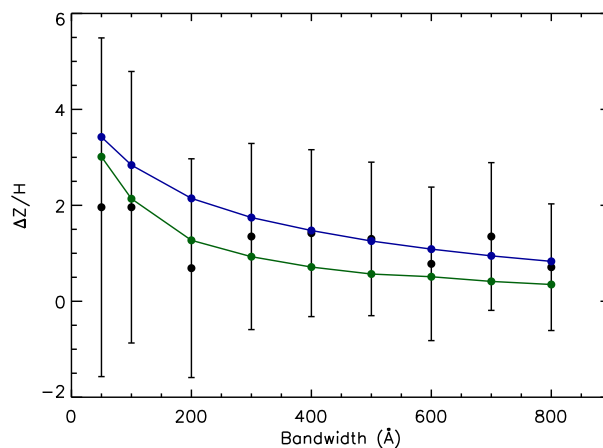


Figure 6.13: Differential AD measurements in the K I feature compared to the continuum for a range of “in” band sizes (shown as “bandwidth” on the x axis). The continuum band is the “out” band given in Table 6.9. Model values are shown with circles joined by solid lines (blue for the Fortney et al. (2010, 2008) models and green for the Burrows et al. (2010); Howe & Burrows (2012) models).

For the Na I feature, I initially investigated bands similar to those given in Table 6.9 in case the systematics seen previously were a function of the specific wavelengths chosen and changing the bands slightly might improve the stability of the measurement. The blue “out” of Na I band defined in Table 6.9 lies very near the spectral edge of the STIS response curve (see Figure 6.14). Therefore, I also tried to calculate the differential absorption in the [Na] index using smaller “out” bands. The results were very similar to using the full “out” bands. I tried using only the red “out” band also, but found that this still gave significantly different results depending on the de-trending model used. Therefore, the problem could be some sort of complex interplay between the systematics in the “in” and “out” bands. Since the measurements of differential AD in the sodium feature were so dependent on the choice of de-trending model used, I do not quote those values here.

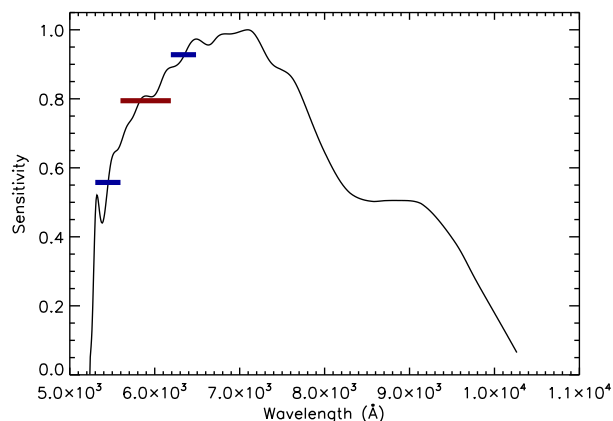


Figure 6.14: The “in” (red) and “out” (blue) Na I bands shown on a normalised response curve for the STIS G750L grating. The height of each band on this plot is equal to the mean sensitivity value within that band. The response curve was obtained from using a uniform illumination source along with the STIS exposure time calculator, available at <http://etc.stsci.edu/etc/input/stis/spectroscopic/> [accessed 03-Sep-2013].

However, I found that the spectrum around the sodium region was better behaved than the spectrum in the “out” bands, with the measured R_P/R_\star values changing less significantly than the differential measurement when varying the de-trending model. Figure 6.15 shows the behaviour of the measured planetary radius around the predicted Na I feature as a function of bandwidth, where the band is centred on the Na I doublet centre at 5893 Å. I find an R_P/R_\star value of 0.1383 ± 0.0032 in a 30 Å band centred around the Na I feature, where photon noise dominates. In a wider, 100 Å band centred around the Na I feature, instrumental systematics become more important and I obtain an R_P/R_\star value of 0.1359 ± 0.0019 (random) ± 0.0038 (syst). The difference between measured R_P/R_\star values is smaller than the measurement uncertainties. The corresponding difference in model prediction between the R_P/R_\star values binned over a 30 Å band and the R_P/R_\star values binned over a 100 Å band, both centred on the Na I feature, is 0.0004 to 0.0008 depending on the model. Figure 6.15 demonstrates that my uncertainties are too large to confirm or rule out the presence of the predicted Na I feature in the transmission spectrum of WASP-19b.

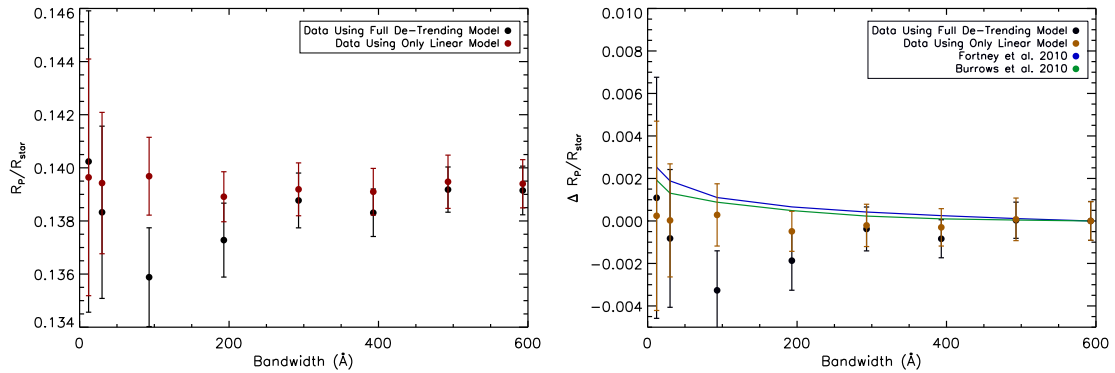


Figure 6.15: *Left:* R_p/R_{\star} values in bands centred around the Na I feature for a range of band sizes (shown as “bandwidth” on the x axis). Results from two different de-trending models are shown. The “full” model is that used for the wide bins in the transmission spectrum, and includes a 4th order polynomial of HST orbital phase, a linear baseline trend and linear offsets of the spectrum on the detector. The “linear” model includes only a linear baseline trend. *Right:* The same plot but normalised to the transit radius in a 600 \AA bin, showing that the radius variation as a function of bandwidth is similar for both de-trending methods. Model R_p/R_{\star} values are shown with solid lines (blue for the Fortney et al. (2010, 2008) models and green for the Burrows et al. (2010); Howe & Burrows (2012) models).

6.4 WFC3 Analysis

There was no variability monitoring taking place during the WFC3 observation. However, I can estimate the maximum degree to which the measured R_P/R_\star values can shift assuming that the flux of the star behaved in a similar way a year before the STIS observations. The maximum flux dimming in the ANDICAM V band (which does not coincide with a transit) is $\Delta f_o \approx 0.06$. Averaged over the WFC3 band, the wavelength-dependent scaling factor for flux variations is 0.46, assuming a spot temperature of $T_{\text{spot}} = 5000$ K (with the non-spotted surface having $T_{\text{star}} = 5500$ K). The resulting maximum flux dimming, and change in depth would be $\Delta f = 0.06 \times 0.46 = 0.0276$, assuming that the star's inherent brightness variations have not changed over the time between the WFC3 and STIS observations. The dimming, Δf , is equal to the change in depth, $\Delta d/d$, or $\Delta(R_P/R_\star)^2/(R_P/R_\star)^2$ so the change in the planetary radius is

$$\Delta(R_P/R_\star) \simeq \frac{1}{2} \Delta f (R_P/R_\star), \quad (6.7)$$

to first order (as also used by Berta et al. 2012, Sing et al. 2011b, Pont et al. 2013).

Assuming that the stellar activity has remained similar over the course of a year, the un-occulted spot correction is equal to 0.0138 (R_P/R_\star). The correction is probably an overestimate because it represents the maximum dimming observed during the monitoring for this project. Also, any occulted starspots which are within the noise in the measurements have the same level of effect on the radius measurement but in the opposite direction (they will make the transit appear shallower) even though they are not seen. This is common in the near-IR, as the spot amplitudes and photometric precision are both lower. Therefore, I do not correct for the effect of un-occulted starspots. The unknown stellar activity level during the WFC3 observations means that I am not able to place the planetary radii on an absolute scale, but I can still draw conclusions from the relative transit depths. The wavelength-dependent effect of starspots on the near-IR planetary transmission spectrum is discussed in Section 6.5.3.

6.4.1 De-Trending the WFC3 Light Curves

Figure 6.16 shows the raw white light curve for the WFC3 transit, which clearly shows an exponential-like ramp effect that occurs regularly every 20 exposures. Berta et al. (2012) suggest that the ramp trend could be due to charge trapping. Charge traps gradually fill up during one batch of 20 exposures and then are completely filled towards the end of the batch, causing the ramp to flatten off. After 20 exposures, there is a small delay before the start of the next batch, which could be due to a small instrument buffer dump, which would reset the charge traps.

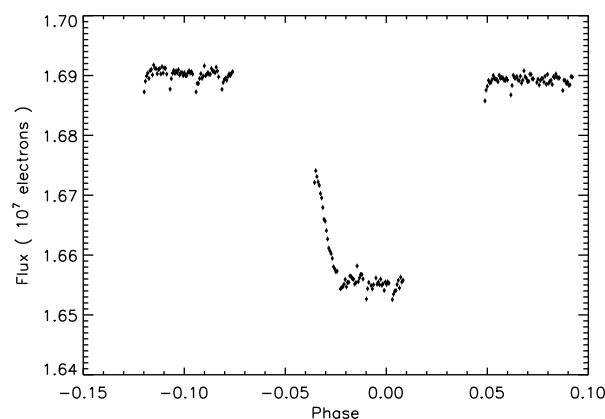


Figure 6.16: WFC3 white light curve before removal of systematics. Ramp effects can be seen to occur on a timescale of 20 exposures.

Firstly, I tried removing the systematics using the divide-oot method described by Berta et al. (2012), where a template is made using the mean of the two out-of-transit orbits and then each orbit is divided by the template. The divide-oot method works very well if the systematics are repeatable over each orbit. Apart from the ramp-like effect, I also see the temperature-based variations as a function of HST phase, as also seen in the STIS data. HST-phase trends should also be repeatable for each orbit and be removed using the divide-oot method. After performing the divide-oot method, I then fitted for the transit using the transit models of Mandel & Agol (2002) along with a linear slope as a function of planetary phase. Figure 6.17 shows the corrected white light curve with the transit fit, and the corresponding residuals. Again, I used the IDL MPFIT package. Parameter uncertainties were re-scaled for remaining red noise in the residuals using the binning technique and the β factor. No occulted spots are visible in the light curve and so I do not account for them in the fit. Any very small spots that are below the white noise level should not have a significant effect, and any remaining effects are treated as a source of red noise. The standard deviation of the residuals is 2.8×10^{-4} , which is dominated by white noise. The fit assuming photon noise uncertainties on the data points gives $\chi^2_\nu = 1.22$. Fitting also for any trends as a function of HST phase after performing divide-oot did not change the fit, but significantly increased the BIC. The large increase in the BIC indicates that such extra parameters were not justified in the model.

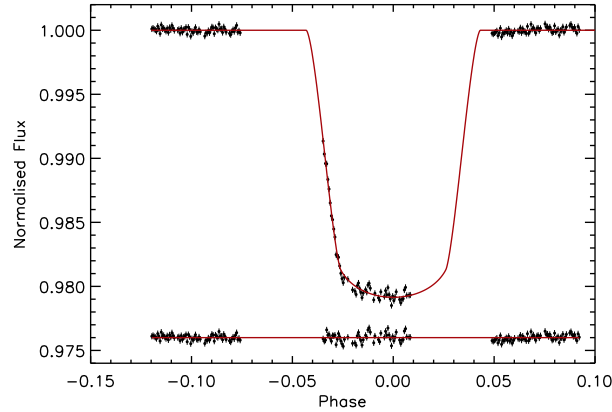


Figure 6.17: WFC3 white light curve after using the divide-out method. The transits are fitted with a linear slope in planetary phase and the transit models of Mandel & Agol (2002), after performing the divide-out method. Residuals are shown underneath with an arbitrary flux offset. The in-transit orbit has increased white noise from the divide-out method compared to the two out-of-transit orbits which make the template, but white noise should not affect spectroscopic results. Photometric uncertainties compared to baseline flux are higher after performing divide-out than for the raw light curve, because they include the uncertainty in each point of the template.

The divide-out method appears to remove the majority of the ramp effect, but I also tested whether I could remove the systematics by modelling the ramp with an exponential function of the form

$$F_0(a\phi_P + f(\phi_{\text{HST}}) + 1)(1 - be^{-(t-c)/\tau}), \quad (6.8)$$

where a , b and c are fitted constants, ϕ_P is the planetary phase, $f(\phi_{\text{HST}})$ is a 4th order polynomial of HST phase, t is the time of an exposure within a batch between ramps and τ is the timescale of the ramp (20 exposures). The first term deals with linear variations over a whole visit, the second term deals with orbital variations, primarily due to thermal breathing, and the last term deals with the ramp effect. I also fitted an exponential polynomial of the form

$$F_0(a\phi_P + f(\phi_{\text{HST}}) + 1)(1 - b_1e^{-(t-c)/\tau} - b_2e^{-2(t-c)/\tau} - b_3e^{-3(t-c)/\tau} - b_4e^{-4(t-c)/\tau}). \quad (6.9)$$

The results from both ramp models are less satisfactory than using the divide-out method, partly because each ramp in a given orbit does not have exactly the same shape (see Figure 6.18 for an example). I also tried simply removing the first 3 exposures in each batch and fitting a 4th order polynomial as a function of HST phase. This also was not as satisfactory as using the divide-out method, although not using these exposures along with performing divide-out was an improvement on including them. Table 6.11 shows the results of the different fits.

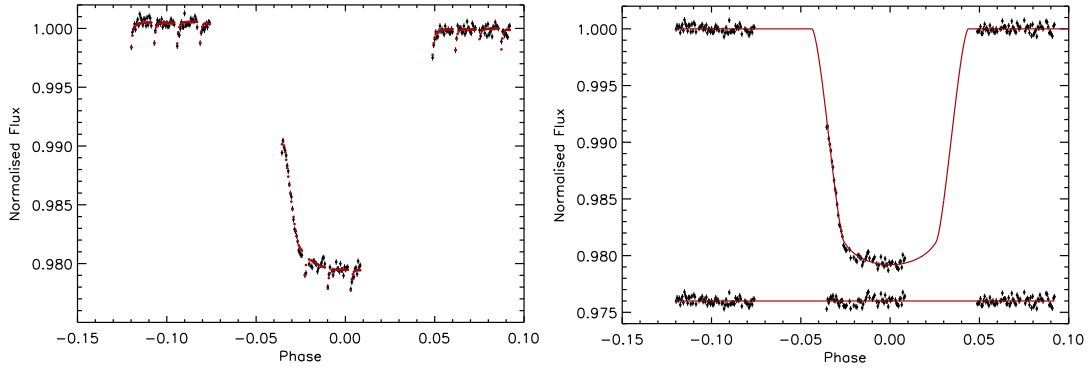


Figure 6.18: *Left*: Raw WFC3 white light curve overplotted with the best fitting exponential ramp model. *Right*: WFC3 white light curve after subtracting the systematics model overplotted with the best-fitting analytical transit models of Mandel & Agol (2002). The transit was fitted simultaneously with the systematics. Residuals are shown underneath with an arbitrary flux offset. The error bars look larger than in the un-normalised light curve, most probably because the determination of the baseline level flux is difficult in the presence of an inadequate systematics model (note that it is hard to see, but the error bars here are slightly smaller than when using the divide-out method).

Model	Fit First 3 points?	χ^2_v	BIC	σ_r ($\times 10^{-5}$)
Divide-out	no	1.22	280	6
Divide-out	yes	1.36	310	6
Exponential	no	1.79	350	6
Exponential	yes	1.85	409	11
Exponential polynomial	no	1.96	422	11
Exponential polynomial	yes	1.83	417	9
HST phase fit only	no	1.92	354	8

Table 6.11: Fitting statistics for different systematic removal methods for the WFC3 white light curve. The χ^2_v values are from using only photon noise as the uncertainties on the fitted data points.

Given that the statistics of the divide-out technique are better than the other models and the residuals appear flatter, I decided to use this method for analysing the planet's spectrum. However, I also produced the transmission spectrum using all of the other methods, and fitting only a linear slope in time with no other corrections, and found the same spectral features, simply with slightly larger error bars. The fact that different de-trending methods agree on the relative transit depths confirms the assumption that the systematics are very repeatable from orbit to orbit and hence do not significantly affect the relative transit depths.

6.4.2 System Parameters

The WFC3 data are of good enough quality to allow me to constrain the system parameters. The system parameters resulting from the L-M fit to the white light time-series are given in Table 6.12. I also measured the system parameters using EXOFAST, and these results are also shown in Table 6.12. Conversions between MJD and BJD_{TDB} made use of the online time utilities developed by J. Eastman⁷. I found that the two analysis methods produced similar results, although the value of a/R_{\star} was higher when fitting with EXOFAST. The discrepancy in the fitted a/R_{\star} value is most likely due to the fact that EXOFAST uses a quadratic limb darkening model free to vary within the stellar model grid and constrained by priors on the stellar properties; I was unable to use a 3-parameter model with fixed parameters, as I used with MPFIT. In addition, in EXOFAST the stellar parameters themselves are free to vary and are constrained by the Torres et al. (2010) mass-radius relation. The resulting parameters match well with those determined by Hellier et al. (2011), which are shown in the table also. The stellar radius and mass were given very tight priors in my EXOFAST fits based on the values quoted by Hellier et al. (2011).

Parameter	MPFIT	EXOFAST	Hellier et al. (2011)
i (deg)	79.8 ± 0.5	79.7 ± 0.6	79.4 ± 0.4
a/R_{\star}	3.60 ± 0.05	3.872 ± 0.16	3.60 ± 0.04
T_0 (BJD_{TDB})	2455168.96898 ± 0.0006	2455168.96843 ± 0.0019	2455168.96879 ± 0.00009
b	0.635 ± 0.02	$0.695^{+0.028}_{-0.03}$	0.657 ± 0.015

Table 6.12: System parameters for the WASP-19b system determined from the WFC3 white light curve compared with literature values. The red noise in the residuals when using EXOFAST was higher than when using MPFIT, which is why the error bars are larger. The larger correlated noise level is most probably the result of having to use quadratic limb darkening, affecting the shape of the fit.

⁷<http://astrutils.astronomy.ohio-state.edu/time/> [accessed 03-Sep-2013].

6.4.3 Near-IR Transmission Spectrum

The system parameters, i , a/R_\star and T_0 were fixed to the values found for the white light curve. The spectral timeseries was broken up into spectral bins $\sim 1000 \text{ \AA}$ wide. I then subtracted the white light residuals from each spectral light curve to remove common-mode trends. This reduced the red noise error bars on the measured radii but had no other effect on the measured spectrum. Once the white-light residuals were removed, the divide-out method was performed on each light curve. Each light curve was then fitted for R_P/R_\star and a linear trend over the whole visit. The raw and corrected light curves for each band are shown in Figure 6.19 along with residuals. Again, I see no clear occulted starspots, so I cannot justify correcting the spectrum for occulted starspots, and any remaining low-level occulted spots are treated as red noise. The limb darkening values are fixed to the model outputs, given in Table 6.13.

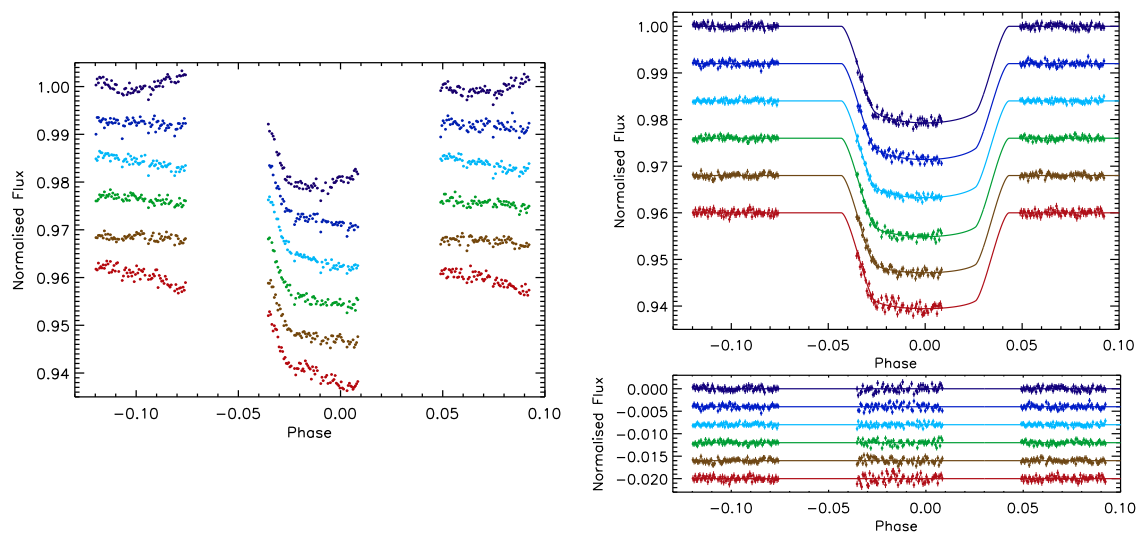


Figure 6.19: *Left*: Raw spectral light curves before performing divide-out, with each light curve normalised to its out-of-transit flux level. The bluest bands are at the top and the reddest bands at the bottom, with arbitrary flux offsets for clarity. The ramp effect in the spectral bins is less significant compared to white noise scatter than it was for the white light curve. Error bars assume photon noise and are within the point symbols. *Right*: Corrected spectral light curves overplotted with the best-fitting transit models from Mandel & Agol (2002). The bluest bands are at the top and the reddest are at the bottom, with arbitrary flux offsets for clarity. Underneath are residuals with the bluest bands at the top and the reddest bands at the bottom, with arbitrary flux offsets for clarity. For the corrected data and the residuals, error bars assume photon noise and also include the error in the out-of-transit template used for the divide-out procedure for each point.

Waveband (μm)	c_2	c_3	c_4
1.087 - 1.187	1.4098	-1.3968	0.48859
1.187 - 1.287	1.4080	-1.3847	0.48165
1.287 - 1.387	1.5450	-1.6282	0.58416
1.387 - 1.487	1.7834	-2.0855	0.79436
1.487 - 1.587	2.0182	-2.5803	1.0382
1.587 - 1.687	1.9108	-2.4396	0.9865

Table 6.13: Limb darkening coefficients for the WFC3 bands, from the Kurucz (1993) stellar atmospheric models.

The resulting transmission spectrum is shown in Figure 6.20. The fitted R_p/R_\star values are given in Table 6.14. I also tried bins of 500 and 250 Å and also tried shifting these bins by half the bin size. The resulting spectra were very similar, but considerably noisier due to the dominance of photon noise in smaller bin sizes. The errors on the fitted R_p/R_\star values are the parameter uncertainties from `MPFIT` based on a fit using photon noise uncertainties for the data points, scaled to include remaining red noise by β . I find that the standard deviation of the white noise is at the photon noise level, so I did not also re-scale the parameter uncertainties with white noise. As a final check for any remaining non-linearity, I also extracted the spectrum using the middle two reads, where the number of counts per exposure are within the linear regime, and the resulting spectra agree to well within 1σ with the spectrum extracted from the final read.

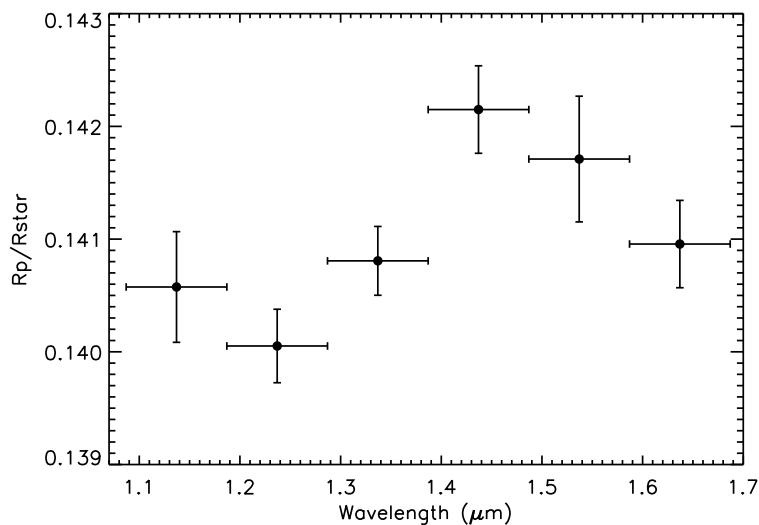


Figure 6.20: Transmission spectrum of WASP-19b from WFC3 G141. Errors are from a fit based on photon noise uncertainties on the individual exposures, with fitted parameter uncertainties scaled with β .

Waveband (μm)	R_p/R_\star	χ^2	DOF	σ_w	σ_r	β
				($\times 10^{-4}$)		
1.087 - 1.187	0.1406 ± 0.00049	153	201	5.4	1.3	1.41
1.187 - 1.287	0.1401 ± 0.00033	202	198	5.5	0.7	1.05
1.287 - 1.387	0.1408 ± 0.00031	93	201	3.7	0	1.00
1.387 - 1.487	0.1421 ± 0.00039	172	201	5.0	0.9	1.27
1.487 - 1.587	0.1417 ± 0.00056	136	201	4.7	1.5	1.68
1.587 - 1.687	0.1410 ± 0.00039	207	202	6.9	0.3	1.02

Table 6.14: R_p/R_\star values for the WFC3 transmission spectrum of WASP-19b. Uncertainties on fitted parameters are based on using photon noise for the photometric errors in the fits and then re-scaling the fitted parameter uncertainties with β . The red noise, σ_r , white noise for the unbinned data, σ_w , and the scaling factors, β , are also listed along with fitting statistics. Note that, for β values less than 1, I set $\beta = 1$ so that there is no scaling of parameter uncertainties.

6.5 Discussion

The transit depths of the spectra for the two different datasets (STIS and WFC3) are measured at different times, and so will not be on the same absolute scale as one another because the stellar brightness will be different at the two epochs by an unknown amount. Un-occulted starspots could cause the near-IR R_p/R_\star values to be overestimated by up to 1.38 % relative to the optical data, assuming a spot temperature of 5000 K and non-spotted stellar surface temperature of 5500 K, and assuming that the un-occulted spot correction is accurate for the STIS radii. I also have to assume no significant changes in stellar variability amplitude between the times of the two observations. Unseen occulted spots could reduce this effect.

For the STIS spectrum, there are uncertainties in the un-occulted spot correction through uncertainties in Δf_0 and uncertainties in the spot temperature. There is also an uncertainty on the estimated value of the non-spotted stellar flux. The error in Δf_0 and the non-spotted stellar flux will alter the planet's effective baseline radius, and will not significantly change the shape of the transmission spectrum (relative R_p/R_\star as a function of wavelength). From Table 6.3, the errors in Δf_0 translate to errors of less than 0.1 % on the absolute R_p/R_\star values. Uncertainty in the spot temperature will change the shape of the spectrum by altering its slope as a function of wavelength and, due to features in the stellar spectra, could affect the measured planetary atmospheric spectral features. I discuss the effects of uncertainty in assumed un-occulted stellar spot temperature on the STIS results in Section 6.5.2.

For the WFC3 spectrum, the un-occulted spot corrections are less severe, and to some extent may be cancelled out by small occulted spots below the noise level. I am not able to correct for this effect, but expect that differential water features between the stellar spots and the non-spotted surface will be washed out to insignificant levels in my large wavelength bins, meaning that water features in the transmission spectrum will not be significantly affected. Figure 6.21 shows the un-occulted spot dimming over the G141 wavelength range for different temperature spots using the models of Kurucz (1993). These grid models are at low resolution and do not display all the lines present in the stellar spectra, and I discuss the potential of contamination of measured water features in transmission by un-occulted stellar spots in Section 6.5.3.

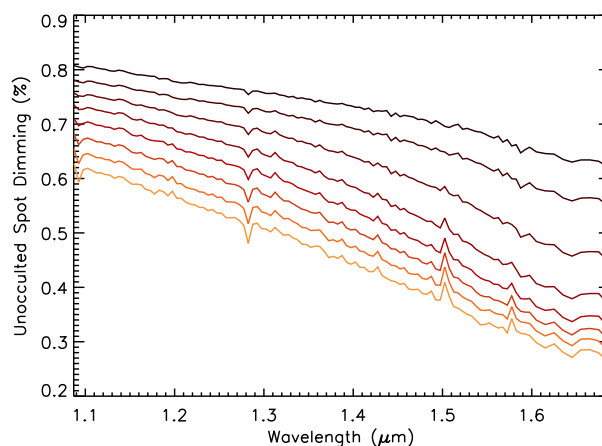


Figure 6.21: Model wavelength dependent un-occulted spot dimming over the G141 wavelength range for spot temperatures of 5250-3500 K in increments of 250 K, normalised to 1 % at 6000 Å. Hotter temperatures are shown in lighter reds, with decreasing temperatures shown with darker reds. The stellar spectrum models are from Kurucz (1993).

As the stellar activity level during the WFC3 transit is not known, the two transmission spectra cannot be joined together to make a single spectrum without an unknown correction in the relative baseline planetary radii of up to 1.38 %. I therefore now draw conclusions from the individual datasets alone, and then use these conclusions together to try to understand the planetary atmosphere.

6.5.1 Optical to Near-IR Transmission Spectrum of WASP-19b

I compared two different sets of models to both datasets; one set based on the formalism of Fortney et al. (2010, 2008) and the other set based on the formalism of Burrows et al. (2010) and Howe & Burrows (2012). In order to compare these different models to the data, I used the pre-calculated models given to me by these authors, allowing them to shift up or down to match the data, with the base radius as the only free parameter. It is important to use more than one set of models since different model

sets have been calculated using different methods and not all models in the literature agree (see Shabram et al. 2011 and Chapter 1).

Both the models from Fortney et al. (2010, 2008) and the models from Burrows et al. (2010) and Howe & Burrows (2012) are specifically generated for the WASP-19 system. Both model suites are self-consistent, meaning that the T - P profile used to calculate each model is consistent with the opacities in the model transmission spectrum (for example, transmission spectra containing TiO and VO opacities will have a T - P profile which has a stratosphere). They are also in radiative, chemical and hydrostatic equilibrium. Both sets of model transmission spectra use 1D day-side T - P profiles, which should dominate the transmission spectrum at the terminator. The models include stellar irradiation with a small fraction of energy lost to the un-modelled night side. The T - P profiles used to calculate the model transmission spectra are shown in Figure 6.22.

Chemical mixing ratios and opacities for both model sets assume solar metallicity and local chemical equilibrium accounting for condensation and thermal ionisation but no photoionisation. The models of Fortney et al. (2010, 2008) use the opacity databases and abundance information of Lodders (1999); Lodders & Fegley (2002); Lodders (2002); Visscher et al. (2006); Lodders (2009); Freedman et al. (2008). The models of Burrows et al. (2010) and Howe & Burrows (2012) use the opacity database from Sharp & Burrows (2007) and the equilibrium chemical abundances from Burrows & Sharp (1999) and Burrows et al. (2001).

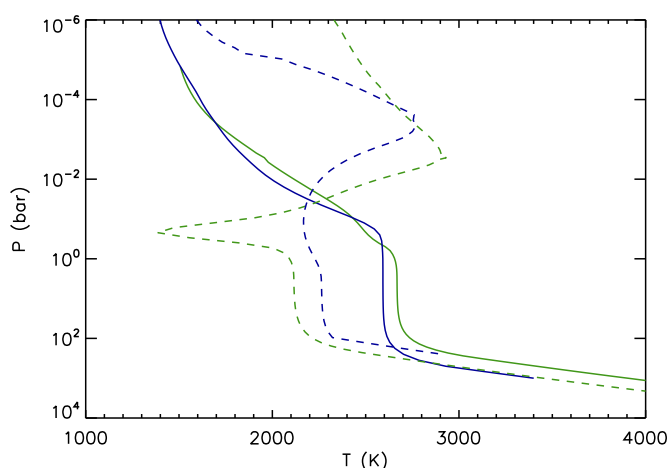


Figure 6.22: Model T - P profiles used in the calculation of the model transmission spectra, for atmospheres containing no TiO and VO (solid lines) and atmospheres with a solar abundance of TiO and VO (dotted lines). Blue lines show the models of Fortney et al. (2010, 2008) and green lines show the models of Burrows et al. (2010); Howe & Burrows (2012).

6.5.2 Optical Transmission Spectrum

The STIS radii are consistent with a flat spectrum (I found $\chi^2 = 2$ for 3 DOF when fitting a flat line to the spectrum), but the predicted alkali line features in the G750L wavelength range are smaller than the observational error bars. Using TiO-free models fitted with an offset in baseline R_p/R_\star gave $\chi^2 = 1.0$ – 1.7 for 3 DOF depending on the model used. Using models with solar-abundance TiO opacities obscuring the alkali lines, again with a fitted R_p/R_\star offset, gave $\chi^2 = 9.1$ – 9.4 for 3 DOF, suggesting a lack of observed TiO features at the 2.7 – 2.9σ level. The data and fitted models are shown in Figure 6.23. The only free parameter in the spectral model fits was an absolute shift in R_p/R_\star , with the shape of the spectrum as a function of wavelength not varying. Tests assuming spot temperatures of 3500 K and 5250 K instead of 5000 K to fit the spectral light curves gave very similar results, suggesting that my choice of spot temperature did not significantly affect the spectral shape and measured features.

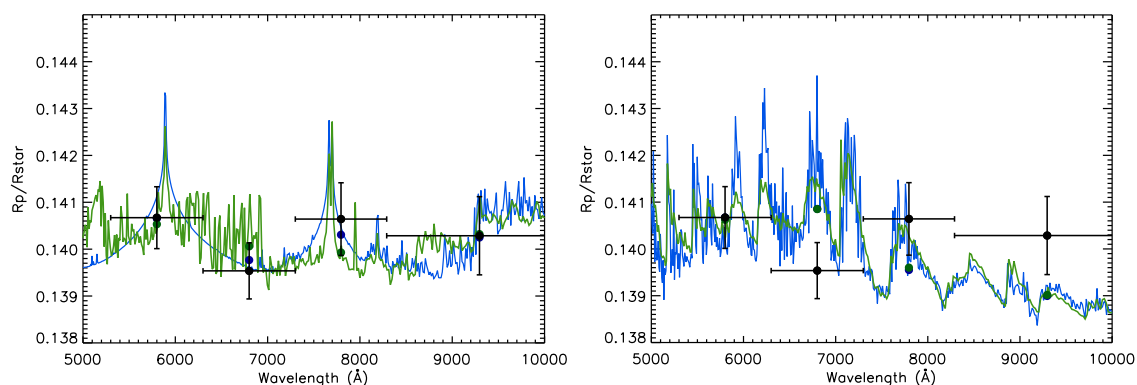


Figure 6.23: The STIS G750L data, with pre-calculated models, fitted to the G750L data baseline level with baseline R_p/R_\star as a free parameter. The left panel shows models with no TiO and the right panel shows models with a solar abundance of TiO. The data points are shown in black with horizontal error bars indicating the bin sizes, the unbinned models are shown with lines and binned model values for my data bins are shown as circles (blue for the Fortney et al. (2010, 2008) models and green for the Burrows et al. (2010); Howe & Burrows (2012) models).

I also produced the spectrum with slightly different binning but similar bin sizes, so that bins were specifically centred around the sodium and potassium lines, and also the region between the lines. I thought that the differences between the TiO-containing and TiO-free models would be greatest using this binning. However, the difference between the TiO-containing and TiO-free models did not increase any further than when using the original binning, due to some of the features in the TiO-containing model being in similar places to the alkali lines. Combined with the bin sizes needing to be decreased, and hence the points having larger photon noise, the method using specific bins centred on alkali lines was no more constraining than the original binning. The original binning is therefore shown in Figure 6.23.

Additionally, I investigated constructing the transmission spectrum using smaller bins than initially used in Figure 6.23. Although Na I and K I were not detected in small spectral bins as investigated in Section 6.3.4, it is possible that the difference between a TiO-containing and TiO-free atmosphere could be revealed when constructing the entire transmission spectrum with small bins.

If I use bin sizes of $\sim 400 \text{ \AA}$ with binning designed such that two bands are centred on the Na I and K I doublets, there is no significant difference in fits between a flat line and a TiO-free atmosphere case. The atmospheres without TiO are favoured over the atmospheric models including TiO opacities at the 2σ level. The lowering of the significance level compared to the spectrum produced using 1000 \AA bins is most likely due to larger photon noise uncertainties. I also calculated the spectrum using 200 \AA binning (for all but the 4 reddest bins, where the STIS response curve is very low and for which I used bin sizes of 500 \AA). The spectrum calculated using 200 \AA wide bins suggests that the flat spectrum is favoured over either the TiO-free or TiO-containing model cases. However, the fit of a flat line to the spectrum is not a good fit, with a χ^2_ν of 1.7. Possibly other absorbers are present in the optical transmission spectrum, but any conclusions about other absorbers not predicted by the models are too tentative at this stage to warrant further discussion. When calculating the spectrum with 100 \AA bin sizes, the errors on radii measured in the bins are so large due to photon noise that there is no significant difference between the fits of the TiO-free atmosphere models, TiO-containing models and a flat spectrum. Figure 6.24 shows the transmission spectrum of WASP-19b obtained using 400 \AA and 200 \AA bins.

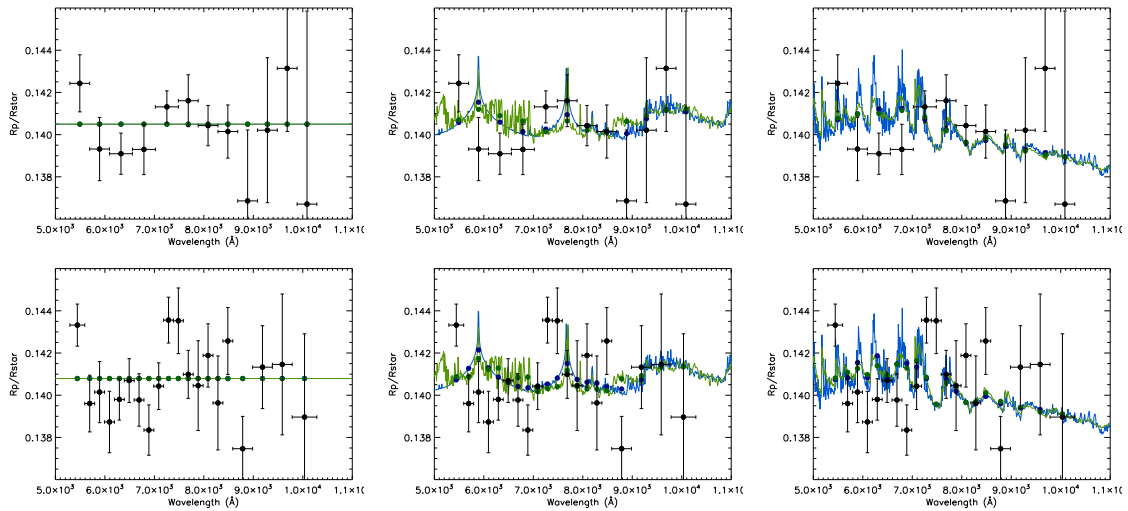


Figure 6.24: Optical transmission spectra of WASP-19b obtained using 400 Å bins (top) and using 200 Å bins (bottom) compared with models. In the plots on the bottom, the reddest 4 points are using 500 Å bin widths. Unbinned model values are shown with solid lines and binned model values are shown with filled circles (blue for the Fortney et al. (2010, 2008) models and green for the Burrows et al. (2010); Howe & Burrows (2012) models in the centre and right plots). In each case, the left plot shows a fit with a flat line, the middle plot shows a TiO-free model atmosphere, and the right plot shows a model atmosphere with significant absorption from TiO.

6.5.3 Significance of the Near-IR Water Features

I now consider the near-IR spectrum, which may be combined with the optical to place further constraints on the atmosphere of WASP-19b. The data and pre-calculated models fitted to the baseline R_p/R_\star of the data are shown in Figure 6.25. Comparing the models including a solar abundance of water but with no TiO to the measured spectrum, by fitting only an absolute offset in R_p/R_\star as a free parameter, gave $\chi^2 = 1.5 - 4.1$ for 5 DOF, which are my best fitting models. A flat line, on the other hand, gave $\chi^2 = 22.1$ for 5 DOF, indicating a 4σ confidence in the water-dominated model over the null hypothesis. Using models that include opacities from TiO and VO as well as water gave $\chi^2 = 5.8 - 7.6$ for 5 DOF, indicating that the WFC3 data suggest a lack of observable TiO features. Comparing each model including TiO and VO opacities to the corresponding TiO-free model shows that the TiO-free atmosphere case is a better fit at the 1.8 to 2 σ level.

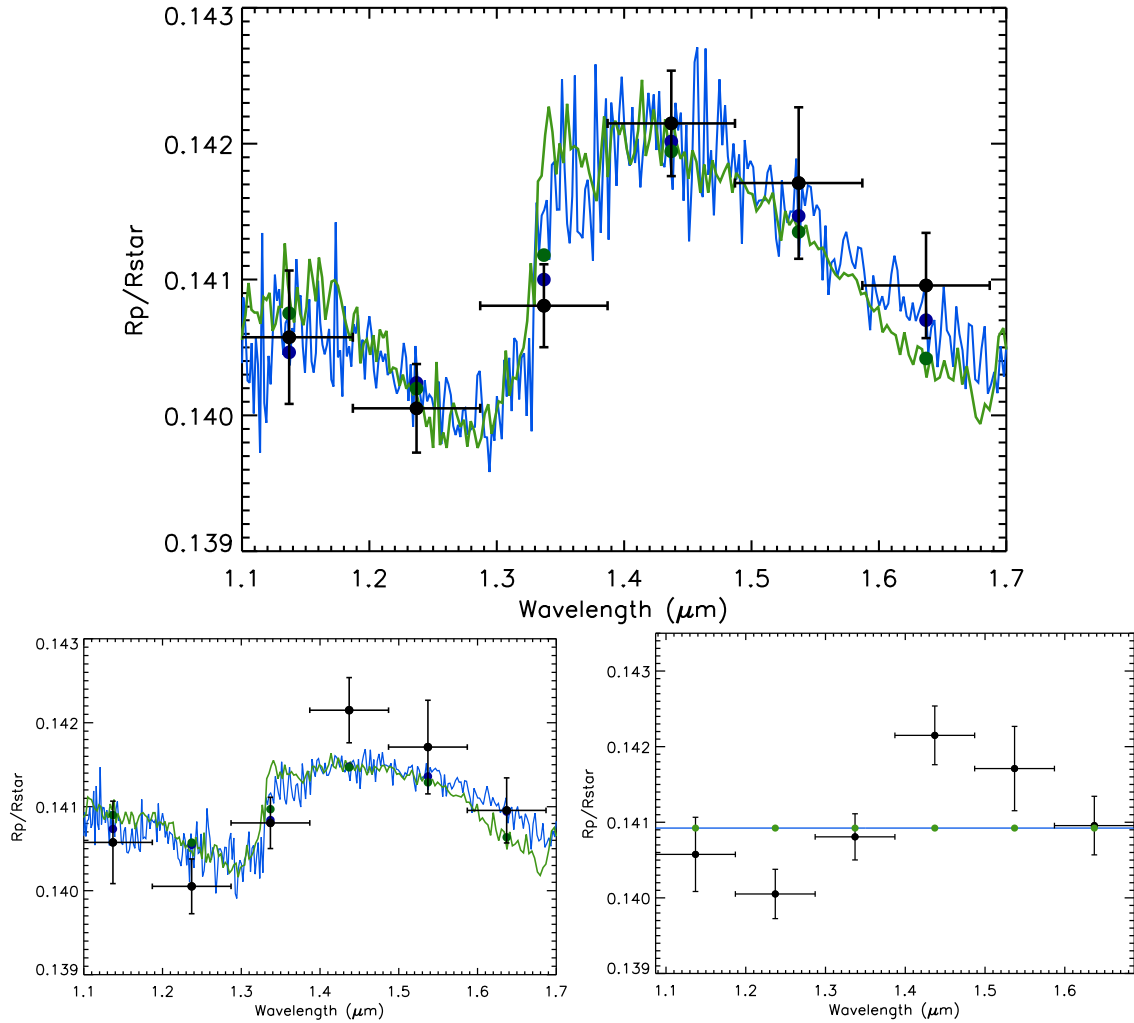


Figure 6.25: *Top*: WFC3 data and models including water opacities but no TiO opacities with non-inverted T - P profiles, fitted to the WFC3 data level with baseline R_p/R_{\star} as a free parameter. *Bottom Left*: WFC3 data and models including water and TiO opacities and a strong temperature inversion, fitted to the WFC3 data level with baseline R_p/R_{\star} as a free parameter. *Bottom Right*: Flat line fit to the WFC3 data. For all plots, the data points are shown in black with horizontal error bars indicating the bin sizes, the models are shown with lines and binned model values are shown as circles (blue for the models of Fortney et al. (2010, 2008) and green for the models of Burrows et al. (2010); Howe & Burrows (2012) for the top and bottom left plots).

I have not corrected the WFC3 spectrum for occulted or un-occulted stellar spots. If present, un-occulted spots would increase the measured R_p/R_* values compared to the non-spotted case, while occulted stellar spots would do the opposite. If the star is uniformly spotted, both the effects of occulted and un-occulted spots should cancel out (e.g. Pont et al. 2013). If un-occulted and occulted spots do not cancel out, then the near-IR spectrum could shift in baseline R_p/R_* by 0.0138, although this would not affect measured spectral features. The most significant wavelength-dependent effect on the near-IR spectrum if un-occulted and occulted spots do not cancel out would be to introduce a slope in the transmission spectrum (see Figure 6.21). The slope would be $\sim 0.00027 R_p/R_*$ from the bluest to reddest bin, assuming $T_{\text{spot}} = 5000$ K and an optical dimming of 1%. This slope should not highly affect the detection of water features, particularly not the feature at $1.4 \mu\text{m}$, which is well encompassed by the G141 band, and so has a peak in R_p/R_* as a function of wavelength rather than a slope as a function of wavelength. Furthermore, I do not see a significant slope in the spectrum compared to the predicted spectral features, suggesting that occulted and un-occulted spots have indeed cancelled out to a large extent.

Another possible effect is due to the presence of water features in the stellar spots. If the water features in the spots are significantly different from the non-spotted stellar spectrum, un-occulted spots will artificially increase the amplitude of water features in the planet's transmission spectrum (e.g. Deming et al. 2013). There are no significant water features seen in the Kurucz (1993) grid of stellar spectra for the G141 wavelength range (Figure 6.21). To test whether my assumed un-occulted spot dimming models as a function of wavelength are reasonable, I also investigated the much higher resolution models of R.L. Kurucz for HD 209458 and HD 189733, where water features in the stellar spectra can clearly be seen. I used the stellar model of HD 209458 ($T = 6100$ K) as the non-spotted surface and the stellar model of HD 189733 ($T = 5050$ K) as the spot spectrum. I found that, although water features are clearly seen in the stellar spectra at higher resolution, the differential effect of the spot spectrum compared to the non-spotted surface is negligible in the large wavelength bins used for the transmission spectrum (see Figure 6.26).

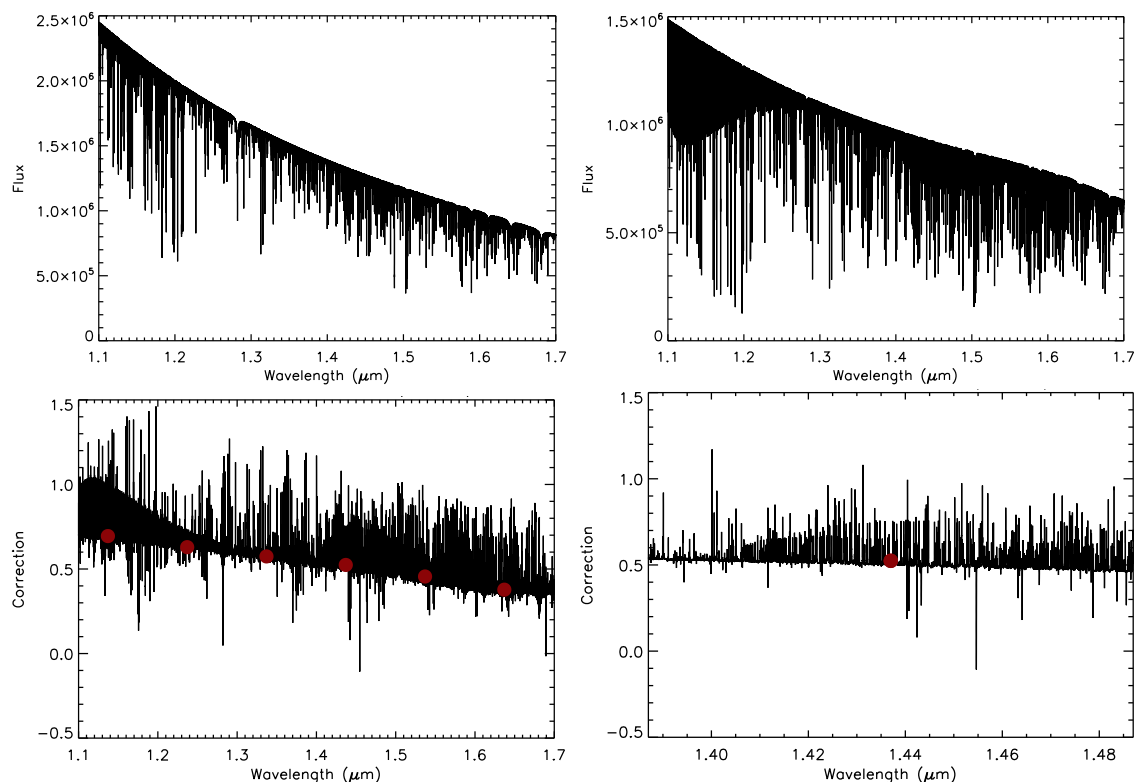


Figure 6.26: *Top*: High-resolution model atmospheres from Kurucz (1993) for HD 209458b (left) and HD 189733b (right) over the WFC3 wavelength range. Both stellar atmosphere models use the same wavelength grid. *Bottom*: Stellar spot dimming as a function of wavelength, obtained by using the stellar spectrum of HD 209458b as the non-spotted stellar surface and the stellar spectrum of HD 189733b as the spotted surface, normalised to 1 at 6000 Å. The left plot shows the flux dimming correction over the WFC3 wavelength range, with values corresponding to the WFC3 data bins shown with red circles. The binned values appear low, but on closer inspection (right plot) this occurs because there is a lot of space between lines which is not visible on the left-hand plot. There are therefore no visible differential features at the resolution used for the data.

6.5.4 Interpretation

Although I cannot put the spectra from the STIS G750L and WFC3 G141 instruments together on an absolute scale due to unknown differences in stellar brightness between the two observations, I can still place constraints on the atmospheric type. Water is detected in the near-IR, and my optical observations suggest a lack of observable large TiO features (note that observations published since this work have also suggested water absorption and a lack of TiO features in the transmission spectrum of WASP-19b, but none of these studies were conclusive: Mancini et al. 2013; Bean et al. 2013).

The C/O ratio of WASP-19b is currently unconstrained from secondary eclipse observations (Anderson et al. 2013; Burton et al. 2012; Lendl et al. 2013), but models predict that the water abundance will drop dramatically compared to a solar-composition atmosphere if the C/O ratio is greater than 1 (Madhusudhan 2012; Moses et al. 2013). Therefore, the presence of water in the transmission spectrum at the level seen here suggests that the atmosphere does not have a high C/O ratio. Additionally, the amplitude of the measured water features match solar abundance models with no cloud cover, in contrast to observations of HD 189733b, HD 209458b and XO-1b (Gibson et al. 2012a; Pont et al. 2013; Deming et al. 2013). However, with my low resolution, it is hard to tell whether the water features may be slightly muted at a similar level to XO-1b, since 1σ shifts in only two of my bins would show a smaller feature consistent with low cloud cover. Water features muted at the level observed in HD 209458b ($0.57 \times$ solar) are likely ruled out.

Due to grazing geometry, atmospheric pressures probed in transmission are ~ 50 times lower than for the same wavelength observed in secondary eclipse (Fortney 2005). However, the increased opacity in the IR compared to the optical means that the same altitude regions are sampled in optical transmission spectroscopy as in Spitzer emission spectroscopy, and thus the absorbers responsible for stratospheric inversions should be directly detectable. Therefore, the probable lack of a TiO detection in transmission agrees with previous secondary eclipse observations of an atmosphere without a strong temperature inversion provided that TiO is the absorber responsible for inversions (Anderson et al. 2013; Madhusudhan 2012). However, HD 209458b displays a stratospheric inversion without prominent TiO features in the transmission spectrum, and where TiO levels are not abundant enough to be responsible for a strong inversion (Désert et al. 2008; Spiegel et al. 2009). The results therefore suggest that a different absorber may be responsible for inversions, and although no candidates have been observed so far, the red to near-IR part of the spectrum of HD 209458b is not well constrained.

A lack of TiO features, if not caused by a high C/O ratio, could mean that TiO is trapped in lower regions of the atmosphere that are opaque to transmission spectroscopy, as described by Spiegel et al. (2009), Showman et al. (2009) and Parmentier et al. (2013). Spiegel et al. (2009) found that in the atmosphere of OGLE-TR-56, a planet only ~ 100 K cooler than WASP-19b, there could be a TiO cold-trap on the planet's day side. Even without a day-side cold-trap, vertical mixing deep in the atmosphere may still not be enough to lift gaseous TiO into the observable upper atmosphere. Furthermore, if TiO escapes these vertical traps, cold-trapping on the night side is also possible if TiO particles condense and reach sizes over a few microns, or if TiO forms condensates with other species (see Chapter 1, Parmentier et al. 2013). Transmission spectroscopy measures the spectrum at the planetary terminator, and it is currently unclear how day side and night side conditions affect the terminator region. Since the strength of vertical mixing is coupled with the horizontal flow, the terminator region experiences time-variations in the abundances of atmospheric species, as the upward flow changes (Parmentier et al. 2013).

An alternative explanation for a lack of TiO features could be that stellar UV radiation breaks down the molecule, as proposed by Knutson et al. (2010). WASP-19 is an active star with $\log(R'_{\text{HK}}) = -4.660$, compared to -4.970 for the inactive HD 209458, which hosts a planet with a stratosphere. WASP-19b is also very close to the star at only 0.0166 AU, and so is very highly irradiated.

It is also possible that a less than solar abundance of gaseous TiO exists in the upper atmosphere, but is concealed by high-altitude hazes, clouds or dust. Without knowing to what extent occulted stellar spots have cancelled out the effect of unocculted spots on the WFC3 dataset, I am unable to determine whether the optical radii are high compared to the near-IR radii. Therefore, an optical absorber remains a possibility. However, if water is observed in the near-IR, such an obscuring layer would have to be optically thin in the near-IR. Also, at the high temperatures of the atmosphere of WASP-19b, many dominant condensates are not able to form (Fortney 2005). Without being able to use the G430L data to construct a transmission spectrum, I cannot distinguish between Rayleigh scattering from small-particle hazes or clouds and dust composed of larger grains, which may also show features blueward of 4500 \AA , such as absorption from HS (Zahnle et al. 2009b). Other features specifically just in the G750L wavelength regime could also dilute TiO features. For example, the cross-sections of VO would cause absorption that will hide the TiO bands if the abundance of VO is high compared to TiO in the upper atmosphere (e.g. both TiO and observable quantities of VO are consistent with the observed transmission spectrum of HD 209458b although not confirmed (Désert et al. 2008)). VO hiding TiO signatures would require a significant departure of abundances from equilibrium in

the upper atmosphere, since VO is already included in the TiO-containing models at the solar abundance level ($\sim 1/20$ times the abundance of TiO).

6.6 Conclusions

I measured the optical transmission spectrum of WASP-19b with HST STIS G750L from 5300-10300 Å during one planetary transit and with HST STIS G430L from 2900-5700 Å during two transits. The STIS results are the first from a large HST survey of 8 hot Jupiters. I combined the STIS results with archive WFC3 data of one transit of WASP-19b from 1.1-1.7 μm .

The WFC3 data show evidence of water in the atmosphere of WASP-19b at the 4σ confidence level, with a feature amplitude in agreement with solar-abundance models. Although I cannot rule out low levels of muting, features muted to the extent of those seen in HD 189733b and HD 209458b are ruled out. The presence of non-muted water features suggests a non-cloudy upper atmosphere or only low-level clouds, and also indicates that the planet does not have a high C/O ratio. Observations using the WFC3 G102 grism, with wavelength coverage of 8000-11500 Å, can be used to place the existing optical and near-IR transmission spectra on the same absolute radius scale, since the wavelength range of the G102 grism overlaps with those of both existing observations. A proposal has now been accepted as part of a large programme (GO-13467, P.I. J. Bean) which will observe four transits of WASP-19b in each of the G141 and G102 grisms, and will hopefully provide the missing information. The programme will also be able to confirm the water feature detected here with improved signal-to-noise.

The STIS G750L data show no evidence for TiO features in either the broadband transmission spectral data (2.7 - 2.9σ confidence) or two specifically tailored bands (2σ for the red-edge and cross-correlation indices). There could be several possible reasons for a lack of observable TiO features, including no TiO being present in the upper atmosphere due to rainout or low vertical mixing, possible breakdown of TiO by the intense activity of the host star, or an obscuring haze, cloud or dust layer of unknown composition. A high C/O ratio is unlikely if water is observed in the transmission spectrum at the amplitude seen here. A lack of TiO features in the transmission spectrum is not unexpected for a planet which likely has no strong stratospheric thermal inversion. In order to try to understand the reasons behind the lack of observable TiO in the upper atmosphere of WASP-19b, I have had a proposal accepted to observe the near-IR thermal phase curve with WFC3 (GO-13431, P.I. C. Huitson). More detail is given in Chapter 7, but essentially such an observation should constrain the day to night temperature contrast and horizontal wind speeds at a deeper altitude

than observed before, and will complement *Spitzer* phase curves which have also been obtained (H. Knutson, N.K. Lewis, priv. comm).

I was unable to determine the planetary transmission spectrum in the G430L wavelength range because of having to fit for occulted starspots, radii and systematics simultaneously with very few exposures, and with no spot-free exposures between 2nd and 3rd contact. I was only able to loosely constrain the stellar spot temperature, although my results agree with other work. If the stellar spot temperature is better known, then the spot amplitude parameter can be much better constrained for each wavelength. One possible method of inferring the mean stellar spot temperature would be to obtain data for the 3000-5000 Å range from the ground, where complete light curves should increase the chance of having at least some in-transit exposures not occulting starspots. Having non-spotted exposures during the transit between 2nd and 3rd contact should help break the degeneracy between occulted spot amplitudes in each band and measured planetary radii. Simultaneous ground and space based observations from 3000-5000 Å could also provide an even better constraint, since there would be no difference in un-occulted starspot level between the two observations and systematic trends could be better characterised. I would then have to assume that the occulted spots represent the mean temperature of un-occulted spots to enable full correction of the transmission spectrum.

Although I have not planned to observe WASP-19b from the ground in this manner, I am currently drafting a proposal to observe the long-term variability from the ground with CTIO ANDICAM to complement the phase curve observations, as was done for the large survey. ANDICAM actually has the facility to observe in the optical and near-IR simultaneously with no loss to the precision or cadence of the optical observations. Thus, it is possible that these observations would provide some temperature constraints for the stellar spots of WASP-19. This is secondary to the main science case of that proposal, however, and the precision of the near-IR detector for this purpose has not yet been tested.

I found that WFC3 performs very well for transit observations, with the majority of systematic trends repeating very closely from orbit to orbit. I found that non-linearity in pixels was the only data-quality issue that affected the spectrum by greater than 1σ , and even then only in the flagged pixels. Saturation will be easier to avoid with the new “spatial scanning” mode, where the spectrum is smeared across the non-dispersion direction during an exposure. For bright targets, the spatial scanning mode can also improve the duty cycle by reducing the number of buffer dumps, even though overheads are 3 times longer for spatial-scan exposures than for regular exposures.

The WASP-19b results presented here are only the first of the 8-planet HST survey, and already there are striking differences between the transmission spectrum

and the spectra of planets previously observed. The results of WASP-19b paint a very hopeful picture for the future of the survey as well, since WASP-19 is the dimmest and most active star of all the targets and WASP-19b has the smallest atmospheric scale height. Even in this case, I am able to confirm the presence of atmospheric water with high confidence and to be reasonably confident that TiO is not present in the upper atmosphere. The precision and signal expected from the other targets will be larger, with the potential to constrain the presence of alkali metals and to make use of the blue data to search for Rayleigh slopes and other potential signatures of high-altitude absorbers.

Chapter 7

Conclusions

The motivation for this thesis was to improve understanding of exoplanet atmospheres by studying hot Jupiters in two complementary ways. Firstly, I have attempted to refine the known properties of the most favourable targets, so that they can serve as benchmarks for further studies. Chapters 3 and 4 detail the successful resolving of an atmospheric feature at medium resolution in the atmosphere of HD 189733b and the resulting derived atmospheric temperature profile for this planet and for HD 209458b.

My second goal was to expand the current knowledge to a wider sample of planets, and to be involved in the start of survey-type observations. Large self-consistent surveys of many hot Jupiters provide the possibility of meaningful comparisons across the hot-Jupiter planetary class. Chapters 5 and 6 detail the first results from a ground-based survey of 10 hot Jupiters and a space based survey of 8 hot Jupiters respectively.

Furthermore, I think that it is important to constantly try to extend exoplanet observations by making use of new techniques, and by trying to branch out beyond the hot Jupiter class. The results given in Chapter 5 were the first to make use of long-slit spectroscopy to measure an exoplanet atmosphere, and I learnt important information which will help improve future observations.

7.1 Summary of Achievements

7.1.1 The Medium-Resolution Transmission Spectrum of HD 189733b

I obtained the transmission spectrum at medium resolution ($\sim 1.2 \text{ \AA}$) around the sodium D doublet in the atmosphere of HD 189733b (Chapter 3). I confirmed a previous measurement which shows that sodium is present in the atmosphere. Furthermore, I was able to increase the precision by almost a factor of 3 over that previous work, and to confidently rule out sodium absorption in the line wings. The resolved shape of the sodium doublet presents confirmation that the atmosphere of HD 189733b is largely featureless with only the narrow cores of the sodium feature visible, which suggests that the upper atmosphere contains a high-altitude scattering haze. Comparison with IR data suggests that the abundance ratio of sodium to water is super-solar.

7.1.2 The Upper Atmospheric Terminator T - P Profiles of HD 189733b and HD 209458b

Another advantage of being able to resolve the sodium doublet in the atmosphere of HD 189733b is that the derivative of AD with respect to wavelength can yield information about the temperature profile of the atmospheric regions sampled (Chapter 4). Under the assumption that atmospheric abundance is constant over the regions measured and that the atmosphere is dominated by H_2 , the calculated T - P profile shows a thermal inversion. The inversion observed is most likely the base of the exoplanet's thermosphere. Comparison with the observed T - P profile of HD 209458b (also confirmed in Chapter 4) suggests that the upper atmospheres of the two planets have similar temperature properties, although higher resolution observations of the Na I line cores in the atmosphere of HD 189733b would confirm this.

7.1.3 Transmission Spectrum of XO-2b Using Ground-Based Long-Slit Spectroscopy

In Chapter 5, I observed the first long-slit transmission spectrum of an extrasolar planet: XO-2b. While I was not able to construct the full transmission spectrum of XO-2b, I was able to detect the Na I doublet at the 2.9σ confidence level, with a total confidence level of 5.2σ when combined with results from another transit. XO-2b is therefore now the only planet where Na I and K I have both been detected in the transmission spectrum. Fitting the data using the models derived in Chapter 4, I confirmed at the $3.5 - 4 \sigma$ significance level that the observed feature lacks the predicted line wings and is confined to a total width of $< 50 \text{ \AA}$. Without being able to resolve the feature, I am unable to confirm whether the line wings are obscured by a high altitude haze, or whether there is a drop in the sodium abundance in some region of the atmosphere, which causes the observed narrow doublet shape. With only one data point in the spectral feature, a comparison with the previously observed K I feature is not able to constrain the atmospheric properties any further. Based on the experiences during this work, the GTC staff have made a 10 arcsecond slit, which has removed the majority of the systematics which limited this observation.

7.1.4 The Optical to Near-IR Transmission Spectrum of WASP-19b

The results detailed in Chapter 6 present the optical to near-IR transmission spectrum of WASP-19b; only the third planet to be studied across the optical and near-IR ranges homogeneously at the time of the study. Due to contaminating signal from occulted starspots, I was unable to obtain the transmission spectrum blueward of 5300 \AA , but was able to construct the red optical ($5300\text{-}10300 \text{ \AA}$) and near-IR ($1.087 - 1.687 \text{ \mu m}$) spectra. I found a likely lack of TiO in the upper atmosphere of WASP-19b ($2.7 - 2.9 \sigma$ confidence) and a water feature at the level predicted by solar-abundance models (4σ confidence). The results suggest that there is no significant cloud cover in the near-IR in the atmosphere of WASP-19b, and that the planet does not have a high C/O ratio. I was, however, unable to confirm or rule out the presence of predicted Na I and K I features. The results are still very promising for the 8-planet HST survey, since WASP-19b is the least-favourable target out of those in the survey.

7.2 Further Work

As mentioned above, my continuing goals are to improve the understanding of hot Jupiters by refining and studying the detailed properties of the most favourable targets, and by engaging in surveys to detect and understand broad properties of the wider hot Jupiter exoplanet class. I have several ongoing projects which continue in these directions, but which I also believe fit into the wider goals of the exoplanet research field as a whole.

At the start of this thesis, I highlighted the importance of developing new techniques, and trying to branch out from studying only hot Jupiters. Whilst hot Jupiters are important and interesting to study, the boundaries between different exoplanet classes are not clear, and it is important to study as many types of object as is possible, to understand the mechanisms behind key observational differences. Furthermore, the study of smaller objects acts as a motivation for improving instrumental capabilities, which I believe will eventually lead to the ability to characterise Earth-like exoplanets. My current and future work also leads further into the directions of developing new techniques and exploring beyond hot Jupiters than the work outlined in this thesis. In the following sections, I have listed the projects that I am and will be involved in.

7.2.1 Current Projects

- I am involved in a project to measure the extent of atmospheric escape from HD 209458b, by looking at the transmission spectrum in the UV. I am responsible for the data reduction and spectral analysis while others are responsible for the interpretation, and the project is led by A. Vidal-Madjar. We have detected absorption from Mg I in the upper atmosphere of HD 209458b using a STIS echelle grating, with an AD relative to the continuum of 6.4 ± 1.6 %. This AD corresponds to $\sim 2 R_P$, which is in the planetary exosphere, and where the “blow-off” process starts to be effective (Koskinen et al. 2012a,b). Furthermore, we have detected a possible cometary tail at the 1.8σ significance level, by observing that the flux after transit was lower than the flux before transit by 4.0 ± 2.2 % in the Mg I feature compared to the continuum (Vidal-Madjar, A., Huitson, C.M., et al., A&A, submitted).
- The work in Chapters 3 and 4 demonstrates that valuable information can be obtained from high-resolution observations of specific spectral features, including their abundance profiles and atmospheric temperatures. During the course of this thesis, a ground-based spectral AD profile of the Na I feature in WASP-17b was measured by another group with the ground-based IFU FLAMES at the VLT (Wood et al. 2011). Seeing the potential of such observations to constrain atmospheric abundances and possibly temperatures from the ground, I obtained time on VLT FLAMES to measure the spectral AD profiles of Na I in WASP-31b and WASP-39b, two planets with large scale heights. The observations will also serve as a further test of the feasibility of using ground-based IFU spectroscopy. The data are currently being analysed.
- I am also working on a methodology for interpreting the data from the Exeter surveys. With the surveys starting to produce results, it is important to have a way of classifying hot-Jupiter atmospheres to first order to allow us to more easily draw comparisons between observed properties and other physical variables. To this end, I have defined spectral indices specifically placed to look for features such as Rayleigh signatures, large TiO features and alkali lines. The defined indices include the $[\text{TiO}]_{\text{red}}$, $[\text{TiO}]_{\text{comb}}$, $[\text{Na}]$ and $[\text{K}]$ indices mentioned in Chapter 6. I have then applied these bands to ~ 100 different generic model types from J. Fortney. Comparing and contrasting the model results in multiple bands on ‘colour-colour’ plots separates out different atmospheric types such as clear, hazy, inverted and non-inverted and allows for comparison with observations.

7.2.2 Future Projects

- In Chapter 6, I found that TiO was most likely absent from the upper atmosphere of WASP-19b. Many explanations have been put forward for the reason that some planets show temperature inversions and some do not, but there is no way to distinguish between the possible mechanisms for WASP-19b with the existing observations. I therefore plan to observe the phase curve of WASP-19b in the near-IR with HST WFC3 (GO-13431, P.I. C.M. Huitson). This observation will be the first near-IR phase curve measurement of an extrasolar planet, and also the first spectroscopic phase curve, allowing the observations to sample deeper into an exoplanet atmosphere than before, and also to sample multiple altitudes simultaneously. I hope to place constraints on horizontal wind speeds and day to night temperature contrast in the exoplanet's atmosphere, which will help in understanding whether TiO could have rained out of the upper atmosphere.
- I also now have the opportunity to engage in work towards my goal of studying unexplored atmospheric types. Firstly, I have had a proposal accepted to observe HAT-P-17b, an eccentric, warm Jupiter with HST STIS and WFC3 ($e = 0.346$ and $T \sim 650 - 960$ K). The observations of HAT-P-17b will cover the optical to near-IR range with low-resolution transmission spectroscopy (GO-12956, P.I. C.M. Huitson). They will constitute the first atmospheric measurements of an eccentric warm Jupiter exoplanet, which periodically crosses the CO/CH₄ boundary during its orbit. The broad wavelength coverage should allow abundance and temperature constraints to be placed on the planet's atmosphere, enabling an understanding of how the high orbital eccentricity affects the atmospheric properties.
- After my PhD, I also plan to work with J.-M. Désert at the University of Colorado, Boulder on two large survey programmes which he is leading; one from space with *Spitzer* and one from the ground with Gemini. The *Spitzer* programme is set to observe a large number of close-in smaller planets ($\sim 0.5 M_{\text{Jup}}$). Several planets on the target list are further away from their host stars than the hot Jupiters studied here, which will allow us to observe in a previously unobserved temperature regime. The programme also includes observations of the hot Jupiters in the Exeter optical survey to extend the transmission spectra. The Gemini programme aims to observe 10 hot Jupiters using multi-object spectroscopy, which will enable low-resolution transmission spectra to be obtained across the whole optical range for each target.

7.3 Final Thoughts

I believe that the field of exoplanet characterisation is advancing rapidly thanks to a constant motivation to observe beyond the planned limits of current technology. As a field, we are finally starting to see survey-size studies begin, which will give us insight into the underlying principles that govern hot-Jupiter atmospheres. We are also finally starting to explore the atmospheres of other types of exoplanets, and with new spectroscopic techniques. The goals outlined in this thesis and followed in my current and planned work are things which I think are important to the advancement of the field. I plan to continue in these directions, along with many others involved in exoplanet research, with the hope of one day being able to characterise Earth-like planets in the search for life.

Appendices

A Constants

Quantity	Value	Symbol	Comments
Mass of Jupiter	1.898×10^{27} kg	M_{Jup}	
Radius of Jupiter	69,911 km	R_{Jup}	Mean radius
Mass of the Sun	1.989×10^{30} kg	M_{\odot}	
Radius of the Sun	695,500 km	R_{\odot}	Mean radius
Density of the Sun	1.41×10^3 kg m ⁻³	ρ_{\odot}	Mean density
Mass of Earth	5.972×10^{24} kg	M_{\oplus}	
Radius of Earth	6,371 km	R_{\oplus}	Mean value of distance from centre to surface
Astronomical Unit	1.496×10^{11} m	AU	Semi-major axis between the Earth and the Sun
Gravitational constant	6.67×10^{-11} m ³ kg ⁻¹ s ⁻²	G	6.67×10^{-8} cm ³ g ⁻¹ s ⁻²
Boltzmann constant	1.38×10^{-23} m ² kg s ⁻² K ⁻¹	k_B	1.38×10^{-16} erg K ⁻¹
Stefan-Boltzmann constant	5.67×10^{-8} W m ⁻² K ⁻⁴	σ_{SB}	5.67×10^{-5} erg cm ⁻² K ⁻⁴ s ⁻¹
Speed of light in a vacuum	2.998×10^8 m s ⁻¹	c	
Planck's constant	6.63×10^{-34} m ² kg s ⁻¹	h	6.63×10^{-27} cm ² g s ⁻¹
Mass of a proton	1.67×10^{-27} kg	m_p	
Mass of an electron	9.11×10^{-31} kg	m_e	
Electronic charge	1.60×10^{-19} C	e	

Table 1: Constants used in this work. Note that the radii of the Sun and Jupiter vary slightly over their surfaces due to their rotation causing a small oblateness. Note that $1 \text{ J} = 10^7 \text{ erg}$.

B Acronyms

AD	Absorption Depth
ADC	Atmospheric Dispersion Compensator
ADU	Analogue to Digital Unit
AIC	Akaike Information Criterion
ANDICAM	A Novel Double-Imaging CAMera
AO	Adaptive Optics
AU	Astronomical Unit
BIC	Bayesian Information Criterion
CCD	Charge Coupled Device
CTIO	Cerro Tololo Inter-American Observatory
DN	Data Number
DOF	Degrees of Freedom
ESA	European Space Agency
ESO	European Southern Observatory
FLAMES	Fibre Large Array Multi-Element Spectrograph
FOV	Field of View
FWHM	Full Width at Half Maximum
GCM	General Circulation Model
GP	Gaussian Process
GTC	Grand Telescopio Canarias
HST	Hubble Space Telescope
IDL	Interactive Data Language
IFU	Integral Field Unit
IR	Infra-Red
IRAF	Image Reduction and Analysis Facility
KPNO	Kitt Peak National Observatory
L-M	Levenberg-Marquardt
MCMC	Markov Chain Monte Carlo
NASA	National Aeronautics and Space Administration
NICMOS	Near Infrared Camera and Multi-Object Spectrometer
NOAO	National Optical Astronomy Observatory
OSIRIS	Optical System for Imaging and low Resolution Integrated Spectroscopy
PSF	Point Spread Function
RV	Radial Velocity
S/N	Signal-to-Noise
STFC	Science and Technology Facilities Council

STIS	Space Telescope Imaging Spectrograph
T-P	Temperature-Pressure
UV	Ultra-Violet
VLT	Very Large Telescope
WFC3	Wide Field Camera 3

C Definitions

A-to-D Conversion: Conversion of output signal into data number (DN) is performed using an analogue to digital converter (as such DN can also be referred to as analogue to digital units or ADU). The gain of the device refers to the number of received electrons or photons required to produce 1 ADU. The largest output DN or ADU that can be produced is set by the number of bits in the A/D converter. A/D saturation can occur when reaching the limit of the A/D converter. Hence some detectors have multiple gain settings which can reduce the number of DN recorded for a given number of electrons.

Absorption Oscillator Strength: See “Oscillator Strength”.

Activity: Stellar “activity” refers to the degree of flux variation due to the level of starspots on the stellar surface. There is a strong component of brightness variation due to the rotation of the star compared to the observer, rotating starspots into and out of view.

Advective Timescale: Characteristic timescale for energy to be advected around the planet. It is usually calculated as the ratio of some length scale (e.g. the size of the planet) to a flow velocity.

Albedo: A measure of the reflectivity of the planet.

Bond Albedo: The reflectivity of the object at all wavelengths over all phase angles. This is equal to integrating the geometric albedo over all phase angles. The Bond albedo has values between 0 and 1.

Geometric Albedo: The reflectivity of the object compared to a perfectly reflecting flat disc as a function of phase angle. Usually, the “geometric albedo” quoted for an astronomical object is that measured at a phase angle of 0 (secondary eclipse for an exoplanet).

Atmosphere (for a gas planet): For a terrestrial planet, the atmosphere is the region where the solid body stops. However, for a gas giant, the atmosphere is defined as the region where the gas becomes sufficiently translucent to allow transmission spectroscopy. The transit radius, where the atmosphere becomes opaque enough to block stellar light, is found to have an optical depth $\tau_{\text{eq}} = 0.56$ (Lecavelier Des Etangs et al. 2008a).

Cold Trap: A region of atmosphere cooler than the atmosphere above and below it. Cold-trapping occurs when a gas condenses into a solid in such a region and is then unable to be lifted up into hotter regions where it could exist in the gaseous state again.

Collisional Broadening: See “Line broadening”.

Common Mode: Systematics which have the same structure in each waveband and hence can be easily subtracted by comparing each spectral light curve with the white light curve. Such a process preserves relative transit depth as a function of wavelengths, but removes any information about absolute transit depth.

Conjunction: These are used to refer to specific points in a transit light curve.

Inferior Conjunction: The point at which the planet is directly between the Earth and the star. The point at which the primary transit is observed.

Superior Conjunction: The point at which the star is directly between the Earth and the planet. The point at which the secondary eclipse is observed.

Contacts: These are used to refer to specific points in a transit light curve as viewed by the observer.

First Contact: The point just at the start of ingress where the leading edge of the planet touches the edge of the star from the observer’s point of view.

Second Contact: The point just after ingress where the entire planet is inside the stellar disc for the first time and the trailing edge of the planet is in contact with the edge of the star from the observer’s point of view.

Third Contact: The point just before egress where the entire planet is inside the stellar disc for the last time and the leading edge of the planet is in contact with the edge of the star from the observer’s point of view.

Fourth Contact: The point just at the end of egress where the trailing edge of the planet touches the edge of the star from the observer’s point of view.

Cross-Section: The probability that incoming radiation will be absorbed. An absorption cross-section is given in the form of an area that is presented to incoming radiation. Cross-sections are calculated from opacity databases, which give the central wavelengths of electron transitions and their strengths. The final cross-sections are then determined by adding in various broadening effects, meaning that radiation has some chance to be absorbed away from the line centres, depending on temperature, pressure, and random effects.

Detectors: A detector is meant to collect photons and produce a signal that is proportional to the number of incoming photons by a known amount, meaning that the number of photons received can be measured. Ideally, a detector should be linear, meaning that the signal out of the detector (e.g. the charge or voltage produced) is proportional the number of incoming photons. Deviation from a linear relationship (non-linearity) can occur, and the dynamic range of a detector is the range of signal where useful information can be obtained. This region does not necessarily have to be in the linear regime, as long as the degree of non-linearity can be estimated.

Doppler Broadening: See “Line broadening”.

Doublet: Fine splitting of excited states. For example, the sodium D_1 and D_2 lines are both excitations from the ground state (S) to the first excited level (P state). Note that the name D is historical. The two lines are fine splitting of the P energy level due to coupling between the electron angular momentum and the nuclear angular momentum, meaning that an electron can be in different states with different momenta. See Steck (2010) and Rybicki & Lightman (1979) for more information.

Dual-Band: In exoplanet atmosphere radiative transfer modelling, this usually refers to using two different wavelength components and treating the optical and IR radiation as the two distinct components.

Dynamic Range: See “Detectors”.

Eccentricity: The degree to which a planet’s orbit deviates from circular. A circular orbit has $e = 0$. Hot Jupiters typically have zero eccentricity because they have been tidally circularised from being so close to their host star. Values of e between 0 and 1 indicate elliptical orbits, while $e = 1$ indicates a parabolic escape orbit.

Egress: The time during the planetary transit when the planet is leaving the stellar disc from the observer’s point of view, and only part of the planet is in front of the stellar disc. This occurs between 3rd and 4th contact.

Emission Spectrum: The spectrum that is obtained by measuring the secondary eclipse depth of a planet as a function of wavelength. This is the spectrum emitted by the planet and the name does not necessarily mean that spectral features will be in emission. Whether or not features are in emission, absorption or not seen at all depends on the planet’s day-side temperature structure.

Equation of State: An equation which relates state variables (macroscopically measurable variables that are a function of the current state of the system). For example, an equation of state can link density to temperature and pressure.

Equilibrium: A system is in equilibrium if there is no net energy exchange around the system i.e. any energy into the system is balanced by energy out of the system.

Chemical: The case where concentrations in a system do not change over time.

Dynamic: A system is in dynamic equilibrium if compounds in the system are subject to a reversible reaction but there is no net change in the composition. The reaction can still be ongoing, but the reaction proceeds with equal rates in both directions, meaning that there is no observable change in the composition.

Hydrostatic: A fluid is in hydrostatic equilibrium if it is at rest and if the pressure at any point in the fluid is balanced by the gravitational force. For example, hydrostatic equilibrium occurs in a star, where the outward radiation pressure is balanced by gravity. The fluid in a planetary atmosphere is not at rest, but the hydrostatic equation is still approximately satisfied if the acceleration is small, and Pierrehumbert (2010) find that the relation is accurate for large-scale problems involving planetary atmospheres.

Radiative: The energy received through irradiation is equal to the amount of energy re-radiated from a system. Also, it can mean that the transfer of energy through a system by radiation, absorption and re-radiation results in a uniform surface temperature.

Thermal: The temperature within a system is uniform with time and space. Alternatively, this could mean that two systems (e.g. a star and planet) are connected thermally, but no thermal energy flows between the two systems.

Thermochemical: The energy changes which accompany chemical reactions and changes of state are such that equilibrium in the system is maintained. If two different compounds with different specific heat capacities react with one another, then they will reach a common equilibrium temperature where the energy lost by one compound is equal to the energy gained by the other.

Thermodynamic: The system is in thermal, mechanical, radiative and chemical equilibrium and the state of the system does not change with time (mechanical equilibrium means that no net force is acting on a system). There is no net flow of matter or energy, no phase changes and no net forces within the system.

Equilibrium Temperature: The expected temperature of the planet if the energy emitted by the planet is equal to that which it absorbs from the star. A planet's day side has different equilibrium temperatures depending on the thermal redistribution efficiency. I use the term "equilibrium temperature" to mean the case of totally efficient

thermal redistribution from the irradiated day side of a tidally locked planet to the night side, meaning that each hemisphere will have the same temperature, unless otherwise stated. I also assume zero albedo.

Exoplanet: A shortened name for an “extrasolar planet”, a planet outside our solar system. This definition can also be used to refer to free-floating planets not gravitationally bound to a star.

Gravity Waves: Transverse waves caused by convection overshoot. They are called “gravity waves” because gravity acts as the restoring force. Additionally, they may be important in lifting dust into upper atmospheres of planets and brown dwarfs (Freytag et al. 2010).

Hot Jupiter: A gas giant planet of similar mass to Jupiter, but with a very close orbit to its host star of ≤ 0.1 AU. Some hot Jupiters have lower densities than Jupiter.

Ideal Gas: A gas which is composed of randomly-moving, non-interacting point particles. The kinetic energy of ideal gas particles is much more important than interactions between particles. A gas behaves more like an ideal gas for higher temperatures, lower densities and smaller molecules. In these cases, the space between molecules is large compared to the size of the molecules.

Impact Parameter: Projected distance between the path of the centre of the planet and the centre of the star from the point of view of the observer.

Inclination: The angle between the plane normal to an exoplanet’s orbit and the observer. An inclination of 90° would mean that the planet will be seen to pass directly across the centre of the star during transit.

Ingress: The time during which the planet transit has begun, and part of the planet is in front of the star, but before the point where the whole planet is in front of the stellar disc.

In-Transit: The portion of a transit light curve where the planet is transiting the star, usually meant to include ingress and egress.

Lambert Sphere: A reflecting surface where the intensity of reflected radiation is proportional to the cosine of the angle α between the observer’s line of sight and the surface normal. The phase function for the geometric albedo is $\Phi_\lambda(\alpha) = \cos \alpha$ (see Seager 2010).

Light Curve: A measurement of flux as a function of time. For example a transit light curve is a measure of flux over time just before, during and after a transit, demonstrating the flux drop during transit. A variability monitoring light curve is long-duration monitoring of the flux of a star to observe the degree of starspot-related flux variations.

Limb: The ‘edge’ of a body, in this case usually a star. The word “limb” is used since the gas does not have a well-defined edge. For transmission spectroscopy, the limb of the star would be the edge of the photosphere in the wavelength in question.

Limb Darkening: The reduction in intensity of the observed stellar disc near the limb compared to the centre. The path length for photons emitted at a given stellar altitude through the stellar atmosphere along the line of sight is shorter near the centre of the observed disc. Therefore, more photons from the deeper atmosphere escape at the centre of the disc, while photons observed near the limb emerge from cooler, higher, regions of the atmosphere. The severity of limb darkening is wavelength-dependent, and is less pronounced at redder wavelengths.

Line Broadening: Observed spectral lines are not sharp delta functions around the central wavelength of absorption or emission. Rather, they have a distribution around that central point depending on certain physical conditions. The mechanisms responsible for spreading out a feature from its central point are referred to as “broadening” mechanisms. There are various types of broadening, but I will list here the ones which are included in the Voigt functions which I use to model spectral lines and which are the main ones to be considered for exoplanet spectra.

Collisional Broadening: Also referred to as “pressure broadening”. If an atom collides with another atom whilst it is emitting, then the phase of the emitted radiation is suddenly altered, meaning that information about the frequency of the emitted radiation is lost (Rybicki & Lightman 1979). Also, forces from other particles may perturb emitted radiation, but that effect is not considered here.

Doppler Broadening: Doppler broadening occurs because an atom is in thermal motion whilst it emits or absorbs. Thus, the frequency of emission or absorption in the atom’s rest frame is shifted when it is observed. The line is spread out rather than shifted because individual atoms will have different velocities with varying components and speeds towards or away from the observer.

Natural Broadening: Even without Doppler or collisional broadening, a spectral line has a certain width due to the uncertainty principle. The spread in energy, ΔE , of a state is related with the time, Δt , spent in that state by $\Delta E \Delta t \sim \hbar$. Thus a state with a short lifetime will have a distribution of energies which has a Lorentz profile. The spontaneous decay of an atomic state proceeds at a rate

γ , meaning that the line broadening has a Lorentz profile which depends on γ (Rybicki & Lightman 1979).

Linearity: See “Detectors”.

Natural Broadening: See “Line broadening”.

Occultation: Generally used to describe one object passing in front of the other. In exoplanet science, the term “occultation” is often used to refer to the secondary eclipse (the occultation of the planet).

Opacity: A measure of impermeability to radiation. For dominant opacity sources in exoplanetary atmospheres, there are numerous opacity databases which give opacity as a function of wavelength depending on which molecules are in the atmosphere.

Optical Depth: A measure of transparency. Rybicki & Lightman (1979) define the optical depth as $d\tau_\nu = \alpha_\nu ds$, where α_ν is the absorption coefficient defined by $dI_\nu = -\alpha_\nu I_\nu ds$. Integrating over the optical path, the intensity of radiation after passing through the material is given by $I/I_0 = e^{-\tau}$. In transmission spectroscopy, τ_{eq} is the optical depth at Δz , such that a sharp occulting disc of radius $R_p + \Delta z$ produces the same absorption depth as the planet with its translucent atmosphere.

Oscillator Strength: Rybicki & Lightman (1979) explain that the “oscillator strength” comes from a classical description of quantum mechanics, where a particle that is harmonically bound to a centre of force will oscillate sinusoidally. The total energy extracted from a beam of radiation can be linked to the probability for absorption for a harmonic oscillator.

Out-Of-Transit: The portion of a transit light curve before ingress and after egress, which should measure the baseline flux of the star alone.

Phase Curve: An observation where the flux from the planetary system is measured over the duration of a planet’s orbit. The amplitude of the variation in brightness during an orbit for a tidally locked planet gives an indication of the difference in temperature of the planet between the day and night sides. The location in orbital phase of the brightest point can be used to infer horizontal wind speeds in the planet’s atmosphere, since strong planetary winds can shift the hottest point away from the sub-stellar point.

Pixel Binning: The timing pattern of the readout is altered so that charge from multiple pixels are added together. Binning reduces the spatial resolution of the detector but can improve the rate of data acquisition. It can also improve read noise and increases the charge capacity and hence dynamic range.

Pulsar: A dense, rotating neutron star which has a strong magnetic field. It emits beams of radiation where its magnetic field lines converge, and observers at the earth see pulses whenever this beam is directed towards us.

Radiative Timescale: Characteristic timescale of radiation to move through the planetary atmosphere.

Rainout: The process where a compound condenses and then falls out of the atmosphere due to gravity.

Responsivity: A measure of the signal (e.g. amps) out per watt of signal in. Ideally, the responsivity (or “response”) should be very similar for all pixels, otherwise the flux level measured for a source of constant brightness can vary with time as the source moves across the detector during an observation. Such variations in response are a problem for time-series observations such as transit and secondary eclipse observations.

Saturation: The point at which a detector can no longer change its response to incoming photons, and so no further measurement of photons is possible in a given exposure. Full-well saturation occurs when a pixel reaches the maximum charge that it can hold. A-to-D saturation is set by the number of bits in the A/D converter.

Scale Height: In this work, when I use the term “scale height”, I refer to the pressure scale height, which is the altitude in a planet’s atmosphere over which the pressure changes by a factor e . Assuming that the atmosphere is in hydrostatic equilibrium and that it behaves like an ideal gas, the scale height, H , is given by $H = k_B T / \mu g$, where k_B is Boltzmann’s constant, T is the atmospheric temperature, μ is the mean molecular weight of the atmosphere and g is the surface gravity.

Secondary Eclipse: The point during a planet’s orbit at which the planet is seen to pass behind the star from the point of view of the observer. The resulting dimming can be used to determine the brightness of the planet and hence its temperature or reflectivity, depending on the observational wavelength.

Semi-major Axis: The major axis of an ellipse is its longest diameter, and the semi-major axis is one half of the major axis.

Shallow-Water Approximation: Shallow water models consider the atmosphere to be a thin layer such that the horizontal length scale is larger than the vertical length scale and certain simplifications can be made.

Slit Losses: Light losses due to the PSF of the observational target not being properly centred within a telescope slit, or being too wide for the slit. In these cases, a substantial part of the source can be cut off by the slit. If the amount of slit loss changes over time, it can be very difficult to correct the resulting flux variations.

Starspots: Starspots (a shortened word for stellar spots) are dark spots on the surface of a star where magnetic activity inhibits convection. Starspots are temporary because the magnetic field density at any given point is constantly changing due to the differential rotation between the stellar equator and poles. Starspots are cooler than the surrounding surface, meaning that their intensity contrast with the surrounding surface is greater at shorter wavelengths.

Occulted Starspots: Starspots on the stellar surface which are crossed by the planet during transit from the observer's point of view. In this case, the planet blocks less light than when crossing a non-spotted region of the stellar surface, causing the planetary radius to be underestimated.

Un-occulted Starspots: Starspots on the stellar surface which are not crossed by the planet during transit from the observer's point of view. Un-occulted starspots cause an overall dimming of the star and hence cause planetary radii measured during transit to be overestimated.

Stratosphere: See "Thermal Inversion".

Systematic: A contaminating flux variation as a function of some instrumental, Earth-based or astrophysical origin. A source of correlated noise.

Thermal Inversion: A region of atmosphere where the temperature increases as a function of increasing altitude. A thermal inversion at around 0.01 bar is referred to as the "stratosphere" and is typically due to some absorber trapping heat in the upper atmosphere. Much higher in the atmosphere ($P \sim 10^{-6}$ bar or lower), there is a thermal inversion due to the intense heat from the host star. This region is referred to as the "thermosphere".

Thermosphere: See "Thermal Inversion".

Transit: If an exoplanet's orbital inclination is close to 90° with respect to the observer, the planet is seen to pass in front of the star at certain points during its orbit, obscuring some of the stellar light. The passage of the planet in front of the star is called a transit (sometimes "primary transit").

Transmission Spectrum: The measurement of flux dimming during transit as a function of wavelength, which measures the spectrum of stellar light filtered through the planet's atmosphere. It can be used to measure elemental and molecular constituents of the planet's atmosphere.

D Derivations

D.1 Transit Geometry

Transit Duration as a Function of Orbital Parameters

A planet's transit across a star will vary with the observer's viewing angle compared to the orbital plane of the planet (this angle is called the orbital inclination, i). The planet will appear to move across the stellar surface at a higher or lower position depending on the inclination of the planet's orbit, which will alter the transit duration. Here, I derive the transit duration as a function of orbital parameters based on the workings in Haswell (2010). The impact parameter, b , is the vertical distance at mid-transit of the centre of the planet from the centre of the star as viewed by the observer (see Figure 1).

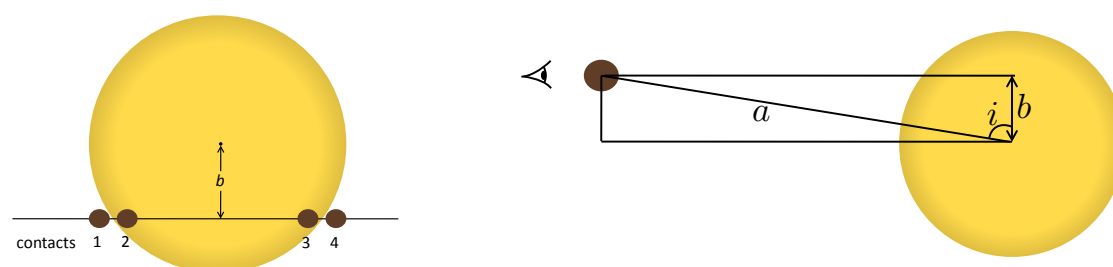


Figure 1: Images reproduced from Haswell (2010) showing a planet's transit across a star and how its angle of inclination, i , and orbital distance, a , relate to the impact parameter b .

From Figure 1 it can be seen that $b = a \cos i$, where a is the orbital separation of the star and planet. Note that I assume the planet's orbit to be circular. As the planet crosses the star, the observer sees it at a vertical distance $a \cos i$ and horizontal distance l from the star's centre as shown in Figure 2.

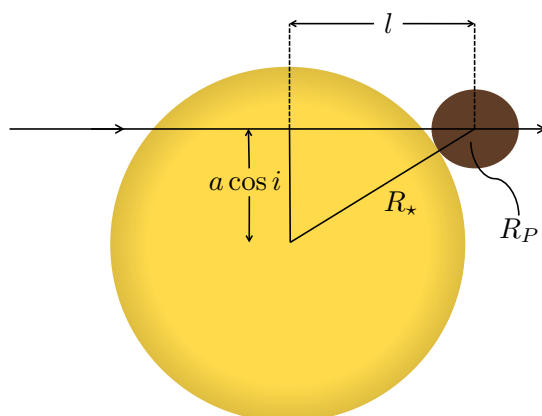


Figure 2: Image showing a planet at first contact with the star reproduced from Haswell (2010). The parameter l is the horizontal distance between the centre of the star and the centre of the planet as seen by the observer.

Using Pythagoras' theorem gives the distance l :

$$l = \sqrt{(R_{\star} + R_P)^2 - a^2 \cos^2 i}. \quad (\text{D.1})$$

The transit duration as a function of inclination can be worked out from the angle α that the planet sweeps out as it passes from one edge of the star to the other (1st to 4th contact) from the point of view of the observer. The orbit is illustrated in Figure 3, where A and B are the edges of the transit as seen by the observer.

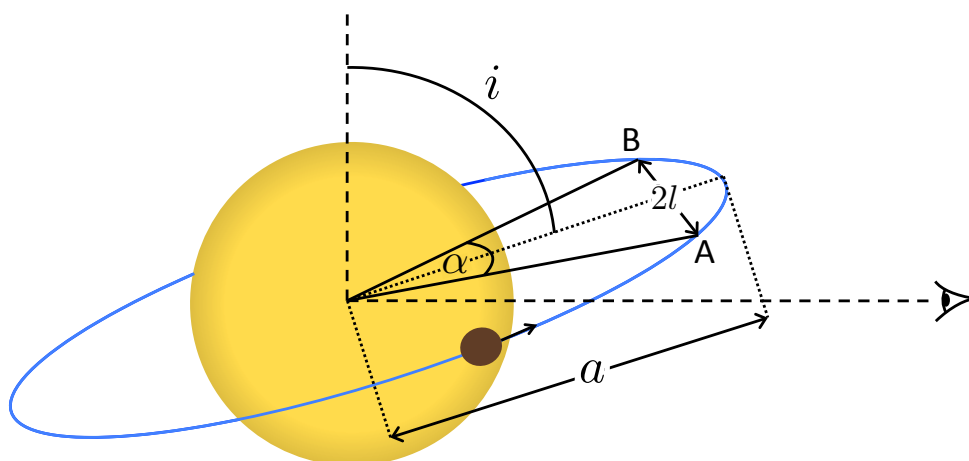


Figure 3: Image showing a planet transiting a star reproduced from Haswell (2010). Here, i is the orbital inclination, a is the orbital separation, A and B are the two points along the orbit between which the observer sees the planet in transit, α is the angle between these two points, and $2l$ is the linear distance between them.

The transit duration, T_{dur} , is given by

$$T_{\text{dur}} = P \frac{\alpha}{2\pi}, \quad (\text{D.2})$$

which is the orbital period, P , multiplied by the angular fraction of the planet's orbit where the planet is in transit from the point of view of the observer. The duration will be smaller for a smaller angle crossed. From the triangle formed by A, B and the centre of the star, it can be seen that

$$\sin\left(\frac{\alpha}{2}\right) = \frac{l}{a}. \quad (\text{D.3})$$

So, the transit duration becomes

$$T_{\text{dur}} = \frac{P}{\pi} \sin^{-1}\left(\frac{l}{a}\right). \quad (\text{D.4})$$

Substituting in for l gives

$$T_{\text{dur}} = \frac{P}{\pi} \sin^{-1}\left(\frac{\sqrt{(R_{\star} + R_{\text{p}})^2 - a^2 \cos^2 i}}{a}\right). \quad (\text{D.5})$$

Assuming $a \gg R_{\star} \gg R_{\text{p}}$ means that $\left(\frac{\sqrt{(R_{\star} + R_{\text{p}})^2 - a^2 \cos^2 i}}{a}\right)$ is small, so

$$\sin^{-1}\left(\frac{\sqrt{(R_{\star} + R_{\text{p}})^2 - a^2 \cos^2 i}}{a}\right) \approx \left(\frac{\sqrt{(R_{\star} + R_{\text{p}})^2 - a^2 \cos^2 i}}{a}\right), \quad (\text{D.6})$$

which then means that

$$T_{\text{dur}} \approx \frac{P}{\pi} \left(\frac{\sqrt{(R_{\star} + R_{\text{p}})^2 - a^2 \cos^2 i}}{a}\right). \quad (\text{D.7})$$

Assuming $R_{\star} \gg R_{\text{p}} \Rightarrow R_{\star} + R_{\text{p}} \rightarrow R_{\star}$ gives

$$T_{\text{dur}} \approx \frac{P}{\pi} \left(\frac{\sqrt{R_{\star}^2 - a^2 \cos^2 i}}{a}\right) = \frac{P}{\pi} \left[\left(\frac{R_{\star}}{a}\right)^2 - \cos^2 i\right]^{1/2}. \quad (\text{D.8})$$

Parameters for Analytic Transit Models

In order to use the analytic models of Mandel & Agol (2002), the normalised separation of the centres, $z = d/r_*$, must be calculated. The distance d is shown by Figure 4, which shows illustrations taken from Mandel & Agol (2002) and reproduced from Haswell (2010).

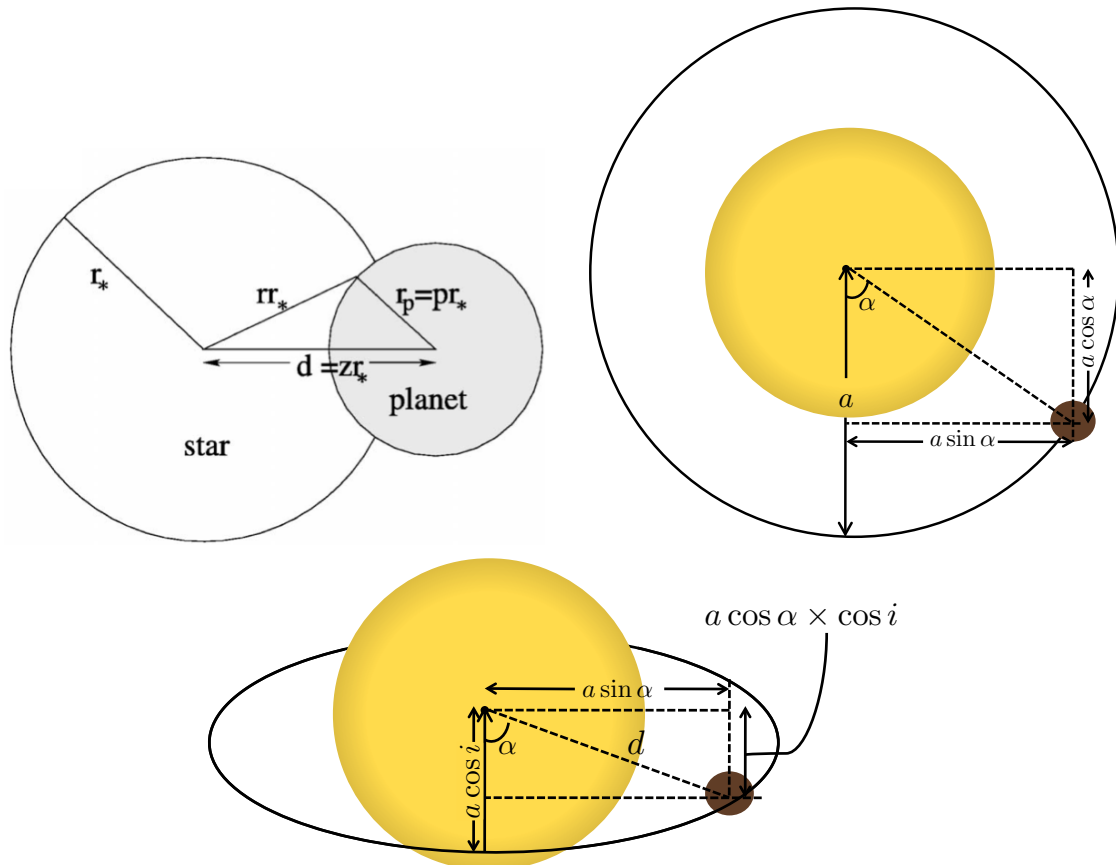


Figure 4: *Top Left:* Image from Mandel & Agol (2002) showing a planet transiting a star along with various geometrical parameters, including the z parameter required in their light curve modelling algorithm. *Top Right and Bottom:* Figures reproduced from Haswell (2010) showing a planet orbiting a star and how to obtain a value for d and hence z . The top right plot shows a top-down view of the orbital system and the bottom plot shows a face-on view which an observer may see of a transiting planet. Note that Figure 2 is an approximation of the bottom plot for the case near transit, since near the transit, the factor $\cos \alpha$ becomes close to 1 because α is close to zero.

Using Pythagoras' theorem, the distance, d , is simply given by

$$d^2 = (a \cos \alpha \cos i)^2 + (a \sin \alpha)^2. \quad (\text{D.9})$$

The angle α ranges from 0 to 2π as the planetary phase, ϕ , ranges from 0 to 1. Thus, α can be written in terms of planetary phase; $\alpha = 2\pi\phi$. Knowing the period and central transit time, the planetary phase of each data point in a transit observation can be calculated. Substituting in for α and re-arranging gives

$$d = a[(\cos(2\pi\phi) \cos i)^2 + (\sin(2\pi\phi))^2]^{1/2}. \quad (\text{D.10})$$

Then dividing through by R_\star gives the normalised separation of centres, z :

$$z = \frac{a}{R_\star} [(\cos(2\pi\phi) \cos i)^2 + (\sin(2\pi\phi))^2]^{1/2}. \quad (\text{D.11})$$

D.2 Derivation of Atmospheric Scale Height

The purpose of the following derivation is to give an expression for the atmospheric scale height assuming hydrostatic equilibrium and assuming that the atmosphere behaves like an ideal gas. Hydrostatic equilibrium means that the pressure at any point in a fluid at rest is balanced by the gravitational force. Assuming that the density, ρ , and surface gravity, g , are constant, the hydrostatic equation is as follows (e.g. de Pater & Lissauer 2010):

$$dP = -g\rho dz. \quad (\text{D.12})$$

In a real atmosphere, the density is not constant and there is also a dependence of the density on temperature, but the assumption used here is valid in the case of the atmosphere being small compared to the size of the planet. The fluid is also not at rest, but the equation is still approximately satisfied if the acceleration is small, and Pierrehumbert (2010) find that the relation is accurate for large-scale problems involving planetary atmospheres. For an atmospheric region of height H , Equation (D.12) becomes

$$P = g\rho H. \quad (\text{D.13})$$

The quantities P and ρ change throughout the atmosphere, but in spectroscopy each different wavelength measurement can be thought of as sampling one of different homogeneous regions of constant P and ρ , and Equation (D.13) is valid. Rearranging Equation (D.13) gives $H = P/g\rho$, and means that the height of the atmosphere can be evaluated for a constant P , g and ρ .

In transmission and emission spectroscopy, the pressure in the atmospheric region being sampled is not always known, so the equation for H must be re-written. For high altitude regions, a good approximation of the equation of state is that of an ideal gas, meaning that $PV = Nk_B T \Rightarrow P = nk_B T$, where n is the number density of the gas and k_B is Boltzmann's constant. Substituting this into Equation (D.13) gives

$$H = nk_B T / g\rho, \quad (\text{D.14})$$

which is equivalent to

$$H = k_B T / \mu g, \quad (\text{D.15})$$

where μ is the mean molecular weight of the atmosphere. The height H can be considered to be the characteristic height of a region of atmosphere of constant T , P and ρ . It is the atmospheric scale height, and it can be seen below that this atmospheric

scale height is the height over which the atmospheric pressure changes by a factor of e .

D.3 Derivation of the Barometric Law

This derivation is aimed at finding a function which links the pressures, P , at each altitude, z , in the atmosphere to some reference pressure, P_o , at some reference altitude. The quantity of interest here is dP/P . The barometric law here is derived from hydrostatic equilibrium and the ideal gas law. The equation of state for an ideal gas, $P = nk_B T$ can be written as $P = \rho k_B T / \mu$. Substituting the ideal gas equation of state into the hydrostatic equation (Equation (D.12)) and dividing both by P gives

$$dP = -g\rho dz \Rightarrow \frac{dP}{P} = \frac{-g\rho dz}{\rho k_B T / \mu} = \frac{-g\mu dz}{k_B T}. \quad (\text{D.16})$$

Integrating and then substituting in for the scale height using Equation (D.15) gives:

$$\begin{aligned} \int_{P_o}^P \frac{dP}{P} &= - \int_{z_o}^{z_o+\Delta z} \frac{g\mu dz}{k_B T} \Rightarrow \ln(P/P_o) = - \int_{z_o}^{z_o+\Delta z} \frac{g\mu dz}{k_B T} \\ &\Rightarrow P = P_o \exp\left(- \int_{z_o}^{z_o+\Delta z} \frac{g\mu dz}{k_B T}\right) = P_o \exp\left(-\Delta z \frac{g\mu}{k_B T}\right) = P_o e^{-\Delta z/H}. \end{aligned} \quad (\text{D.17})$$

This equation is also given by Chamberlain & Hunten (1987) and Fortney (2005).

D.4 Determining Day-Side Temperature from Secondary Eclipse Depth

The derivations in this Section are included for information and are mostly reproduced from Haswell (2010). The flux from the planet compared to that of its host star at a given wavelength is given by Haswell (2010) as

$$\frac{f_{\text{day},\lambda}(\alpha)}{f_{\star,\lambda}} = \left(\frac{R_p}{a}\right)^2 p_\lambda \Phi_\lambda(\alpha) + \frac{B_\lambda(T_{\text{day}})}{B_\lambda(T_\star)} \left(\frac{R_p}{R_\star}\right)^2. \quad (\text{D.18})$$

The first term is the reflected light contribution. The fraction of starlight reflected is a function of wavelength, which is expressed in the wavelength-dependent geometric albedo, p_λ . The amount of light reflected to an observer varies with phase angle, α , where $\alpha = 0$ when the planet passes behind the star. $\Phi(\alpha)$ is the phase function that gives the flux at phase angle α . This varies from 0, when the dark face of the planet is viewed around inferior conjunction (in front of the star), to 1, where the planet is behind the star (secondary eclipse or superior conjunction). The second

term is the thermal emission contribution, where $B_\lambda(T_{\text{day}})$ is the emitted blackbody spectrum of the planet, and $B_\lambda(T_\star)$ is the brightness temperature of the star, estimated as a function of wavelength by knowing the star's spectral type (Haswell 2010; Cowan et al. 2007). Here, a is the distance of the planet from the star, R_P is the radius of the planet and R_\star is the radius of the star. For IR observations, observers can neglect the reflection component and treat the planet as a blackbody emitter. Also, the flux from the day side of the planet is equal to the secondary eclipse depth, ΔF_{SE} , that is observed at the corresponding wavelength, so $f_{\text{day},\lambda}$ can be substituted with ΔF_{SE} . Also note here that I refer to $f_{\star,\lambda}$ simply as F . This gives the following equation:

$$\frac{\Delta F_{SE}}{F} = \frac{B_\lambda(T_{\text{day}})}{B_\lambda(T_\star)} \left(\frac{R_P}{R_\star} \right)^2. \quad (\text{D.19})$$

The blackbody functions for the star and planet are given by Planck's law:

$$B_\lambda(T_{\text{day}}) = \frac{2hc^2}{\lambda^5} \frac{1}{e^{hc/\lambda k_B T_{\text{day}}} - 1} \quad \text{and} \quad B_\lambda(T_\star) = \frac{2hc^2}{\lambda^5} \frac{1}{e^{hc/\lambda k_B T_\star} - 1}, \quad (\text{D.20})$$

where h is Planck's constant, c is the speed of light in a vacuum, λ is the wavelength of observation and k_B is Boltzmann's constant. Substituting into Equation D.19 gives

$$\frac{\Delta F_{SE}}{F} = \left(\frac{R_P}{R_\star} \right)^2 \left(\frac{2hc^2}{\lambda^5} \frac{1}{e^{hc/\lambda k_B T_{\text{day}}} - 1} \right) / \left(\frac{2hc^2}{\lambda^5} \frac{1}{e^{hc/\lambda k_B T_\star} - 1} \right) = \left(\frac{R_P}{R_\star} \right)^2 \frac{e^{hc/\lambda k_B T_\star} - 1}{e^{hc/\lambda k_B T_{\text{day}}} - 1}. \quad (\text{D.21})$$

Then it is a matter of re-arranging to get the day side temperature as a function of secondary eclipse depth:

$$e^{hc/\lambda k_B T_{\text{day}}} = \left(\exp\left(\frac{hc}{\lambda k_B T_\star}\right) - 1 \right) \frac{F}{\Delta F_{SE}} \left(\frac{R_P}{R_\star} \right)^2 + 1 \quad (\text{D.22})$$

$$\Rightarrow T_{\text{day}} = \frac{hc}{\lambda k_B} \left[\ln \left[\left(\exp\left(\frac{hc}{\lambda k_B T_\star}\right) - 1 \right) \frac{F}{\Delta F_{SE}} \left(\frac{R_P}{R_\star} \right)^2 + 1 \right] \right]^{-1}.$$

D.5 Day-Side Temperature as a Function of Different Recirculation Factors

These workings derive the formulae in Chapter 1 relating the day side temperature of a planet to that of the star as a function of some efficiency of redistribution and an albedo. These derivations do not include a derivation of the factor due to the beaming effect, which is discussed in more detail in Spiegel & Burrows (2010) and references therein.

Firstly, I derive the day-side temperature as a function of the geometrical factor f . The derivation is based on the workings in Spiegel & Burrows (2010), and more

details can be found there and in the references therein. The luminosity of the star is given by

$$L_{\star} = 4\pi R_{\star}^2 \sigma_{SB} T_{\star}^4, \quad (\text{D.23})$$

where R_{\star} is the radius of the star, σ_{SB} is the Stefan-Boltzmann constant, and T_{\star} is the temperature of the star. The energy received at the planet is given by assuming that the surface area of the planet receiving the flux is a disc of area πR_p^2 . Therefore, the flux received at the planet is

$$F_{\text{in}} = \frac{\pi R_p^2 L_{\star}}{4\pi a^2} = \frac{\pi R_p^2 4\pi R_{\star}^2 \sigma_{SB} T_{\star}^4}{4\pi a^2} = \frac{\pi R_p^2 R_{\star}^2 \sigma_{SB} T_{\star}^4}{a^2}, \quad (\text{D.24})$$

where a is the orbital distance from planet to star. Spiegel & Burrows (2010) define the luminosity of the planet as

$$L_P = \frac{\pi}{f} R_p^2 \sigma_{SB} T_{\text{day}}^4, \quad (\text{D.25})$$

where T_{day} is the planet's day-side temperature. It can be seen that, for totally efficient redistribution, f must equal 1/4, and the area emitted from is then $4\pi R_p^2$, the total surface area of the planet. Combining the two equations gives:

$$\frac{\pi R_p^2 R_{\star}^2 \sigma_{SB} T_{\star}^4}{a^2} = \frac{\pi}{f} R_p^2 \sigma_{SB} T_{\text{day}}^4 \Rightarrow T_{\text{day}}^4 = f \left(\frac{R_{\star}}{a} \right)^2 T_{\star}^4. \quad (\text{D.26})$$

In the presence of some of the light being reflected, only the non-reflected fraction of the stellar flux is absorbed and re-emitted by the planet. If A_B is the Bond albedo, then the fraction of stellar flux absorbed by the planet is $(1 - A_B)$, and Equation (D.26) becomes

$$T_{\text{day}}^4 = f(1 - A_B) \left(\frac{R_{\star}}{a} \right)^2 T_{\star}^4. \quad (\text{D.27})$$

Secondly, I derive the day side temperature assuming that some fraction, P_n , of the stellar flux incident on the day side is redistributed to the night side. Both the above formalism and the following one are used in the literature. This derivation is based on the workings in Haswell (2010) and more details can be found there. As before, the stellar flux incident on the planet is given by

$$F_{\text{in}} = \frac{\pi R_p^2 R_{\star}^2 \sigma_{SB} T_{\star}^4}{a^2}. \quad (\text{D.28})$$

If the planet reflects some fraction of the incident stellar light, then the stellar flux absorbed by the planet is

$$F_{\text{in}} = (1 - A_B) \frac{\pi R_p^2 R_\star^2 \sigma_{SB} T_\star^4}{a^2}. \quad (\text{D.29})$$

Assuming equilibrium and that the two hemispheres of the planet have equal surface area gives

$$(1 - A_B) \frac{\pi R_p^2 R_\star^2 \sigma_{SB} T_\star^4}{a^2} = 2\pi R_p^2 \sigma_{SB} T_{\text{day}}^4 + 2\pi R_p^2 \sigma_{SB} T_{\text{night}}^4, \quad (\text{D.30})$$

where T_{day} is the temperature of the planet's day side and T_{night} is the temperature of the planet's night side. Knowing how much energy reaches the planet and the fraction of energy distributed to the night side, it can be seen that

$$(1 - P_n)F_{\text{in}} = 2\pi R_p^2 \sigma_{SB} T_{\text{day}}^4 \quad \text{and} \quad P_n F_{\text{in}} = 2\pi R_p^2 \sigma_{SB} T_{\text{night}}^4. \quad (\text{D.31})$$

Therefore, for the day side temperature, substituting into Equation (D.31) using Equation (D.29) gives:

$$(1 - P_n)(1 - A_B) \frac{\pi R_p^2 R_\star^2 \sigma_{SB} T_\star^4}{a^2} = 2\pi R_p^2 \sigma_{SB} T_{\text{day}}^4$$

$$\Rightarrow T_{\text{day}}^4 = \frac{1}{2} (1 - P_n)(1 - A_B) \left(\frac{R_\star}{a}\right)^2 T_\star^4 \quad (\text{D.32})$$

D.6 Equations for Grating Spectrometers

Here, I derive the grating equations for a transmission and reflection grating based on the derivations given in Palmer (2005). Firstly, consider light which is incident on a transmission grating at an angle perpendicular to the grating surface. Figure 5 shows the setup.

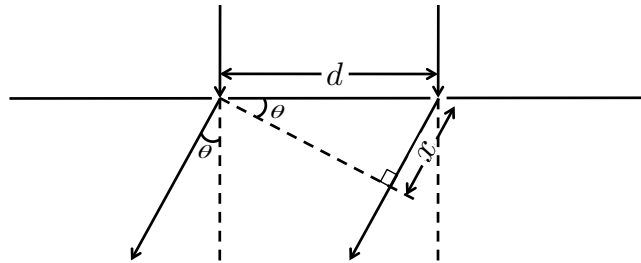


Figure 5: Illustration of the path of light through a transmission grating. The light is incident on the grating at an angle perpendicular to the grating surface, and is then deflected by the grating with an angle θ .

In order to have constructive interference, the light from the two incident rays must be in phase with one another. This can only happen if the path difference, x , is a

whole number of complete wavelengths. This means that $x = m\lambda$, where $m = 0, 1, 2, 3, \dots$. From Figure 5, it can be seen that the distance x is given by $x = d \sin \theta$. Therefore, the points at which maxima occur are given by:

$$m\lambda = d \sin \theta \quad m = 0, 1, 2, 3, \dots \quad (\text{D.33})$$

This is one form of the grating equation. The grating equation is different if the light incident on the grating is at an angle, α , to the grating normal. I will illustrate this case using a reflection grating, but the principle is the same for a transmission grating. Figure 6 shows a reflection grating with incoming light incident at an angle α to the grating normal.

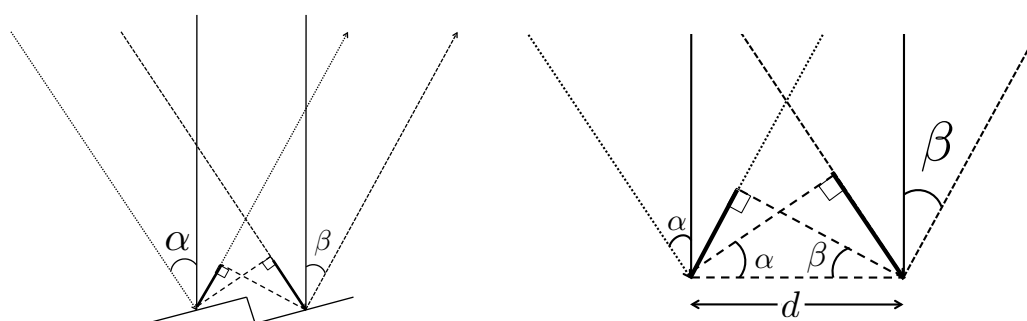


Figure 6: Illustration of the path of light through a reflection grating, adapted from Palmer (2005). The light is incident on the grating at an angle α to the grating normal. The light is then reflected so that it is at an angle β to the grating normal. The left picture shows the setup as a whole, while the right picture shows a zoomed-in portion so that it is easier to see how the path difference between the two light beams is calculated.

In the case of incident light at an angle to the grating normal, there is a path difference between the two incoming light beams and between the two outgoing light beams. In order to have constructive interference, the total path difference must be an integer number of wavelengths. The path difference between the incoming light beams can be seen from Figure 6 to be $d \sin \alpha$, and the path difference between the outgoing light beams is $d \sin \beta$. The total path difference is then $d \sin \alpha + d \sin \beta$. As before, maxima occur where the path difference is equal to $m\lambda$, which means that maxima occur when

$$m\lambda = d(\sin \alpha + \sin \beta), \quad (\text{D.34})$$

which is the more general grating equation.

Bibliography

- Abe, L., Gonçalves, I., Agabi, A., et al. 2013, *A&A*, 553, A49
- Agol, E., Cowan, N. B., Knutson, H. A., et al. 2010, *ApJ*, 721, 1861
- Aigrain, S., Pont, F., & Zucker, S. 2012, *MNRAS*, 419, 3147
- Akaike, H. 1974a, *IEEE Transactions on Automatic Control*, 19, 716
- Akaike, H. 1974b, *IEEE Transactions on Automatic Control*, 19, 667
- Anderson, D. R., Gillon, M., Maxted, P. F. L., et al. 2010, *A&A*, 513, L3+
- Anderson, D. R., Smith, A. M. S., Madhusudhan, N., et al. 2013, *MNRAS*, 430, 3422
- Arribas, S., Gilliland, R. L., Sparks, W. B., et al. 2006, *PASP*, 118, 21
- Astudillo-Defru, N. & Rojo, P. 2013, *A&A*, 557, A56
- Ballester, G. E., Sing, D. K., & Herbert, F. 2007, *Nature*, 445, 511
- Barman, T. 2007, *ApJL*, 661, L191
- Baskin, N. J., Knutson, H. A., Burrows, A., et al. 2013, *ApJ*, 773, 124
- Bean, J. L., Désert, J.-M., Kabath, P., et al. 2011, *ApJ*, 743, 92
- Bean, J. L., Désert, J.-M., Seifahrt, A., et al. 2013, *ApJ*, 771, 108
- Bean, J. L., Miller-Ricci Kempton, E., & Homeier, D. 2010, *Nature*, 468, 669
- Beaulieu, J. P., Carey, S., Ribas, I., & Tinetti, G. 2008, *ApJ*, 677, 1343
- Beaulieu, J. P., Kipping, D. M., Batista, V., et al. 2010, *MNRAS*, 409, 963
- Ben-Jaffel, L. & Ballester, G. E. 2013, *A&A*, 553, A52
- Bergfors, C., Brandner, W., Daemgen, S., et al. 2013, *MNRAS*, 428, 182
- Bergfors, C., Brandner, W., Henning, T., & Daemgen, S. 2011, in *IAU Symposium*, Vol. 276, IAU Symposium, ed. A. Sozzetti, M. G. Lattanzi, & A. P. Boss, 397–398
- Berta, Z. K., Charbonneau, D., Désert, J.-M., et al. 2012, *ApJ*, 747, 35
- Bevington, P. R. & Robinson, D. K. 2003, *Data Reduction and Error Analysis for the Physical Sciences*, 3rd edn. (McGraw Hill)
- Bigot, L., Kervella, P., Thévenin, F., & Ségransan, D. 2006, *A&A*, 446, 635
- Blecic, J., Harrington, J., Madhusudhan, N., et al. 2011, *ArXiv e-prints*, 1111.2363
- Blecic, J., Harrington, J., Madhusudhan, N., et al. 2013, *ArXiv e-prints*, 1302.7003
- Bourrier, V., Lecavelier des Etangs, A., Dupuy, H., et al. 2013, *A&A*, 551, A63
- Brown, T. M. 2001, *ApJ*, 553, 1006
- Burrows, A., Budaj, J., & Hubeny, I. 2008, *ApJ*, 678, 1436
- Burrows, A., Hubbard, W. B., Lunine, J. I., & Liebert, J. 2001, *Reviews of Modern Physics*, 73, 719

- Burrows, A., Hubeny, I., Budaj, J., Knutson, H. A., & Charbonneau, D. 2007, *ApJL*, 668, L171
- Burrows, A., Rauscher, E., Spiegel, D. S., & Menou, K. 2010, *ApJ*, 719, 341
- Burrows, A. & Sharp, C. M. 1999, *ApJ*, 512, 843
- Burrows, A., Sudarsky, D., & Hubeny, I. 2006, *ApJ*, 650, 1140
- Burton, J. R., Watson, C. A., Littlefair, S. P., et al. 2012, *ApJS*, 201, 36
- Carter, J. A. & Winn, J. N. 2009, *ApJ*, 704, 51
- Cepa, J., Aguiar, M., Escalera, V. G., et al. 2000, in *Society of Photo-Optical Instrumentation Engineers (SPIE) Conference Series*, ed. M. Iye & A. F. Moorwood, Vol. 4008, 623–631
- Cepa, J., Aguiar-Gonzalez, M., Bland-Hawthorn, J., et al. 2003, in *Society of Photo-Optical Instrumentation Engineers (SPIE) Conference Series*, ed. M. Iye & A. F. M. Moorwood, Vol. 4841, 1739–1749
- Chamberlain, J. W. & Hunten, D. M. 1987, *Theory of planetary atmospheres: An introduction to their physics and chemistry* (Academic Press, Orlando)
- Charbonneau, D., Berta, Z. K., Irwin, J., et al. 2009, *Nature*, 462, 891
- Charbonneau, D., Brown, T. M., Latham, D. W., & Mayor, M. 2000, *ApJL*, 529, L45
- Charbonneau, D., Brown, T. M., Noyes, R. W., & Gilliland, R. L. 2002, *ApJ*, 568, 377
- Charbonneau, D., Knutson, H. A., Barman, T., et al. 2008, *ApJ*, 686, 1341
- Christiansen, J. L., Ballard, S., Charbonneau, D., et al. 2011, *ApJ*, 726, 94
- Christie, D., Arras, P., & Li, Z.-Y. 2013, *ApJ*, 772, 144
- Claret, A. 2000, *A&A*, 363, 1081
- Colón, K. D., Ford, E. B., Redfield, S., et al. 2012, *MNRAS*, 419, 2233
- Copperwheat, C. M., Wheatley, P. J., Southworth, J., et al. 2013, *MNRAS*, 434, 661
- Cowan, N. B. & Agol, E. 2011, *ApJ*, 729, 54
- Cowan, N. B., Agol, E., & Charbonneau, D. 2007, *MNRAS*, 379, 641
- Cowan, N. B., Machalek, P., Croll, B., et al. 2012, *ApJ*, 747, 82
- Croll, B., Albert, L., Jayawardhana, R., et al. 2011a, *ApJ*, 736, 78
- Croll, B., Lafreniere, D., Albert, L., et al. 2011b, *AJ*, 141, 30
- Crossfield, I. J. M., Barman, T., & Hansen, B. M. S. 2011, *ApJ*, 736, 132
- Crossfield, I. J. M., Barman, T., Hansen, B. M. S., Tanaka, I., & Kodama, T. 2012a, *ApJ*, 760, 140
- Crossfield, I. J. M., Hansen, B. M. S., & Barman, T. 2012b, *ApJ*, 746, 46
- Crossfield, I. J. M., Hansen, B. M. S., Harrington, J., et al. 2010, *ApJ*, 723, 1436
- Crossfield, I. J. M., Knutson, H., Fortney, J., et al. 2012c, *ApJ*, 752, 81
- Crouzet, N., McCullough, P. R., Burke, C., & Long, D. 2012, *ApJ*, 761, 7
- Cumming, A., Butler, R. P., Marcy, G. W., et al. 2008, *PASP*, 120, 531
- de Kok, R. J., Brogi, M., Snellen, I. A. G., et al. 2013, *A&A*, 554, A82
- de Kok, R. J., Helling, C., Stam, D. M., Woitke, P., & Witte, S. 2011, *A&A*, 531, A67
- de Mooij, E. J. W., Brogi, M., de Kok, R. J., et al. 2012, *A&A*, 538, A46
- de Mooij, E. J. W., Brogi, M., de Kok, R. J., et al. 2013, *ApJ*, 771, 109
- de Pater, I. & Lissauer, J. 2010, *Planetary Sciences*, 2nd edn. (Cambridge University Press)
- Deming, D., Brown, T. M., Charbonneau, D., Harrington, J., & Richardson, L. J. 2005, *ApJ*, 622, 1149

- Deming, D., Harrington, J., Seager, S., & Richardson, L. J. 2006, *ApJ*, 644, 560
- Deming, D., Wilkins, A., McCullough, P., et al. 2013, *ApJ*, 774, 95
- Désert, J.-M., Bean, J., Miller-Ricci Kempton, E., et al. 2011a, *ApJL*, 731, L40+
- Désert, J.-M., Lecavelier des Etangs, A., Hébrard, G., et al. 2009, *ApJ*, 699, 478
- Désert, J.-M., Sing, D., Vidal-Madjar, A., et al. 2011b, *A&A*, 526, A12+
- Désert, J.-M., Vidal-Madjar, A., Lecavelier Des Etangs, A., et al. 2008, *A&A*, 492, 585
- Dragomir, D., Kane, S. R., Pilyavsky, G., et al. 2011, *AJ*, 142, 115
- Eastman, J., Gaudi, B. S., & Agol, E. 2013, *PASP*, 125, 83
- Efron, B. 1979, *The Annals of Statistics*, 7, 1
- Ehrenreich, D., Bourrier, V., Bonfils, X., et al. 2012, *A&A*, 547, A18
- Ehrenreich, D. & Désert, J.-M. 2011, *A&A*, 529, A136+
- Ehrenreich, D., Hébrard, G., Lecavelier des Etangs, A., et al. 2007, *ApJL*, 668, L179
- Ehrenreich, D., Lecavelier Des Etangs, A., & Delfosse, X. 2011, *A&A*, 529, A80+
- Evans, T. M., Pont, F., Sing, D. K., et al. 2013, *ApJL*, 772, L16
- Ford, E. B. 2006, *ApJ*, 642, 505
- Fortney, J. J. 2005, *MNRAS*, 364, 649
- Fortney, J. J., Lodders, K., Marley, M. S., & Freedman, R. S. 2008, *ApJ*, 678, 1419
- Fortney, J. J., Shabram, M., Showman, A. P., et al. 2010, *ApJ*, 709, 1396
- Fossati, L., Haswell, C. A., Froning, C. S., et al. 2010, *ApJL*, 714, L222
- Fraine, J. D., Deming, D., Gillon, M., et al. 2013, *ApJ*, 765, 127
- Freedman, R. S., Marley, M. S., & Lodders, K. 2008, *ApJS*, 174, 504
- Freytag, B., Allard, F., Ludwig, H.-G., Homeier, D., & Steffen, M. 2010, *A&A*, 513, A19
- García Muñoz, A. 2007, *Planet. Space Sci.*, 55, 1426
- Gelman, A., Carlin, J. B., Stern, H. S., & Rubin, D. B. 2003, *Bayesian Data Analysis*, 2nd edn. (Chapman and Hall/CRC)
- Gibson, N. P., Aigrain, S., Pollacco, D. L., et al. 2010, *MNRAS*, 404, L114
- Gibson, N. P., Aigrain, S., Pont, F., et al. 2012a, *MNRAS*, 422, 753
- Gibson, N. P., Aigrain, S., Roberts, S., et al. 2012b, *MNRAS*, 419, 2683
- Gibson, N. P., Pont, F., & Aigrain, S. 2011, *MNRAS*, 411, 2199
- Gillon, M., Demory, B.-O., Barman, T., et al. 2007, *A&A*, 471, L51
- Gough, D. 2012, *Science*, 337, 1611
- Grillmair, C. J., Burrows, A., Charbonneau, D., et al. 2008, *Nature*, 456, 767
- Grillmair, C. J., Charbonneau, D., Burrows, A., et al. 2007, *ApJL*, 658, L115
- Guillot, T. 2010, *A&A*, 520, A27+
- Hajian, A. R., Armstrong, J. T., Hummel, C. A., et al. 1998, *ApJ*, 496, 484
- Harrington, J., Hansen, B. M., Luszcz, S. H., et al. 2006, *Science*, 314, 623
- Haswell, C. A. 2010, *Transiting Exoplanets* (Cambridge University Press)
- Hayek, W., Sing, D., Pont, F., & Asplund, M. 2012, *A&A*, 539, A102
- Hebb, L., Collier-Cameron, A., Triaud, A. H. M. J., et al. 2010, *ApJ*, 708, 224
- Hellier, C., Anderson, D. R., Collier-Cameron, A., et al. 2011, *ApJL*, 730, L31+
- Heng, K., Hayek, W., Pont, F., & Sing, D. K. 2012, *MNRAS*, 420, 20

- Henry, G. W., Marcy, G. W., Butler, R. P., & Vogt, S. S. 2000, *ApJL*, 529, L41
- Henry, G. W. & Winn, J. N. 2008, *AJ*, 135, 68
- Hogg, D. W., Bovy, J., & Lang, D. 2010, *ArXiv e-prints*, 1008.4686
- Horne, J. H. & Baliunas, S. L. 1986, *ApJ*, 302, 757
- Howard, A. W. 2013, *Science*, 340, 572
- Howard, A. W., Marcy, G. W., Bryson, S. T., et al. 2012, *ApJS*, 201, 15
- Howard, A. W., Marcy, G. W., Johnson, J. A., et al. 2010, *Science*, 330, 653
- Howe, A. R. & Burrows, A. S. 2012, *ApJ*, 756, 176
- Howell, S. B. 2000, *Handbook of CCD Astronomy*, Cambridge Observing Handbooks for Research Astronomers (Cambridge University Press)
- Hubbard, W. B., Fortney, J. J., Lunine, J. I., et al. 2001, *ApJ*, 560, 413
- Hubeny, I., Burrows, A., & Sudarsky, D. 2003, *ApJ*, 594, 1011
- Huitson, C. M., Sing, D. K., Pont, F., et al. 2013, *ArXiv e-prints*, 1307.2083
- Huitson, C. M., Sing, D. K., Vidal-Madjar, A., et al. 2012, *MNRAS*, 422, 2477
- Iro, N., Bézard, B., & Guillot, T. 2005, *A&A*, 436, 719
- Jensen, A. G., Redfield, S., Endl, M., et al. 2012, *ApJ*, 751, 86
- Jensen, A. G., Redfield, S., Endl, M., et al. 2011, *ApJ*, 743, 203
- Kaspi, S., Brandt, W. N., Netzer, H., et al. 2001, *ApJ*, 554, 216
- Kitzmann, D., Patzer, A. B. C., von Paris, P., Godolt, M., & Rauer, H. 2011, *A&A*, 531, A62+
- Knutson, H. A., Charbonneau, D., Allen, L. E., Burrows, A., & Megeath, S. T. 2008, *ApJ*, 673, 526
- Knutson, H. A., Charbonneau, D., Allen, L. E., et al. 2007a, *Nature*, 447, 183
- Knutson, H. A., Charbonneau, D., Cowan, N. B., et al. 2009a, *ApJ*, 703, 769
- Knutson, H. A., Charbonneau, D., Cowan, N. B., et al. 2009b, *ApJ*, 690, 822
- Knutson, H. A., Charbonneau, D., Noyes, R. W., Brown, T. M., & Gilliland, R. L. 2007b, *ApJ*, 655, 564
- Knutson, H. A., Howard, A. W., & Isaacson, H. 2010, *ApJ*, 720, 1569
- Knutson, H. A., Lewis, N., Fortney, J. J., et al. 2012, *ApJ*, 754, 22
- Koskinen, T. T., Harris, M. J., Yelle, R. V., & Lavvas, P. 2012a, *ArXiv e-prints*, 1210.1536
- Koskinen, T. T., Yelle, R. V., Harris, M. J., & Lavvas, P. 2012b, *ArXiv e-prints*, 1210.1543
- Kundurthy, P., Barnes, R., Becker, A. C., et al. 2013, *ApJ*, 770, 36
- Lammer, H., Selsis, F., Ribas, I., et al. 2003, *ApJL*, 598, L121
- Lecavelier des Etangs, A., Bourrier, V., Wheatley, P. J., et al. 2012, *A&A*, 543, L4
- Lecavelier Des Etangs, A., Ehrenreich, D., Vidal-Madjar, A., et al. 2010, *A&A*, 514, A72
- Lecavelier Des Etangs, A., Pont, F., Vidal-Madjar, A., & Sing, D. 2008a, *A&A*, 481, L83
- Lecavelier Des Etangs, A., Vidal-Madjar, A., Désert, J.-M., & Sing, D. 2008b, *A&A*, 485, 865
- Lecavelier des Etangs, A., Vidal-Madjar, A., McConnell, J. C., & Hébrard, G. 2004, *A&A*, 418, L1
- Lendl, M., Gillon, M., Queloz, D., et al. 2013, *A&A*, 552, A2
- Lewis, N. K., Knutson, H. A., Showman, A. P., et al. 2013, *ApJ*, 766, 95
- Linsky, J. L., Yang, H., France, K., et al. 2010, *ApJ*, 717, 1291

- Llama, J., Wood, K., Jardine, M., et al. 2011, *MNRAS*, 416, L41
- Lodders, K. 1999, *ApJ*, 519, 793
- Lodders, K. 2002, *ApJ*, 577, 974
- Lodders, K. 2003, *ApJ*, 591, 1220
- Lodders, K. 2009, ArXiv e-prints, 0910.0811
- Lodders, K. & Fegley, B. 2002, *Icarus*, 155, 393
- Lomb, N. 1976, *Astrophysics and Space Science*, 39, 447
- López-Morales, M. 2011, in *Highlights of Spanish Astrophysics VI*, ed. M. R. Zapatero Osorio, J. Gorgas, J. Maíz Apellániz, J. R. Pardo, & A. Gil de Paz, 60–72
- López-Morales, M., Coughlin, J. L., Sing, D. K., et al. 2010, *ApJL*, 716, L36
- López-Morales, M. & Seager, S. 2007, *ApJL*, 667, L191
- Madhusudhan, N. 2012, *ApJ*, 758, 36
- Madhusudhan, N., Harrington, J., Stevenson, K. B., et al. 2011a, *Nature*, 469, 64
- Madhusudhan, N., Mousis, O., Johnson, T. V., & Lunine, J. I. 2011b, *ApJ*, 743, 191
- Mancini, L., Ciceri, S., Chen, G., et al. 2013, ArXiv e-prints, 1306.6384
- Mandel, K. & Agol, E. 2002, *ApJL*, 580, L171
- Mandell, A. M., Drake Deming, L., Blake, G. A., et al. 2011, *ApJ*, 728, 18
- Mandell, A. M., Haynes, K., Sinukoff, E., et al. 2013, submitted
- Markwardt, C. B. 2009, in *ASPC Conf. Ser.*, Vol. 411, *Astronomical Data Analysis Software and Systems XVIII*, ed. D. A. Bohlender, D. Durand, & P. Dowler, 251
- Marquardt, D. W. 1963, *Journal of the Society for Industrial and Applied Mathematics*, 11, 431
- Mathews, J. H. & Fink, K. K. 2004, *Numerical Methods Using Matlab*, 4th edn. (Prentice Hall)
- Maxted, P. F. L., Anderson, D. R., Doyle, A. P., et al. 2013, *MNRAS*, 428, 2645
- Mayor, M., Marmier, M., Lovis, C., et al. 2011, ArXiv e-prints, 1109.2497
- Mayor, M. & Queloz, D. 1995, *Nature*, 378, 355
- Mérand, A., Kervella, P., Barban, C., et al. 2010, *A&A*, 517, A64
- Morley, C. V., Fortney, J. J., Marley, M. S., et al. 2012, *ApJ*, 756, 172
- Moses, J. I., Madhusudhan, N., Visscher, C., & Freedman, R. S. 2013, *ApJ*, 763, 25
- Moses, J. I., Visscher, C., Fortney, J. J., et al. 2011, *ApJ*, 737, 15
- Moutou, C., Pont, F., Bouchy, F., & Mayor, M. 2004, *A&A*, 424, L31
- Murgas, F., Pallé, E., Cabrera-Lavers, A., et al. 2012, *A&A*, 544, A41
- Narita, N., Fukui, A., Ikoma, M., et al. 2013a, *ApJ*, 773, 144
- Narita, N., Nagayama, T., Suenaga, T., et al. 2013b, *PASJ*, 65, 27
- Narita, N., Suto, Y., Winn, J. N., et al. 2005, *PASJ*, 57, 471
- Nelder, J. A. & Mead, R. 1965, *Computer Journal*, 7, 308
- Nikolov, N., Chen, G., Fortney, J. J., et al. 2013a, *A&A*, 553, A26
- Nikolov, N., Sing, D. K., Pont, F., et al. 2013b, *MNRAS*, submitted
- Noyes, R. W., Hartmann, L. W., Baliunas, S. L., Duncan, D. K., & Vaughan, A. H. 1984, *ApJ*, 279, 763
- Palmer, C. 2005, *Diffraction Grating Handbook* (Richardson Gratings, Newport Corporation)
- Parmentier, V., Showman, A. P., & Lian, Y. 2013, ArXiv e-prints, 1301.4522

- Perez-Becker, D. & Showman, A. P. 2013, ArXiv e-prints, 1306.4673
- Perna, R., Heng, K., & Pont, F. 2012, *ApJ*, 751, 59
- Petigura, E. A., Marcy, G. W., & Howard, A. W. 2013, *ApJ*, 770, 69
- Pierrehumbert, R. T. 2010, *Principles of Planetary Climate* (Cambridge University Press)
- Pillitteri, I., Günther, H. M., Wolk, S. J., Kashyap, V. L., & Cohen, O. 2011, *ApJL*, 741, L18
- Pillitteri, I., Wolk, S. J., Cohen, O., et al. 2010, *ApJ*, 722, 1216
- Pont, F., Gilliland, R. L., Moutou, C., et al. 2007, *A&A*, 476, 1347
- Pont, F., Knutson, H., Gilliland, R. L., Moutou, C., & Charbonneau, D. 2008, *MNRAS*, 385, 109
- Pont, F., Sing, D. K., Gibson, N. P., et al. 2013, *MNRAS*, 432, 2917
- Pont, F., Zucker, S., & Queloz, D. 2006, *MNRAS*, 373, 231
- Poppenhaeger, K., Schmitt, J. H. M. M., & Wolk, S. J. 2013, *ApJ*, 773, 62
- Press, W. H., Teukolsky, S. A., Vetterling, W. T., & Flannery, B. P. 2007, *Numerical Recipes in C: The Art of Scientific Computing*, 2nd edn. (Foundation Books)
- Quenouille, M. H. 1949, *Journal of the Royal Statistical Society*, 11, 68
- Redfield, S., Endl, M., Cochran, W. D., & Koesterke, L. 2008, *ApJL*, 673, L87
- Richardson, L. J., Harrington, J., Seager, S., & Deming, D. 2006, *ApJ*, 649, 1043
- Roberts, G. O., Gelman, A., & Gilks, W. R. 1997, *The Annals of Applied Probability*, 7, 110
- Rodler, F., Kürster, M., & Barnes, J. R. 2013, *MNRAS*, 432, 1980
- Rogers, J. C., Apai, D., López-Morales, M., Sing, D. K., & Burrows, A. 2009, *ApJ*, 707, 1707
- Rybicki, G. B. & Lightman, A. P. 1979, *Radiative Processes in Astrophysics* (Wiley)
- Scargle, J. 1982, *ApJ*, 263, 835
- Schwarz, G. 1978, *The Annals of Statistics*, 6, 461
- Seager, S. 2010, *Exoplanet Atmospheres; Physical Processes*, Princeton Series in Astrophysics (Princeton University Press)
- Seager, S. & Mallén-Ornelas, G. 2003, *ApJ*, 585, 1038
- Seager, S. & Sasselov, D. D. 2000, *ApJ*, 537, 916
- Seager, S., Whitney, B. A., & Sasselov, D. D. 2000, *ApJ*, 540, 504
- Shabram, M., Fortney, J. J., Greene, T. P., & Freedman, R. S. 2011, *ApJ*, 727, 65
- Sharp, C. M. & Burrows, A. 2007, *ApJS*, 168, 140
- Showman, A. P., Fortney, J. J., Lian, Y., et al. 2009, *ApJ*, 699, 564
- Showman, A. P. & Guillot, T. 2002, *A&A*, 385, 166
- Showman, A. P. & Polvani, L. M. 2011, *ApJ*, 738, 71
- Sing, D. K. 2010, *A&A*, 510, A21
- Sing, D. K., Désert, J.-M., Fortney, J. J., et al. 2011a, *A&A*, 527, A73+
- Sing, D. K., Désert, J.-M., Lecavelier Des Etangs, A., et al. 2009, *A&A*, 505, 891
- Sing, D. K., Huitson, C. M., Lopez-Morales, M., et al. 2012, *MNRAS*, 426, 1663
- Sing, D. K., Lecavelier des Etangs, A., Fortney, J. J., et al. 2013, *MNRAS*, submitted
- Sing, D. K., Pont, F., Aigrain, S., et al. 2011b, *MNRAS*, 416, 1443
- Sing, D. K., Vidal-Madjar, A., Désert, J.-M., Lecavelier des Etangs, A., & Ballester, G. 2008a, *ApJ*, 686, 658
- Sing, D. K., Vidal-Madjar, A., Lecavelier des Etangs, A., et al. 2008b, *ApJ*, 686, 667

- Smith, A. M. S., Anderson, D. R., Madhusudhan, N., et al. 2012, *A&A*, 545, A93
- Snellen, I. A. G., Albrecht, S., de Mooij, E. J. W., & Le Poole, R. S. 2008, *A&A*, 487, 357
- Snellen, I. A. G., de Kok, R. J., de Mooij, E. J. W., & Albrecht, S. 2010, *Nature*, 465, 1049
- Spiegel, D. S. & Burrows, A. 2010, *ApJ*, 722, 871
- Spiegel, D. S., Silverio, K., & Burrows, A. 2009, *ApJ*, 699, 1487
- Steffen, J. H., Ragozzine, D., Fabrycky, D. C., et al. 2012, *Proceedings of the National Academy of Science*, 109, 7982
- Stevenson, K. B., Bean, J. L., Seifahrt, A., et al. 2013, *ArXiv e-prints*, 1305.1670
- Stevenson, K. B., Harrington, J., Fortney, J. J., et al. 2012a, *ApJ*, 754, 136
- Stevenson, K. B., Harrington, J., Lust, N. B., et al. 2012b, *ApJ*, 755, 9
- Sudarsky, D., Burrows, A., & Pinto, P. 2000, *ApJ*, 538, 885
- Swain, M., Deroo, P., Tinetti, G., et al. 2013, *Icarus*, 225, 432
- Swain, M. R., Deroo, P., Griffith, C. A., et al. 2010, *Nature*, 463, 637
- Swain, M. R., Vasisht, G., & Tinetti, G. 2008, *Nature*, 452, 329
- Swain, M. R., Vasisht, G., Tinetti, G., et al. 2009, *ApJL*, 690, L114
- ter Braak, C. J. F. 2006, *Statistics and Computing*, 16, 239
- Teske, J. K., Turner, J. D., Mueller, M., & Griffith, C. A. 2013, *MNRAS*, 431, 1669
- Tian, F., Toon, O. B., Pavlov, A. A., & De Sterck, H. 2005, *ApJ*, 621, 1049
- Tinetti, G., Deroo, P., Swain, M. R., et al. 2010, *ApJL*, 712, L139
- Tinetti, G., Vidal-Madjar, A., Liang, M.-C., et al. 2007, *Nature*, 448, 169
- Torres, G., Andersen, J., & Giménez, A. 2010, *A&A Rev.*, 18, 67
- Tregloan-Reed, J., Southworth, J., & Tappert, C. 2013, *MNRAS*, 428, 3671
- Vidal-Madjar, A., Désert, J.-M., Lecavelier des Etangs, A., et al. 2004, *ApJL*, 604, L69
- Vidal-Madjar, A., Huitson, C. M., Lecavelier Des Etangs, A., et al. 2011a, *A&A*, 533, C4
- Vidal-Madjar, A., Lecavelier des Etangs, A., Désert, J.-M., et al. 2003, *Nature*, 422, 143
- Vidal-Madjar, A., Sing, D. K., Lecavelier Des Etangs, A., et al. 2011b, *A&A*, 527, A110
- Visscher, C., Lodders, K., & Fegley, Jr., B. 2006, *ApJ*, 648, 1181
- Wakeford, H. R., Sing, D. K., Deming, D., et al. 2013, *ArXiv e-prints*, 1308.2106
- Waldmann, I. P., Tinetti, G., Drossart, P., et al. 2012, *ApJ*, 744, 35
- Wall, J. V. & Jenkins, C. R. 2009, *Practical Statistics for Astronomers*, Cambridge Observing Handbooks for Research Astronomers (Cambridge University Press)
- Winn, J. N., Holman, M. J., Bakos, G. Á., et al. 2007, *AJ*, 134, 1707
- Winn, J. N., Holman, M. J., Torres, G., et al. 2008, *ApJ*, 683, 1076
- Wolszczan, A. & Frail, D. A. 1992, *Nature*, 355, 145
- Wolter, U., Schmitt, J. H. M. M., Huber, K. F., et al. 2009, *A&A*, 504, 561
- Wood, P. L., Maxted, P. F. L., Smalley, B., & Iro, N. 2011, *MNRAS*, 412, 2376
- Wright, J. T., Marcy, G. W., Howard, A. W., et al. 2012, *ApJ*, 753, 160
- Yelle, R. V. 2004, *Icarus*, 170, 167
- Young, G. A. & Smith, R. L. 2010, *Essentials of Statistical Inference*, Cambridge Series in Statistical and Probabilistic Mathematics (Cambridge University Press)
- Zahnle, K., Marley, M. S., & Fortney, J. J. 2009a, *ArXiv e-prints*, 0911.0728

-
- Zahnle, K., Marley, M. S., Freedman, R. S., Lodders, K., & Fortney, J. J. 2009b, *ApJL*, 701, L20
- Zhao, M., Monnier, J. D., Swain, M. R., Barman, T., & Hinkley, S. 2012, *ApJ*, 744, 122
- Zhou, G. & Bayliss, D. D. R. 2012, *MNRAS*, 426, 2483